THÈSE

Présentée à

L'UNIVERSITÉ BORDEAUX 1

ÉCOLE DOCTORALE DES SCIENCES CHIMIQUES

Par

Min-Tzu Kao

Pour obtenir le grade de

DOCTEUR

SPÉCIALITÉ : CHIMIE

Nano-rubans et cristaux anisotropes d'anthracènes et tétracènes à émission accordable : étude de la photophysique et des transferts d'énergie par microscopie confocale de fluorescence

Directeur de thèse : Dr. André Del Guerzo

Soutenance prévue le 12 décembre 2012

COMMISSION D'EXAMEN :

Mme Evelyne FARGIN, Professeur (Université Bordeaux1)	Président
Mme Suzanne FERY-FORGUES, Directeur de recherche (CNRS, Toulouse)	Rapporteur
M. Ross BROWN, Directeur de recherche (CNRS, Pau)	Rapporteur
M. Rémi MÉTIVIER, Chargé de Recherche (CNRS, Paris)	Examinateur
M. André DEL GUERZO, Maître de Conférences (Université Bordeaux 1)	Directeur de thèse

Acknowledgement

First, I would like to express my sincere gratitude to my advisor, Dr. André Del Guerzo (ISM) in University Bordeaux 1. Without his encouragement and scientific inspiration, this thesis can never be completed. During these years in France, numerous problems both in science and daily life depressed me a lot. There're several times, the thoughts of giving up almost overwhelmed me. However, the understanding and faith you've shown me gave me the strength to keep going and finally overcame those challenges. I am really glad to have him as my supervisor.

Next, I would like to thank the people who contributed a lot in these projects. Mr. Guillaume Raffy, without your patient guidance I would never be able to do any experiment by CFM. And all the wonderful software you developed by Labview are extremely helpful for data analysis and simulation. Also Dr. Christian Schäfer, who synthesized most of the compounds I studied and then established all the synthetic routes. Dr. Carlo Giansante, who instructed me about all the instruments and experimental details to allow me measure photophysical properties of samples. Dr. Stéphane Massip, who helped us to obtain all the crystal structures of our compounds. Ms. Colette Belin for AFM measurements. And Région Aquitane for the funding of my fellowship. Without any of you I wouldn't be able to accomplish my works.

And then I want to thank all the dearest NEO members, all the professors and team members. You guys saved my life several times, helping me to survive in a foreign country with an extremely high language barrier. Thank you so much for creating such a great atmosphere in the group and sharing experiences.

In the end, I would like to thank my family and all my friends for all the supports and care.

Résumé

De nouveaux nano-objets anisotropes fluorescents sont obtenus par l'assemblage d'acènes spécifiquement conçus. Dans des cristaux, nano-rubans et nanoparticules anisotropes de 2,3-dialkyldiphenylanthracènes, les efficacités et la polarisation de l'émission bleue sont remarquables. La couleur de l'émission est accordée par le dopage avec des émetteurs verts et oranges (di- et tétra-phényltétracènes). La microscopie confocale de fluorescence permet d'étudier les cinétiques des états excités et des transferts d'énergie photo-induits, ainsi que la dispersion et les orientations des émetteurs. Pour la première fois, l'influence de la largeur de nano-rubans sur la cinétique d'annihilations triplet-triplet de tétracènes est mise en évidence. La microscopie révèle également le polymorphisme inhabituel d'un dérivé diéthynylphényl-anthracène. Ce travail ouvre des perspectives pour le développement et l'étude de processus fondamentaux de nano-matériaux luminescents.

Mots clés : microscopie confocale de fluorescence, transferts d'énergie, nano-matériaux, annihilations triplet-triplet, auto-assemblage, anthracène, tetracène

Abstract

New fluorescent anisotropic nano-objects are obtained by the assembly of specifically designed acenes. In crystals, nano-ribbons and anisotropic nanoparticles of 2,3-dialkyldiphenylanthracenes, the efficiencies and the polarization of the blue emission is remarkable. The color of the emission is tuned by doping with green and orange emitters (di-and tetra-phenyltetracenes). Confocal fluorescence microscopy is used to study the kinetics of excited states and photo-induced energy transfers, as well as the dispersion and orientation of the emitters. For the first time, the influence of the width of the nano-ribbons on the kinetics of tetracene triplet-triplet annihilations is highlighted. Microscopy also reveals the unusual polymorphism of a diethynylphenyl anthracene derivative. This work opens perspectives for the development and study of fundamental processes of luminescent nano-materials.

Keywords: confocal fluorescence microscopy, energy transfer, nano-materials, triplet-triplet annihilation, self-assembly, anthracene, tetracene

Summary

Nanomaterials based on low-molecular-weight organic compounds with unique optical and electronic functionalities are explored in photonics for light generation, optical information treatment and energy transport. 2,3-dialkoxy substituted linear acenes, with significantly improved solubility compared to pure acenes have been extensively explored as good candidates to fabricate nanostructures.[1] Nevertheless, limitations have been due to their sensitivity to photo-degradation and insufficient emission quantum yields in the solid state.[2]

To achieve a breakthrough, a substitution in the 9,10 position is required. Since this modification was known to impede the formation of structures identical to those of previously studied acenes, new approaches in the molecular design and nanostructure formation had to be adopted.

In a first system, a series of 9,10-substituted anthracene derivatives are synthesized and used to construct nanostructures via self-assembly.

9,10-diphenyl substituted anthracenes (**B**s) with different length of dialkoxy chains can tune the molecular packing and photophysical properties in the solid state.

Bs with short side chains are crystallized easily and their packing, determined by X-ray crystallography, slightly differs from that of 9,10-diphenylanthracene. It yields blue emitting crystals (CIE: x=0.154, y=0.033) displaying an exceptional fluorescence quantum yield of up to 97%. The polarization of the emission of single anisotropic crystals has been measured by confocal fluorescence microscopy (CFM) and reaches very high values of 0.75 (on a scale limited to 1). The increase of the chain length reduces the size of the needle/fiber-like crystals. Furthermore, the crystal structures show that the angle between the planes of the emissive anthracene core decreases, leading to an almost co-planar packing of all the emitters of the octyl derivative. In contrast, with hexadecyl chains ribbons typically 100 nm high and 1 μm wide are formed. These also emit highly polarized light, although with lower quantum yields of 33% and inhomogeneous decay times distributions.

Since the dimethoxy substituted diphenyl anthracene **B1** is shown to exhibit exceptional photophysical properties in the solid state, it is chosen to be nano-sized and then investigated as a light-harvesting matrix to perform excitation energy transfer study.

Uniformly sized **B1** nanorods (length: ~4μm, width: 300-500 nm) which exhibit polarized blue emission ($-0.40 < P < 0.35$) are fabricated in aqueous solution with assistance of CTAB as a soft template, the morphology of nanorods being revealed by optical transmission microscopy and SEM. A specifically designed green emitting **GT1** is synthesized and co-assembled with **B1** to yield color-tunable and distinguishable dual color emission nanorods. The color tuning is achieved by excitation energy transfer from the blue light-emitting **B1** to the green light emitting **GT1**, which is revealed by steady state and dynamic emission spectroscopy. Microscopy studies reveal that the dual color emission from single nanorods is due to the higher concentration of **GT1** molecules in the central part of the nanorods.

The heterogeneity of **GT1** distribution in the NRs is first revealed by the FLIM images (fluorescent lifetime microscopy imaging) recorded with CFM and further investigated by

spectroscopy coupled with CFM to measure the emission spectra of single nanoobjects. In addition, the heterogeneity of **GT1** distribution further supported the proposed NRs formation mechanism and also shows the difficulty to homogeneously dope the nano-scaled light-harvesting matrices and simultaneously preserve the original structures.

B16 is shown to form nano-ribbons through recrystallization in the previous chapter and was also used as light-harvesting nanoscaled matrices. These are doped with highly fluorescent tetracenes (**G16**, **R16**) to yield nanoribbons with tunable photophysical properties. Two component (**B16—G16**, **B16—R16**) and three component (**B16—G16—R16**) nanoribbons are therefore fabricated and investigated. SEM images of nanoribbons revealed that the morphology of nanoribbons (length: tens of μm, width: 0.5~1.0 μm) and further indicated that it is not influenced by the addition of small amount of dopants (0.01 e.q. of **G16**; 0.02 e.q. of **R16**).

The homogeneous dispersion of the acceptors, within the range of maximum 2% equivalents each, is suggested by the steady variation of the spectral properties of the NBs with increasing doping concentrations of the tetracenes. This property yields color-tunable fluorescent nanoribbons, showing controllable blue, green, orange and white-light polarized emission (-0.50 to +0.35). The CIE coordinates can be fine-tuned, by adapting the proportions of **B16**, **G16** and **R16**, within the range of values determined by the extreme concentrations of **G16** and **R16** tested (Figure 1).

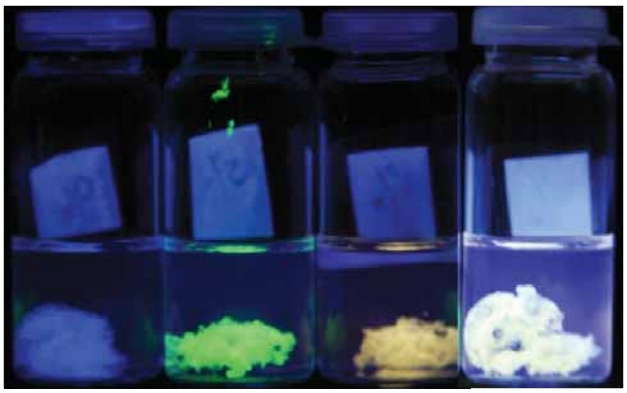

Figure 1: Picture of sample vials with pure **B16**, 1% G-NBs , 2% R-NB and 0.5% R-NB (from left to right) under UV light, λ_{ex} = 365 nm

Steady-state and time-resolved emission spectroscopy reveals that this color-tunable property of nanoribbons results from the partial excitation energy transfer occurring between the blue-emitting **B16** and the green-/red- emitting tetracenes. In a three component system, the latter emission is shown to be further sensitized through the green component.

CFM studies demonstrate that the nanoribbons individually emit light with similar photophysical properties in all the ribbons. The acceptor molecules are thus quite homogeneously dispersed into the ribbons. In addition, the polarization measurement allows us to gain an insight of the way these acceptor molecules are integrated into the nano-scaled

matrix.

Moreover, the delayed fluorescence of **G16** and **R16** sensitized by **B16** is revealed and characterized by CFM. The tails of **G16** and **R16** emission trace can be fitted with a t^{-2} power law, suggesting that a triplet-triplet annihilation process is involved. The slowest decay time of **G16** obtained by approximating the decays with a tri-exponential fitting is shown to be dependent with the density of excited states, indicating that a bi-molecular process such as a ^3T-^3T annihilation process is involved. This system provides thus also an interesting tuneable nano-system for the investigation of fundamental photophysical processes and the parameters that influence them. Triplet fusion and singlet fission are phenomena that could be optimized in these nano-systems with controlled assembly of tetracenes.

In the last part of this thesis, several 9,10-substituted **DDOA** derivatives are synthesized and investigated as novel organogelator candidates. The self-assembling properties are successfully induced with 2,3-didecyloxy substitutions and in some cases gelification occurs in the millimolar range. The extended conjugation along the short axis of the anthracene core induces the elongation of the transition dipole moment and the red-shift of the fluorescence from blue to green and yellow. Moreover, the quantum yield and the photostability increase.

DDPEA (9,10-bisphenylethynyl-DDOA), displays a very unusual polymorphism in the gel state. The variation of its photophysical properties in the aggregated state reveals that the **DDPEA** gel readily evolves into another more thermally stable state with time. The CFM study further shows that this kinetic metastable gel-state is constituted of nanofibers, while the thermodynamically stable state is constituted of crystal-like structures. Simultaneous observation of both morphs was also obtained.

The dicyano-substituted **DCNA** is shown to have the best gelation performance, but the quantum yield of emission is only slightly higher than that of **DDOA**. **DCNA** in solution displays solvent dependent emission due to the charge-transfer character of the excited state. However, this behaviour is not transferred to the aggregated state since in that case the gelator-gelator interactions lead to J-aggregates that emit with an energy lower to that of the charge transfer state. The **DCNA** gels emission is thus not sensitive to the solvent polarity. However, CFM and kinetic studies show that the solvent influences the fiber formation and that smaller gel fibers are formed in the nonpolar solvent (CYH), while larger ones are obtained in the polar solvent (ACE).

Two **DPA**-based (diphenylanthacene) organogelators with perfluorinated alkyl chains are synthesized to fabricate uniformly sized nanostructures. **F17** is designed according to the 2,3-dialkoxy substitution strategy, which demonstrated to provide highly emissive **DPAs** in the solid state. In contrast, **PT** is synthesized by esterification at 2- position of **DPA** with a perfluoro-ponytail-mono acid. The quantum yield of emission of **PT** nanofibers is only 20%, which is lower than other **DPA**s. However, **PT** gel fibers tend to entangle together to yield intriguing ponytail-like microstructures. These observations indicate that 2,3-alkyl chain substituted **DPAs** exhibit better photophysical properties in the solid state. However, the perfluorinated chain designs open new prospectives to tune microstructure formation.

References

1. Bouas-Laurent, H. ; Castellan, A. ; Desvergne, J.-P. ; Lapouyade, R. *Chem. Soc. Rev.* **2001**, *30*, 248.
2. Reichwagen, J.; Hopf, H.; Del Guerzo, A.; Belin, C.; Bouas-Laurent, H.; Desvergne, J.-P. *Org. Letters* **2005**, *7*, 971.

Outline

Chapter 1 General Introduction

Chapter 2 Crystals and nanorods of 9,10-diphenylanthracene derivatives

Chapter 5 Experimental Section

Chapter 1

General Introduction

1.1 Outline

Self-assembly of chemical species by weak non-covalent interactions is a widespread strategy exploited by nature in its forms and functions[1] and is attracting increasing interest in the realization of artificial systems.[2] Self-assembly has brought considerable advantages in the bottom-up approach to highly emissive multichromophoric nanostructures for light-harvesting and opto-electronic purposes.[3-6]

Extensive attention was drawn to self-assembly of low molecular weight organic chromophores into micro/nanostructures, not only in fundamental science but also in potential technological applications.[7-12] Many reports have demonstrated that the properties of these micro/nanostructures can be easily tailored by molecular design, chemical modification of their structures, doping treatment, or chemical conversion.

Linear acenes, i.e., linear condensed aromatic hydrocarbons such as anthracene, tetracene and pentacene, have been appreciated for years in solid-state photonics for their exceptional optical properties, and in the design of optically active molecular constituents for their efficient fluorescence and photochemistry.[13] However, the limited solubility of pure acenes and synthetic challenges has limited their applications and the knowledge of their properties (especially for tetracene and pentacene).

It is known that the substitution of the anthracene core by two long linear alkoxy chains (O-*n*-$C_{10}H_{21}$) at 2, 3 positions significantly improved the solubility of the materials which can be therefore easily dissolved in a large variety of common organic solvents. In fact, 2,3-didecyloxyanthracene (**DDOA**) has been exploited extensively as a super-gelator, in particular of alcohols[14] and polar solvents such as DMSO and formed also composite materials with nanoparticles, [15] aerogels in supercritical fluids[16] and mixed gels with charge-transfer interactions.[17] In particular, the soft organogel displayed blue fluorescence which could act as a light-harvesting matrix and be color-tuned by controllable sensitization of tetracene derivatives through efficient energy transfer processes.[18] 2,3-Didecyloxytetracene (**DDOT**) and 2,3-dihexadecyloxytetracene (**DHDOT**) yield orange-coloured solids [19] which are soluble in a large variety of organic solvents in contrast to the parent molecule tetracene. As predicted, these two compounds are able to rigidify organic fluids at low concentration, especially **DHDOT** (*n* = 5) (Scheme 1.1), which is more efficient than **DDOT** (*n* = 3) and could be considered as a supergelator. [20]

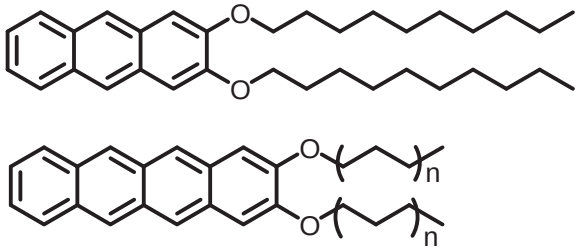

Scheme 1.1: molecular structure of **DDOA** and **D*n*OT**; n=3: **DDOT**, n=5: **DHDOT**

Although this linear acene system has a very good self-assembling ability, their performance and applications are limited by their photophysical properties especially in solid state. For **DDOA**, the quantum yield is 0.22 in THF solution, 0.10 in nanoparticles and 0.24 in DMSO gel. These not so impressive quantum yields are due to efficient intersystem crossing (ISC) from the singlet excited state to the second triplet state[21] of the anthracene core. For **D*n*OT**, the emission intensity significantly drops in the gel state compared to the monomer.[19]

Moreover, linear acenes are highly sensitive to photo-degradation, which can be attributed to the predominant electron density on some positions (9,10- for anthracene; 5,6,11,12- for tetracene). This also creates a lot of difficulties in experimental operation.

The aim of this thesis is to develop a novel system, which overcomes the limitation of linear acenes system and leads to highly emissive, robust and versatile nano-scaled matrices to allow further investigation on the intermolecular photophysical processes in nano-domain.

To achieve better photophysic performance in the mean time preserve a good self-assemble ability, the 2,3-alkoxy substituted skeleton is adapted and modified.

Recently, our group reported an individual fiber white light-emitting gel that is achieved by doping novel 5, 12-phenyl and 5,6,11,12-tetraphenyl tetracene derivatives into **DDOA** gel matrix.[18] The phenyl substituents block the photo-reactive positions on tetracenes and simultaneously extend the tetracene dipole moment to yield longer wavelength emission with better quantum yield (0.17 for tetracene,[22] 0.53 for 5,12-diphenyl DHdOT, 0.69 for 5,6,11,12-tetraphenyl DHdOT[18]). The same strategy is applied to anthracene system, a serial 9,10-substituted anthracene derivatives are synthesized and studied. Detailed investigations are carried out on these compounds to reveal their unique properties.

The outline of this thesis with the 5 main chapters is:

Chapter 1 is a general introduction to self-assembling nanostructures and photophysical mechanisms.

Chapter 2 focuses on the study of 9,10-diphenylanthracene derivatives in crystals and further investigation on nanorods derived from dimethoxy-substituted **DPA**.

Chapter 3 is a detailed study on the photophysical properties of energy transfer inducing color-tuning nanoribbons derived from dihexadecyloxy-substituted **DPA**

Chapter 4 demonstrates several 9,10-substituted **DDOA** derivatives as organogelators.

Chapter 5 reports experiment details concerning synthesis, characterization and studies.

1.2 Nanomaterials

In the last few decades, nanoscience and technology have been developed rapidly. More and more attention has been drawn to nanomaterials— those functional materials comprised of objects with at least one dimension below 100 nm— due to their quantum size effect,[23] surface effect,[24] quantum tunneling effect,[25] and so on. These effects result in unique properties of nanomaterials superior to those of their bulk counterparts.[26-29] In addition the unique optoelectronic properties of nanomaterials have made then been widely applied in various fields, e.g., novel luminescent materials,[30-32] nonlinear optics,[33,34] photocatalyst,[35] bio-labeling,[36,37] etc.

From the viewpoint of chemical composition of materials, in general, nanomaterials can be divided into inorganic materials, organic macromolecular materials, and those based on organic low-molecular-weight compounds. Inorganic nanomaterials have been most widely investigated from the beginning of the rise of the nanoscience, moreover, great achievement have been obtained in various aspects. Zero-dimensional inorganic nanostructure, including nanoparticles, clusters and quantum dots, have been well studied on the preparation,[38-40] shape control,[41] and morphology-dependent optoelectronic properties.[42] Since the discovery of carbon nanotubes in 1991,[43] one-dimension nanostructures, including wires,[44,45] tubes,[46,47]rods,[48] and belts[49] have also attracted extensive attention. It is due to the fact that 1D structures are more suitable for the construction of active devices and interconnects for the 2D quantum confinement effect.

Another important area of nanomaterials is those composed of organic macromolecules— polymers, dendrimers, biomolecules, graphene, etc.— have also been extensively studied in recent years. First, the micro/nanostructures conductive polymers, such as polyaniline[50] and polypyrrole,[51] attracted growing research interest for their promising electrical conductivity and environmental stability. Second, nanostructures based on conjugated polymers, such as polyfluorene, polythiophene and polyphenylenevinylene, are attracting significant attention. This can be attributed to their novel optoelectronic properties and applications as field effect transistors,[52] optically pumped lasers,[53] photodetectors,[54] and electroluminescent diodes.[55] Finally, some macromolecules other than polymers can form nanostructures via self-assembly. Meijer *et al.*[56] and Grimsdale and Müllen[57] investigated the electronic properties and chemistry of the nanostructures prepared from a series of π-conjugated systems, especially graphene molecules. Dendritic macromolecules[58-60] and some amphiphilic long-chain molecules[61] were also successfully designed for the fabrication of tubular structures via self-assembly.

However, nanomaterials fabricated with functional low-molecular-weight molecules have been the subject of research interest only in recent years, which may be due to their thermal instability and poor mechanical properties compared to inorganic compounds. The top-down approach for producing inorganic nanostructures is difficult to be adapted to organic materials. Therefore, new strategy for fabricating small organic compounds into nanostructures is necessary to be developed. In the bottom-up approach, the nanostructures are constructed

through self-assembly processes of molecules. Due to the weak intermolecular interactions in self-assembling organic material, the optical and electronic properties of organic nanomaterials are fundamentally different from inorganic materials. As a consequence of variety, multifunctionality, designability, and tailorbility of self-assembling organic nanomaterials, more and more works are being carried out to extend research on nano-scaled organic molecular structures.

According to Grimsdale and Müllen,[57] the most important issues that must be considered in designing a new compound that will act as a nanomaterial are the properties of individual molecules and the interactions between these molecules and how they affect the properties of discrete ensemble of molecules. Therefore, ahead of the overview of the fluorescent nanomaterials based on low-molecular-weight organic compound, let's first start with a small introduction of the key intermolecular interaction in self-assembly system—non-covalent bonding and then how to fabricate organic nanostructures via self-assembling process.

1.3 Non-covalent intermolecular interactions

The non-covalent interactions are the basis of supermolecular chemistry.[62] The energy released in the formation of noncovalent bonds is on the order of 1-50 kJ per mol.[63] There are four commonly mentioned types of non-covalent interactions:

a) hydrophobic interaction <40 kJ/mol
b) electrostatic interaction ~20 kJ/mol
c) hydrogen bond interaction 5-30 kJ/mol
d) van der Waals interaction 0.4-20 kJ/mol
e) π-π stacking 0-50 kJ/mol

These interactions can be separated into two groups: Coulombic interactions and dipolar interactions which are known as van der Waal forces.
The van der Waal interactions include the forces following:

- force between two permanent dipoles (Keesom force, 0.5~3 kJ/mol)
- force between a permanent dipole and a corresponding induced dipole (Debye force, 0.02~0.5 kJ/mol)
- force between two instantaneously induced dipoles (London dispersion force, 0.5~30 kJ/mol).

The hydrogen bond is a special case of dipole forces. A hydrogen bond is the attractive force between the hydrogen attached to an electronegative atom of one molecule and an electronegative atom of a different molecule or different part moiety of the same molecule. Usually the electronegative atom is oxygen, nitrogen, or fluorine, which has a partial negative charge. The hydrogen then has the partial positive charge. The hydrogen bond (5 ~ 30 kJ/mol) is stronger than a van der Waals interaction.

The π-π stacking is the interactions between organic aromatic compounds. It involves quadropole interactions between delocalized electrons in π-orbitals. In other words, aromaticity should be required for this interaction to occur. Hunter and Sanders published several articles about the properties of π-π interaction.[64]

1.4 Construction of organic nanostructures

To fabricate nanostructures from self-assembling small organic molecules is the main issue of this field, which is mentioned previously. Yao *et al.* reported the strategies that have been developed for achieving organic nanostructures in detail.[65] Inspired by their work, we selected several common strategies and the works were achieved at following section.

1. Reprecipitation

Reprecipitation, which is a solvent exchange method, was first reported by Nakanishi's group.[66] It is a very simple and versatile way to prepare organic nanoparticle dispersions. A rapid mixing of a small amount of concentrated stock solution of the target compound in a good solvent with excess of a poor solvent is the main concept of this method. Horn and coworkers fabricated nanoparticles from β-carotene and observed the influence of both supramolecular structure and particle size on the absorption spectra.[67] Majima's group[68] and Barbara's group[69] fabricated nanocrystals from perylene and a perylene derivative, respectively, and investigated the spectroscopy of single nanoparticles. Olive *et al.* reported a **DDOA** nanoparticles doped with tetracene and perylene to achieve fluorescence enhancement by energy transfer.[70] Park *et al.* reported a new class of fluorescent nanoparticles (Figure 1.2 a), 1-cyano-trans-1,2-bis-(4'-methylbiphenyl)-ethylene (**CN-MBE**) which is very weakly fluorescent in solution but the intensity was has enhanced about 700 times in nanoparticles.[71a] Fery-Forgues and coworkers prepared fluorescent nanofibers from coumarin derivatives with little molecular structure modifications.[72]

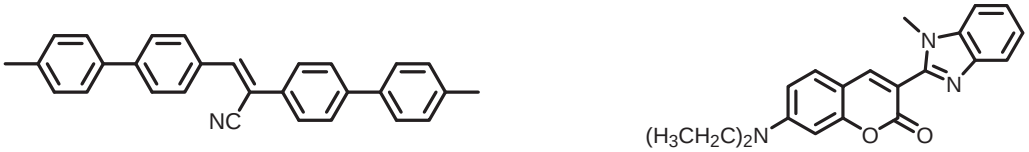

Figure 1.1: Chemical structure of **CN-MBE** (left) and coumarin derivatives (right)

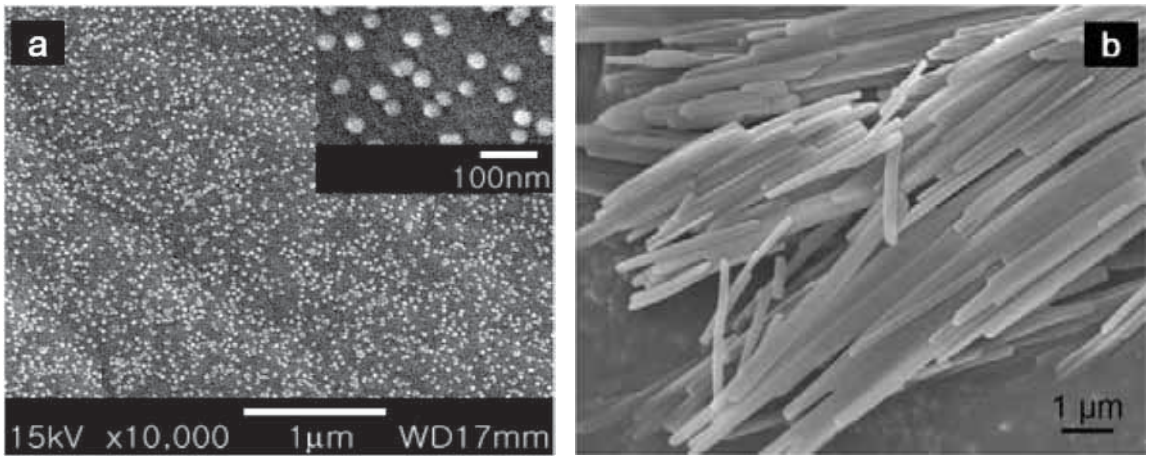

Figure 1.2: FESEM images of as-prepared organic nanostructures by the reprecipitation method. Where a: **CN-MBE** nanoparticles,[70a] b: coumarin dereivatives nanofibers[71]

2. Self-assembly through organogelation

The network structures of gels formed from low molecular mass organogelators (LMOGs) are held together by non-covalent interactions such as π-π stacking, or hydrogen bonding. Additionally, solvophobic effects are also very important in the organogels formation.

It has been realized that forming organogels is a very effective way to fabricate organic 1D nanomaterials with a variety of structures and properties.[14,73] Common organogelators include carbohydrate derivatives,[74] amphiphilic molecules,[75] cholesterol derivatives[76] and long alkyl chain associated molecules.[77] Usually, effective gelation is achieved by steroidal groups and long alkyl chains incorporated into molecular structures of gelators. Park's group presented an organogelator 1-cyano-trans-1,2-bis(3',5'-bistrifluoromethyl-biphenyl)ethylene (**CN-TFMBE**) with simple CF_3 substituents.[71b] The gelation process of this compound induced strong fluorescence emission, although **CN-TFMBE** monomers are almost non-emissive.

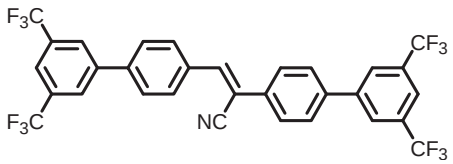

Figure 1.3: molecular structure of **CN-TFMBE**

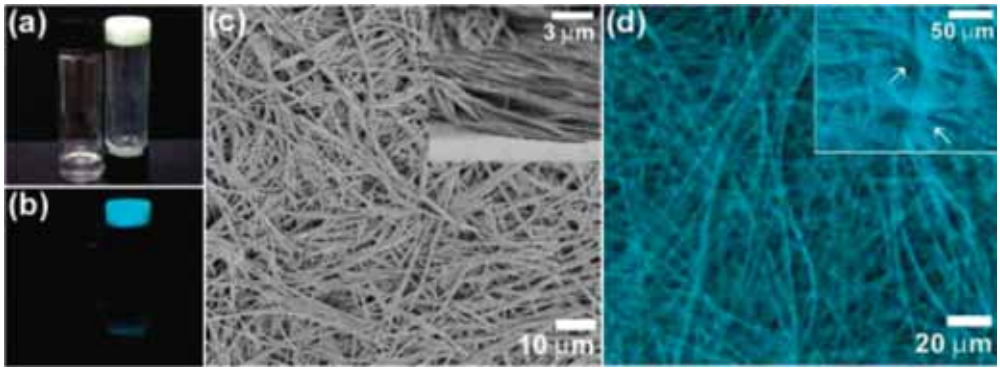

Figure 1.4[71b]: (a) Photo of **CN-TFMBE** (0.8 wt/vol %) dissolved in 1,2-dichloroethane at 60 °C (left vial) and the corresponding organogel at 20°C (right vial). (b) Fluorescence emission of **CN-TFMBE** solution (left vial) and **CN-TFMBE** gel (right vial) under the UV light (365 nm), the same vials as in a. (c) SEM images of a dried gel of **CN-TFMBE** in 1,2-dichloroethane. (d) Fluorescence microscopy images of a **CN-TFMBE** organogel. The arrows in the inset photo indicate the node where the fibrous structures of **CN-TFMBE** are largely bundled and knotted.

3. Template Method: soft Templates

The template method is a straightforward way to synthesize nanostructures by inducing the target materials to grow according to the patterns of the templates. This strategy provides an easy way for the synthesis of nanomaterials with desired morphology, and has been widely applied in the construction of 1D nanostructures. The templates adopted in this method can be generally divided into two sorts: soft and hard ones. The soft templates are those that can be dissolved in the liquid phase, including surfactant micelles,[78] complexes,[79] biomolecules,[80] and copolymers.[81] It is well known that micelles (or inverse micelles) with different shapes, such as rodlike or spherical, will be formed in the solutions when the concentration reaches the critical micelle concentrations (CMC).[82] These can then be used as soft templates for the fabrication of nanostructures. Yao *et al.* prepared nanofibers of 1,3-diphenyl-2-pyrazoline (**DP**) induced by **CTAB** micelles.[83] (Figure 1.5) It is found that the shape and size of the nanostructures can be controlled via varying the molar ratio of the target compound and surfactant. As shown in Figure 6, at lower **DP**/**CTAB** molar ratios, **CTAB** tends to form spherical micelles, and increasing the **DP**/**CTAB** ratio will induce the sphere-to-rod transition of the micelles, which act as a template to direct the growth of molecules. In addition, the morphology of nanostructures also can be varied with surfactant. Zhang and coworkers prepared several novel nanostructures of 9,10-diphenylanthracene such as nanowires, microrods and microoctahedrons with different ratio of **DPA**/**P123** (poly(ethylene glycol)-block-poly(propylene glycol-block-poly(ethylene glycol)) (Figure 1.7); whereas the nanospheres of **DPA** were obtained by using **PVP** (polyvinylpyrrolidone) instead of **P123**.[84]

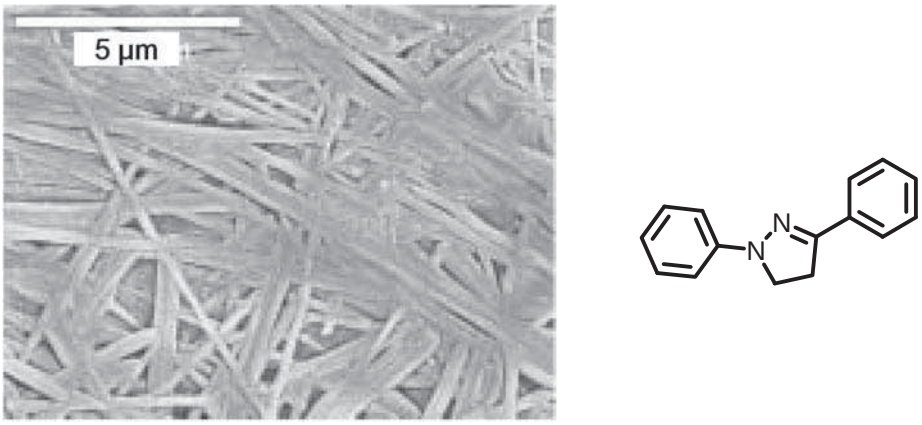

Figure 1.5[83]: SEM image of the prepared **DP** nanofibers (left), molecular structure of **DP** (right)

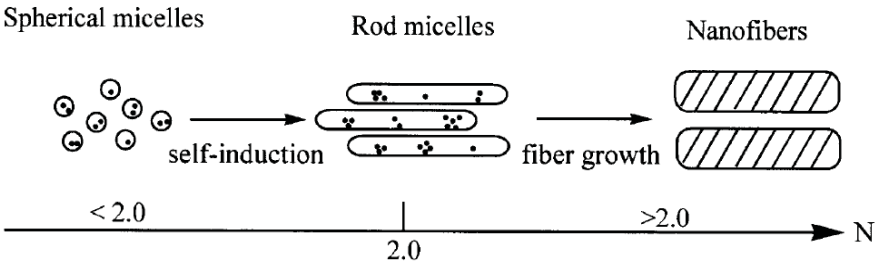

Figure 1.6[83]: Schematic processes of self-inducing templates growth for **DP** nanofiber, where N is the molar ratio **DP**/**CTAB**

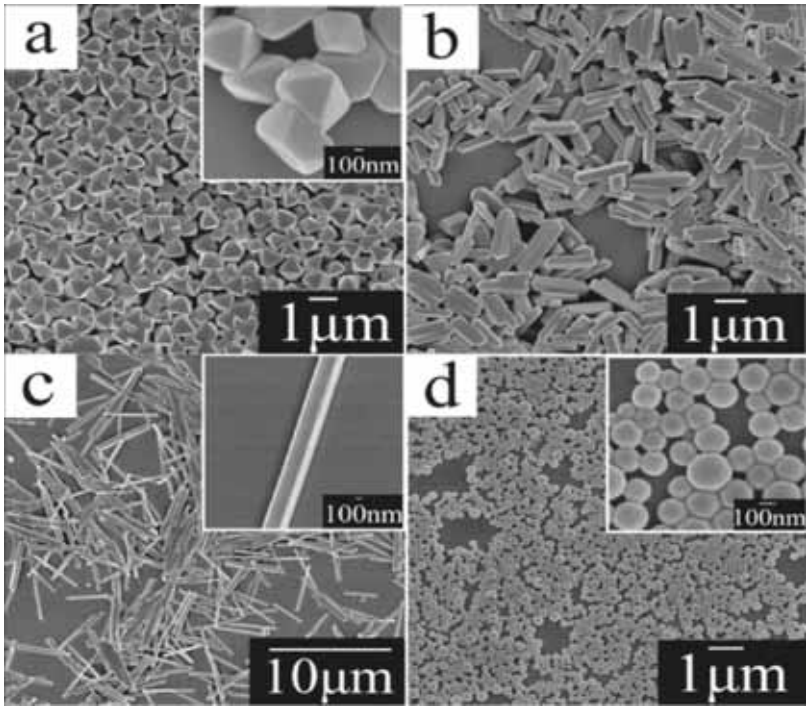

Figure 1.7[84]**:** FESEM images of different morphologies of **DPA** particles:(a)microoctahedrons, (b)microrods; (c)nanowires; (d)nanospheres. The insert is the magnified area.

4. Template Method: hard templates

The fabrication of nanostructures with hard templates has developed independently in various fields of nanotechnology and it has become one of the most applied methods in the fabrication of inorganic 1D nanomaterials.[85] Possin was the pioneer to use this technique to synthesize semiconductor nanowires in the 1970s,[86] and Martin further developed this method and first put forward the term ‘‘template synthesis’’ in the 1990s.[85] Now the commonly used templates include but are not limited to ordered porous membranes prepared with anodized aluminum oxide (AAO),[87] silica,[88] nanochannel glass,[89] and iontrack-etched polymers.[90] Recently, this technique has also been applied to fabricate nanostructures from low molecular weight organic compounds. Lee *et al.* reported the synthesis of organic nanowires by introducing 1,4-bis[2-(5-phenyloxazolyl)]benzene molecules into the AAO membranes through sublimation.[91] Yao’s group fabricated perylene[92] and dibenzoylmethane (**DBM**)[93] nanotubes by the dip-and-dry template method followed by heat treatment to increase the crystallinity. Al-Kaysi and Bardeen did a serial of detailed investigation on the highly crystalline nanorods yielded via solvent-annealing method (Figure 1.8).[94-96] They even used photoreactive

anthracene derivatives (9-anthracene carboxylic acid, **9-AC**) to fabricate nanorods which exhibit unique photomechanical properties. When large micron-sized crystals of **9-AC** were irradiated with UV light (365 nm), the crystal photodimerizes via a [4+4] photocycloaddition to form the photodimer. The photochemical reaction produced internal stress that resulted in crystal disintegration.[96] In other cases when long (60 μm) **9-AC** nanorods were briefly irradiated, the nanorods could reversibly flex and then revert back to their original shape in the dark.[97]

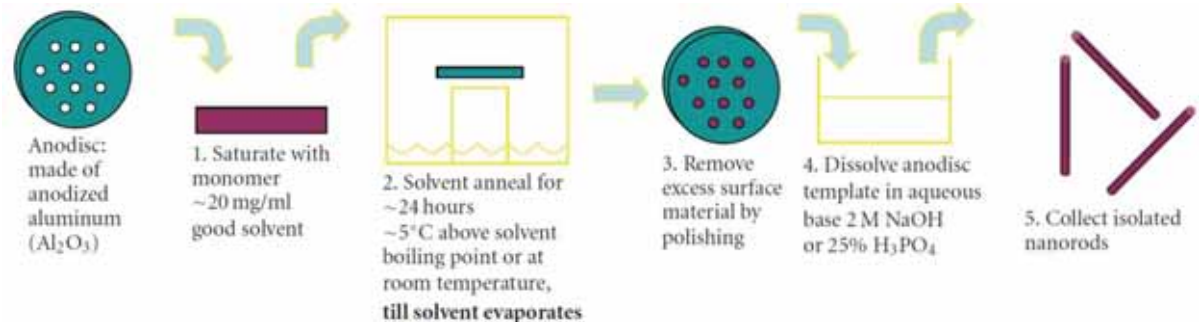

Figure 1.8[94]: Scheme of steps for fabricating solvent annealed molecular crystal nanorods

Figure 1.9: molecular structure of 2, 7-di-t-butylpyrene (left) and 9-anthracene carboxylic acid (right)

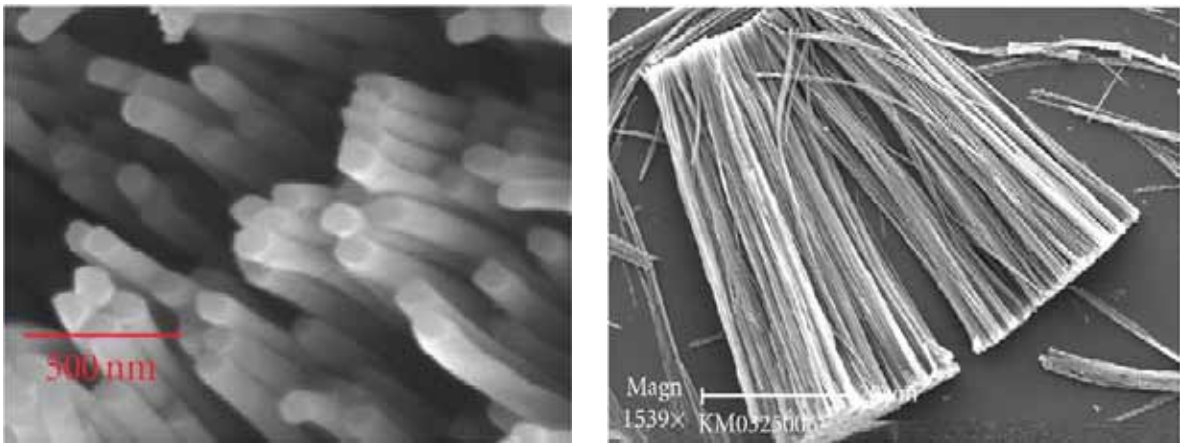

F**igure 1.10**: (a) SEM image of a 200 nm 2, 7-di-t-buthylpyrene nanorods. [95] (b) SEM image of a 200 nm 9-anthracene carboxylic acid nanorod bundle. [96]

5. Vapor deposition

Vapor deposition (VD) is a facile and feasible method for fabricating nanomaterials and has obtained great achievement in preparing inorganic nanostructures, polymeric thin films, and inorganic–polymer nanocomposites. However, the monodispersity of the products is hard

to control when small organic molecules are selected as target material. It is known that for VD the degree of saturation is the predominant factor in controlling the morphology and dispersity of the products,[98] and it should be possible to process most solid materials into 1D nanostructures by maintaining the vapor saturation at a low level. Several techniques have been adopted to control the local supersaturation in the preparation of organic 1D nanomaterials by VD. For example, Lee and coworkers applied AAO templates to the VD experiment,[91] Rubahn *et al.*[99] and Perng's group[100] controlled the substrate temperatures to ensure the uniform 1D growth of organic molecules, and Li and coworkers[101] introduced solid-phase reactions into the VD method to control the supersaturation. Yao *et al.* reported an absorbent-assisted physical vapor deposition (PVD). The absorbents such as silica gel and neutral aluminum oxide, which are used widely in column chromatography, were introduced into the PVD process to control the degree of saturation, considering that the presence of absorption-desorption equilibrium between organic compounds and the absorbents. In 2008, a doped binary white-emitting nanowires system fabricated by PVD method was reported[102] by Yao's group. The white light is achieved by blending a blue-light emitter (1,3,5-triphenyl-2-pyrzoline, TPP) and an orange dye (rubrene) via excitation energy transfer.

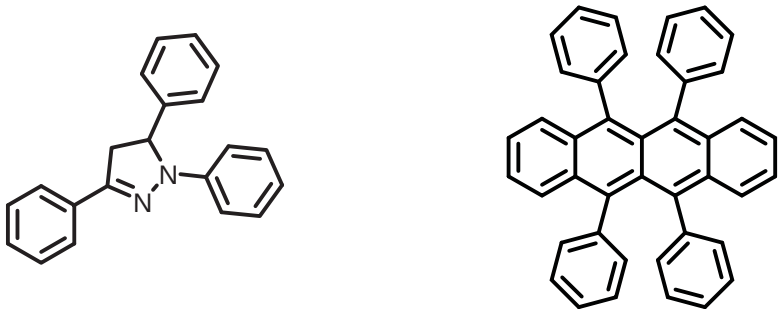

Figure 1.11: Molecular structure of **TPP** (left) and Rubrene (right)

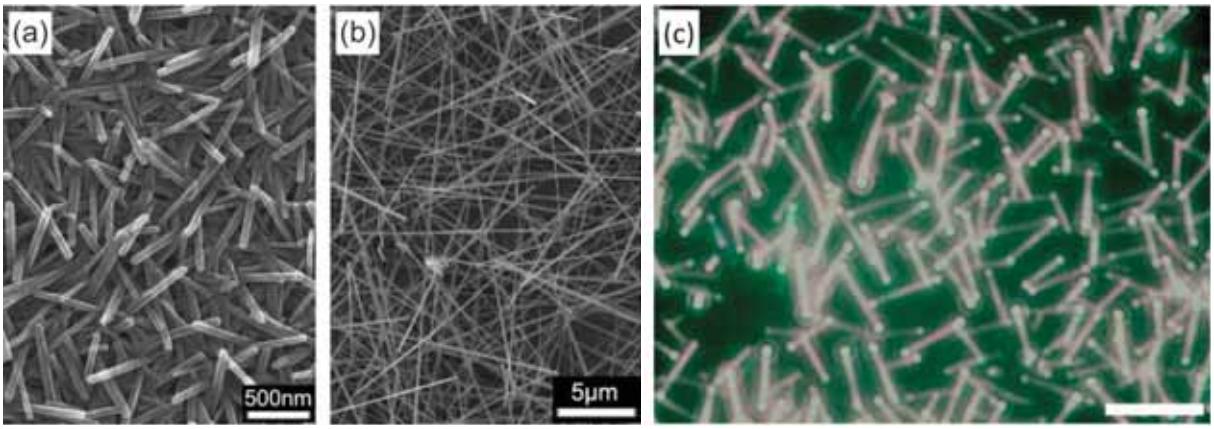

Figure 1.12[102]**:** FESEM (a, b) images of the binary nanostructures with a **TPP**/rubrene molar ratio of 100:1; (c) Fluorescence microscopy images 100:1 molar ratio **TPP**/rubrene, excited with UV.

1.5 Fluorescence emission characteristics

The crucial issue in the design of fluorescent nanostructures resides in the photophysical behavior of chromophores in the aggregated state. In this section, we start from the photophysical behavior of a single molecule; and then we can go further into the intermolecular photophysical processes, which can lead us to a better understanding of the unique photophysical properties of organic nanomaterials.

A molecule at the singlet excited state (S_1) can rapidly relax via several pathway: radiative relaxation with a radiative constant k_f, internal conversion k_{ic}, and k_{isc} for intersystem crossing. k_{ic} and k_{isc} are non-radiative decay constants. A Jablonski-Perrin diagram allows the visualization of possible processes after one molecule absorbs a photon (Figure 1.13).

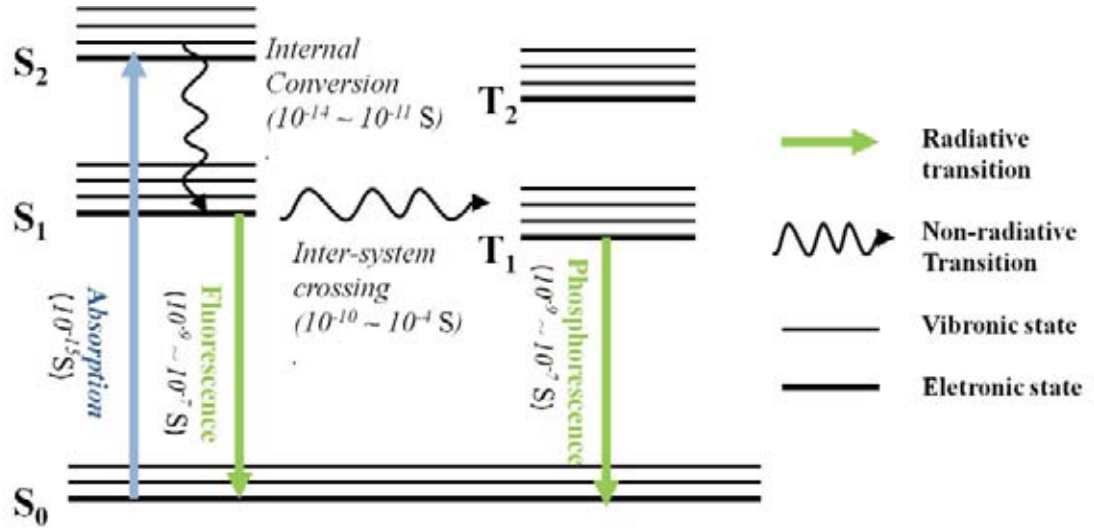

Figure 1.13: Jablonski-Perrin diagram[103]

In the simplified case, one solution containing fluorescence-emitted species M is excited with a short light pulse at time=0, a certain portion of these molecules is promoted to the excited state S_1. The kinetics of deactivation process after excitation can be described as following equation:

$$M \underset{k_r + k_{nr}}{\overset{k_{ex}}{\rightleftharpoons}} M^* \qquad \frac{-d[M^*]}{dt} = (k_r + k_{nr})[M^*]$$

Where $[M^*]$ represents the number of molecules populating the excited state S_1, k_r is the radiative decay constant and k_{nr} is the non-radiative decay constant.

The integration of this equation represents the excited state concentration as a function of time:

$$[M^*] = [M^*]_0 \exp\{-(k_r + k_{nr})\boldsymbol{t}\}$$

Where $[M^*]_0$ is the number of molecules populating the excited state at initial time.

The fluorescence intensity (I_f) measured at time t is proportional to the number of molecules that populates the excited state with a constant k_r.

$$I_f = k_r[M^*]_0 \exp\{-(k_r + k_{nr})\boldsymbol{t}\}$$

This equation suggests exponential decay of fluorescence intensity with time, which is characterized as lifetime $\tau = {}^{1}/_{(k_r + k_{nr})}$.

The lifetime measurement of one homogeneous solution with chromophores is generally independent of the excitation and emission wavelength.

The emission quantum yield ϕ_f is defined as the ratio of number of photons emitted to the number of photons absorbed. And it can also be described as the fraction of chromophores in the excited states that decay through radiative process.[104]

$$\phi_f = \frac{k_r}{k_r + k_{nr}} = k_r\tau$$

With the value of ϕ_f and τ, the rate constants k_r and k_{nr} can be easily deduced.

1.5.1 Energy transfer

The energy transfer could take place via a non-radiative interaction between an excited donor (D*), and a ground-state acceptor (A). It is an irreversible process, but it can be reinitiated upon excitation of the donor.

$$D^* + A \longrightarrow D + A^*$$

The donor molecules typically emit at shorter wavelengths that overlap with the absorption spectrum of the acceptor.

There are two main mechanisms of energy transfer process, Dexter type and Förster type.

1.5.1.1 Dexter type energy transfer

Dexter energy transfer is a process in which two molecules (intermolecular) or two parts of a molecule (intramolecular) bilaterally exchange their electrons. This exchange interaction occurs via overlap of electronic clouds and requires most of the time a contact between donor and acceptor.[105] An intramolecular transfer can also occur through appropriate spacers.[106]

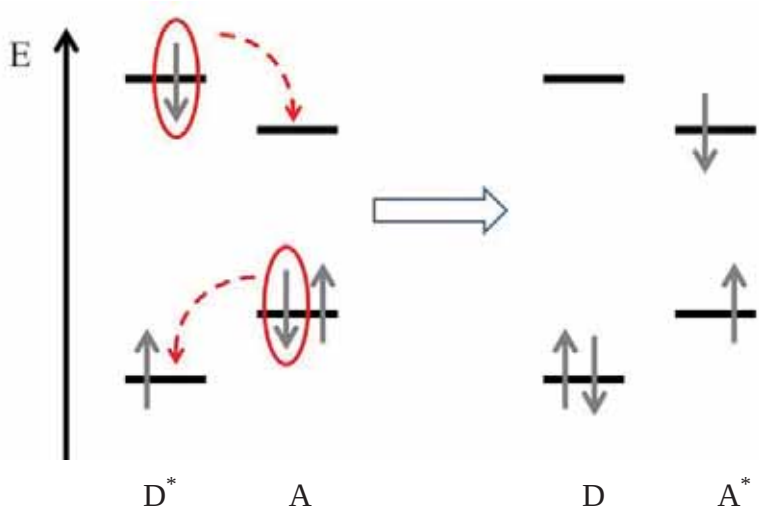

Figure 1.14: Schematic diagram for Dexter type energy transfer mechanism

The reaction rate constant of Dexter energy transfer falls exponentially as the distance between these two parties increase. On account of the exponential relationship to the distance, the exchange mechanism typically occurs within 10 Å. Hence, the exchange mechanism is also called the short-range energy transfer.

The rate constant of exchange energy transfer is given by:

$$k_{\mathrm{Dexter}} = KJ\exp(-2\mathrm{r}_{\mathrm{DA}}/\mathrm{L})$$

Where K is related to the specific orbital interactions, J is a spectral overlap integral normalized for the extinction coefficient of the acceptor, and r_{DA} is the donor-acceptor distance, and L is the sum of their van der Waals radius.

1.5.1.2 Förster type energy transfer

Förster resonance energy transfer is also known as coulombic interaction. It occurs via the electromagnetic field and does not require contact of the donor and acceptors. The basic mechanism involves the induction of a dipole oscillation in acceptor (A) at ground state by a excited donor (D^*).[107]

With sufficient energetic coupling between these molecules (overlap of the emission spectrum of the donor and absorption spectrum of the acceptor), both processes may occur simultaneously, resulting in a transfer of excitation from the donor to the acceptor molecule.

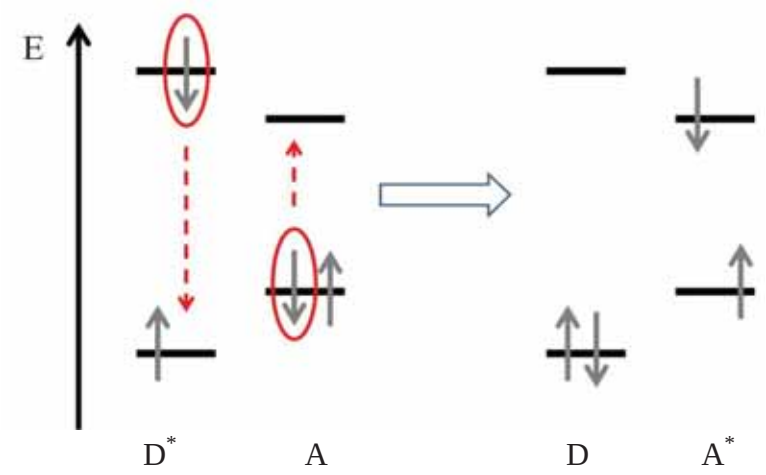

Figure 1.15: Schematic diagram for Förster type energy transfer mechanism

The interaction energy is of a dipole-dipole nature and depends on the distance between the molecules as well as the relative orientation of the dipoles. The rate of transfer (k_T) of excitation energy is given by:

$$k_T = (1/\tau_D)(R_0/r)^6$$

Where τ_D is the fluorescence lifetime of the donor in the absence of acceptor, *r* the distance between the centers of the donor and acceptor molecules and R_0 the Förster critical distance at which 50% of the excitation energy is transferred to the acceptor .

Förster critical distance R_0 is defined as:

$$R_0 = 0.0211\left(n^{-4}\kappa^2\Phi_D J(\lambda)\right)^{1/6}$$

Where Φ_D is the donor fluorescence quantum yield in absence of acceptor, κ^2 is the orientation factor for the dipole-dipole interaction, *n* is the refractive index, and *J* is the normalized spectral overlap integral, which is defined by:

$$J(\lambda) = \frac{\int_0^\infty F_D(\lambda)\varepsilon_A(\lambda)\lambda^4 d\lambda}{\int_0^\infty F_D(\lambda)d\lambda}$$

Where $F_D(\lambda)$ is the emission spectrum of the donor and is dimensionless, and ε_A is the absorption spectrum of the acceptor expressed in $M^{-1}cm^{-1}$.

The orientation factor κ^2

$$\kappa^2 = (\cos\theta_{DA} - 3\cos\theta_A \cos\theta_D)^2$$

Where θ_{DA} is the angle between the D and A dipole moments, θ_D and θ_A are the angles between the separation vector R, and the D and A moment, respectively (Figure 1.16).

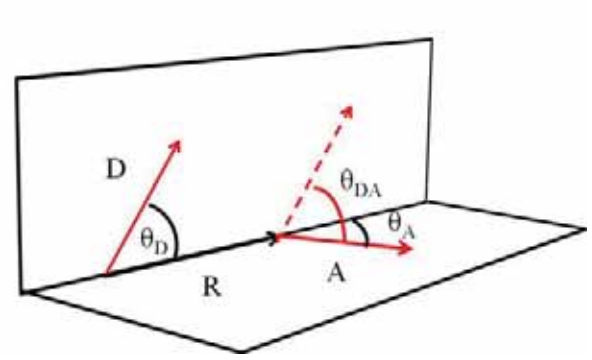

Figure 1.16: Angles of the definition of κ

The limits for κ^2 are 0 to 4,
The value of 4 is only obtained when both transition moments are in line with the vector R.
The value of 0 can be achieved when dipoles are perpendicular to each other. If the molecules undergo fast isotropic motions (dynamic averaging) then $\kappa^2 = 2/3$.

1.5.2 Triplet-triplet annihilation

Two atoms or molecular entities both in a triplet state often interact (usually upon collision) to produce one atom or molecular entity in an excited singlet state and another in its ground singlet state. This is often followed by delayed fluorescence.[108]

The triplet-triplet annihilation is an important case of exchange energy transfer. Two triplet chemical groups, ^{3}D* and ^{3}A*, interact to produce an excited singlet state and another in its ground state. Generally, the energy gap between S_0 and T_1 is bigger than the energy gap between T_1 and S_1. Hence, if two triplet excited-state molecules encounter, the process might have enough energy to excite one of them to the higher singlet states, which can make the fluorescence happen in this system, which is known as delayed fluorescence.

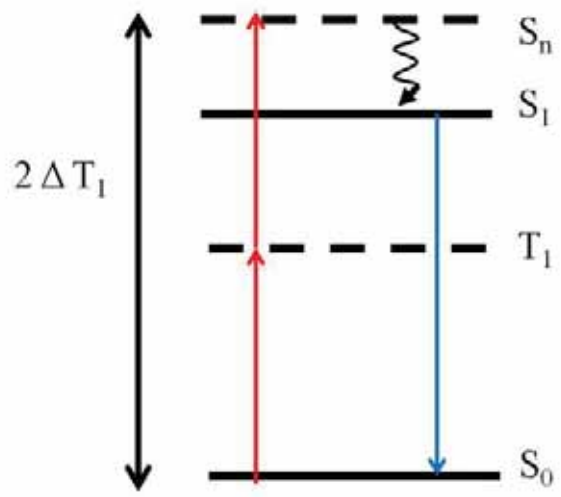

Figure 1.17: Schematic diagram for triplet-triplet annihilation

The rate of decay of T_1 in general is equal to:

$$\text{Rate} = k_T [T_1] + k_{TTA} [T_1]^2$$

Where k_T is the inherent unimolecular decay rate of T_1, and k_{TTA} is the rate of quenching of T_1 by its interaction with another excited state T_1. The triplet-triplet annihilation induced delayed fluorescence mechanism can be described as:

$$T_1 + T_1 \longrightarrow S_1 + S_0$$

$$S_1 \longrightarrow S_0 + h\upsilon$$

The delayed fluorescence emission of S_1 then may be observed with a lifetime similar to that of the triplet because excitation has resided temporarily in T_1. The yield of this delayed fluorescence, since it results from a two-photon process, will depend upon the square of the intensity of the incident light if T-T annihilation is rate-determining.

1.5.3 Excitons

An exciton is a bound state of an electron and hole pair which are attracted to each other by the electrostatic Coulomb force. It is regarded as an elementary excitation of condensed matter that can transport energy without transporting net electric charge.[109]

Excitons can be treated in two limiting cases, depending on the properties of the material in question.

a. Frenkel:
   The electron-hole pair is bounded strongly with a binding energy ~1eV and confined with a radius ~10Å. It's observed mostly in organic crystals composed with aromatic compounds and alkali halides.
b. Mott-Wannier:
   The electron-hole pair is loosely bounded with a binding energy ~10 meV and an average radius about 100 Å. It is typically found in semiconductor crystals with small energy gaps and high dielectric constants given the fact that it tends to reduce the Coulomb interaction between electrons and holes.

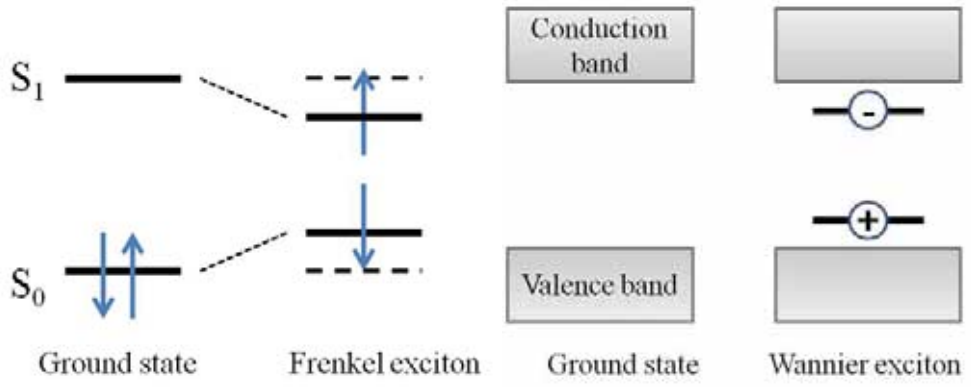

Figure 1.18: Different types of exciton

The non-covalent intermolecular interactions in self-assembling condensed phase play an essential role on the properties of energy transfer and exciton migration. The main interaction forces will be presented at following.

1.5.4 J- and H- aggregates

According to Kasha's exitonic coupling theory,[110] a molecule can be regarded as a point dipole and the excited state of the molecular aggregate splits into two levels through the interaction of transition dipoles. The molecules can pack where their transition dipole moments are aligned in a parallel way (face to face) to form H-aggregate or in a head-to-tail arrangement (end to end) to form J-aggregate.

Furthermore, the optical excitation is only allowed from the ground state to one of the two excitonic states depending on the angle between two neighbored transition dipole moments θ (Figure 1.19). For $\theta < 54.7^{o}$, the lower energy state is allowed (affording a red-shifted J-band with respect to the monomer absorption), while for $\theta > 54.7^{o}$ the allowed state is at higher energy (leading to a blue-shifted H-band).

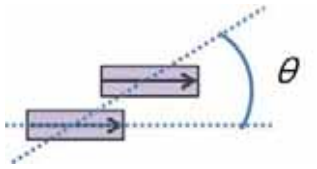

Figure 1.19: The angle between transition dipole moments

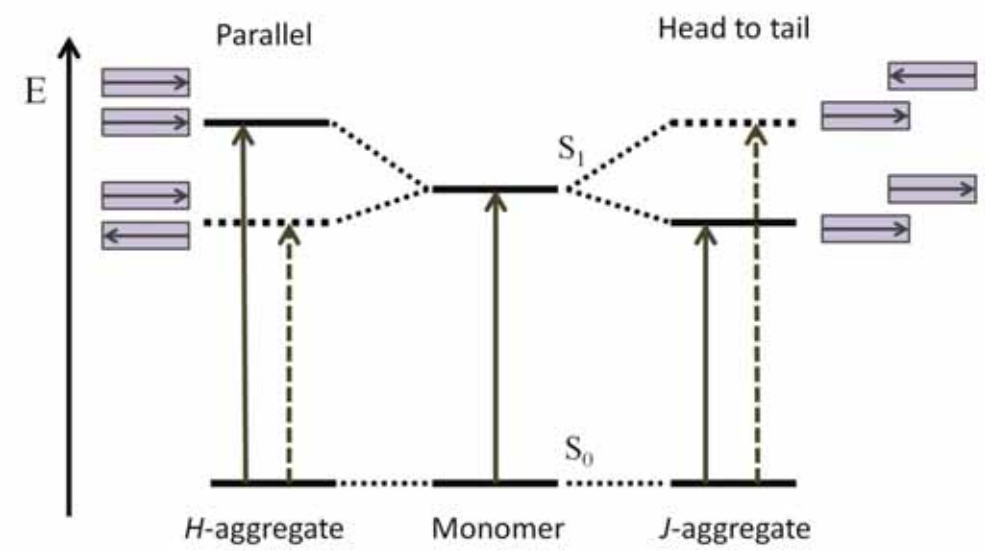

Figure 1.20: Scheme of J and H aggregates energy levels

1.6 Photophysical properties of nanostructures

As mentioned above, due to the tight molecular packing, special molecular orientations, and facile introduction of dopant compounds into the host matrices, numerous unique photophysical behaviors are observed in nano-structures. In this section, we give an overview of current studies on the photoluminescent properties of organic nanostructures.

1. AIEE

Generally, the fluorescence quantum yield of organic chromophores decreases in the solid state, as a result of concentration quenching. However, some fluorophores are demonstrated that their emission is enhanced instead of quenched in the solid state. It is named aggregation induced emission enhancement (AIEE). In the work of Park and co-workers,[71a,b] they proposed that aggregation induced the molecular conformation change in the nano-structures (which is planarization of the **CN-MBE** molecules here, figure 1.21),[70a] which in turn resulted in the strong intermolecular interactions causing a certain molecular packing mode. On the basis of this work, they designed a multifunctional molecule for photoswitchable memory media by modifying the tolyl group on the **CN-MBE** to a 1,2-bisthienylethene (**BTE**) moiety.[110] This compound provided an opportunity to combine the AIEE property of the **CN-MBE** unit with the bistable photochromism of the **BTE** unit to solve the general problem of concentration quenching in the fluorescence switch system (Figure 1.22).

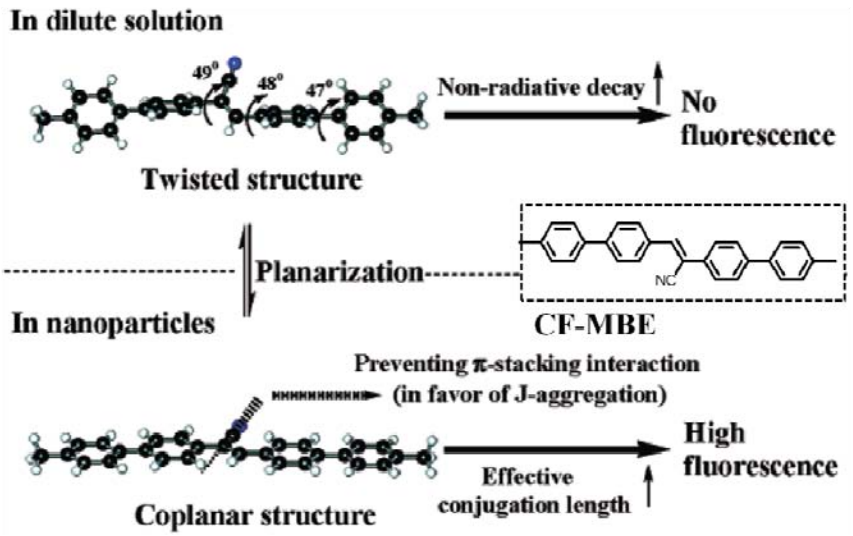

Figure 1.21[71a]**:** Proposed mechanism of enhanced emission in **CN-MBE** nanoparticles

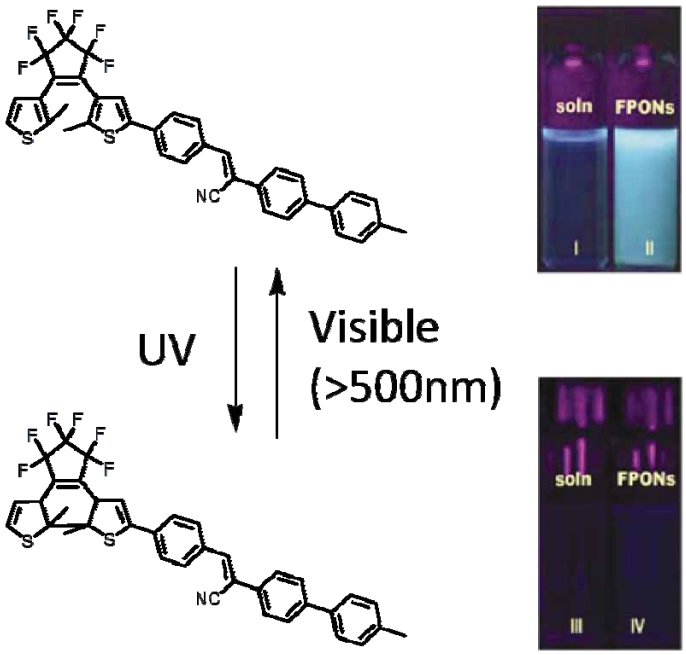

Figure 1.22[110]: Molecular structures and fluorescence images of the open-ring (top) and closed-ring (bottom) **BTE-CN-MBE**

2. Size-dependent optical properties

The size-dependent optical properties of perylene nanocrystals was first reported by Nakanishi's group in 1996.[111] In addition, Horn and coworkers investigated the effect of both supramolecular structure and particle size on the absorption spectra of β-carotene nanoparticles.[67] Yao *et al.* prepared organic nanoparticles with average diameters ranging from 40 to 160 nm from 1,3-diphenyl-5-(2-anthryl-)2-pyrazoline (**DAP**) (Figure 1.23, left).[112] As shown in figure 1.23, the nanoparticle emission in the blue region from the pyrazoline chromophore was shifted to shorter wavelengths with an increase in particle size, accompanied by a relatively gradual dominance of the emission at about 540 nm from the exciplex formed by the pyrazoline ring and the anthracene moiety of the neighboring molecule. This blue-shift is due to the configuration reorganization induced by increased intermolecular interaction.

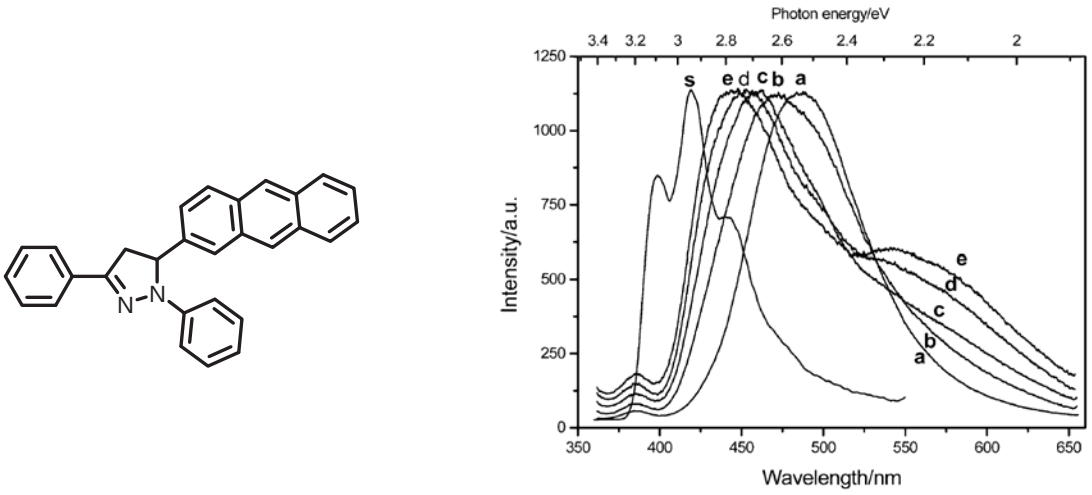

Figure 1.23[112]**:** (left) molecular structure of **DAP** and (right) the fluorescence emission spectra of **DAP**

nanoparticle dispersions with different sizes and **DAP** solution in acetonitrile : Curve a) 40nm, b) 60nm, c) 90 nm, d) 120nm, e) 160 nm. λ_{ex}=350 nm

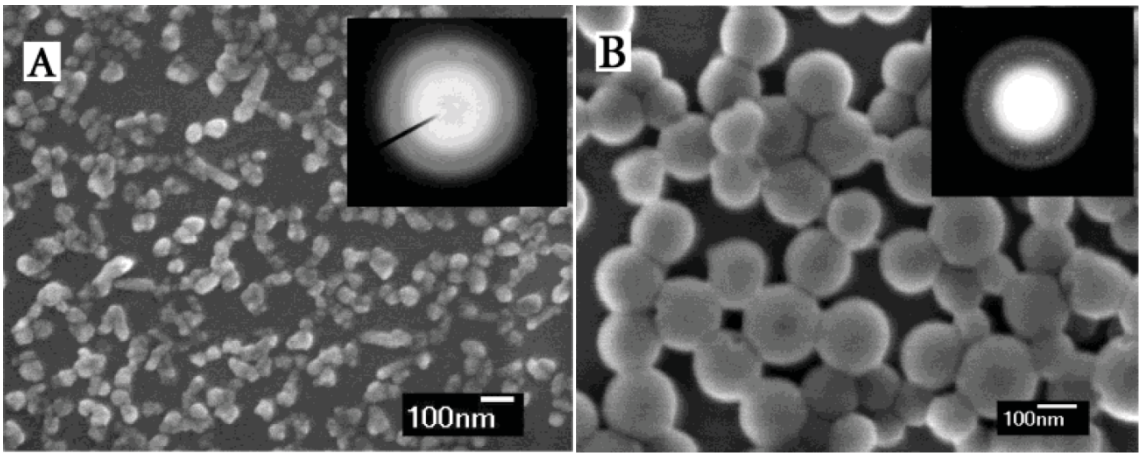

Figure 1.24[112]: FESEM images of **DAP** nanoparticles with average diameters of (A) 60 nm and (B) 160 nm. The insert are electron diffraction patterns of the corresponding particles.

3. Multicolor emission

Generally, multicolor emissions are realized with blends of dyes or polymers emitting red, green, and blue light. In 2007 and 2008, Yao's group and He *et al.* demonstrated that it is possible to obtain multicolor emission from crystalline nanomaterials based on low-molecular-weight organic compounds.[113,114] In He's work, they fabricated porous network thin films constructed of pyrene nanowires via PVD (physical vapor deposition) method (Figure 1.25). This pyrene thin film displayed a multicolor emission property, that is, blue, green and red emission was achieved by exciting the same sample with appropriate wavelengths. As shown in figure 1.26, the totally different curve shapes and emission intensities indicate that the green and red emissions are not related to the excited states of pyrene monomers. This can be attributed to the energy levels of defects.[113] Figure 1.25 indicates that the surfaces of the nanowires are not smooth and there are possibly many defect areas with polycrystalline structures at the surface and cross points of the nanostructures. This kind of defect emission can be tuned by changing the excitation wavelength.

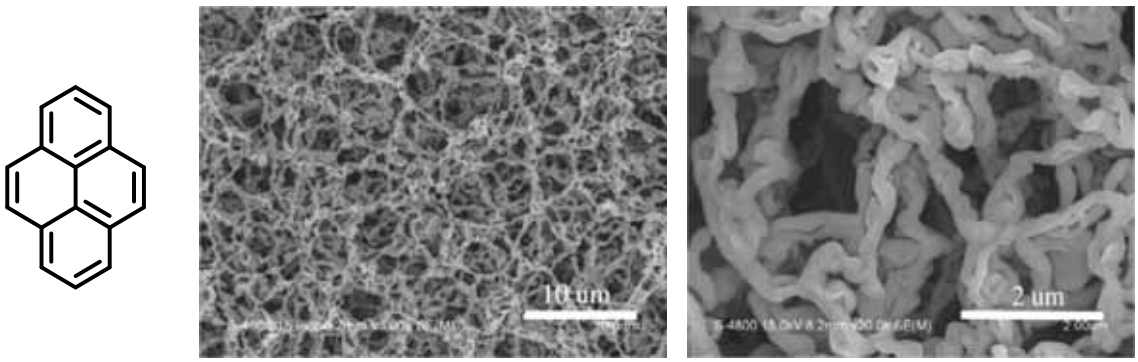

Figure 1.25[114]**:** (from left to right) molecular structure of pyrene; FESEM images of pyrene nanowires with different magnifications.

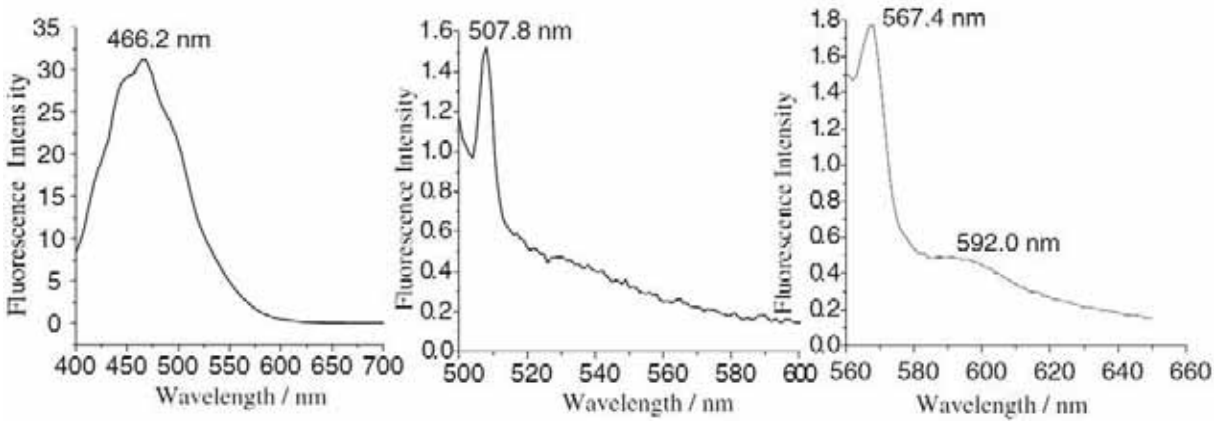

Figure 1.26[114]**:** Emission spectra of typical **UPNTF**s (uniform porous network thin films) excited at 380 nm, 480 nm, and 540 nm (from left to right).

4. Amplified energy transfer and exciton migration

In doped self-assembling systems, excitation of donor species results in rapid transfer of excitation energy to acceptor sites and observation of emission from acceptors. The matrices comprise a large excess of donor species to facilitate energy migration from excited donors to the acceptor species. In view of the fibrillar architecture, many donor species will serve relatively few acceptor molecules and each acceptor will be rapidly excited by the closest excited donor. Additionally, the particular molecular arrangements of the materials offer multiple pathways for exciton hopping and energy transfer.[77b]

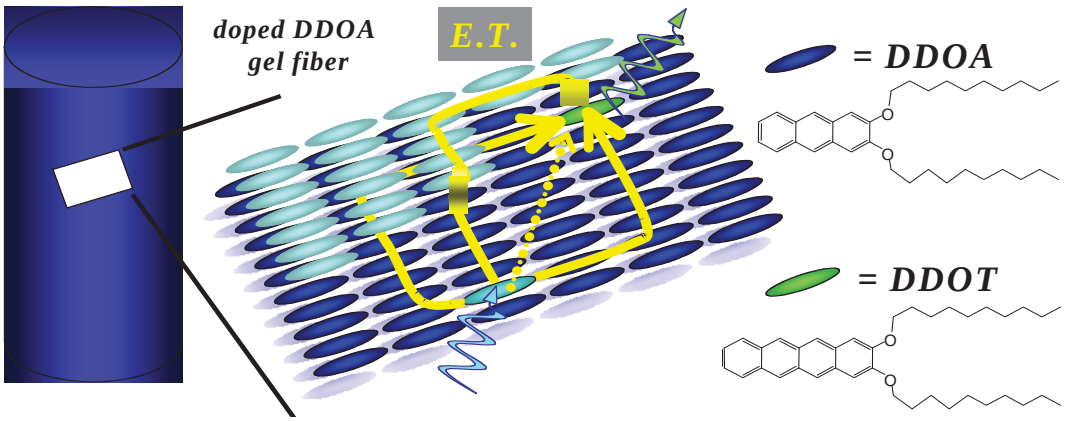

Figure 1.27[77b]**:** Simplified representation of a doped **DDOA** gel-fiber (enlargement of 3 layers of sheets of **DDOA**). Are represented one excited donor (*light blue*) and one emissive acceptor (*green*), as well as energy transfer pathways (*E.T.*, *yellow arrows*) for the direct process (dotted arrow) and several possibilities for exciton migration. (right) Chemical structures of **DDOA** and **DDOT**.

5. Tunable and white light emission

By adding dopants into light-harvesting matrix, the slight variation of the content of energy acceptors will result in significant emission color change via FRET process. Most important example is white light emission, which is vital to full-color displays and the backlight of portable display devices. Del Guerzo's group reported a white-light emitting organogel by doping green and red dyes into anthracene blue matrices to form

homogeneously white-light emitting nanofibers.[18] In addition, white light emission via energy transfer can also be achieved by block heterostructure nanomaterials.[115] Yao and coworkers prepared the triblock microrods of 1,3-diphenyl-2-pyroline (**DP**) doped with an orange dye 4-(dicyanomethylene)-2-methyl-6-(*p*-dimethyl-aminostyryl)-4*H*-pyran (**DCM**) selectively at both ends via soft-template method.

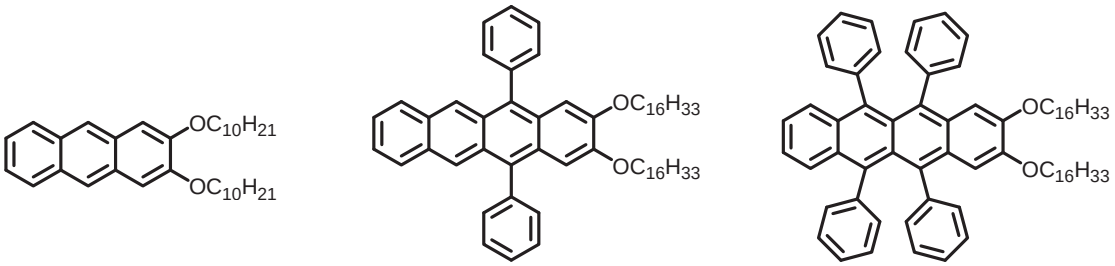

Figure 1.28: molecular structure of blue light-emitting host (**DDOA**), green and red emitting dye (5,12-diphenyl tetracene and 5,6,11,12-tetraphenyl tetracene derivatives) (from left to right)

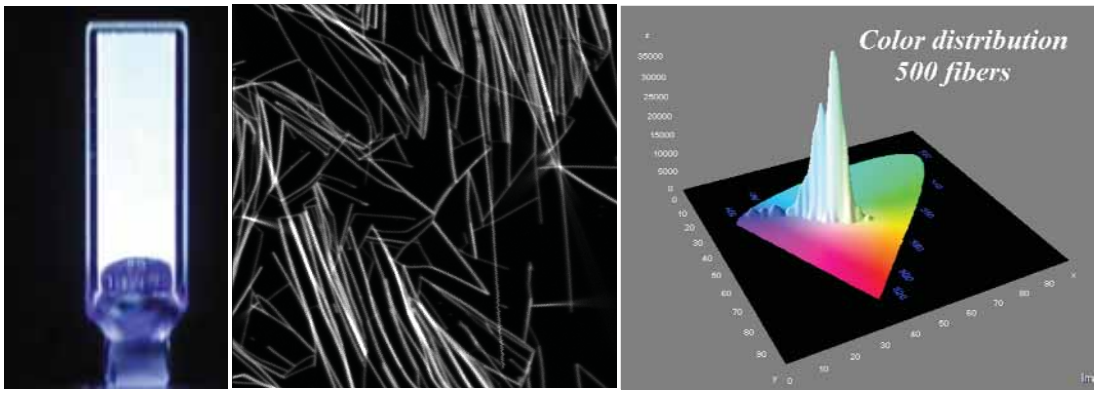

Figure 1.29[18]**:** (from left to right) Pictures of cuvettes with DMSO organogel (**W**-gel) under UV irradiation, fluorescence intensity confocal microscopy image (30 × 30 μm, 80 × 80 nm/pixel) of the gel and the distribution of the CIE 1931 coordinates of 500 fluorescence spectra, the *z*-scale represents the number of photons yielding the given coordinates.

Figure 1.30: Molecular Structures of **DP** (left) and **DCM** (right)

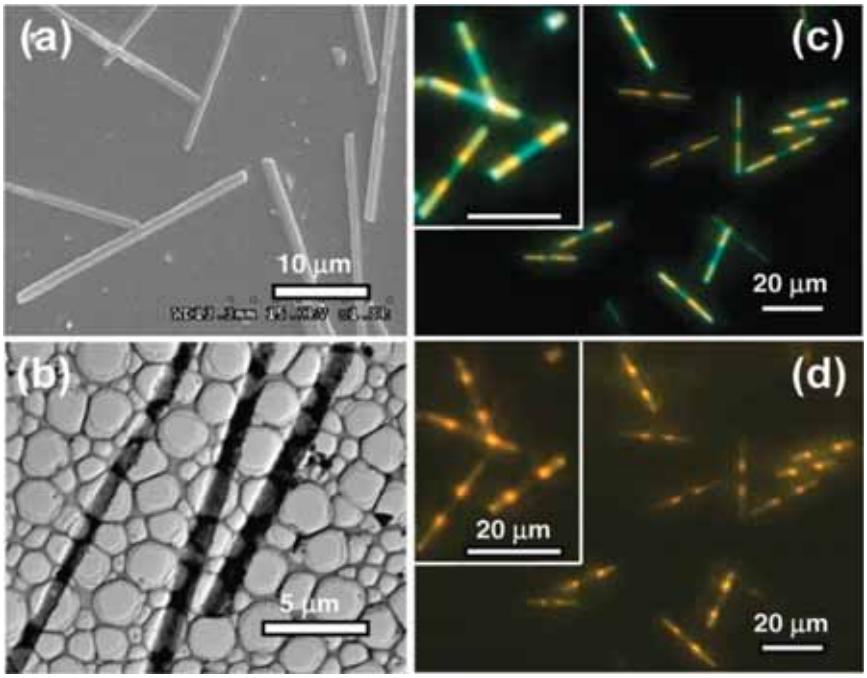

Figure 1.31[115]**:** (a) FESEM and (b) TEM images of triblock microrods. (c and d) Fluorescence microscopy images of same microrods excited with unfocused UV (330-380 nm) and blue light (460-490 nm), respectively.

With a glance of literature, we can see that the research interests for luminescent organic nanostructures have recently emerged. This field is still in its youth, and much remains to be explored. Several directions should be paid attention, such as developing methods for general fabrication of organic nanomaterials with desired morphologies, and the investigation of photophysical properties on single nano-objects, which is a key step to allow us to retrieve important information like the composition within the objects. With this in mind, in the next few chapters, we are going to present a highly emissive nano-scaled system and detailed spectroscopic and microscopic studies.

1.7 References

1. Cramer, F. *Chaos and order*; Wiley-VCH: Weinheim, Germany,1993.
2. Lehn, J.-M. *Chem. Soc. Rev.* **2007**, *36*, 151.
3. (a) Jonkheijm, P.; van der Schoot, P. P. A. M.; Schenning, A. P. H. J.; Meijer, E. W. *Science* **2006**, *313*, 80. (b) Hirschberg, J. H. K. K.; Brunsveld, L.; Ramzi, A.; Vekemans, J. A. J. M.; Sijbesma, R. P.; Meijer, E. W. *Nature* **2000**, *407*, 167. (c) Sijbesma, R. P.; Beijer, F. H.; Brunsveld, L.; Folmer, B. J. B.; Hirschberg, J. H. K. K.; Lange, R. F. M.; Lowe, J. K. L.; Meijer, E. W. *Science* **1997**, *278*, 1601.
4. (a) Kaiser, T. E.; Stepanenko, V.; Würthner, F. *J. Am. Chem. Soc.* **2009**, *131*, 6719. (b) Kaiser, T. E.; Scheblykin, I. G.; Thomsson, D.; Würthner, F. *J. Phys. Chem. B* **2009**, *113*, 15836. (c) Zhang, X.; Rehm, S.; Safont-Sempere, M. M.; Würthner, F. *Nat. Chem.* **2009**, *1*, 623. (d) Uemura, S.; Sengupta, S.; Würthner, F. *Angew. Chem., Int. Ed.* **2009**, *48*, 7825.
5. (a) Zabala Ruiz, A.; Li, H.; Calzaferri, G. *Angew. Chem., Int. Ed.* **2006**, *118*, 5408. (b) Zabala Ruiz, A.; Li, H.; Calzaferri, G. *Angew. Chem. Int. Ed*. **2006**, *45*, 5282. (c) Yunus, S.; Spano, F.; Patrinoiu, G.; Bolognesi, A.; Botta, C.; Brühwiler, D.; Zabala Ruiz, A.; Calzaferri, G. *Adv. Funct. Mater.* **2006**, *16*, 2213.
6. (a) Ajayaghosh, A.; Praveen, V. K. *Acc. Chem. Res.* **2007**, *46*, 644. (b) Zang, L.; Che, Y.; Moore, J. S. *Acc. Chem. Res*. **2008**, *41*, 1596. (c) Moore, J. S. *Acc. Chem. Res.* **1997**, *30*, 402. (d) Stupp, S. I. *Chem. Rev.* **2005**, *105*, 1023.
7. (a) Henze, O.; Feast, W. J.; Gardebien, F.; Jonkheijm, P.; Lazzaroni, R.; Leclére, P.; Meijer, E. W.; Schenning, A. P. H. J. *J. Am. Chem. Soc.* **2006**, *128*, 5923. (b) Hoeben, F. J. M.; Jonkheijm, P.; Meijer, E. W.; Schenning, A. P. H. J. *Chem. Rev.* **2005**, *105*, 1491. (c) Feyter, S. D.; Miura, A.; Yao, S.; Chen, Z.; Würthner, F.; Jonkhejm, P.; Schenning, A. P. H. J.; Meijer, E. W.; Schryver, F. C. D. *Nano Lett.* **2005**, *5*, 77. (d) Schenning, A. P. H. J.; Meijer, E. W. *Chem. Comm.* **2005**, 3245.
8. (a) Liu, H.; Xiu, J.; Li, Y.; Li, Y. *Acc. Chem. Res.* **2010,** 43, 1496. (b) Xu, J.; Zheng, H.; Liu, H.; Zhou, C.; Zhao, Y.; Li, Y.; Li, Y. *J. Phys. Chem. C* **2010**, *114*, 2925. (c) Huang, C.; Li, Y.; Yang, J.; Cheng, N.; Liu, H.; Li, Y. *Chem. Comm.* **2010,** 3161. (d) Huang, C.; Wen, L.; Liu, H.; Li, Y.; Liu, X.; Yuan, M.; Zhai, J.; Jiang, L.; Zhu, D. *Adv. Mater.* **2009**, *21*, 1721. (e) Xiao, J.; Xu, J.; Cui, S.; Liu, H.; Wang, S.; Li, Y. *Org. Lett.* **2008**, *10*, 645. (f) Guo, Y.; Tang, Q.; Liu, H.; Zhang, Y.; Li, Y.; Hu, W.; Wang, S.; Zhu, D. *J. Am. Chem. Soc.* **2008**, *130*, 9198.
9. (a) Zhang, X.; Yuan, G.; Li, Q.; Wang, B.; Zhang, X.; Zhang, R.; Chang, J. C.; Lee, C. S.; Lee, S. T. *Chem. Mater.* **2008**, *20*, 6945. (b) Zhang, X.; Zhang, X.; Wang, B.; Zhang, C.; Chang, J. C.; Lee, C. S.; Lee, S. T. *J. Phys. Chem. C.* **2008**, *112*, 16264. (c) Zhang, X.; Zhang, X.; Zou, K.; Lee, C. S.; Lee, S. T. *J. Am. Chem. Soc.* **2007**, *129*, 3527. (d) Zhang, X.; Dong, C.; Zapien, J. A.; Ismathullakhan, S.; Kang, Z.; Jie, J.; Zhang, X.; Chang, J. C.; Lee, C. S.; Lee, S. T. *Angew. Chem., Int. Ed.* **2009**, *48*, 9121.
10. (a) Li, R.; Hu, W.; Liu, Y.; Zhu, D. *Acc. fChem. Res.* **2010**, *43*, 529. (b) Dong, H.; Jiang, S.; Jiang, L.; Liu, Y.; Li, H.; Hu, W.; Wang, E.; Yan, S.; Wei, Z.; Xu, W.; Gong, X. *J. Am.*

Chem. Soc. **2009,** *131*, 17315. (c) Wang, C.; Liu, Y.; Ji, Z.; Wang, E.; Li, R.; Jiang, H.; Tang, Q.; Li, H.; Hu, W. *Chem. Mater.* **2009**, *21*, 2840. (d) Xiao, K.; Li, R.; Tao, J.; Payzant, E. A.; Ivanov, I. N.; Puretzky, A. A.; Hu, W.; Geohegan, D. B. *Adv. Funct. Mater.* **2009**, *19*, 3776. (e) Jiang, L.; Hu, W.; Wei, Z.; Xu, W.; Meng, H. *Adv. Mater.* **2009**, *21*, 3649.

11. (a) Lee, H. S.; Kwak, D.; Lee, W. H.; Cho, J. H.; Cho, K. *J. Phys. Chem. C* **2010**, *114*, 2329. (b) Kim, D. H.; Lee, D. Y.; Lee, H. S.; Lee, W. H.; Kim, Y. H.; Han, J. I.; Cho, K. *Adv. Mater.* **2007**, *19*, 678.
12. (a) Kim, H. J.; Kang, S. K.; Lee, Y. K.; Seok, C.; Lee, J. K.; Zin, W. C.; Lee, M. *Angew. Chem., Int. Ed.* **2010**, *49*, 8471. (b) Kim, J. K.; Lee, E.; Kim, M. C.; Sim, E.; Lee, M. *J. Am. Chem. Soc.* **2009**, *131*, 17768. (c) Lim, Y. B.; Moon, K. S.; Lee, M. *J. Mater. Chem.* **2008**, *18*, 2909. (d) Ryu, J. H.; Kim, H. J.; Huang, Z.; Lee, E.; Lee, M. *Angew. Chem., Int. Ed.* **2006**, *45*, 5304.
13. (a) Schönberg, A. in: *Preparative Organic Photochemistry* **1968**, 99. Springer, Berlin. (b) Bouas-Laurent, H. ; Castellan, A. ; Desvergne, J.-P. ; Lapouyade, R. *Chem. Soc. Rev.* **2000**, *29*, 43. (c) Bouas-Laurent, H. ; Castellan, A. ; Desvergne, J.-P. ; Lapouyade, R. *Chem. Soc. Rev.* **2001**, *30*, 248. (d) Wei, K. S.; Livingston, R. *Photochem. Photobiol.* **1967**, *6*, 229. (e) Lapouyade, R.; Nourmamode, A.; Bouas-Laurent, H. *Tetrahedron* **1980**, *36*, 2311.(f) Bjarneron, D. W.; Petersen, N. O. *J. Photochem. Photobiol. A: Chem.* **1992**, *63*, 327. (g) Dabestani, R.; Nelson, M.; Sigman, M. E. *Photochem. Photobiol.* **1996**, *64*, 80. (h) Birks, J. B. *Photophysics of Aromatic Compounds*. **1970**, Wiley-Interscience, New York, NY.
14. (a) Brotin, T.; Utermöhlen, R.; Fages, F.; Bouas-Laurent, H. ; Desvergne, J.- P. *Chem. Commun.* **1991**, 416. (b) Terech, P.; Bouas-Laurent, H.; Desvergne, J.- P. *J. Colloid Sci.* **1995**, *174***,** 258.
15. Das, R. K.; Bhat, S.; Banerjee, S.; Aymonier, C.; Loppinet-Serani, A.; Terech, P.; Maitra, U.; Raffy, G.; Desvergne, J.- P.; Del Guerzo, A. *J. Mater. Chem.*, **2011**, *21*, 2740.
16. Placin, F.; Desvergne, J. P.; Cansell, F. *Journal of Materials Chemistry* **2000**, *10*, 2147.
17. Placin, F.; Desvergne, J. P.; Lasségues, J.-C. *Chem. Mater.* **2001**, *13***,** 117
18. Giansante, C.; Raffy, G.; Schäfer, C.; Rahma, H.; Kao, M.-T.; Olive, A. G. L.; Del Guerzo, A. *J. Am. Chem. Soc.* **2010**, *133*, 316.
19. Reichwagen, J.; Hopf, H.; Del Guerzo, A.; Belin, C.; Bouas-Laurent, H.; Desvergne, J.-P. *Org. Letters* **2005**, *7*, 971.
20. (a) Gronwald, O.; Snip, E.; Shinkai, S. *Curr. Opin. Colloid Interface Sci*. **2002**, *7*, 148 (b) Menger, F. M.; Caran, K. L., *J. Am. Chem. Soc.* **2000**, *122*, 11679.
21. Fukumura, H.; Kikuchi, K.; Koike, K.; Kokubun, H. J. *Photochem. Photobiol. A: Chem.* **1988,** *42*, 283.
22. Müller, A. M.; Avlasevich, Y. S.; Müllen, K.; Bardeen, C. J. *Chem. Phys. Letters* **2006**, *421*, 518.
23. Goldstein, A. N.; Echer, C. M.; Alivisatos, A. P. *Science* **1992**, *256*, 1425.
24. Ball, P.; Garwin, L. *Nature*, **1992,** *355*, 761

25. Rees, M. A.; Frensley, W. R.; Matyi, R. J.; Randall, J. N.; Seabaugh, A. C. *Appl. Phys. Lett.* **1989**, *54*, 1034
26. Lu, L.; Shen, Y. ; Chen, X. ; Qian, L.; Lu, K. *Science* **2004**, *304*, 422.
27. Alivisatos, A. P.; Barbara, P. F.; Castleman, A. W.; Chang, J.; Dixon, D. A.; Kline, M. L.; McLendon, G. L.; Miller, J. S.; Ratner, M. A.; Rossky, P. J.; Stupp, S. I.; Thompson, M. I. *Adv. Mater.* **1998**, *10*, 1297.
28. *Nanomaterials: Synthesis, Properties and Applications* **1996** (Eds: A. S. Edelstein, R. C. Cammarata), Institute of Physics, Philadelphia, PA.
29. Special issue on nanomaterials, *Chem. Mater.* **1996,** *8*, 1569.
30. Fafard, S.; Hinzer, K.; Raymond, S.; Dion, M.; McCaffrey, J.; Feng, Y.; Charbonneau, S.; *Science* **1996**, *274*, 1350.
31. Parala, H.; Winkler, H.; Kolbe, M.; Wohlfart, A.; Fischer, R. A.; Schmechel, R.; von Seggern, H. *Adv. Mater.* **2000**, *12*, 1050.
32. Mueller, A. H.; Petruska, M. A.; Achermann, M.; Werder, D. J.; Akhadov, E. A.; Koleske, D. D.; Hoffbauer, M. A.; Klimov, V. I.; *Nano Lett.* **2005**, *5*, 1039.
33. Johnson, J. C.; Yan, H.; Schaller, R. D.; Petersen, P. B.; Yang, P.; Saykally, R. J. *Nano Lett.* **2002**, *2*, 279.
34. Wang, Y.; Xie, X.; Goodson, T. III, *Nano Lett.* **2005**, *5*, 2379.
35. Corma, A. *Chem. Rev*. **1997**, *97*, 2373.
36. Chan,W. C. W.; Nie, S. *Science* **1998**, *281*, 2016.
37. Chan, C. P.; Bruemmel, Y.; Seydack, M.; Sin, K.; Wong, L.; Merisko-Liversidge, E.; Trau, D.; Renneberg, R. *Anal. Chem.* **2004**, *76*, 3638.
38. Murray, C. B.; Norris, D. J.; Bawendi, M. G. *J. Am. Chem. Soc*. **1993**,*115*, 8706.
39. Alivisatos, A. P. *Pure Appl. Chem.* **2000**, *72*, 3.
40. Banin, U.; Cao, Y.; Katz, D.; Millo, O. *Nature* **1999**, *400*, 542.
41. Peng, X.; Manna, L.; Yang, W.; Wickham, J.; Scher, E.; Kadavanich, A.; Alivisatos, A. P. *Nature* **2000**, *404*, 59.
42. (a) Yu,W. W.; Qu, L.; Guo, W.; Peng, X. *Chem. Mater.* **2003**, *15*, 2854. (b) Gul, F.; Wang, S,; Cao, H.; Li, C. *Nanotechnology* **2008**, *19*, 095708-1
43. Iijima, S. *Nature* **1991**, *354*, 56.
44. Duan, X.; Huang, Y.; Cui, Y.; Wang, J.; Lieber, C. M. *Nature* **2001**, *409*, 66.
45. Law, M.; Sirbuly, D. J.; Johnson, J. C.; Goldberger, J.; Saykally, R. G.; Yang, P. *Science* **2004**, *305*, 1269.
46. Golberg, D.; Bando, Y.; Tang, C. C.; Zhi, C. Y. *Adv. Mater.* **2007**, *19*, 2413.
47. Schaak, R. E.; Mallouk, T. E. *Chem. Mater.* **2003**, *12*, 3427.
48. Huynh, W. U.; Dittmer, J. J.; Alivisatos, A. P. *Science* **2002**, *295*, 2425.
49. Pan, Z. W.; Dai, Z. R.; Wang, Z. L. *Science* **2001**, *291*, 1947.
50. Wei, Z. X.; Zhang, L. J.; Yu, M.; Yang, Y. S.; Wan, M. X. *Adv. Mater.* **2003**, *15*, 1382.
51. Zhong, W.; Liu, S.; Chen, X.; Wang, Y.; Yang, W. *Macromolecules* **2006**, *39*, 3224.
52. Pinto, N. J.; Johnson, Jr, A. T.; MacDiarmid, A. G.; Mueller, C. H.; Theofylaktos, N.; Robinson, D. C.; Miranda, F. A. *Appl. Phys. Lett.* **2003**, *83*, 4244.

53. O'Carroll, D.; Lieberwirth, I.; Redmond, G. *Nat. Nanotechnol.* **2007**, *2*,180.
54. O'Brien, G. A.; Quinn, A. J.; Tanner, D. A.; Redmond, G. *Adv. Mater.***2006**, *18*, 2379.
55. Granström, M.; Berggren, M.; Inganäs, O. *Science* **1995**, *267*, 1479.
56. Hoeben, F. J. M.; Jonkheijm, P.; Meijer, E. W.; Schenning, A. P. H. J. *Chem. Rev*. **2005**, *105*, 1491.
57. Grimsdale, A. C.; Müllen, K. *Angew. Chem. Int. Ed.* **2005**, *44*, 5592.
58. Yan, D.; Zhou, Y.; Hou, J. *Science* **2004,** *303*, 65.
59. Kim, Y.; Mayer, M. F.; Zimmerman, S. C. *Angew. Chem. Int. Ed.* **2003**, *42*, 1121.
60. Yamaguchi, T.; Ishii, N.; Tashiro, K.; Aida, T. *J. Am. Chem. Soc.* **2003**,*125*, 13934.
61. Shimizu, T.; Masuda, M.; Minamikawa, H. *Chem. Rev.* **2005**, *105*,1401.
62. Lehn, J.-M. *La chimie supramoléculaire, concept et perspectives,* De Boeck, **1997**, Bruxelles
63. Steed, J. W.; Atwood, J. L. *Supramolecular Chemistry*, Wiley, **2000**
64. Hunter, C. A.; Sanders, J. K. M. *J. Am. Chem. Soc.* **1990**, *112*, 5525. (b) Hunter, C. A.; Lawson, K.R.; Perkins, J.; Urch, C. J. *J. Chem. Soc. , Perkin Trans. 2,* **2001**, 651. (c) Hunter, C. A. *Chem. Soc. Rev.*, **1994**, *23*, 101
65. Zhao, Y. S.; Fu, H.; Peng, A.; Ma, Y.; Xiao, D.; Yao, J. *Adv. Mater.* **2008**, *20*, 2859.
66. (a) Kasai, H.; Nalwa, H. S.; Oikawa, H.; Okada, S.; Matsuda, H.; Minami, N.; Kakuta, A.; Ono, K.; Mukoh, A.; Nakanishi, H. *Jpn. J. Appl. Phys.* **1992**, *31*, L1132.(b) Nalwa, H. S.; Kasai, H.; Kamatani, H.; Okada, S.; Oikawa, H.; Matsuda, H.; Kakuta, A.; Mukoh, A.; Nakanishi, H. *Adv. Mater.* **1993**, *5*, 758. (c) Kasai, H.; Oikawa, H.; Nakanishi, H. Organic Mesoscopic Chemistry (Eds: H. Masuhara, F. C. Schryver), Blackwell Science, Oxford **1999**, 145.
67. Auweter, H.; Haberkorn, H.; Heckmann, W.; Horn, D.; Lüddecke, E.; Rieger, J.; Weiss, H. *Angew. Chem. Int. Ed.* **1999**, *38*, 2188.
68. Tachikawa, T.; Chung, H.-R.; Masuhara, A.; Kasai, H.; Oikawa, H.; Nakanishi, H.; Fujitsuka, M.; Majima, T. *J. Am. Chem. Soc.* **2006**, *128*, 15944.
69. Gesquiere, A. J.; Uwada, T.; Asahi, T.; Masuhara, H.; Barbara, P. F. *Nano Lett.* **2005**, *5*, 1321.
70. Olive, A. G. L.; Del Guerzo, A.; Schäfer, C.; Belin, C.; Raffy, G.; Giansante, C. *J. Phys. Chem. C* **2010**, *114*, 10410.
71. (a) An, B.-K.; Kwon, S.-K.; Jung, S.-D.; Park, S.Y. *J. Am. Chem. Soc.* **2002**, *124*, 14410.(b) An, B.-K.; Lee, D.-S.; Lee, J.-S.; Park, Y.-S.; Song, H.-S.; Park, S. Y. *J. Am. Chem. Soc.* **2004**, *126*, 10232.
72. Fery-Forgues, S.; El-Ayoubi, R.; Lamère, J.-F. *J. Fluor.* **2008**, *18*, 619.
73. (a) Terech, P.; Weiss, R. G.; *Chem. Rev.* **1997**, *97*, 3133.(b) van Esch, J. H.; Feringa, B. L. *Angew. Chem. Int. Ed*. **2000**, *39*, 2263.(c) Ajayaghosh, A.; George, S. J. *J. Am. Chem. Soc.* **2001**, *123*, 5148.
74. Yoza, K.; Ono, Y.; Yoshihara, K.; Akao, T.; Shinmori, H.; Takeuchi, M.; Shinkai, S.; Reinhoudt, D. N. *Chem. Comm.* **1998**, 907
75. Jung, J. H.; Shinkai, S.; Shimizu, T. *Chem. Eur. J.* **2002**, *8*, 2684

76. Ono, Y.; Nakashima, K.; Sano, M.; Kanekiyo, K.; Inoue, K.; Hojo, J.; Shinkai, S. *Chem. Comm.* **1998**, 1477
77. (a) Tseng, K.-P.; Kao, M.-T.; Tsai, T. W. T.; Hsu, C.-H.; Chan, J. C. C.; Shyue, J.-J.; Sun, S.-S.; Wong, K.-T. *Chem. Comm.* **2012**, *48*, 3515. (b) Del Guerzo, A.; Olive, A. G. L.; Reichwagen, J.; Hopf, H.; Desvergne, J.-P. *J. Am. Chem. Soc.* **2005**, *127*, 17984. (c) Würthner, F.; Yao, S.; Beginn, U. *Angew. Chem.Int. Ed.* **2003**, *42*, 3247.
78. Chen, J.; Herricks, T.; Geissler, M.; Xia, Y. *J. Am. Chem. Soc.* **2004,** *126*, 10854.
79. Liu, Y.; Cao, J.; Zeng, J.; Li, C.; Qian, Y.; Zhang, S. *Eur. J. Inorg. Chem.* **2003**, *4*, 644.
80. Becerril, H. A.; Stoltenberg, R. M.; Wheeler, D. R.; Davis, R. C.; Harb, J. N.; Woolley, A. T. *J. Am. Chem. Soc.* **2005**, *127*, 2828.
81. Minelli, C.; Hinderling, C.; Heinzelmann, H.; Pugin, R.; Liley, M. *Langmuir* **2005**, *21*, 7080.
82. Rosen, M. J. *Surfactants and Interfacial phenomena*, 3rd ed., Wiley, New York **2004**
83. Fu, H.; Xiao, D.; Yao, J.; Yang, G. *Angew. Chem. Int. Ed.* **2003**, *42*, 2883.
84. Yang, B.; Xiao, J.; Wong, J. I.; Guo, J.; Wu, Y.; Ong, L.; Lao, L. L.; Boey, F.; Zhang, H.; Yang, H. Y.; Zhang, Q. *J. Phys. Chem. C* **2011**, *115*, 7924.
85. (a) Martin, C. R. *Acc. Chem. Res.* **1995**, *28*, 61. (b) C. R. Martin, *Science* **1994**, *266*, 1961.
86. Possin, G. E. *Rev. Sci. Instrum.* **1970**, *41*, 772.
87. Murakami, H.; Kobayashi, H.; Takeuchi, H.; Kawashima, Y. *Int. J. Pharm.* **1999**, *187*,143
88. Kim, T.; Park, I.; Ryoo, R. *Angew. Chem. Int. Ed.* **2003**, *42*, 4375.
89. Berry, A. D.; Tonucci, R. J.; Fatemi, M. *Appl. Phys. Lett.* **1996**, *69*, 2846.
90. Chakarvarti, S. K.; Vetter, J. *Radiat. Meas.* **1998**, *29*, 149.
91. Lee, J.-K.; Koh, W. K.; Chaeb, W.-S.; Kim, Y.-R. *Chem. Comm.* **2002,** 138.
92. Zhao, L.; Yang, W.; Ma, Y.; Yao, J. ; Li, Y. ; Liu, H. *Chem. Comm.* **2003**, 2442.
93. Zhao, L.; Yang, W.; Luo, Y.; Zhai, T.; Zhang, G.; Yao, J. *Chem. Eur. J.* **2005**, *11*, 3773
94. Al-Kaysi, R. O.; Ghaddar, T. H.; Guirado, G. *J. Nanomater.* **2009**, *2009*.
95. Al-Kaysi, R. O.; Bardeen, C. J. *Chem.Comm.* **2006,** *11*,1224
96. Al-Kaysi, R. O.; Bardeen, C. J. *Adv. Mater.* **2007**, *19*, 1276.
97. Garcia-Garibay, M. A. *Angew. Chem. Int. Ed.* **2007**, *46*, 8945.
98. Dai, Z. R.; Pan, Z. W.; Wang, Z. L.; *Adv. Funct. Mater.* **2003**, *13*, 9.
99. Balzer, F.; Bordo,V. G.; Simonsen, A. C.; Rubahn, H.-G. *Appl. Phys. Lett.* **2003**, *82*, 10.
100. Chiu, J. J.; Kei, C. C.; Perng, T. P.; Wang, W. S.; *Adv. Mater.* **2003**, *15*,1361.
101. Liu, H.; Li, Y.; Xiao, S.; Gan, H.; Jiu, T.; Li, H.; Jiang, L.; Zhu, D.; Yu, D.; Xiang, B.; Chen, Y., *J. Am. Chem. Soc.* **2003**, *125*, 10794.
102. Zhao, Y. S.; Fu, H. B.; Hu, F. Q.; Peng, A. D.; Yang, W. S.; Yao, J. N. *Adv.Mater.* **2008**, *20*, 79.
103. Valeur, B. *Molecular Fluorescence : Principles and Applications.* **2001** Wiley-VCH
104. Lakowicz, J.R. *Principles of Fluorescence Spectroscopy,* **1983**. Plenum Press, New York
105. Dexter, D. L. *J. Chem. Phys.* **1953,** *32*, 836
106. Scholes, G. D. *Annu. Rev. Phys. Chem.* **2003**, *54*, 57.
107. (a) Förster, T. *Faraday Discuss. Chem. Soc.* **1959**, *27*, 7. (b)Turro, N. J. *Modern*

Molecular Photochemistry, **1991,** University Science Books
108. IUPAC Compendium of Chemical Terminology, 2nd ed. Compiled by A.D. McNaught and A. Wilkinson. **1997**, Blackwell Scientific Publications, Oxford.
109. Liang, W Y. *Physics Education* **1970,** *5*, 226.
110. a) McRae, E. G.; Kasha, M. *J. Chem. Phys.* **1958**, *28*, 721; b) Kasha, M.; Rawls, R.; El-Bayoumi, M. A. *Pure Appl. Chem.* **1965,** *11*, 371
111. Lim, S.-J.; An, B.-K.; Jung, S. D.; Chung, M.-A.; Park, S. Y. *Angew. Chem. Int. Ed.* **2004**, *43*, 6346.
112. Kasai, H.; Kamatani, H.; Okada, S.; Oikawa, H.; Matsuda, H.; Nakanishi, H. *Jpn. J. Appl. Phys.* **1996**, *35*, L221.
113. Xiao, D.; Xi, L.; Yang, W.; Fu, H.; Shuai, Z.; Fang, Y.; Yao, J. *J. Am. Chem. Soc*. **2003**, *125*, 6740.
114. Zhao, Y. S.; Fu, H.; Hu, F.; Peng, A. D.; Yao, J. *Adv. Mater.* **2007**, *19*, 3554.
115. Wang, Z.-C.; Xiao, W.-C.; Ding, X.-L.; Ma, Y.-P.; Xue, W.; He, S.-G. *Nanotech.***2008**, *19*, 505703.
116. Lei, Y.; Liao, Q.; Fu, H.; Yao, J. *J. Am. Chem. Soc*. **2010**, *132*, 1742.

Chapter 2

Crystals and nanorods of 9,10-diphenylanthracene derivatives

In this chapter, we present the work of bottom-up study on building a nanometer-scaled light-harvesting system and tuning the photophysical properties by energy transfer process. A series of 9,10-diphenyl anthracene derivatives with different length of alkoxy chain substituent are synthesized and investigated both in monomer and in the solid state (crystal). With the knowledge of these derivatives, nano-structures of uniform size are fabricated and exploited as light-harvesting matrices.

2.1 9,10-diphenylanthracene derivatives

9,10-Diphenylanthracene (**DPA**) is a long known polyaromatic compound[1] with a high fluorescence quantum yield of 0.88±0.03.[2] Its crystal structure was first published in 1979 by Adams and Ramdas. [3] In recent publications, **DPA** and its derivatives were used for a variety of optical and electronic purposes, such as organic light emitting devices (OLEDs),[4-7] semiconducting materials,[8-9] electronic chemiluminescence[10] and photovoltaics[11]. All this ongoing research in **DPAs** shows how valuable it is to understand how these properties came to be and how we can change them to our advantage. Lee *et al.* described in 2008 the self-assembling of **DPA** to nanoribbons and nanorods[12] and provided an insight into the growth mechanism of **DPA** and its nano-objects.

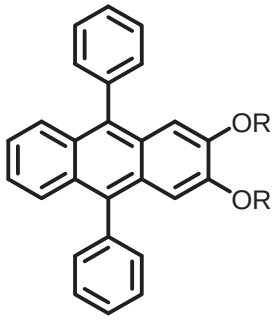

R -CH_3 (**B1**) -C_8H_{17} (**5/B8**)
-C_2H_5 (**2/B2**) -$C_{10}H_{21}$ (**6/B10**)
-C_4H_9 (**3/B4**) -$C_{16}H_{33}$ (**7/B16**)
-C_6H_{13} (**4/B6**)

Scheme 2.1: 9,10-diphenyl anthracene derivatives

In this part of work, we describe a detailed study of **DPA** derivatives especially focusing on the solid state (crystal). Different techniques and microscopy were applied to allow us obtain the perspective of the changes in structural arrangement and optical properties of **DPA**, when alkyloxy-chains are attached to the anthracene-backbone in 2- and 3-position and how the chain-length influences the alignment of the anthracene backbone in the solid state and therefore defines the properties of the solid structure. The optical properties were investigated in solution and the solid state, and related to the corresponding molecular arrangements in the crystal.

2.1.1 Results

2.1.1.1 Synthesis

The reaction sequence is shown in scheme 2.2. The hydroxyl groups were deprotonated

with potassium carbonate in DMF and the corresponding bromoalkane (or methyliodide in case of 2,3-dimethoxy-anthraquinone) was added to get the corresponding 2,3-dialkyloxy-anthraquinone in high yields as reported before by Bouas-Laurent *et al.*[13] Phenyl lithium was used to attach phenyl rings to the quinone and the resulting hydroxy groups were removed with hydrogen iodide as a reducing reagent in boiling ether. All final products were purified by column chromatography on silica gel. This synthetic strategy was previously developed by Dr. Christian Schäfer and scaled up during this thesis to yield large amounts of compounds for further studies.

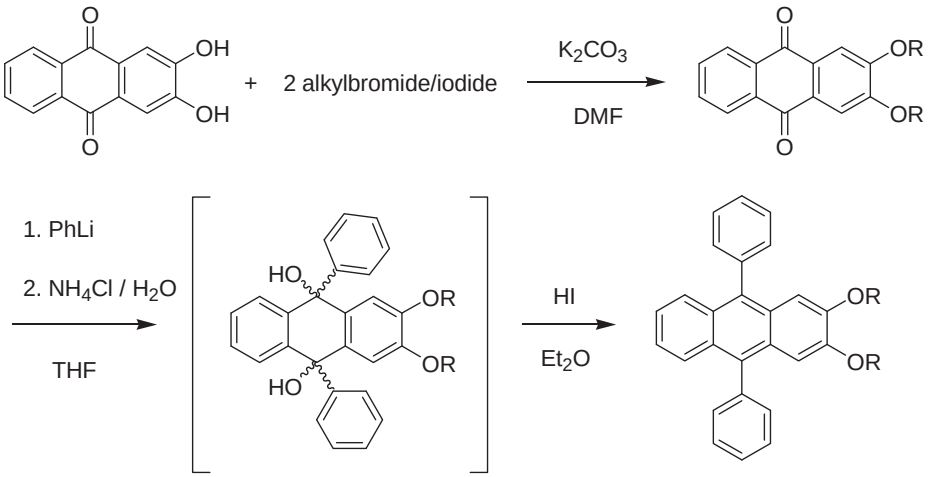

Scheme 2.2: Reaction sequence for 2,3-dialkyloxy-9,10-diphenyl-anthracenes.

2.1.1.2 Crystals structure

Compounds **B1**, **B2**, **B4** and **B8** crystallize from dichloromethane solutions upon diffusion of methanol. The crystal structure of 2,3-dimethoxy-9,10-diphenyl-anthracene (**B1**) is orthorhombic and of the space group Pbca. Interestingly, this structure already deviates from the reported structure of 9,10-diphenyl-anthracene (**DPA**), which is monoclinic (although the β-angle of the elementary cell is very close to 90°) and of the space group B2/c and therefore less symmetric. Obviously the space requirement of the methoxy groups is responsible for this change, although a less symmetrical structure would be expected upon asymmetric addition of methoxy groups to one side of the anthracene core. As shown in Figure 2.1, arrangement of the anthracene backbones in **DPA** [a) view along a-axis] differs from **B1** [b) view along b-axis]. The angle from one layer of anthracenes to the next grows wider with **B1**, a point we will keep in mind for the following structures.

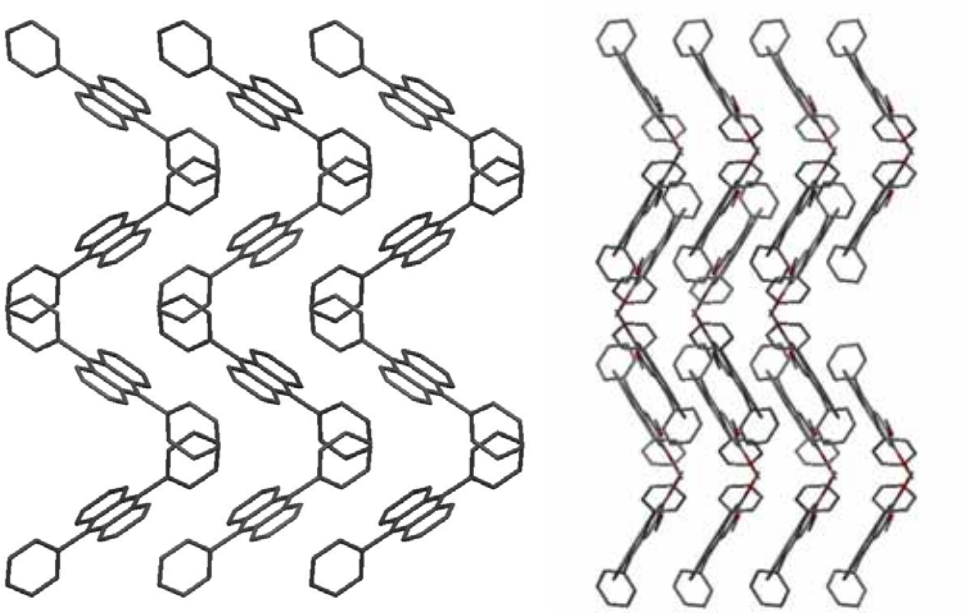

Figure 2.1: Crystal structures of **DPA** (left, view along a-axis) and **B1** (right, view along b-axis). Hydrogens were omitted for clarity.

The crystal structure of 2,3-diethoxy-9,10-diphenyl-anthracene (**B2**) has the same orthorhombic space group (Pbca) as **B1**. The volume of the unit cell is as expected a little bigger than in **B1**, but the structural arrangement is very similar. Although the two ethoxy groups are rather short, one of them already bears a disorder for two possible arrangements within the crystal structure. In case of **B2**, the angle of anthracene backbones from one layer to the next is slightly wider than in **B1**.

2,3-Dibutyloxy-9,10-diphenyl-anthracene (**B4**) could be crystallized in two polymorphic structures, which are both monoclinic and in the space group $P2_1/c$, but have different values for side lengths a, b and c and the β angle. Interestingly, the butyloxy-chains show no disorder in both cases, although this could be expected for these long chains. The first structure **B4a** we obtained deviates a lot from the ones previously observed (see p.57, figure 2.31). The asymmetric unit contains two molecules (in case of **B1** and **B2** only one molecule) and within the packing, no layered arrangements of the anthracene cores is visible. In the second case **B4b** we observed similarities to **B1** and **B2**. The asymmetric unit contains only one molecule and the structure is made of layers of anthracenes again. Compared to **B1** and **B2**, the angle between anthracene backbones widens up even more. Another point of interest is the positioning of the chains within the crystal. In Figure 2.2, the structure of **B4b** is shown with and without chains.

Considering a layered arrangement of the anthracene cores, the last one or (in case of the second chain of each molecule) two carbon atoms of each chain stick out of the layer and the rest stays in.

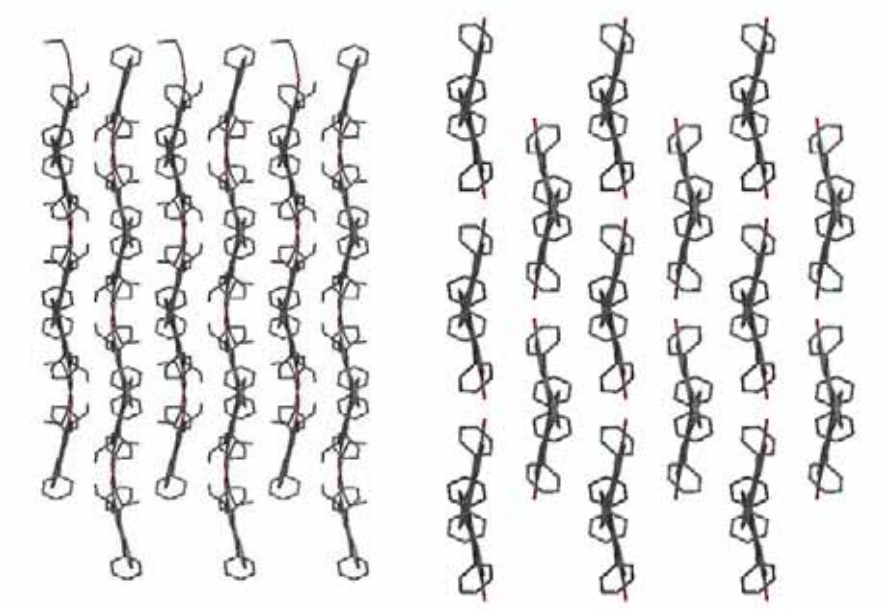

Figure 2.2: Crystal structure of **B4b** (view along c-axis) with (left) and without (right) chains. Hydrogens were omitted for clarity.

The last and most unusual crystal structure we could obtain is the one of 2,3-dioctyloxy-9,10-diphenyl-anthracene (**B8**), which is monoclinic and of the space group $P2_1/a$ (the β-angle is 90.015° very close to 90°, which would make the crystal orthorhombic like in **B1** and **B2**). All anthracene backbones in this structure are almost in one plane within the different layers. Figure 2.3 shows the structure with (left) and without (right) chains.

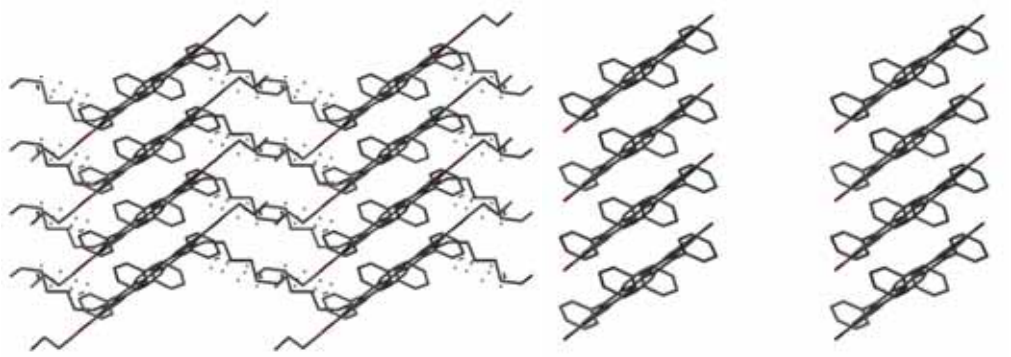

Figure 2.3: Crystal structure of **B8** (view along b-axis) with (left) and without (right) chains. The unconnected dots are disordered carbon atoms of the chains. Hydrogens were omitted for clarity.

The alkoxy chains occupy the space between two anthracenes and connect one layer of anthracene backbones with another one. The dots in figure 2.3 (left) represent disordered carbon atoms of the octyloxy-chains. In each chain, the last four carbon atoms are disordered and can be found in two or even three different positions, which is not unusual for chains this long. Figure 2.4 shows the view of **B8** along the a- and the c-axis. For clarity only the oxygen-atoms of each chain are shown, which makes it easier to see that any anthracene is rotated about 90° to the next within the anthracene's aromatic plane. In the view along the a-axis of figure 2.4 is a lot of space between the two anthracene layers, which is occupied by the chains.

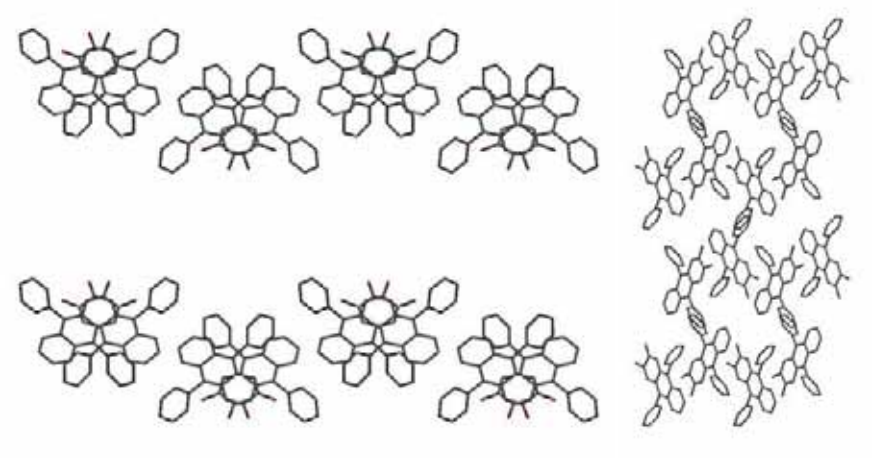

Figure 2.4: Crystal structure of **5/B8**, view along a- (left) and c-axis (right). Chains and hydrogens were omitted for clarity

The different crystal structures of **DPA** show the influence of the length of the alkoxy-chains on the arrangement of anthracene backbones towards each other (see also table 2.1). Starting from **DPA**, were the angle between two planes of the anthracene core is 114°, addition of longer alkoxy-chains leads to wider angles and reaches 166° for **B8**.

Table 2.1: Comparison of the different crystal structures.

Compound	Crystal system	Space group	Volume per unit cell (Å³)	Molecules per unit cell	Volume per molecule (Å³)	Density calc. (g/cm^3)	Angle(s) between anthracene layers (°)
DPA	monoclinic	B2/c	1784.04	6	297.34	1.846	114.04
1/B1	orthorhombic	Pbca	4154.43	8	519.30	1.322	119.97, 120.92, 170.03
2/B2	orthorhombic	Pbca	4571.46	8	571.43	1.282	121.83, 122.14, 174.49
3/B4b	monoclinic	$P2_1/c$	2669.15	4	667.29	1.238	157.05
5/B8	monoclinic	$P2_1/a$	3528.08	4	881.02	1.148	165.69

2.1.1.3 Macroscopic Changes

For the shorter chains (**B1**, **B2** and **B4**), the crystals have a needle-like shape (Figure 2.5a, 2.5b). However, the needles get thinner the longer the chain and with the hexyloxy-chain (**B6**), the crystals look more fiber-like. **B10** and **B16** precipitate as a powder and bear the fiber-like shape (Figure 2.5c, 2.5d). These properties are more precisely evidenced in the forthcoming microscopy sections. **B10** and **B16** do not provide large enough crystals for X-ray diffraction

studies and were characterized by scanning electron (SEM) and atomic force (AFM) microscopies.

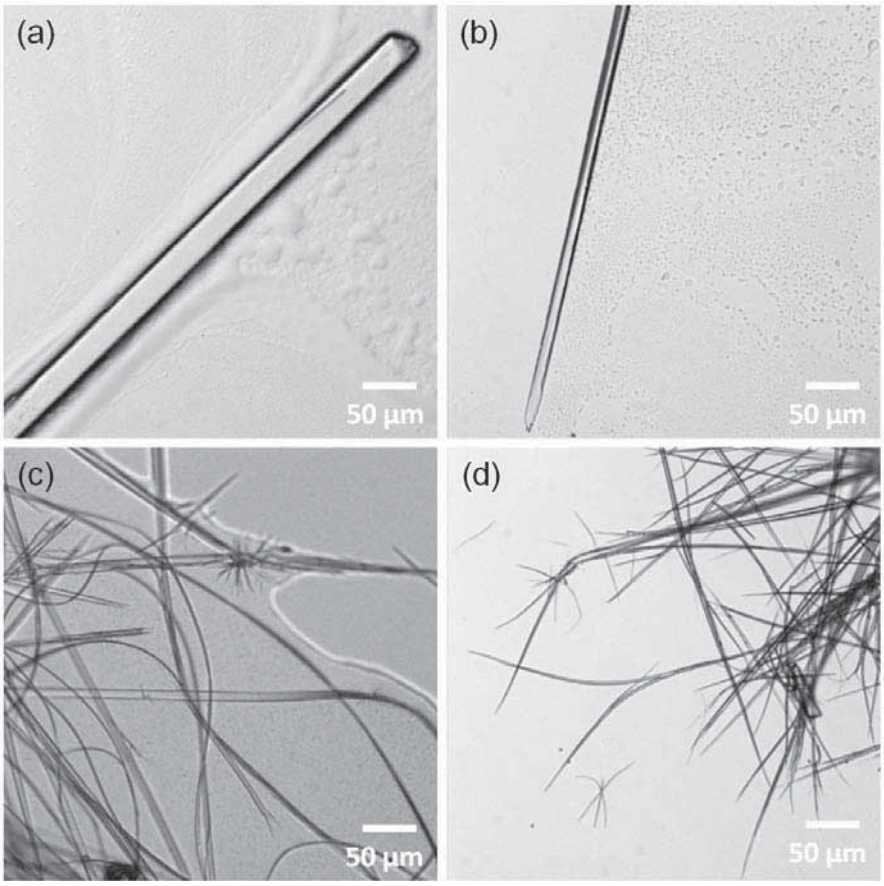

Figure 2.5: Optical transmission images of crystals of (a) **B1,** (b) **B2,** (c) **B6** and (d) **B10**, image size: 400 × 400 µm

SEM images reveal that these compounds form very long ribbons (Figure 2.6). Quantitative measurements by AFM (Figure 2.7) indicate that the ribbons of **B10** are ~7 µm wide and ~0.4 µm thick (average value of 10 objects on 5 AFM images), while ribbons of **B16** are smaller, ~1.7 µm wide and ~140 nm high (average of 20 objects on 5 AFM images).

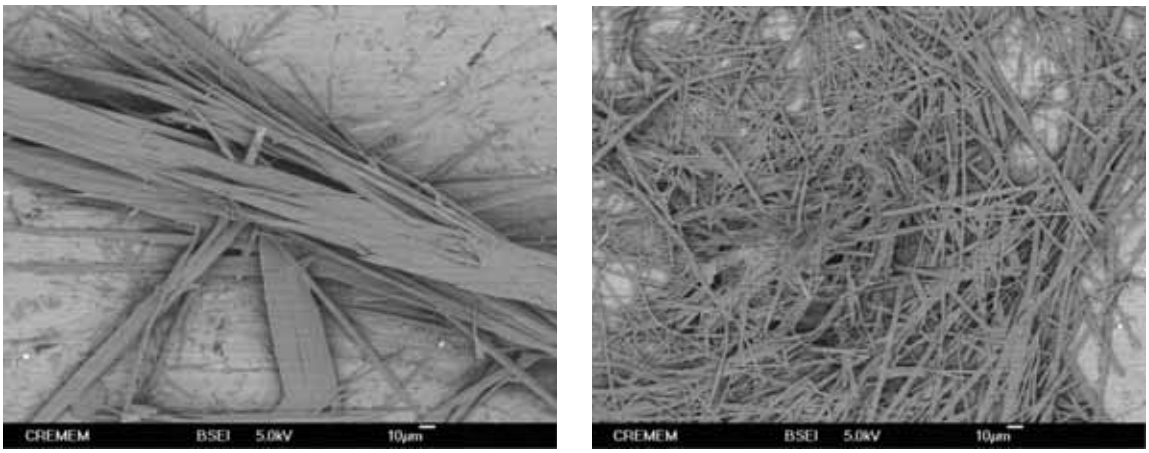

Figure 2.6: SEM images of **B10** (left) and **B16** (right), magnification : 350 x

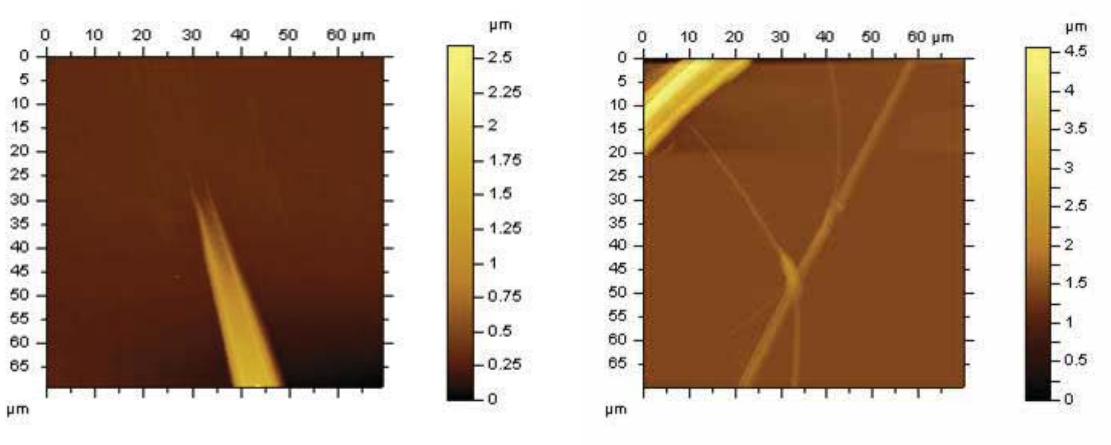

Figure 2.7: Topography AFM images of **B10** (left) and **B16** (right), 70 µm × 70 µm, drop-casting (**B10)** and spin-coating at 2000 rpm (**B16**) on mica

2.1.1.4 Spectroscopic properties

9,10-diphenyl-anthracenes derivatives are good near-UV absorbers and excellent blue-light emitters in solution (Table 2.2).

The 2,3-dialkyloxy-DPAs with a 2-carbon chain or longer absorb at 373 nm and 393/394 nm, with an emission maximum at 433 nm and a fluorescence quantum yield in THF ranging from 0.74 to 0.77. As compared to **DPA** (Figure 2.8), while the absorption is unchanged, the emission is red-shifted by 6-7 nm and slightly weaker. In contrast, **B1** is the most hypsochromic absorber of all and emits at a slightly lower energy than the other 2,3-dialkyloxy-DPAs. Interestingly, **B1** displays a QY that reaches 0.95 and is even higher than the standard **DPA** with an identical radiative constant $k_r = 1.3\times10^8$ s^{-1} and a lower non-radiative component $k_{nr} = 7\times10^6$ s^{-1}. The other compounds display a lower k_r of ~1.3×10^8 s^{-1} and a higher k_{nr} of ~3×10^7 s^{-1}.

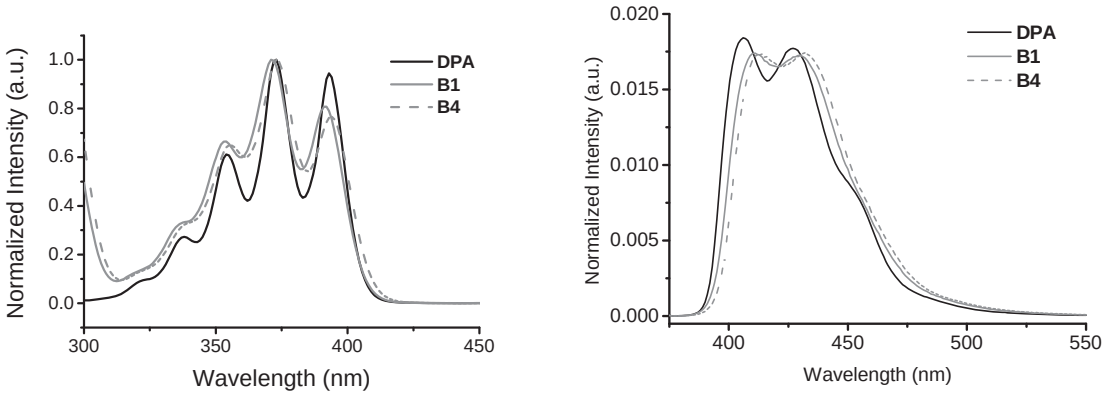

Figure 2.8: Normalized absorption (left) and emission spectra (versus Q.Y., right) of **DPA**, **B1** and **B4**

Table 2.2: Optical and photophysical properties of **DPA**s **B1 - B16** in solution

Compound	λ^{abs}_{max} [nm]	λ^{abs}_{0-0} [nm]	$\varepsilon_{\lambda max}$ [$\times 10^4$ $M^{-1}cm^{-1}$]	λ^{em}_{max} [nm]	$\Phi_{ex373}{}^{em}$ soln.[a,b]	τ [ns]	k_r [$\times 10^8$ s^{-1}]	k_{nr} [$\times 10^7$ s^{-1}]
DPA[d]	373	393	1.40[e]	406, 427	0.90	7.6[f]	1.2	1.3
B1	371	392	1.10	411, 430	0.95	6.7	1.4	0.7
B2	373	393	1.12	412, 432	0.77	7.1	1.1	3.2
B4	373	394	1.14	413, 433	0.74	6.9	1.1	3.8
B6	373	394	1.10	413, 433	0.79	6.9	1.1	3.0
B8	373	394	1.14	413, 433	0.76	6.9	1.1	3.5
B10	373	394	1.09	413, 433	0.77	7.0	1.1	3.3
B16	373	394	1.00	413, 433	0.75	6.9	1.1	3.6

[a] Samples in deoxygenated THF (1.0×10^{-5} M).

[b] Measured with 9,10-diphenyl-anthracene in deoxygenated cyclohexane as reference

[c] Measured with an integrating sphere.

[d] Measured in deoxygenated cyclohexane

[e] I. B. Berlman, *Handbook of Fluorescence Spectra of Aromatic Molecules,* Academic Press, 1971

[f] John V. Morris, Mary A. Mahaney, and J. Robert Huber *J. Phys. Chem.*, **80**, 969-974, 1976

In the solid state, larger differences between these emitters clearly appear (Table 2.3). Crystalline powder, pressed into a KBr slice to measure absorption spectra, or used as such in an integration sphere to obtain emission spectra and quantum yields, revealed the solid-state photophysical properties. **B1**, **B2** and **B4** display very high quantum yields, between 0.97 and 0.86. It has to be noticed that such a high QY is almost unprecedented at room temperature in the solid state.[17] Interestingly, **B1** and **B4** emit more in the solid state than in solution.

With increasing chain length, a progressive decrease of the QY occurs from 0.69 to 0.33. The variations of QY are partially correlated to the emission maxima. Indeed, **B1**, **B2** and **B4** are the most hypsochromic emitters and absorbers, and display the smallest apparent Stokes shifts (the emission maxima are originating from a 0-1 transition). **B6**, **B8** and **B10** absorb and emit more similarly to **DPA**, with larger Stokes shifts. All absorbances and emissions are slightly red-shifted as compared to the solution (Figure 2.9). The emission vibronic structure of **B1**, **B2** and **B4** quite resemble **DPA** (Figure 2.10). With the longest chains, the vibronic structures are attenuated (Figure 2.10). **B16** is a more particular case, since it displays a higher energy emission like **B1**, **B2**, **B4**, but an attenuated vibronic structure with a small shoulder at higher energy (Figure 2.11), as well as the lowest quantum yield and absorption maximum of all.

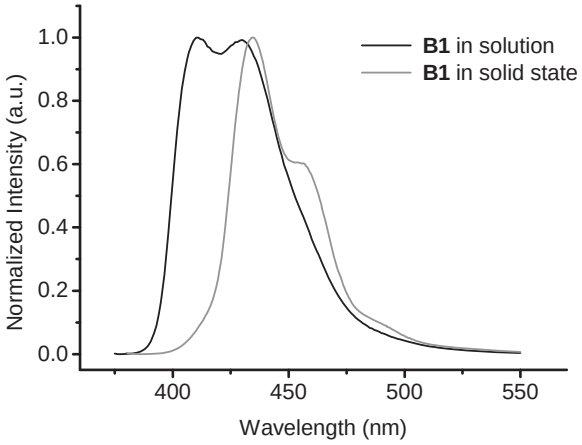

Figure 2.9: Normalized emission spectra of **B1** in THF solution (1×10^{-5}M, black line) and in solid state (gray line)

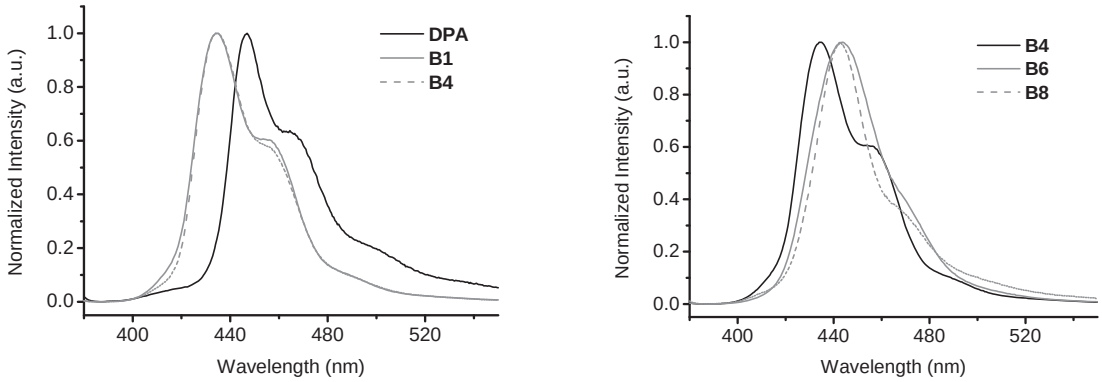

Figure 2.10: Normalized emission spectra of **DPA**, **B1**, **B4** (left) and **B4**, **B6**, **B8** (right) in solid state

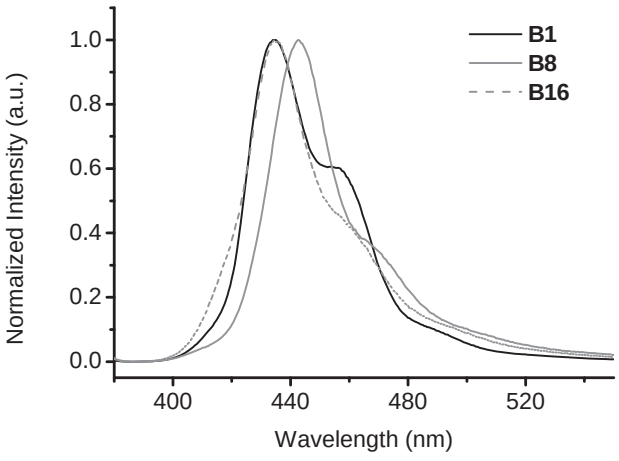

Figure 2.11: Normalized emission spectra of **B1**, **B8** and **B16**

Average decay times (bi-exponential fittings, Figure 2.12) on powders revealed that the emissive crystals with QY>0.6 display the highest values (<5.1 ns) and similar radiative constants in the range $1.2\text{-}1.3\times10^{8}$ s^{-1}. While for **DPA** and **B1** this means a slightly lower k_r than in solution, it reflects an increase for **B2 – B6**. A decrease of the radiative constant is

only observed for the ribbons **B10** and **B16**. The non-radiative processes increase significantly for **B6** – **B16**.

Table 2.3: Absorption and emission of **B1 - B16** in the solid state.

Compound	$\lambda^{abs}{}_{max}{}^{a}$ [nm]	$\lambda^{abs}{}_{0\text{-}0}{}^{a}$ [nm]	$\lambda^{em}{}_{max}$ [nm]	$\Phi_{ex373}{}^{em}$ powder [b]	τ^{d} [ns]	kr [$\times 10^8$ s^{-1}]
DPA	380	404	446.5	0.63	5.1	1.2
B1	375	398	435	0.97[c]	8.3	1.2
B2	377	401	437	0.86	7.3	1.2
B4	377	399	435	0.90	6.9	1.3
B6	378	403	443.5	0.69	5.7	1.2
B8	379	404	443	0.47	4.5	1.1
B10	380	404	443.5	0.42	4.7	0.9
B16	375	399	435.5	0.33	3.8	0.9

[a] Measured within KBr slice [b] Measured with an integrating sphere

[c] Three measurements were carried out, the standard deviation value is 0.04. Approximatly expected to be similar fro all the samples. [d] Arithmetic average value , $\bar{\tau} = \sum_i \alpha_i \tau_i$, $\sum \alpha_i = 1$

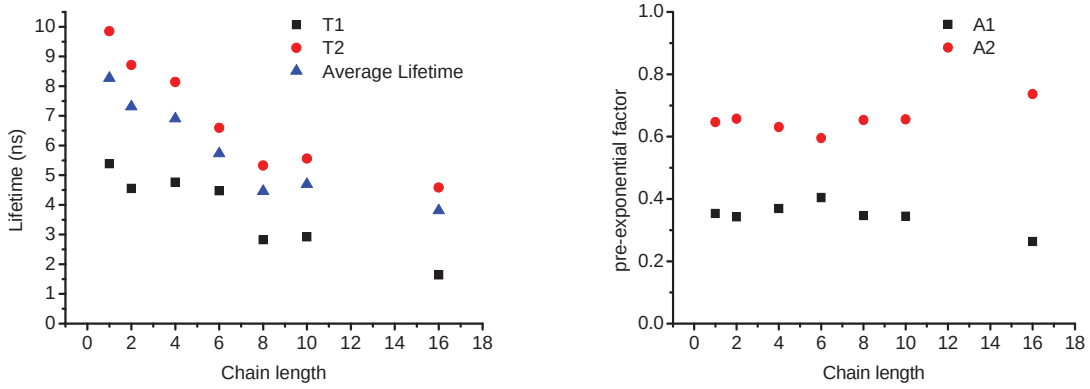

Figure 2.12: The two decay and average lifetime of bi-exponential fitting versus chain length (left), and relative amplitude of these two decays versus chain length (right).

Figure 2.12 displays the similar trends of the first decay time, the second decay time and the average lifetime with chain length. Meanwhile, the relative amplitude of each decay time does not vary with chain length respectively. In some cases, the average lifetime is used as a represented character.

2.1.1.5 Single Crystals and Ribbons

Confocal fluorescence microscopy allows analyses of the distribution of spectroscopic features and excited state dynamics within single crystals or ribbons, while additionally providing information on the polarization of the emission of these anisotropic objects.

2.1.1.5.1 Principles of Confocal Fluorescence Microscopy

The confocal fluorescence microscopy principle is presented in scheme 2.3.

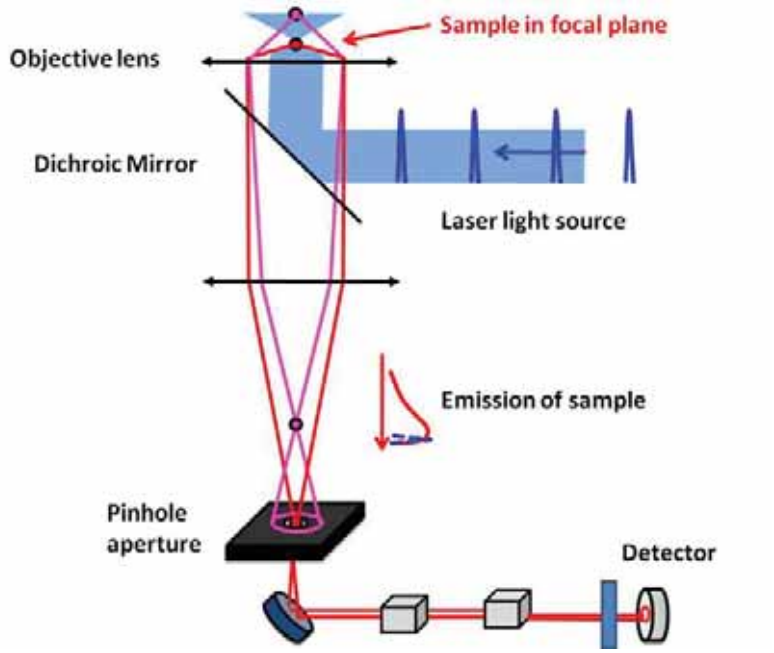

Scheme 2.3: The optical pathway and principle of confocal fluorescence microscopy

The laser beam is focused on the sample positioned at the objective lens' focal point. As the laser is reflected by a dichroic mirror and projected onto the samples in a defined focal plane, the light emitted from the points on the samples (in the same focal plane) pass back through the dichroic mirror which suppresses the laser diffraction on glass or nano-objects and is focused as a confocal point at the detector pinhole aperture.

Any light that occurs at points out of the objective focal plane will be obstructed by this detector pinhole (as shown by the dotted pink line in the image). Only a small fraction of this out-of-focus fluorescence emission is delivered through the pinhole aperture. Most of the fluorescence is blocked by the pinhole and does not contribute to the resulting image. It results in sharper images than those from conventional fluorescence microscopy techniques and permits us to obtain images of planes at various depths within the sample.

After passing the pinhole, the light intensity is detected by a CCD camera for spectroscopy or avalanche photodiodes, transforming the light signal into an electrical one that is recorded by a computer.

Images are obtained by reconstruction with the emission intensity and lifetime at each point recorded with high-speed avalanche photodiodes (SPAD: Single Photon Avalanche Diodes) coupled to a time correlated single photon counter in (TSCPC Time Correlated Single photon counting). All the data is processed with the software Sympho Time V. 4.721. The sample is laterally moved with the assistance of the piezo x-y stage which allows to scan the sample and to obtain an image. Information of different focal planes can be collected by raising or lowering the objective lens in z direction.

The resolution in confocal fluorescence microscopy is limited by the diffraction of emitted light. The lateral resolution (d_{min}) and axial resolution (Z_{min}) are defined as :

$$d_{\min} = \frac{0.6\lambda}{N.A.} \qquad \text{(Rayleigh's criterion)} \quad \text{and} \quad Z_{\min} = \frac{1.44\lambda}{N.A.^2} n$$

where λ is the emission wavelength, NA is the numerical aperture of objective lens, and n the index of refraction of the medium.

For **DPA** derivatives crystal study, the emission wavelength is around 440 nm and the numerical aperture of the 100 times objective lens is 1.4. It results the lateral and axial resolutions are 190 nm and 460 nm respectively under ideal conditions.

When acquiring an image, the number of nanometers per pixel should be chosen properly. According to Nyquist sampling theorem, the number of nm / pix must be at least equal to twice the highest frequency, yielding the following simplified formula: $\#N = \frac{d_{\min}}{2.3}$

For instance, sampled images with a resolution of 80 nm / pix have an optimal resolution in the terms of use of our editing (which corresponds to images with a maximum size of 40 x 40 µm)

2.1.1.5.2 Emission Spectra of single crystals and ribbons

A pixel size of 250 nm and an acquisition time of 1.2 ms per pixel have been used, and each spectrum is the sum of the fluorescence of 60 pixels. For each derivative, 12-15 spots of different objects have been analyzed and differences of only ~20% (for instance **B1** and **B10**, Figure 2.13) in the relative contributions of the bands have been observed. To facilitate further comparison with the bulk measurements, for each derivative an average of the spectra is calculated (Figure 2.14). The difference of these average spectra with the bulk-spectra resides essentially in the observation of the 0-0 transition with a weight of 0.6 to 0.8 relative to the 0-1 transition. The 0-1 transition also appears slightly more hypsochromic in the single crystal study with respect to the bulk measurement, with the exception of **B4**. In the single crystals and in the bulk measurements, the 0-2 transition is visible as a shoulder, with the exception of **B16** (ribbons).

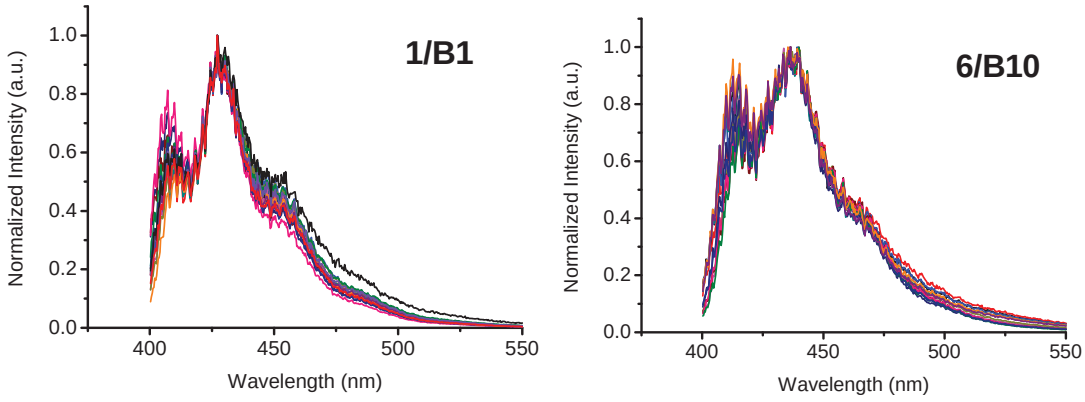

Figure 2.13: Normalized emission spectra on single objects of **B1** (left) and **B10** (right). λ_{ex} 385 nm

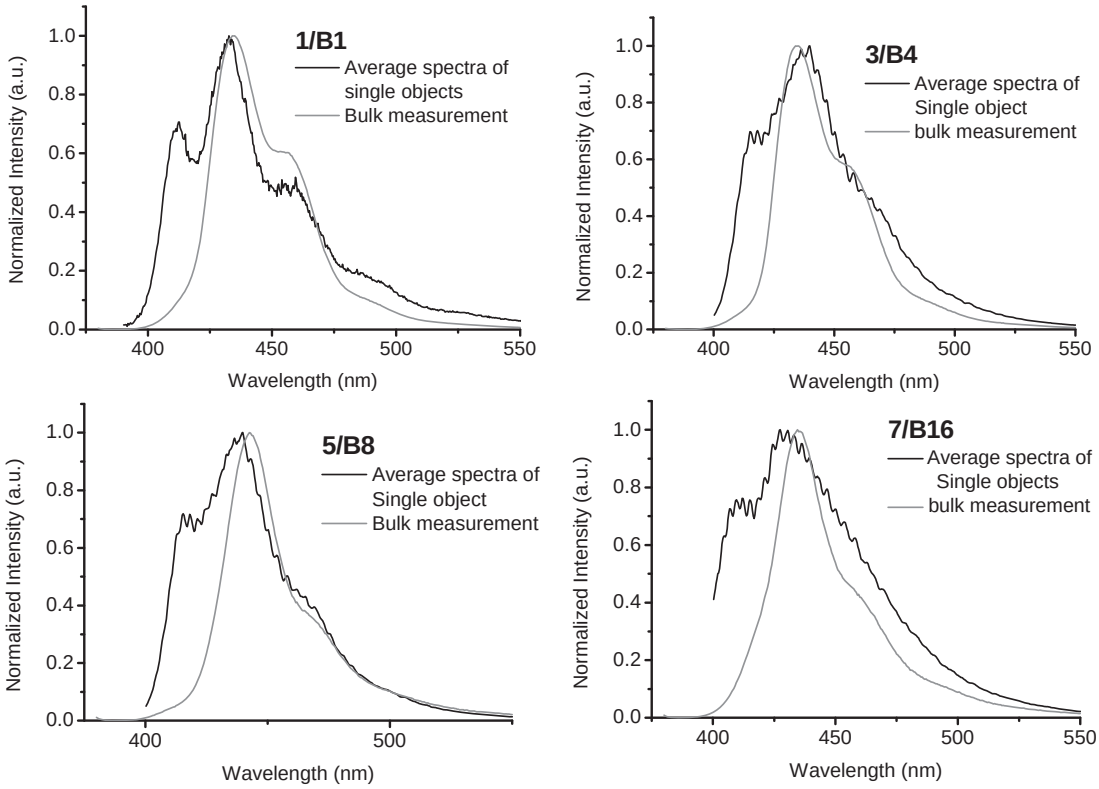

Figure 2.14: Normalized spectra of average single objects and bulk measurement for **B1**, **B4**, **B8** and **B16**

2.1.1.5.3 Decay times

Excited states dynamics were studied on single objects of the **DPA** derivatives. Fluorescence lifetime images (FLIM) reveal the excited decays of **DPAs** can be represented by bi-exponential function $\sum A_i \exp(-t/\tau_i)$, the counts of each pixel are divided into two weighted contributions, $A_1\tau_1/\sum A_i\,\tau_i$, and $A_2\tau_2/\sum A_i\,\tau_i$. The initial value of τ_1 and τ_2 are decided by a fit on accumulated decay of the whole area.

In **B1** and **B2** the average decay time is quite similar within all the areas of all the crystals imaged (Figure 2.15), yielding overall an average value of 6.6 and 6.2 ns (Table 2.4). For all the other crystals, a more heterogeneous distribution of the decay times and lower average values in the range 4.1 to 4.8 ns have been observed (Figure 2.16, 2.17). More particularly, as evidenced in Figure 2.16 for **B4** and **B6**, the decay times at the "ends" of crystals are shorter than in the larger "central" part. For ribbons of **B16**, even larger heterogeneities are observed (Figure 2.18). Indeed, each ribbon differs from another while mostly preserving the same lifetimes along the ribbon over several tenths of microns. Nevertheless, even within a same ribbon variations in the decay times from 3.7 to 4.6 ns are sometimes observed.

Detailed analysis of these decay times and their relative amplitude reveals the major difference between those obtained in the bulk measurement and CFM (Figure 2.19). There is no obvious trend for the variation of the decay times with the chain length, but the relative amplitude of each decay time depends on the chain length. For the longer decay time, the

relative amplitude decreases with the increase of the chain length. However, the contribution of the shorter decay time displays the opposite trend. These decay times differ from those obtained in the bulk, as will be further discussed below.

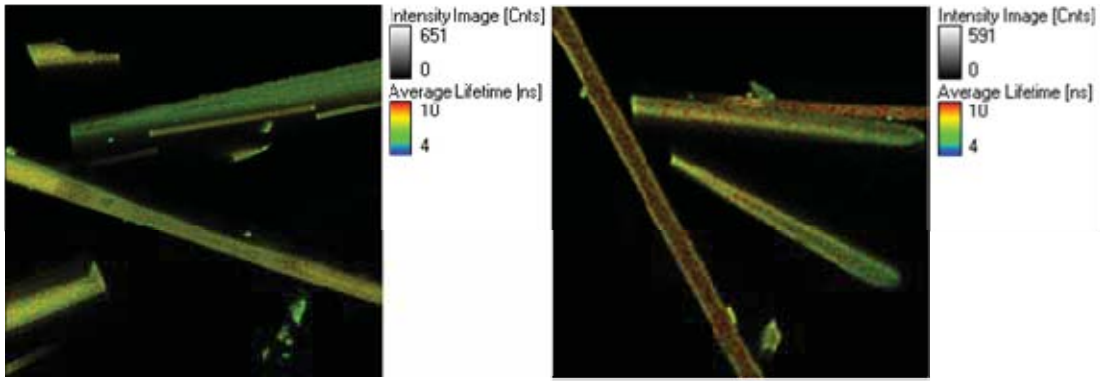

Figure 2.15: FLIM images of **B1** (left) and **B2** (right) (80 × 80 μm), λ_{ex} 385 nm, λ_{em} > 405 nm (color code: average decay time)

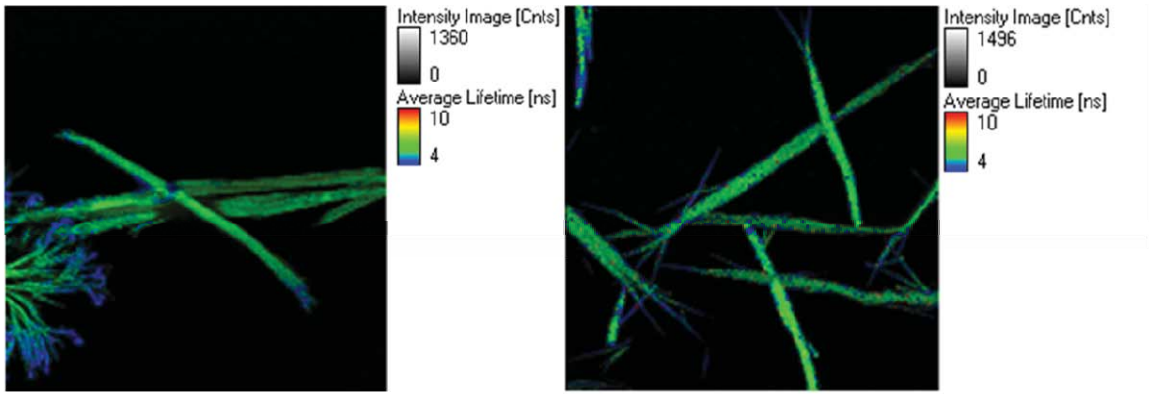

Figure 2.16: FLIM images of **B4** (left) and **B6** (right) (80 × 80 μm), λ_{ex} 385 nm, λ_{em} > 405 nm (color code: average decay time)

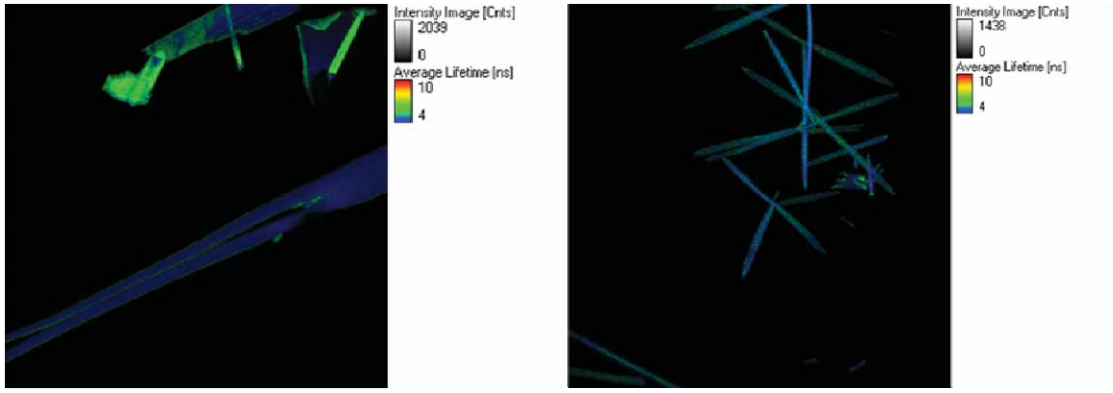

Figure 2.17: FLIM images of **B8** (left) and **B10** (right) (80 × 80 μm), λ_{ex} 385 nm, λ_{em} > 405 nm (color code: average decay time)

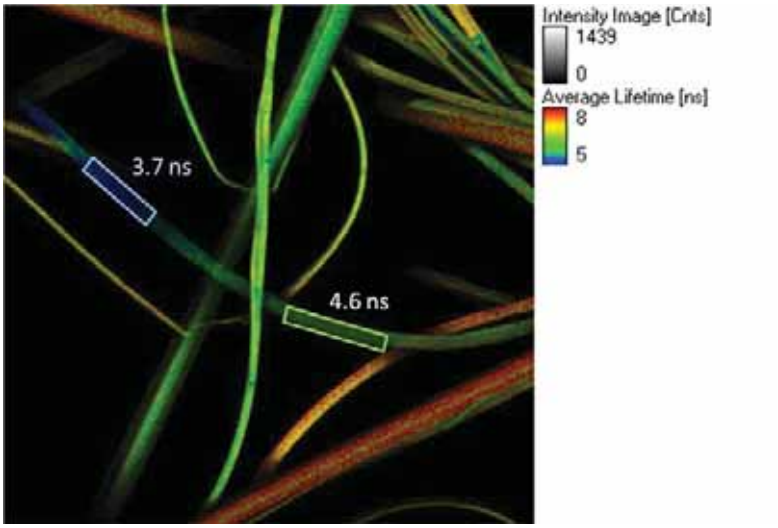

Figure 2.18: FLIM images of **B16** (80 × 80 µm), λ_{ex} 385 nm, λ_{em} > 405 nm (color code: average decay time)

Table 2.4: Average decay time of **B1 - B16** in the solid state obtained by CFM.

Compound	Average τ[a] [ns]	kr [$\times 10^8$ s^{-1}]
DPA	3.6	1.7
B1	6.6	1.5
B2	6.5	1.3
B4	4.8	1.8
B6	4.2	1.6
B8	4.1	1.1
B10	4.2	1.0
B16	4.4	0.8

[a] Arithmetic average value

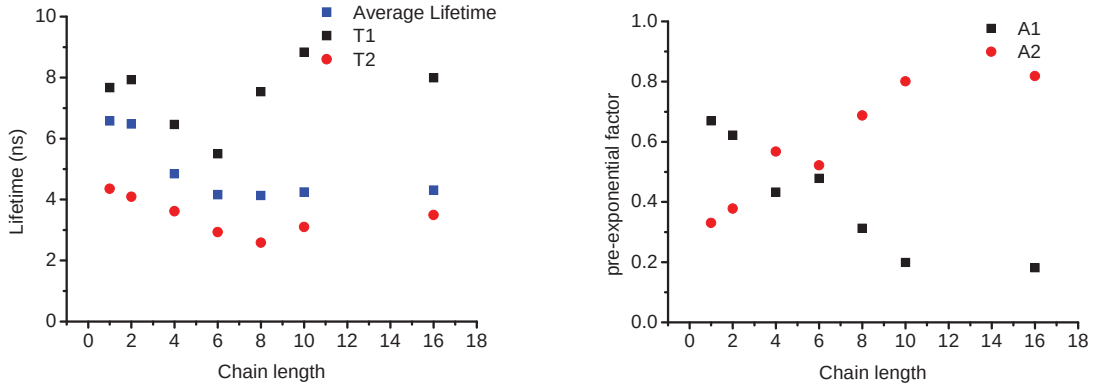

Figure 2.19: The two decay times and average lifetime of bi-exponential fitting versus chain length (left), and the corresponding pre-exponential factor versus chain length (right)

2.1.1.5.4 Photostability

The photo-stability of the crystals of **DPA**, **B1**, **B4**, **B8** and **B16** is examined by irradiating the crystal at a point, which is totally un-bleached in the beginning, continuously for 300s with the laser power ~0.3 W/cm^2 at 385 nm and simultaneously recording the emission intensity. The emission intensity at 300s was then divided by the initial intensity at time 0, the resulting ratio is demonstrated at figure 2.20 as the factor presenting the photostability of these crystals.

The non-substituted **DPA** has the best photostability compared to the other derivatives, only 8% emission intensity was photo-bleached, whereas the emission intensity of **B1** was photo-bleached by 23%. Generally, the intensity ratio decreases with the increase of chain length, with the exception of **B4**. Günter *et al.* proposed that more ordered and dense molecular packing induce a lower exposure to free radicals such as oxygen and thus a decreased degradation by reaction with this radicals.[15] In agreement with this hypothesis, the correlation between packing density and photodegradation is observed in the case of **DPA**'s. In addition to, or in replacement for this interpretation, the size of the crystals has to be considered. Indeed, the shorter chain length crystals are larger and are less photobleached. This correlates also with the surface to volume ratio, suggesting that the molecules at the surface are more exposed to oxygen and can be photobleached faster. In contrast, as shown in figure 2.20, 80% emission of **B4** was photo-bleached, which is even more than the 65% emission lost of **B16.** This surprising result is not easy to be attributed because the density of **B4** crystal is higher than in **B8** (1.238 g/cm^3 for **B4b**, 1.148 g/cm^3 for **B8**, Table 2.1), and the surface to volume ratio of **B4** crystal is also smaller than that of **B16** micro-ribbons.

The kinetic spectra of the **B4** crystal under the same experimental condition were also measured. Figure 2.21 shows that no new emission band appeared upon irradiation for 300s, the only difference between the initial spectrum and final spectrum is only the decrease of intensity. It suggests that the effect of photo-bleaching on **DPA** derivatives is mainly the degradation of molecules, no other emissive species are formed.

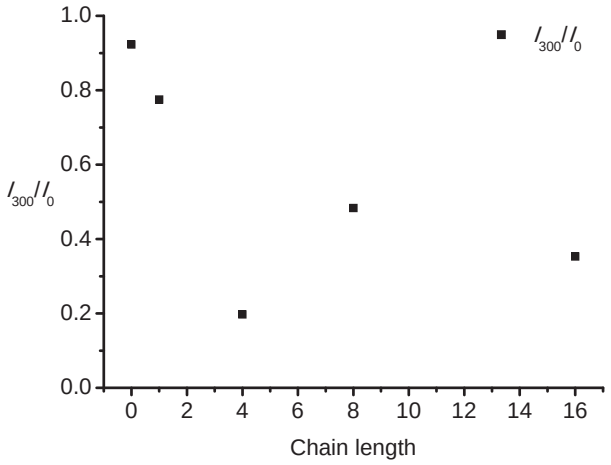

Figure 2.20: The ratio of emission intensity after irradiation/ Initial intensity ($I_{300}/I_{0)}$ versus substituted chain length of **DPA**, **B1**, **B4**, **B8**, **B16**

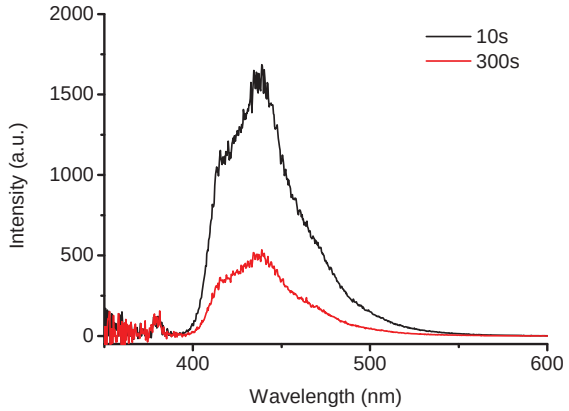

Figure 2.21: Emission spectra of **B4** crystal after 10s (black) and 300s (red) irradiation, λ_{ex} =385 nm

2.1.1.5.5 Polarization

A unique feature that can be evidenced by confocal microscopy is the polarized nature of the emission by the anisotropic crystal and ribbons of the **DPA** derivatives.

2.1.1.5.5.1 Principle of Polarization

The measurement of fluorescence polarization is illustrated in scheme 2.4.

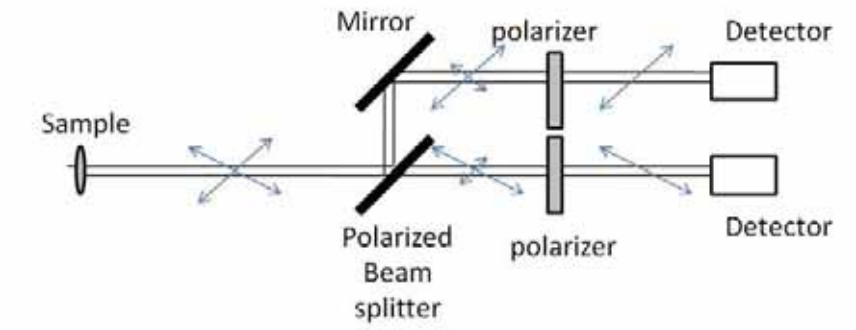

Scheme 2.4: Scheme for measurement of fluorescence polarization

Molecules are excited by selectively absorbing linearly polarized laser light when their dipole is oriented parallel to the axis of the excitation beam. The emission beam is sent through a polarized beam splitter which separates the beam into two orthogonal orientations. Those two polarizers placed in front of detectors are applied to clean up some un-separated light in order to assure the light collected by detectors is one direction. The emission intensities parallel and perpendicular to the polarization of the excitation are $I_{//}$ and $I_{\perp}$. These intensity values are used to calculate the polarization (P) and anisotropy (r):

$$P = \frac{I_{//} - I_{\perp}}{I_{//} + I_{\perp}}, \quad r = \frac{I_{//} - I_{\perp}}{I_{//} + 2I_{\perp}}$$

P can theoretically vary from -1 to +1, and -0.5 to 1 for *r*. In reality depolarization occurs especially with the high numerical aperture (1.4) objective lens we use.

To calculate the actual intensity ratio ($I_{\parallel}/I_{\perp}$) , we need to determine the *G* factor, which is the ratio of the sensitivities of the detection system for vertically and horizontally polarized light. The correction in intensity is necessary for the following reason: for the two measurements (polarizers in parallel and polarizers in perpendicular position) the instruments use the same but not identical optical components such as polarizers and optical filters. These components can show variations within their tolerances (transmission, reflection,...) and are therefore not identical.

The G factor is obtained by measuring a sample with linear polarized excitation light in one certain direction (for example, parallel position), and then the direction of excitation polarization is turned to the perpendicular position, meanwhile the sample is also rotated 90°, and so it keeps the same orientation with respect to the polarization of excitation beam. The G factor can be calculated with the emission intensity ratio recorded by two detectors under these two conditions.

$$G = \sqrt{\left(\frac{I_{//}}{I_{\perp}}\right)\left(\frac{I_{//}'}{I_{\perp}'}\right)}$$

The modified expression is given by:

$$r = \frac{I_{//} - GI_{\perp}}{I_{//} + 2GI_{\perp}}, \quad P = \frac{I_{//} - GI_{\perp}}{I_{//} + GI_{\perp}}$$

The polarization and anisotropy values can be interchanged by $r = \frac{2P}{3 - P}$

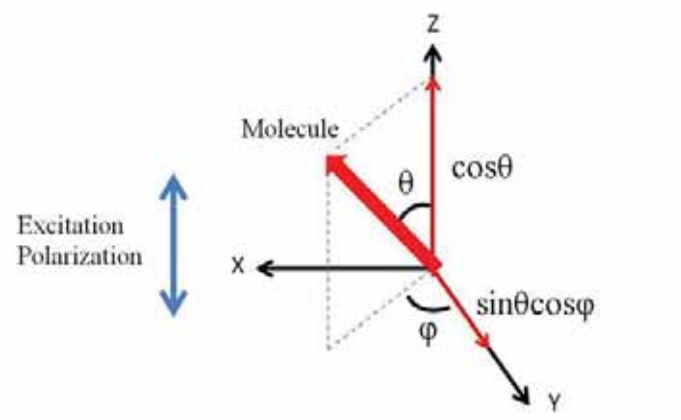

Scheme 2.5: Orientation of a single molecule's emission dipole and the resulting projection on each axis

The theory for fluorescence anisotropy can be derived by consideration of a single excited fluorescent molecule. Scheme 2.5 is a representation of a molecule which has been excited with light polarized along the z axis. It is assumed that the emission dipole is aligned with the axis of the molecule. The polarized light intensity is proportional to the square of the projection of the dipole on the axis. Hence the intensity in parallel and perpendicular direction

of the molecule is given by:

$$I_{//}(\theta,\varphi) = \cos^2\theta\,,\quad I_{\perp}(\theta,\varphi) = \sin^2\theta\cos^2\varphi$$

Meanwhile, by the fact the polarization of the excitation along the z axis, the excitation probability is independent of the angle φ. It allows us to express the anisotropy in following expression:

$$r = \frac{3\cos^2\theta - 1}{2}$$

2.1.1.5.5.2 Polarization of the Crystals and Ribbons

The polarization value is obtained by accumulating photons emitted from a 5 μm × 1 μm area of a single object without any intersection with others. And the angles of selected objects are measured along the main axis directions of them with an error $\pm 1^{\circ}$.

For all the objects analysed, very high values of *P* varying from -0.75 to +0.75 are observed (Figure 2.22). More particularly, all the objects display homogeneously the same *P* values, and these depend on the orientation of the main axis of the objects with respect the excitation beam polarization (which defines an angle θ) (Figure 2.23). Plots of *P vs.* θ for several objects of all the derivatives are displayed in Figure 2.24.

The analyses of the angle dependence of *P* of the emission, in this case obtained by polarized laser excitation, require to take into account photoselection (absorption could depend on the orientation of the ribbon, which would result in the strong modulation of the fluorescence intensity with the angle). In the absence of measureable photoselection (difficult to determine due to the ribbon size-dependence of the emission intensity), the fact that the horizontal fibers emit intensely with negative polarization values that are similar in absolute values with the P values of the vertical fibers indicates that exciton hopping occurs (B to B energy transfer). The absolute values of *P* also don't reach 1, due to the fact that the transition dipoles of molecules are not all oriented in one direction and/or the depolarization induced by the high numerical aperture objective lens and other optical elements. However, the values are very high, indicating a highly ordered structure.

The interesting thing is that the curves of all the derivatives are very similar. From the polarization image of **B4** (Figure 2.25) it appears clearly that most positive *P* values are observed on "north-south" oriented objects, while the most negative *P* values originate from "east-west" oriented objects with a monotonous variation of *P* in-between. This clearly results from an emission polarized perpendicularly to the main axis of the object.

A strong variation of *P* vs. θ reveals a preferential orientation of the molecules within the crystals, the negative P values could be the partial rotation of the emission polarization after excitation by an efficient exciton hopping process, ex: homo-molecular energy transfers shown to occur in organogels[16] and J-aggregates.

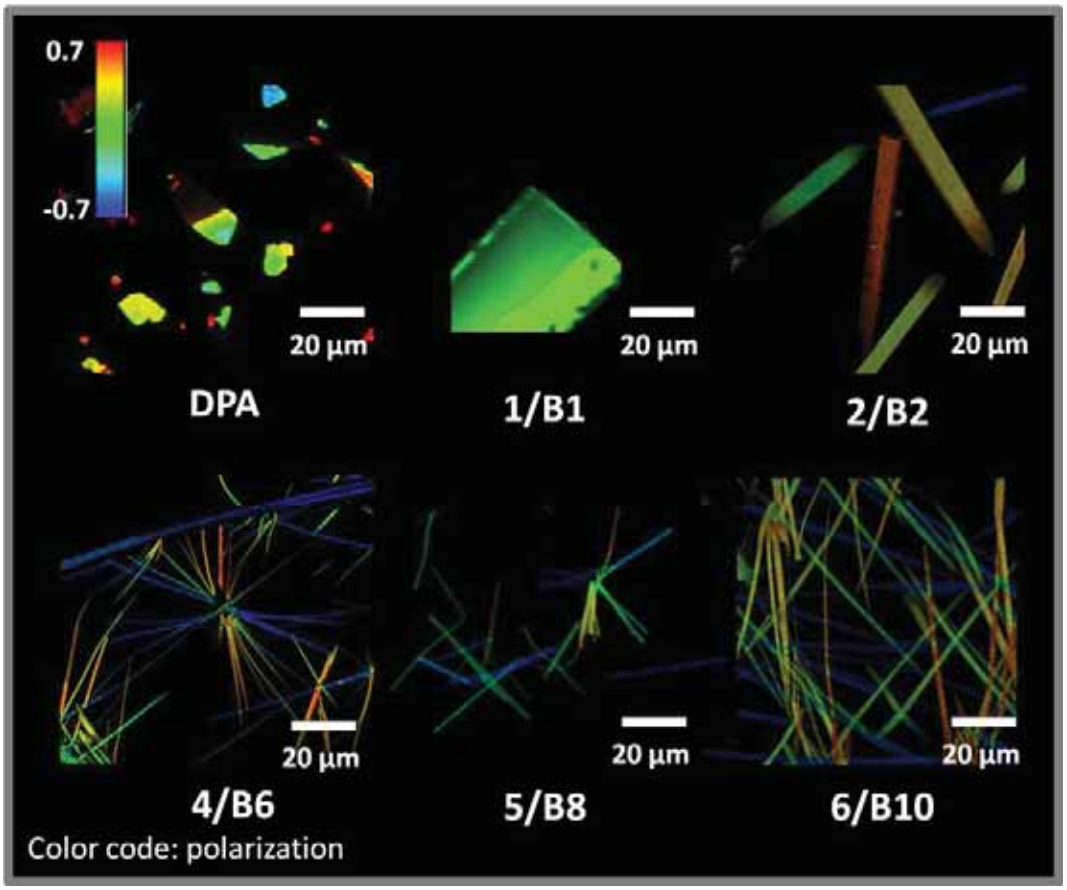

Figure 2.22: Polarization images of **DPA**, **B1**, **B2**, **B6**, **B8** and **B10**. λ_{ex} 385 nm, λ_{em} > 405 nm (color code: polarization)

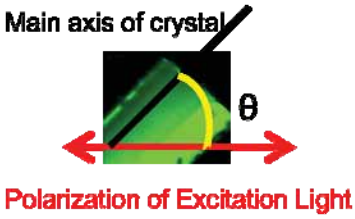

Figure 2.23: Scheme of Angle between the object's main axis and excitation beam polarization

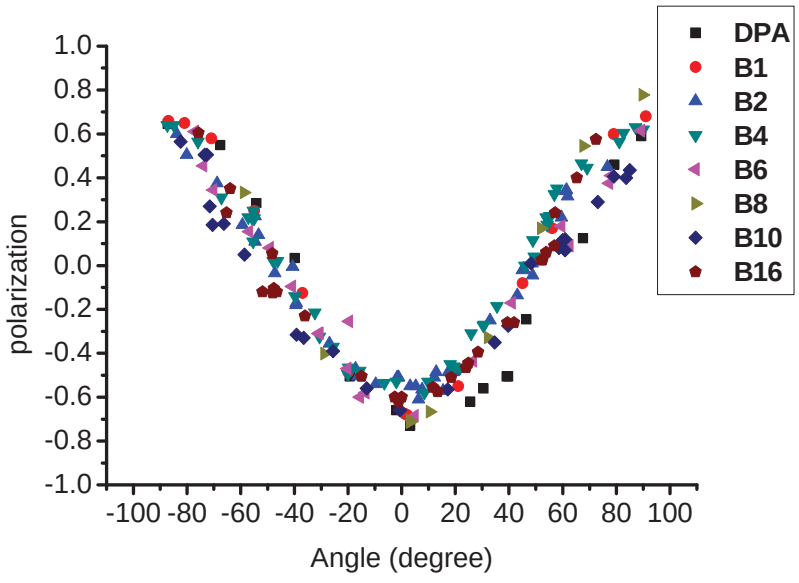

Figure 2.24: Polar plot (polarization versus angle) of all the **DPA** derivatives

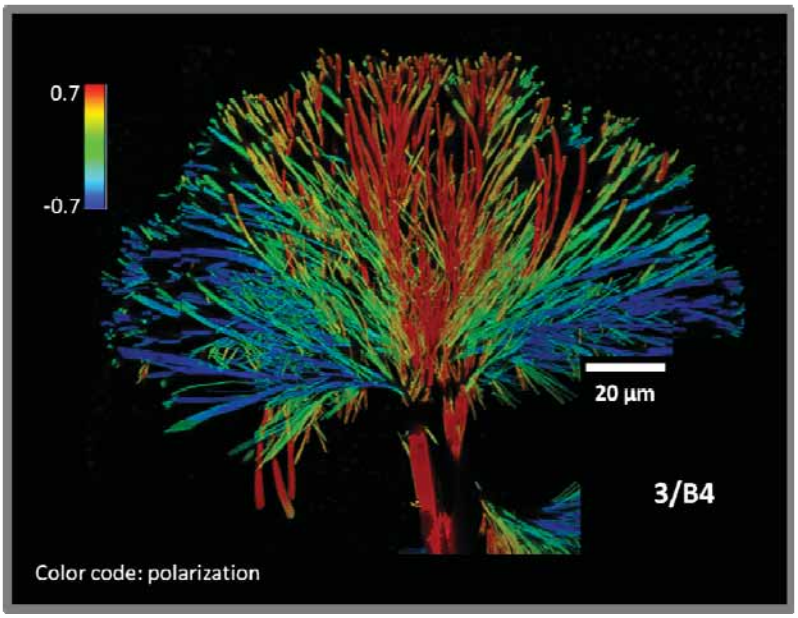

Figure 2.25: Polarization image of **B4,** λ_{ex} 385 nm, λ_{em} > 405 nm (color code: polarization)

2.1.2 Discussion

In solution, the di-methoxy substitution of **DPA** (**B1**) yields an increase of the absorption energy, but a lowering of the emission energy. This resulting increased Stokes shift could be attributed to a conformational reorganization of the excited state, as previously suggested in 2-methoxy anthracene.[17] Moreover, while the radiative constant is the same as in **DPA**, the emission QY is higher due to less efficient non-radiative processes. This effect can be tentatively attributed to a reduced intersystem crossing from the singlet S1 to the triplet T2, which is well-known to cause deactivation of the S1 state in non-substituted anthracene.[18]

In contrast, the other derivatives have a lower transition energy and k_r, indicating a difference between a methylene and a methyl substitution on the conjugation of the alkoxy substituent. Moreover, the lower energy of the excited state combined to longer chains induces an increase of the non-radiative deactivation constants.

In the solid state, an exceptionally high emission quantum yield of 0.97 is obtained for **B1**. An additional particularity resides in the extreme "blue" CIE coordinates (x = 0.154, y = 0.033) of **B1**, as compared to some spirobifluorenes,[19] bi(styryl)benzenes[20] which also emit very intensely with a QY~0.9, but at higher wavelengths. This is also due to the low Stokes shift, 37 nm in the solid as and 33 nm in solution (between 0-0 transitions of **B1**, 18 nm in the solid and 19 nm in the solution). The packing of **B1** revealed by the crystal structure disfavors electronic coupling between the transition dipoles, since angles of ~90° (Figure 2.22) occur between the closest stacked **B1** molecules and the distance between aligned dipoles exceeds 8.6 Å. A low Stokes shift, which is substantially inferior to the one observed for **DPA** (Stokes shift between 0-0 absorption and 0-1 emission bands: 37 nm for **B1** and 42.5 nm for **DPA**), also supports the absence of electronic coupling. The slightly lower radiative constant in the solid state as compared to solution might result from some conformational change between

the two states.

As shown in figure 2.26, the crystal structure of **B1** here is obtained from the oriented single crystal, and the angles of 4 different transition dipoles derived from **B1** crystal structure were applied to simulate the emission polarization of **B1** crystals by a homemade software (mathematical model : scheme 2.6, 2.7, 2.8).

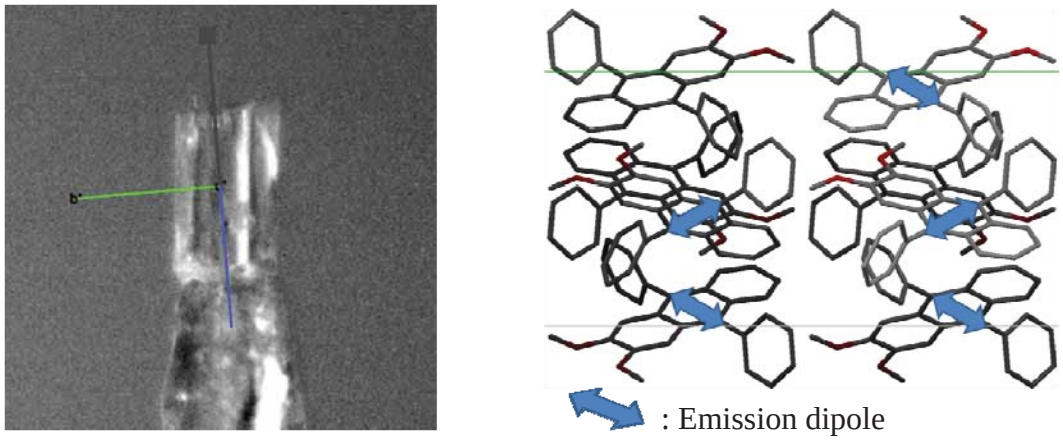

Figure 2.26: (left) Superposition of the picture of an oriented single crystal and of the crystallographic axis determined by X-ray scattering on the same Crystal ; (right) corresponding crystal structure of **B1** andcrystallographic axes oriented in the same directions

With this software, we can simulate the polarization curve (*P* versus θ, here we use sin (θ) function to do the simulation) of emission by the angles of molecular dipole moments with respect to each axis which can be obtained from the crystal structures. Some depolarization processes of excitation and emission are also taken into account. The depolarization of excitation can be due to rapid energy transfer processes after absorption and/or out-of-plane excitations due to the high numerical aperture of the objective lens: these are modeled by a partial or total lack of photoselection. In addition, the loss of polarization of emission due to the high numerical aperture objective lens and other optical components is modeled by taking into account terms in addition to the main axis of propagation of light.

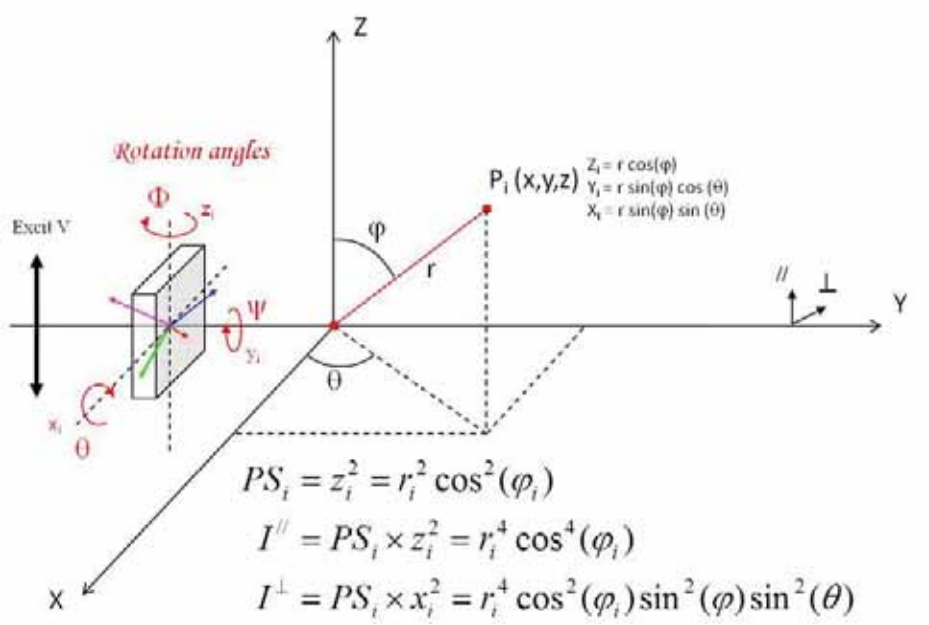

Scheme 2.6: The definition of anisotropy in the coordinate system of software

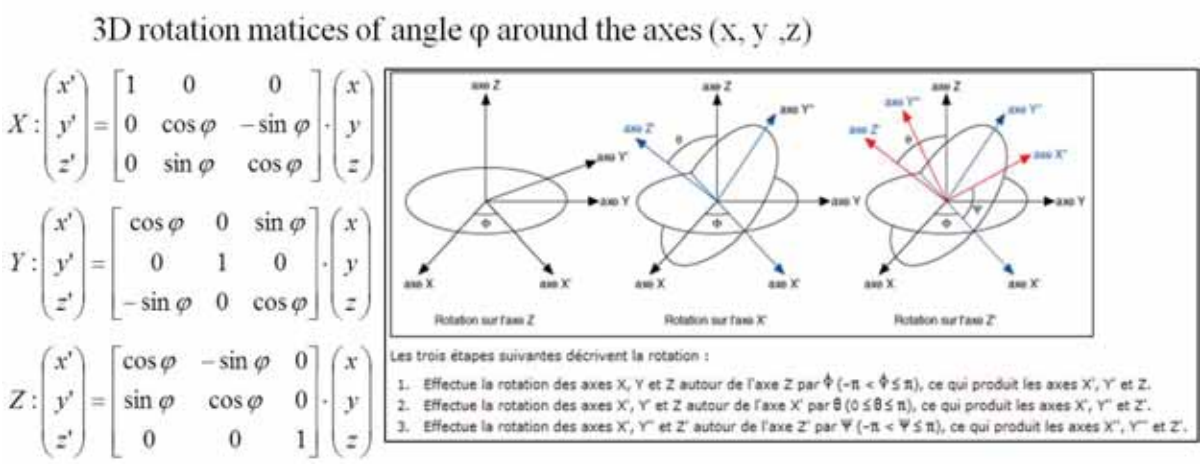

Scheme 2.7: The rotation matrices of the description of the dipole rotate around the axes.

Depolarizaiton of excitation:

$$PS_i = z_i^2 + D_x x_i^2 + D_y y_i^2$$

Depolarization of emission:

$$I^{//} = PS_i \times (C_{xz} x_i^2 + C_{yz} y_i^2 + z_i^2)$$

$$I^{\perp} = PS_i \times (x_i^2 + C_{yz} y_i^2 + C_{xz} z_i^2)$$

Scheme 2.8: The depolarization functions applied in excitation and emission.

The simulated polarization versus angle curve of **B1** is consistent with our experimental result ($-0.70 \leq P \leq +0.65$, Figure 2.27), which supports our strategy to use emission polarization measurement to define the orientation of objects. In addition, this validated polarization simulation model also grants us a way to probe the possible ways of how the molecules orient inside objects. In all the simulations, a 100% depolarization of excitation had to be applied to fit the data, indicating the presence of exciton-hopping mechanism.

However, several orientations of the crystal can lead to very similar polarization curves. As shown in figure 2.27 and 2.28, the crystal of **B1** could be rotated by 90 degree around the axis z of the polarization of the laser without evident effect on the resulting simulation curve. Other rotations did however produce non-matching curves.

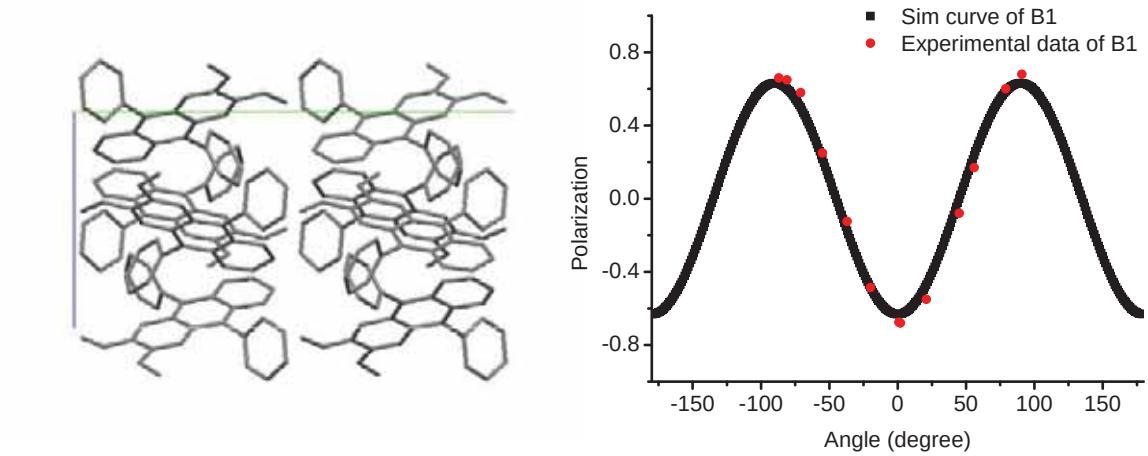

Figure 2.27: (left) Crystal structure of **B1** oriented so to represent a crystal lying on the microscopy slide with an angle of 90° ("vertical crystal") ; (right) Polarization of crystals of **B1** with different orientations (red dots) and the simulated curve of *P* as function of the angle.

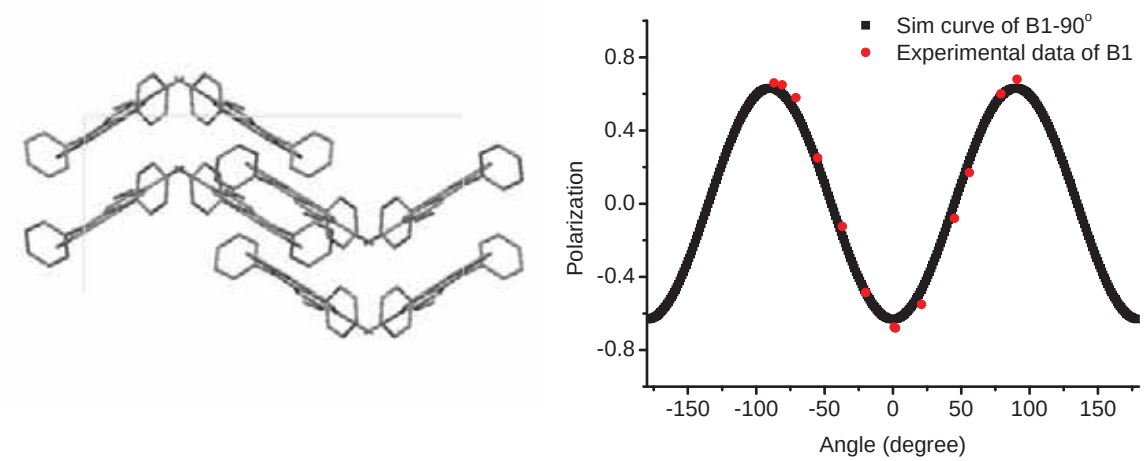

Figure 2.28: (left) Crystal structure of **B1** oriented so to represent a crystal lying on the microscopy slide with an angle of 90° ("vertical crystal") and further rotate 90°around the axis of laser polarization; (right) Polarization of crystals of **B1** with different orientations (red dots) and the simulated curve of *P* as function of the angle.

In the bulk state, **B2** behaves similarly to **B1** but emits with a lower QY. This difference could result from a slightly higher crystalline disorder induced by the ethyl chain, as shown by the X-ray structure (Figure 2.28), and thus higher non-radiative constants due to supplementary deactivation pathways. The inter-dipole distances are higher than in **B1** crystals (9.7 Å for **B2**, 9.4 Å for **B1**), indicating even less probable dipolar couplings.

Simulation of emission polarization on **B2** crystal reveals two possible orientations of the crystal relative to the laser polarization direction (Figure 2.29, 2.30).

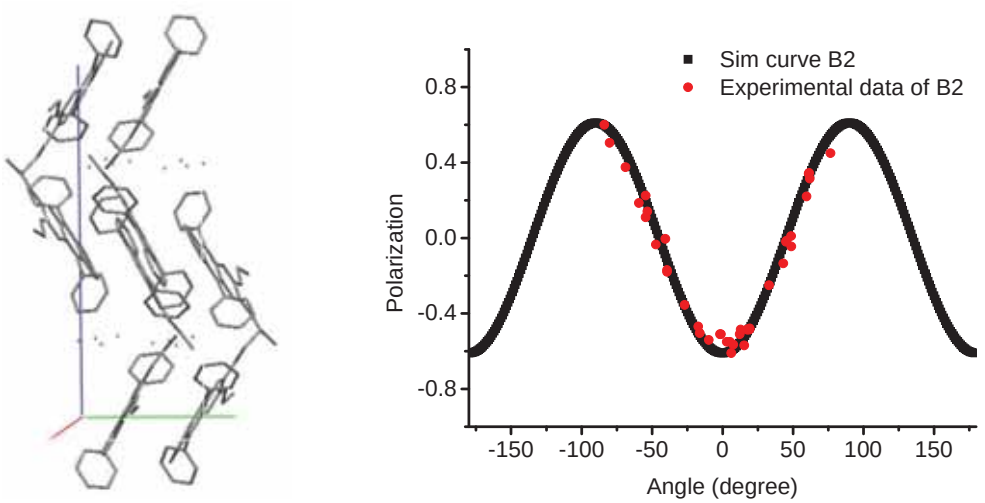

Figure 2.29: (left) Crystal structure of **B2** oriented so to represent a crystal lying on the microscopy slide with an angle of 90° ("vertical crystal") ; (right) Polarization of crystals of **B2** with different orientations (red dots) and the simulated curve of *P* as function of the angle.

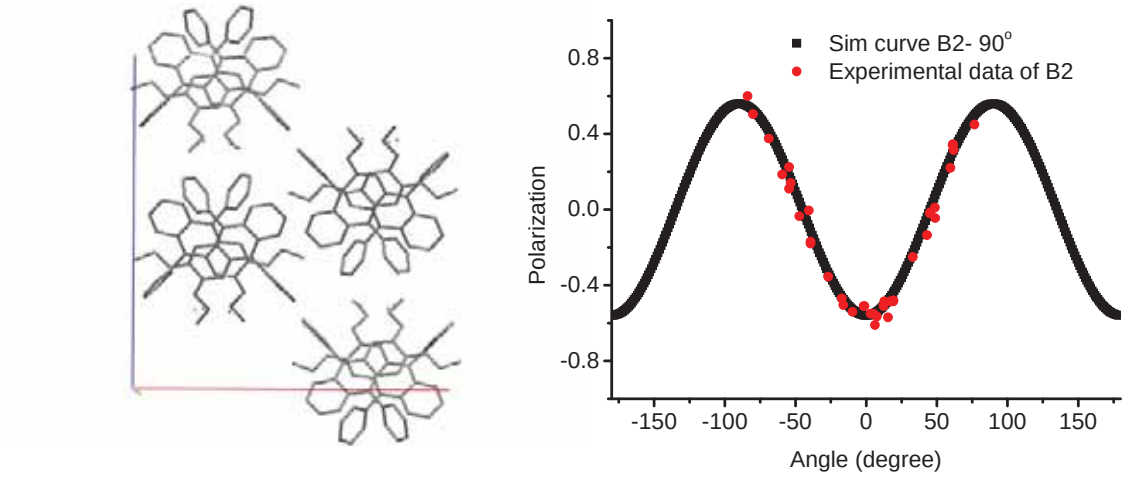

Figure 2.30: (left) Crystal structure of **B2** oriented so to represent a crystal lying on the microscopy slide with an angle of 90° ("vertical crystal") and further rotate 90°around the axis of laser polarization; (right) Polarization of crystals of **B2** with different orientations (red dots) and the simulated curve of *P* as function of the angle.

The **B4** powder is at first sight very similar to **B1** and **B2**, displaying both high quantum yield and emission energy. Nevertheless, crystal structures reveal two packing modes. The first structure **B4a** is apparently more similar to that of **B1** and **B2** with many almost orthogonal transition dipoles (Figure 2.31). However, the distance between the rare aligned transition dipoles is smaller than in the previous cases and is of about 6.8 Å. In the second structure **B4b**, all the aromatic cores are in almost parallel planes and the more frequent aligned transition dipoles are separated by 7.1 Å. X-ray diffraction reveals that the powder is essentially composed of the **B4a** morph that is thus propitious to intense emission. Some differences are the samples used could induce a higher uncertainty in k_r and k_{nr} values, which nevertheless are quite similar to **B2**.

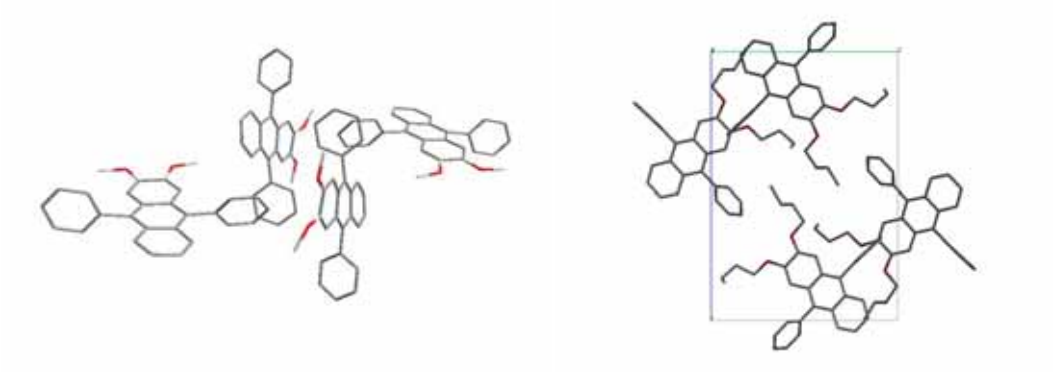

Figure 2.31: crystal structure of **B4a** (left, chain emitted for clarity) and **B4b** (right)

As shown in figure 2.32 and 2.33, the simulation curves derived from both **B4a** and **B4b** are quite in agreement with the experimental data of **B4**. However, if we look more into the details, the simulation curve of **B4b** is more consistent with the experimental data than that of **B4a**. It is tempting to suggest that the **B4b** structure is the dominant structure sampled by microscopy, although the difference is too small to fully support this conclusion.

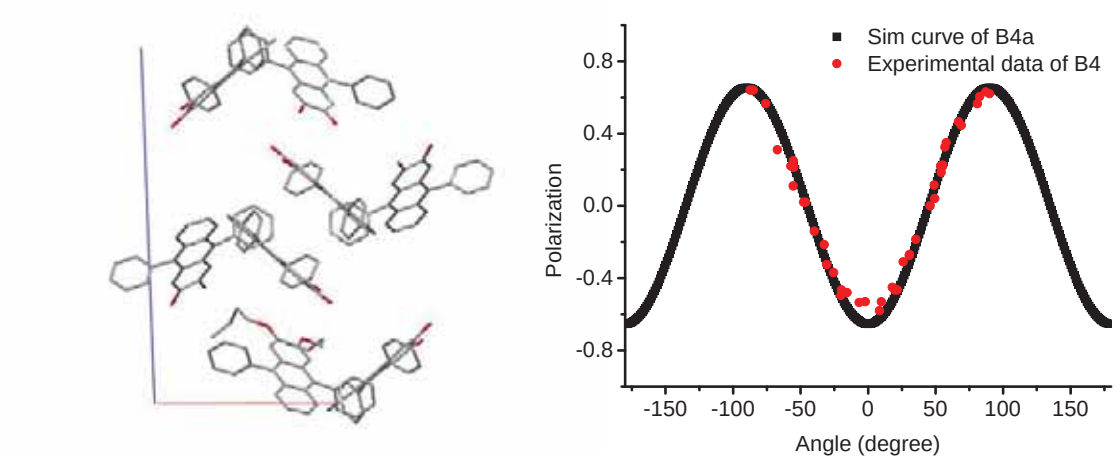

Figure 2.32: (left, chains omitted for clarity) Crystal structure of **B4a** oriented so to represent a crystal lying on the microscopy slide with an angle of 90° ("vertical crystal") ; (right) Polarization of crystals of **B4a** with different orientations (red dots) and the simulated curve of *P* as function of the angle.

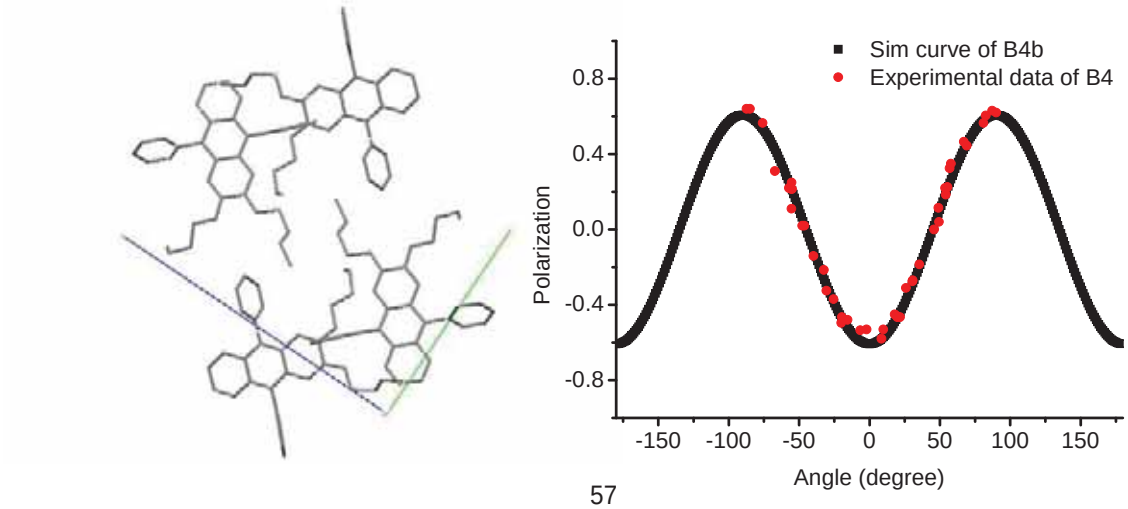

Figure 2.33: (left) Crystal structure of **B4b** oriented so to represent a crystal lying on the microscopy slide with an angle of 90° ("vertical crystal") ; (right) Polarization of crystals of **B4b** with different orientations (red dots) and the simulated curve of *P* as function of the angle.

B6, **B8** and **B10** show a quite different behavior, suggesting a correlation between the "sheet-like" crystal packing of **B8** and the red-shift in emission. Thereby, it could be tentatively extrapolated that **B6**, **B8** and **B10** have a similar packing. The increase in chain length and disorder, clearly observed in the crystal structure of **B8**, could be at the origin of the increased non-radiative processes. Interestingly, ribbons of both **B10** and **B16** display the lowest radiative constants and highest k_{nr}. In this case, the calculated value of k_r could be underestimated due to a decrease of the emission quantum yield by some static quenching. Alternatively, the reduced k_r could also be due to the existence of a supplementary family of possibly packed molecules, given the fact that heterogeneities of decay times are observed in **B16** ribbons (Figure 2.18).

Simulation of emission polarization of **B8** (Figure 2.34) further supports the suggestion that the higher polarization value of **B8** emission ($-0.70 \leq P \leq +0.80$) than other derivatives is due to the almost parallel arrangement of the anthracene cores.

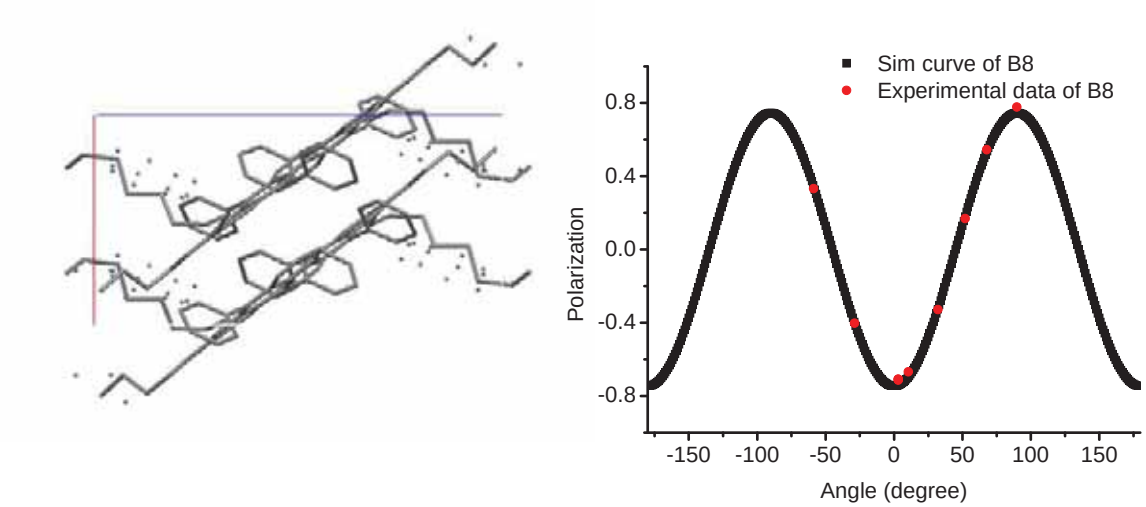

Figure 2.34: (left) Crystal structure of **B8** oriented so to represent a crystal lying on the microscopy slide with an angle of 90° ("vertical crystal") ; (right) Polarization of crystals of **B8** with different orientations (red dots) and the simulated curve of *P* as function of the angle.

Since the polarization simulation models constructed with the transition dipoles angle derived from the crystal structure are consistent with experimental results, the next step is to simulate the polarization of objects without x-ray crystal structures such as **B16** with the models built by **B1**, **B2**, **B4**, or **B8**. It can give us a rough idea about the molecular orientations in the objects.

After a serial of tests, it is found that the simulation models built by **B2** and **B4b** can fit the **B16** experimental data best (Figure 2.35, 2.36). It indicates that the orientations of **B16** molecules in the microribbons should be similar to the common features of these two structures. As shown in figure 2.35 and 2.36 (left), 4 molecules are arranged on a plane in one unit cell, and the aromatic cores are parallel to the nearby ones with orthogonal transition dipole moments.

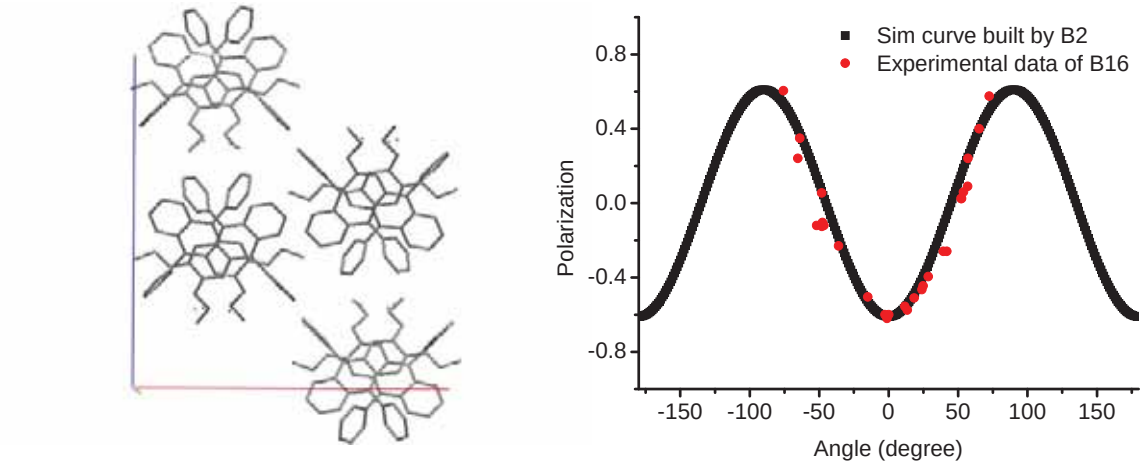

Figure 2.35: (left) Crystal structure of **B2** oriented so to represent a crystal lying on the microscopy slide with an angle of 90° ("vertical crystal") ; (right) Polarization of crystals of **B16** with different orientations (red dots) and the simulated curve of *P* as function of the angle.

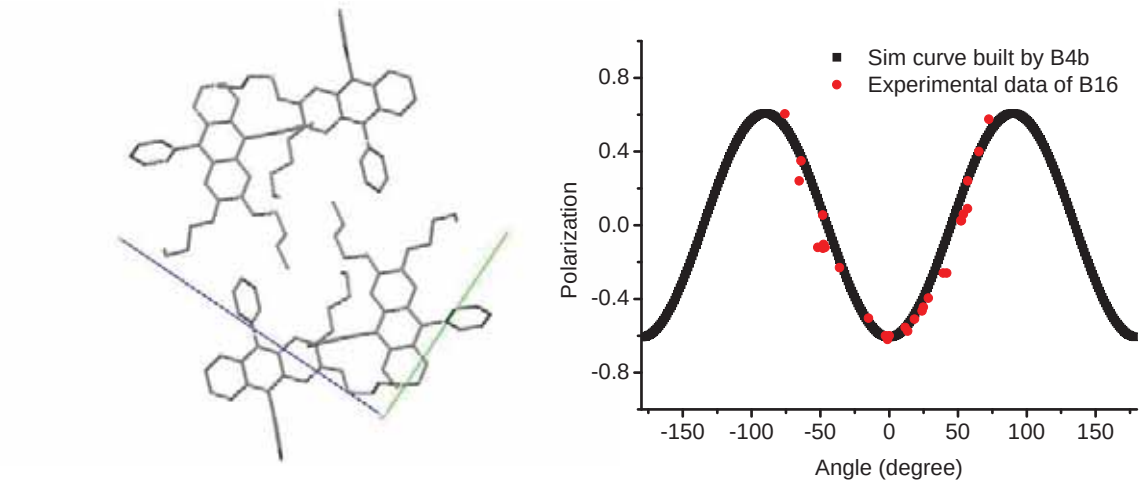

Figure 2.36: (left) Crystal structure of **B4b** oriented so to represent a crystal lying on the microscopy slide with an angle of 90° ("vertical crystal") ; (right) Polarization of crystals of **B16** with different orientations (red dots) and the simulated curve of *P* as function of the angle.

Confocal microscopy allows us to further elucidate the properties in the solid state. The samples analyzed are obtained by deposits of crystals grown slowly in solution, but instant crystallization on glass surface upon solvent evaporation cannot be avoided in certain samples

(see below). Direct comparison of powder measurements and crystal samples have thus to be considered on a case-to-case basis. In the simplest cases **B1** and **B2**, it is interesting to observe by spectroscopy that the 0-0 emission transition clearly appears, indicating that in the bulk measurement emission-reabsorption phenomena play a decisive role in the apparent red-shift.

For **B4**, a striking lower energy emission in single objects as compared to powder is observed. These single crystals emit with emission wavelengths and lifetimes that are more similar to **B6** and **B8**. The analyses of the crystal structures reveals that the morph **B4b** is similar to **B8**, and this could be correlated to the spectroscopic properties. As **B4** is polymorphic, it is suggested that **B4a** is majority in the powder, while **B4b** is majority in the structures sampled by microscopy. This could reveal an interesting feature of **DPA** derivatives.

The reabsorption phenomena are also reflected on the slower decay times of **B1**-**B10** in bulk than that measured by CFM. According to Cazade and Brown's description about the increase of lifetime in condensed phase of sample,[21] the relation between apparent decay time τ_{app} and the true fluorescence decay time τ_{F} can be described by:

$$\tau_{\mathrm{app}} \sim \frac{\tau_{\mathrm{F}}}{1-\varphi Q_{\mathrm{F}}}$$

Where φ is the fraction of light reabsorbed by the sample, and Q_{F} is the fluorescence quantum yield of the sample.

The decay times measured in CFM are taken as τ_{F}, and then by overlaying the bulk emission spectra and the emission spectra taken on single objects we can estimate the fraction of emission reabsorbed in the bulk (0.2~0.3). It is shown that the calculated τ_{app} of **B1**-**B10** crystals have a good agreement with the experimental τ (Table 2.5), indicating the difference of decay times of **B1**, **B2**, **B4**, **B6**, **B8** and **B10** measured in the bulk and CFM can be attributed to the reabsorption effect. In addition, it can be deduced that the resulting radiative constants k_r of CFM data (Table 2.4) should be more correct than the k_r calculated in the bulk (Table 2.3).

Table 2.5: Decaytime of **B1 – B10** obtained by CFM and bulk measurements.

Compound	τ (bulk) [ns]	τ_F (CFM) [ns]	τ_{app} [ns]
B1	8.3	6.6	8.2
B2	7.3	6.5	7.9
B4	6.9	4.8	6.7
B6	5.7	4.2	5.3
B8	4.5	4.1	4.5
B10	4.7	4.2	4.7

2.1.3 Conclusion

1. A series of **DPA** derivatives with surprisingly high quantum yield in the solid state are synthesized and investigated. Most of them can be crystallized from DCM/MeOH. For B10 and B16, ribbon-like microstructures were formed under the same condition. All of these crystals and ribbons display very high value of *P* (-0.75~+0.75) and strong variation of *P* vs. θ, suggesting highly ordered molecular packing within the crystals and even the ribbons.
2. The crystal structures of **DPA**s reveal that the angles between two anthracene cores were varied with substituted alkoxy chain length (scheme 2.6). The photophysical properties of **DPA**s in the solid state display dependency on the substituted chain length. (Figure 2.30)

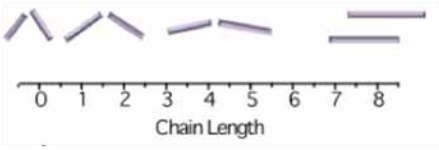

Scheme 2.9: The angle between the two anthracene cores of **DPA**s crystal structure varied with chain length

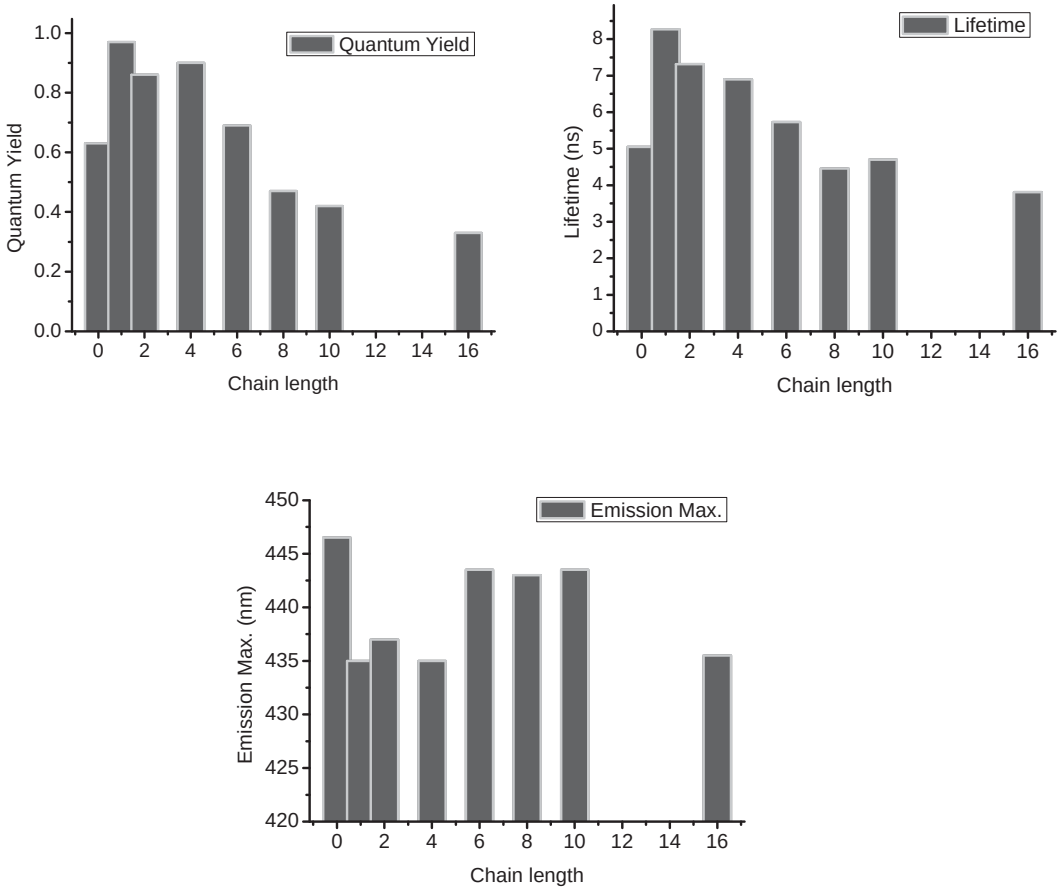

Figure 2.37: Scheme of photophysical properties (quantum yield, lifetime and emission max (0-1) transition) in the solid state of all the derivatives versus substituted chain length

2.2 Nanostructures derived from DPA-derivatives

The investigation of the photophysical properties of **DPA** derivatives in the solid state is correlated to molecular packing in the crystal. However, these crystals can be quite large and are slowly grown. Previous studies have shown that the down-sizing to nano-objects is of interest for the tuning of optical properties and the use in potential applications. Thus, in a next step, we attempted to control the crystallization or exploit the self-assembling ability of acenes to achieve nanostructuration. Since the **B1** crystals display a strikingly high quantum yield of emission (97%) and a highly ordered molecular packing ($-0.75 \leq P \leq +0.75$, P: polarization value), **B1** has been chosen for the formation of nano-objects and light-harvesting matrices.

2.2.1 Results

2.2.1.1. Method of preparing the NRs

In order to achieve nano-objects of **B1**, the method of fabricating **DPA** nanostructures was adapted. Recently, Lee *et al.* have reported that **DPA** molecules readily self-assembled into nanoribbons and nanorods by varying the solubility of **DPA** molecules in the preparation solution with the assistance of a surfactant.[22]

Herein, we adapted this reprecipitation method with self-inducing template growth to produce nanorods of **B1** in the presence of cetyltrimethylammonium bromide (CTAB) molecules in an aqueous phase.

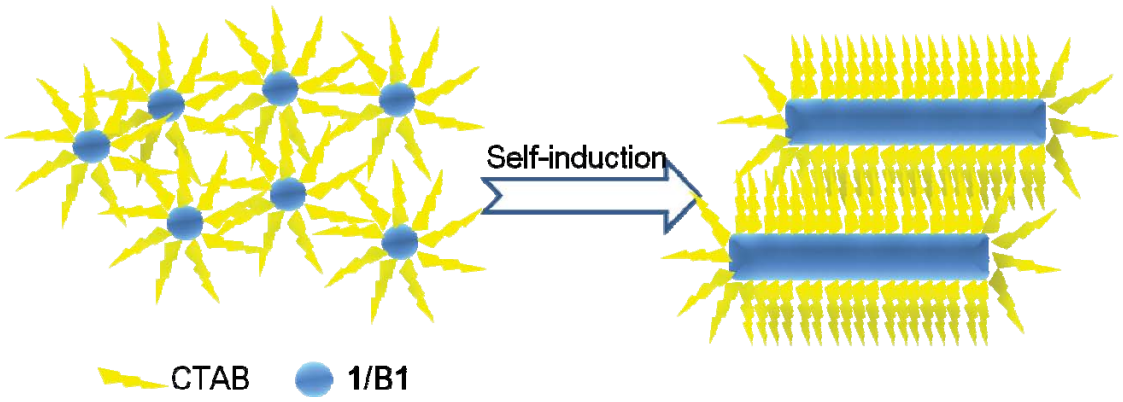

Scheme 2.10: Proposed self-inducing mechanism of **B1** nanorods formation using CTAB as a soft template.[23]

Scheme 2.10 illustrates the formation mechanism of nanorods. By analogy with the mechanism of formation of nanorods of **DPA** established previously by Yao *et al.*, **B1** molecules should first dissolve into the hydrophobic core of spherical CTAB micelles. These dissolved **B1** molecules can induce the sphere-to-rod transition of CTAB micelles. Then the induced rodlike CTAB micelles direct the growth of cylindrical **B1** nanorods like templates.

The morphology of **B1** nanorods strongly depends on the conditions, such as the presence

of surfactant,[24] the temperature of aqueous solution, solvent of **B1** stock solution.[22]

The exact condition for fabricating uniformly shaped nanorods required the adaptation of the temperature of the aqueous solution. The preparation was optimized by analyzing tens of samples by optical microscopy. The detailed investigation is described in the experimental section.

2.2.1.2 Size and Shape of the NRs.

A stock solution of **B1** (100 μL, 0.5mM) of deoxygenated acetonitrile and tetrahydrofuran (1:1, v/v) was rapidly injected into 5 mL 0.25 mM CTAB boiling aqueous solution under continuous stirring and Ar bubbling. After vigorously stirring for 2 min at 100°C, the resulting solution was allowed to ripen at r.t. for two hours and yielded **B1** nanorods.[25] This method is tested more than 10 times and always reproduces the same results. The dispersions of **B1** nanorods in water exhibited an off-white turbidity because of the light scattering by the particles.

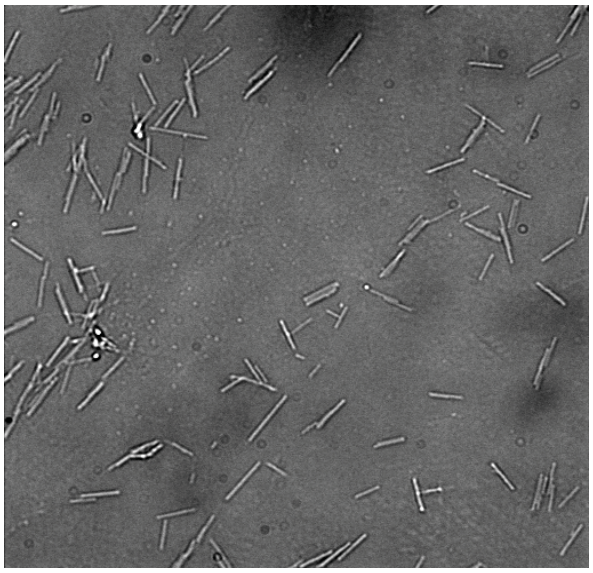

Figure 2.38: Transmission optical microscopy image of **B1** nanorods (80 × 80 μm)

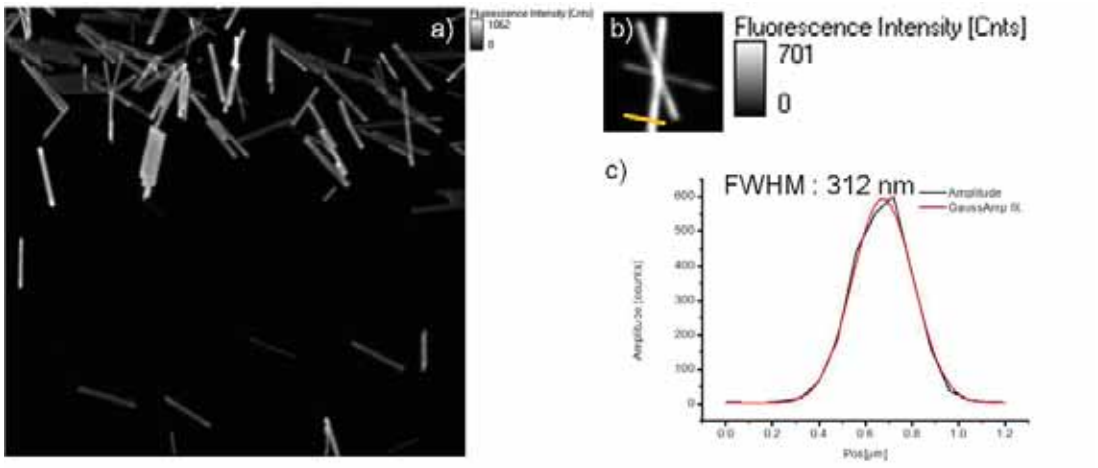

Figure 2.39: a) Fluorescence Intensity image of **B1** nanorods (40 × 40 μm) , λ_{ex} 375 nm, λ_{em} > 405 nm. b) Fluorescence Intensity image of **B1** nanorods, (4.5 × 4.5 μm). c) Cross-section along the yellow line in b) and fitted with Gaussian Amplitude Function curve.

Figure 2.39 is a fluorescence intensity microscopy image of **B1** nanorods. The size of **B1** nanorods is characterized by measuring the cross section of fluorescence intensity and fitted with Gaussian amplitude function to obtain the FWHM value (see experimental section). As shown in figure 2.39, the 1D nanorod have a quite uniform width in the range of 300~400 nm and a length of about 4 μm. These values are statistical average from at least 100 nanorods.

To verify the indispensability of CTAB in the nanorod formation process, one sample is made under exactly the same condition but in absence of the CTAB. Figure 2.40 displays that only amorphous aggregates are formed without the presence of CTAB.

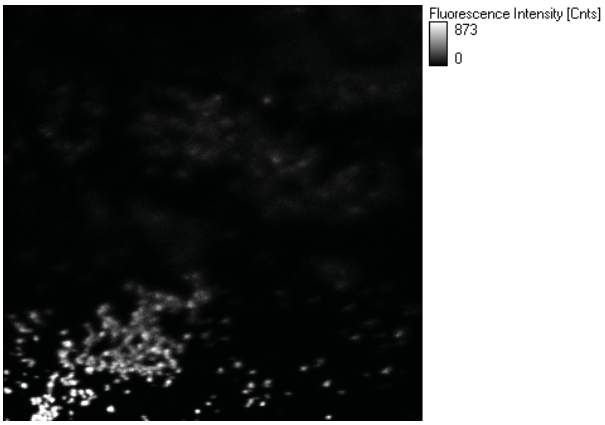

Figure 2.40: Fluorescence Intensity image of **B1** aggregates (40 × 40 μm) , λ_{ex} 375 nm, λ_{em} > 405 nm.

2.2.1.3 Spectral Properties in B1 NRs

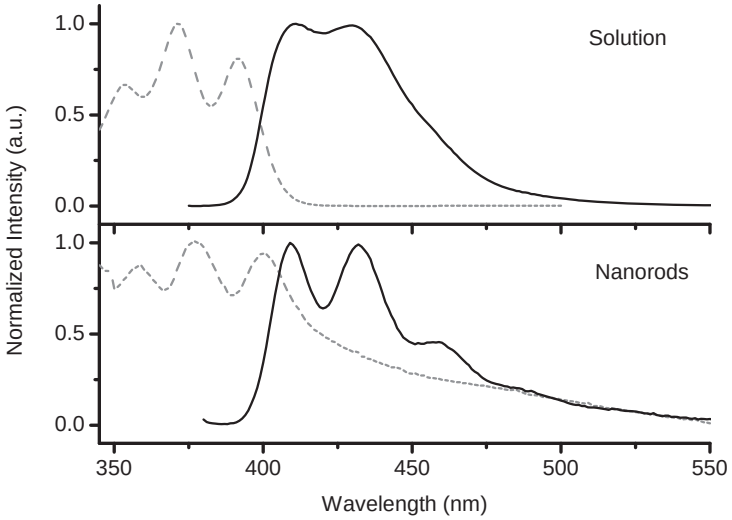

Figure 2.41: Absorption (gray dash line) and emission (black full line) spectra of **B1** in THF solution (1.0×10^{-5} M, top) and **B1** nanorods (bottom).

The absorption and emission spectra of the **B1** nanorods colloidal aqueous solution are shown in Figure 2.41 along with those of the **B1** in solution (1.0×10^{-5} M in THF). The monomers exhibit three resolved absorption bands at 359, 371 and 392 nm. These three bands become less resolved and red-shifted 5 nm (Figure 2.41) in a nanorods colloidal suspension.

Compared with **B1** solution, the emission spectrum of the nanorods colloidal aqueous solution exhibits a clear vibronic structure with λ_{max} = 409 nm (0-0 transition), 0-1 transition at 432 nm and a shoulder of 0-2 transition, which are slightly blue-shifted by 2 nm with respect to that of the monomer. The emission in nanorods displays a lower Stokes shift than in solution, as it was the case for larger crystals of **B1**. In the polar solvent THF, as discussed previously, a larger stablization of the excited state of the monomer could occur.

The emission intensity of the **B1** nanorods suspension drops to 25.8% quantum yield , combining with the average decay time (5.6 ns, bi-exponential fitting) gives $k_r = 4.6 \times 10^7 s^{-1}$.

The difference between the emssion spectra of nanorods and crystals shown in Figure 2.42 clearly stems from the 0-0 transition which disappears in the crystal powder due to emission reabsorption. Indeed, in the colloidal solution the concentration of **B1** is much lower and this effect is minimized. The differences in the ratios of the 0-1, 0-2 and 0-3 bands are not easily attributed.

A further characterization of the nanorods was performed by studying single objects by CFM.

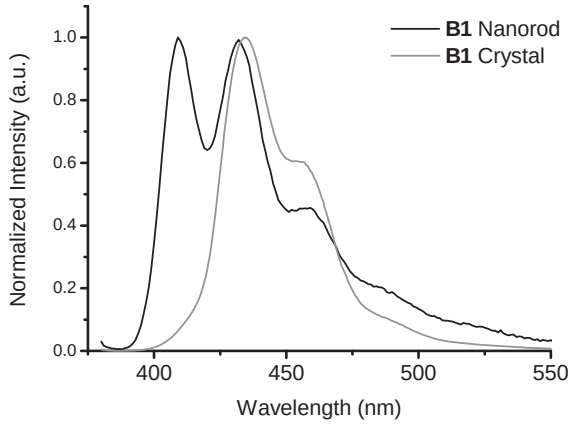

Figure 2.42: Normalized emission spectra of **B1** colloidal nanorods suspension and crystal

2.2.1.4 Emission Spectra of single nanorods

To prepare samples for confocal microscopy analysis, one drop of **B1** nanorods colloidal aqueous solution was casted on glass surface and the solvent was allowed to be evaporated at 40^{o}C.

The emission spectra are recorded in two ways: accumulating emission by scanning an area (40 × 40 μm, at least 30 objects) or directly measuring the spectrum on one single rod. Figure 2.43 displays the resemblance of the two spectra, which suggests the homogeneous spectral properties of the **B1** nanorods.

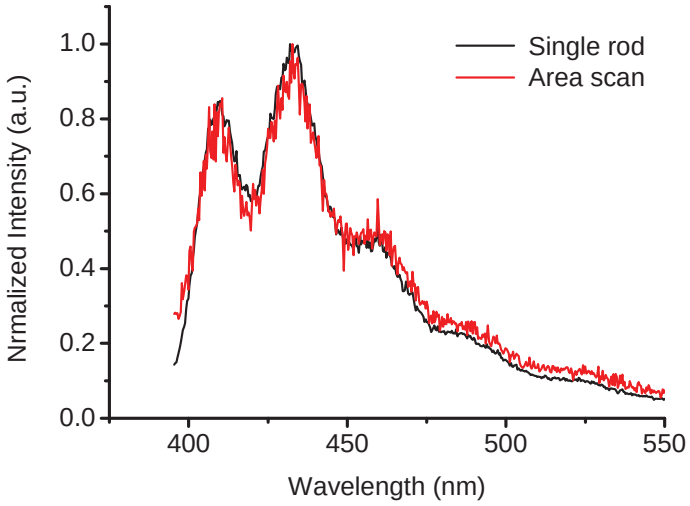

Figure 2.43: Normalized emission spectra of a **B1** single nanorod and average spectra of nanorods acquired while scanning an area (40 × 40 µm)

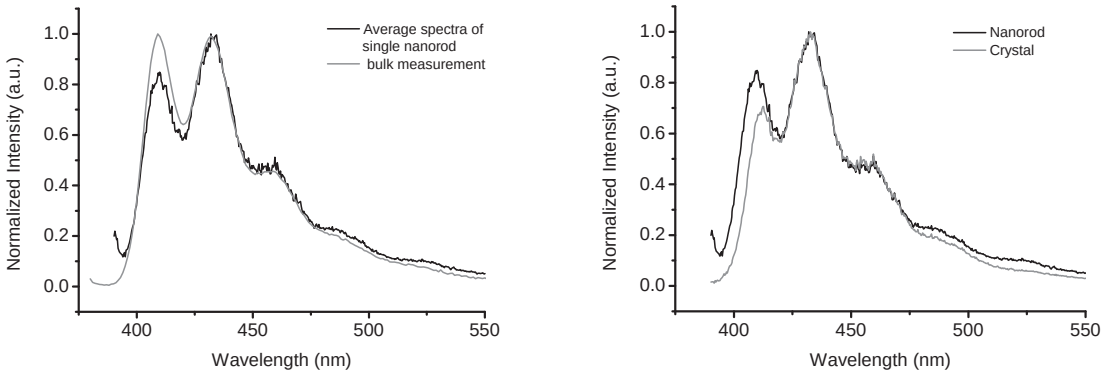

Figure 2.44: Normalized emission spectra of average single nanorods and bulk measurement (left) and crystals (right), λ_{ex} =375 nm for nanorods, 385 nm for crystals

The difference of the average nanorods spectra with the bulk-spectra resides in the weight of the 0-0 transition relative to the 0-1 transition (<20%) (Figure 2.44, left). The spectra of the nanorods display the same features as those of the crystals measured on powders (see Figure 2.44, right). This is in agreement with a high crystallinity of the nanorods and a similar molecular packing.

2.2.1.5 Decay times

Fluorescence lifetime images (FLIM) show that in **B1** nanorods the average decay time is quite similar within all the areas of all the objects imaged (Figure 2.45), yielding overall an average value of 4.60 ns (bi-exponential fitting, T1 = 6.67 ns ,T2= 2.73 ns).

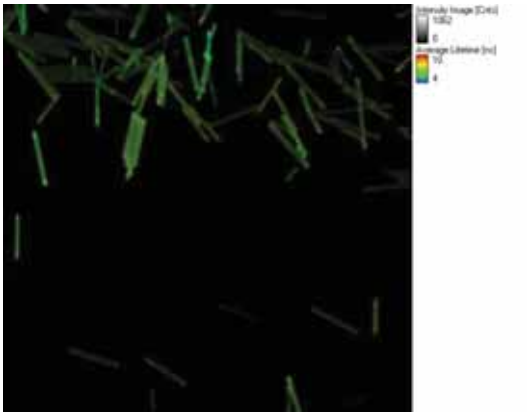

Figure 2.45: FLIM image of **B1** nanorods, (40 × 40 μm) , λ_{ex} 375 nm, λ_{em} > 405 nm, color code : average lifetime.

2.2.1.6 Polarization on NRs

For **B1** nanorods, *P* value varying from -0.40 to +0.35 is observed (Figure 2.46). Plots of *P vs.* θ for several objects are displayed in Figure 2.46. From the polarization image (Figure 2.47) it appears clearly that emission is polarized perpendicularly to the main axis of the object, which has the same trend as the crystals.

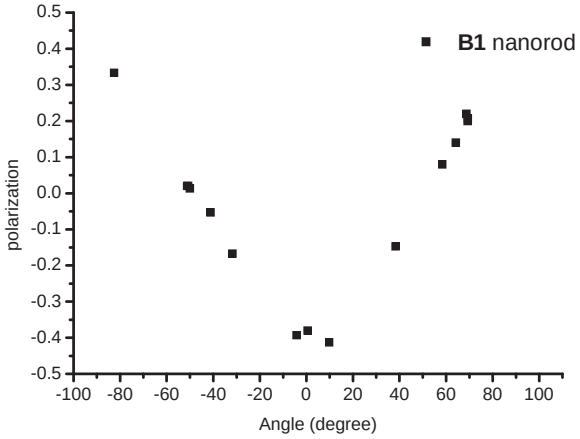

Figure 2.46: Polar plot (polarization versus angle) of **B1** nanorods

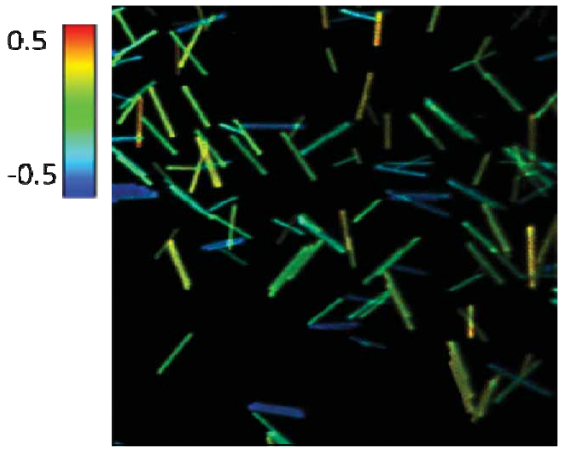

Figure 2.47: Polarization image of **B1** nanorods, (40 × 40 μm), color code: polarization.

2.3 Energy Transfer Study

A well-defined blue light-emitting nano-scaled rod-like system is achieved. In this following work, this system is exploited as a host material for emission tuning.

By the means of energy transfer process, the photophysical properties of nanostructures can be easily varied. It is known that using molecules with similar molecular structures interacts favorably in assembled multicomponent systems.[16] Therefore, the green emitter (2,3-dimethoxy-6,11-diphenyl tetracene, **GT1,** Figure 2.48) is specifically designed and synthesized to *co*-crystallize with **B1** without altering the **B1** nanostructures.

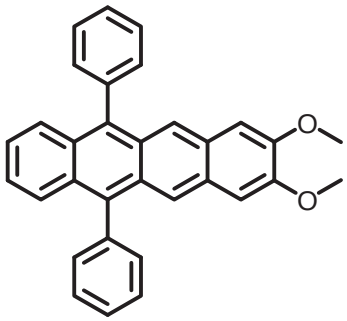

Figure 2.48: molecular structure of **GT1**

2.3.1 Results

2.3.1.1 Synthesis of GT1

The reaction sequence is shown in scheme 2.11. The hydroxyl groups of catechols were deprotonated with potassium carbonate in DMF and the methyliodide was added to get the 1,2-dimethoxy-benzene in quantitative yields. Formaldehyde and HBr was added in the presence of acetic acid to introduce bromo-methyl groups at 4,5 positions of dimethoxybenzene. The resulting product then underwent Diels-Alder addition to 1,4-naphthoquinone to yield the tetraquinone. Finally, phenyl lithium was used to attach

phenyl rings to the quinone and the resulting hydroxy groups were removed with hydrogen iodide as a reducing reagent in boiling ether to yield the 2,3-dimethoxy-6,11-diphenytetracene.

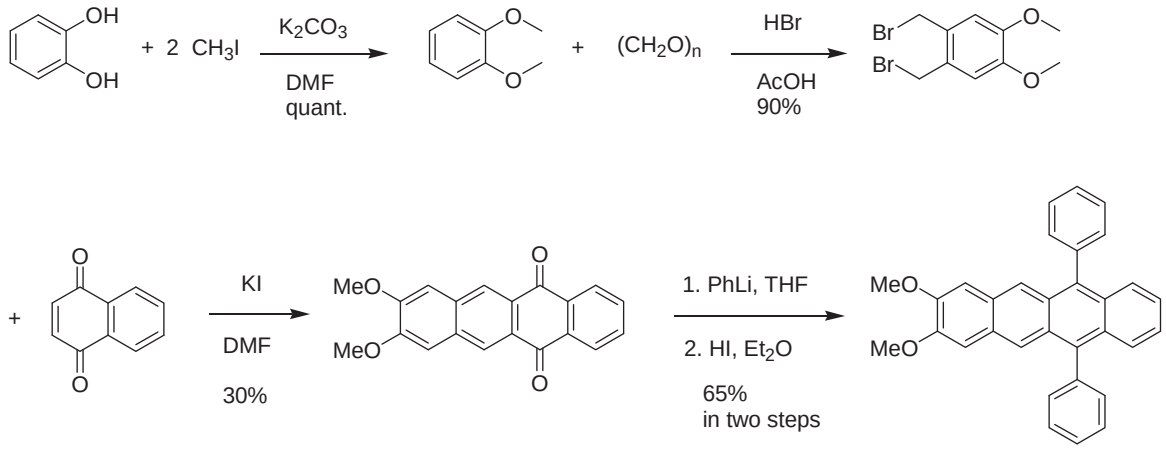

Scheme 2.11: Reaction sequence for 2,3-dialkyloxy-6,11-diphenyl-tetracenes

2.3.1.2 B1—to—GT1 energy transfer

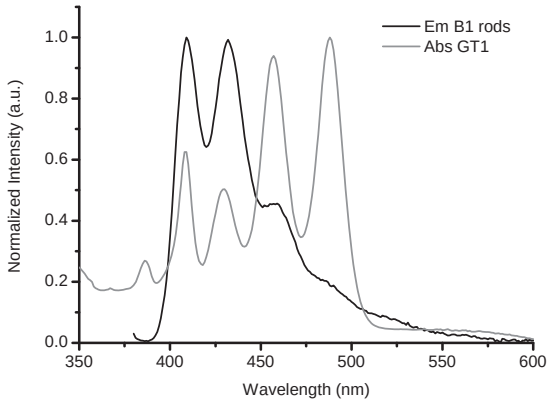

Figure 2.49: Normalized emission spectrum of **B1** nanorods and absorption spectrum of **GT1**

In order to investigate energy transfer from **B1** to **GT1**, 100 µL of a stock solution of **B1** (C_{B1}= 0.5 mM) and **GT1** (C_{GT1}= 5×10^{-6} M) in the mixed solvent of deoxygenated acetonitrile : tetrahydrofuran (1:1, v/v) were rapidly injected into 5 mL 0.25 mM CTAB boiling aqueous solution under continuous stirring and Ar bubbling. After vigorously stirring for 2 min at 100°C, the resulting solution was allowed to ripen at r.t. for two hours. **B1** can be selectively excited due to the low absorbance ($A_{\mathbf{GT1}}$) of **GT1** (at λ_{ex} = 373 nm, $A_{\mathbf{B1}}$ = 0.1 for **B1** $_{373nm}$ = 10710 $M^{-1}cm^{-1}$ and [**B1**] = 10 M, while $A_{\mathbf{GT1}} \leq 2.6\times10^{-4}$ for **GT1** ε_{373nm} = 2607 $M^{-1}cm^{-1}$ and [**GT1**] ≤ 0.1 µM)

The feasibility of a resonant energy transfer process between **B1** donor molecules and **GT1** acceptors is linked to a good overlap integral (J_{BG1}) between **B1** emission and **GT1** absorption (Figure 2.49). J_{BG1} is defined as:

$$J(\lambda) = \frac{\int_0^\infty F_D(\lambda)\varepsilon_A(\lambda)\lambda^4 d\lambda}{\int_0^\infty F_D(\lambda)d\lambda}$$

where $F_D(\lambda)$ is the emission spectrum of the donor and is dimensionless, and ε_A is the absorption spectrum of the acceptor expressed in $M^{-1}cm^{-1}$.

The value of the overlap integral is large enough (J_{BG1} = 2.82×10^{14} $M^{-1}cm^{-1}nm^4$) to allow energy transfer in the nanometer scale.

2.3.1.3 Morphology of doped NRs

The SEM images of 1% **GT1** doped NRs (Figure 2.50) reveals the presence of some amorphous aggregates and the length of NRs are not as uni-sized as pure **B1** NRs, which indicates that the addition of small amount of dopants did influence slightly the morphology of the nanorods.

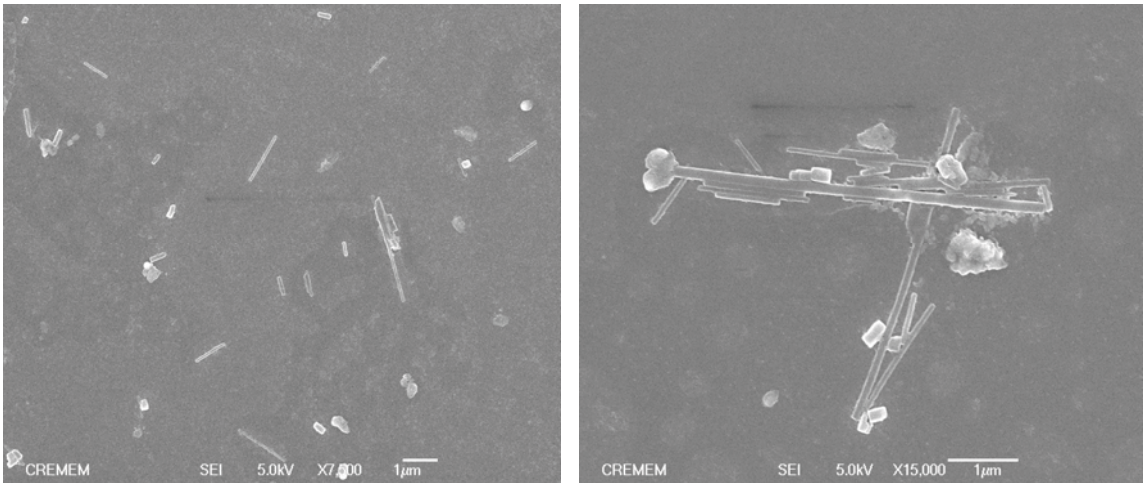

Figure 2.50: SEM images of 1% GT1 doped NRs. Magnification: 7500 X (left), 15000 X (right)

2.3.1.4 Photophysical properties of bulk colloidal aqueous solution

B1 nanorods are doped with **GT1** with 0.25%, 0.5% and 1.0% equivalents and thereupon display an appearance of **GT1** emission (Figure 2.51) when **B1** is selectively excited (λ_{ex} = 373 nm). Thus, the fluorescence of **GT1** is switched on by the NRs. This suggests that the dopant molecules are dispersed in the NR matrix and not self-aggregated in water. Indeed, the application of this reprecipitation procedure to pure **GT1** yields non-emissive aggregates.

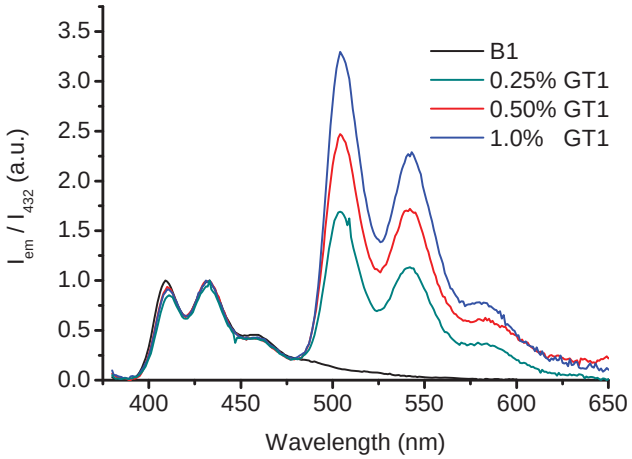

Figure 2.51: Relative emission spectra of **B1** NRs (λ_{ex} = 373 nm) with 0.25%, 0.5% and 1% of **GT1**. λ_{ex} = 373 nm

We have observed an efficient photoinduced energy transfer resulting in 75% quenching of **B1** emission when 0.01 equiv of **GT1** are hosted in the NRs (Table 2.6). The **GT1** emission intensity is remarkably amplified and reaches a value of 67 times higher. Emission amplification (I_{ex373}/I_{ex458}) has been quantified as the ratio of emission intensities of **GT1** at 502 nm for excitation via **B1** (λ_{ex} = 373 nm) over direct excitation of **GT1** (λ_{ex} = 458 nm). It is also proportional to the relative absorption coefficients ($\varepsilon_{\mathbf{B1}}/\varepsilon_{\mathbf{GT1}}$ = 0.73), the relative **GT1**/**B1** concentrations (0.25% to 1%), and the energy transfer efficiency η_{ET} (0.58 to 0.96).

Table 2.6: Signal Amplification, Energy Transfer, Quenching Efficiencies, and Quantum Yields of **B1**/**GT1** NRs 10^{-5} M in bidistilled water at λ_{ex} = 373 nm

[**GT1**]/[**B1**]	I_{ex373}/I_{ex458}[a]	η_{ET}	η_Q[b]	Φ_{ex373}^{em}
0	--	--	--	0.26
0.25%	162	0.58	0.52	0.29[c]
0.50%	100	0.76	0.65	0.28[c]
1.00%	67	0.96	0.75	0.26[c]

[a] $\eta_{ET} = (I_{ex373}/I_{ex458})(\varepsilon_{\mathbf{GT1}}[\mathbf{GT1}]/\varepsilon_{\mathbf{B1}}[\mathbf{B1}])$ with ε_{B1}, 373 nm = 1.1×10^4 M^{-1} cm^{-1} and $\varepsilon_{\mathbf{GT1}}$,458 nm = 1.5×10^4 M^{-1} cm^{-1}.[21]

[b] $\eta_Q = 1 - I_{432}/I_{432}^0$, where the emission intensity at 432 nm with λ_{ex} at373 nm is indicated as I_{432} and I_{432}^0 in the presence and in the absence of **GT1**, respectively.

[c] Determined by using pristine **B1** NRs as reference.

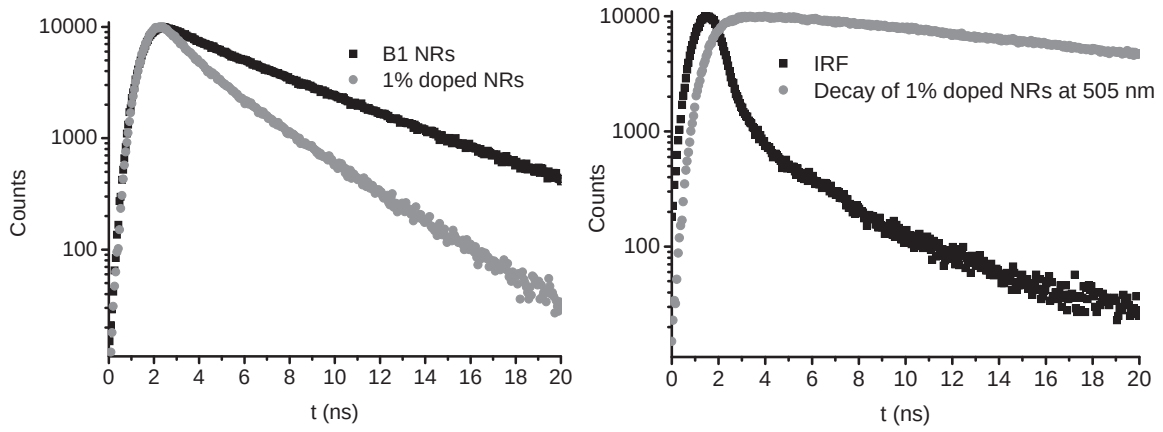

Figure 2.52: (left) Fluorescence decays of **B1** NRs (black) and with 1% **GT1** doping (gray)(λ_{ex} = 371 nm, λ_{em} = 432 nm). (right) Fluorescence decay of 1% **GT1** in **B1** NRs.(λ_{ex} = 371 nm, λ_{em} = 505 nm) (IRF shown for clarity)

The average fluorescence lifetime of **B1** decreases upon addition 1% **GT1** (λ_{ex} = 371 nm, λ_{em} = 432 nm) from 5.6 ns to 2.7 ns (Figure 2.52, left), while a risetime (1.74 ns) is observed in the fluorescence profile of **GT1** upon selective excitation of **B1** (λ_{ex} = 371 nm, λ_{em} = 505 nm) and as well as a decay-time longer than that of **B1** (Figure 2.52, right). All these findings straightforwardly account for a photo-induced energy transfer process from **B1** to **GT1** occurring in the doped nanorods.

Table 2.7: Decay time of **B1** and 1% doped nanorods

	λ_{ex} = 371 nm									
	λ_{em} = 432 nm				λ_{em} = 505 nm					
	Rel. Amp.	τ / ns	Rel. Amp	τ / ns	Rel. Amp.	τ / ns	Rel. Amp.	τ / ns	Rel. Amp.	τ / ns
B1	0.35	2.73	0.65	6.67	--	--	--	--	--	--
1% GT1	0.35	1.24	0.65	3.43	-0.02	1.74	0.29	13.1	0.73	25.7

2.3.1.5 CFM study of the Photophysics within Individual Nanorods

In order to characterize the photophysical properties of both donor and acceptor in mixed NRs, the emission of the donor (**B1**, 400~450 nm blue light is collected) is distinguished from emission of the acceptor (**GT1**, after 500 nm green light is collected) by using band pass filters and two detectors simultaneously.

To assure the data collected with the 500 nm long pass filter are only from **GT1** emission. The two emission spectra of 0.25% doped NRs are taken by selective excitation at **B1** (λ_{ex} = 375 nm) and direct excitation (λ_{ex} = 488 nm) at acceptor (**GT1**) separately with the presence

of 500 nm long pass filter. Figure 2.53 displays the similarity of these two spectra, indicating that using the 500 nm long pass filter can ensure us obtained the emission only coming from **GT1**.

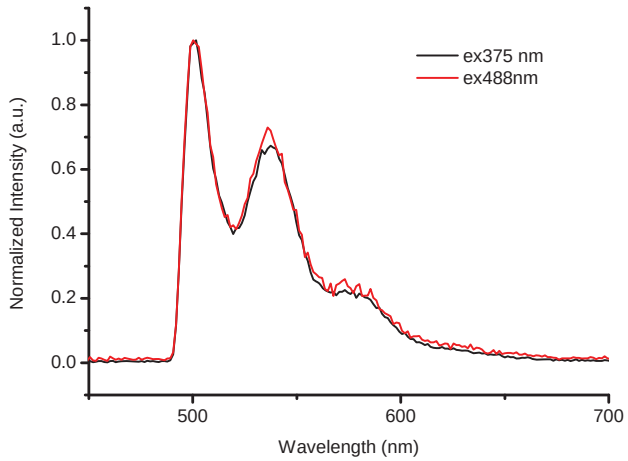

Figure 2.53: Emission spectra of 0.25% doped NRs by indirect excitation λ_{ex} = 375 nm and direct excitation λ_{ex} = 488 nm

Time resolved confocal fluorescence lifetime imaging microscopy (FLIM) for **GT1** emission (λ_{em} > 500 nm) in 0.5% doped single nanorods reveals excited-state decays that can be represented by triexponential functions. The fluorescence of **GT1** rises with time upon selective excitation of **B1** with a distribution of τ around a weighted mean value of 1.1 ns (λ_{ex} = 375 nm, λ_{em} > 500 nm; Figure 2.54). The quenching of **B1** and emission rise for **GT1** on comparable time scales (1.6 ~ 2.0ns, Figure 2.54, 2.55) clearly displays an excitation energy transfer process taking place from **B1** to **GT1** upon selective excitation of **B1.**

These two FLIM images (Figure 2.54, 2.55) are taken simultaneously by two detectors. However, the shape of NRs is not very well-defined in the FLIM image of **GT1** emission. It seems like the end part of some NRs is not observed in this image.

Meanwhile, the FLIM image of **B1** blue emission (Figure 2.55) shows that the average lifetime is longer at the end of NRs and shorter in the middle part. Also, the emission intensity is stronger in the end part. To obtain more information, the detailed analysis of the decay time in three FLIM images with more than 30 objects is done (Table 2.8).

For the blue emission (400 < λ_{em} < 450 nm), the decay times are both shorter in the middle part (3.30, 1.58 ns) than at the end part of NRs (4.03, 2.03 ns). Moreover, the relative amplitude of the shorter decay time is 20% higher in the middle part.

As expected, the relative amplitude of the rising time of green emission (λ_{em} >500 nm) is higher in the middle part of NRs. These observations suggest that the quenching of **B1** blue emission occurs more in the middle part of NRs due to a higher concentration of energy transfer acceptor (**GT1**) molecules.

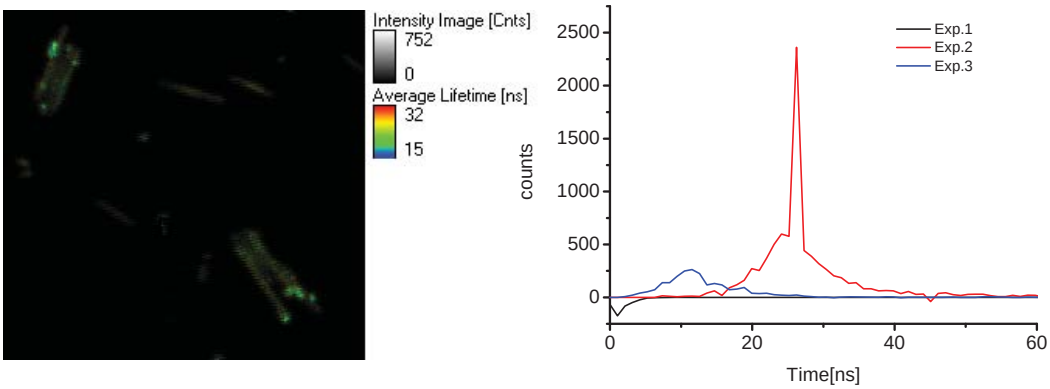

Figure 2.54: FLIM image of 0.5% doped NRs (24 × 24 μm), λ_{ex} = 375 nm, λ_{em} >500 nm, color code: average lifetime (left); decay time distributions obtained by tri-exponential fitting of decays of the image

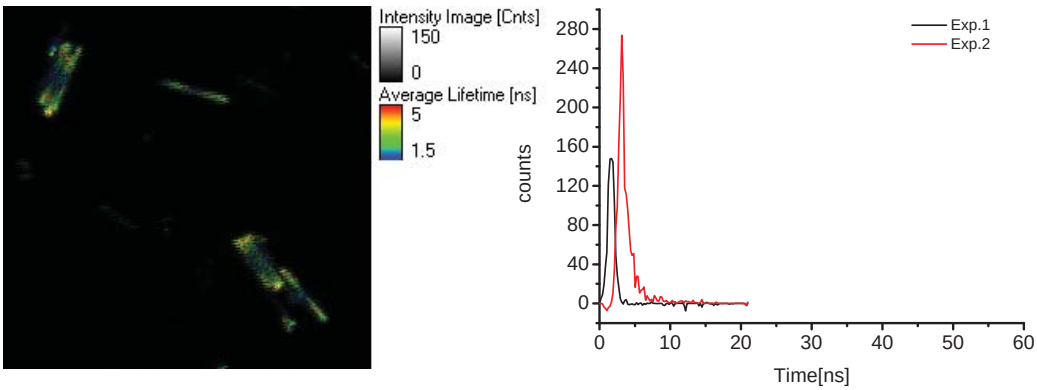

Figure 2.55: FLIM image of 0.5% doped NRs (24 × 24 μm), λ_{ex} = 375 nm, 400 < λ_{em} < 450 nm, color code: average lifetime (left); decay time distributions obtained by bi-exponential fitting of decays of the image

Table 2.8: Decay time analysis of 0.5% doped NRs

	λ_{ex} = 375 nm									
	400 < λ_{em} < 450 nm				λ_{em} >500 nm					
	Rel. Amp.	τ / ns	Rel. Amp	τ / ns	Rel. Amp.	τ / ns	Rel. Amp.	τ / ns	Rel. Amp.	τ / ns
Middle	0.34	3.30	0.66	1.58	0.24	34.9	0.76	16.4	-0.26	0.94
End	0.59	4.03	0.41	2.03	0.36	32.3	0.64	15.3	-0.19	0.83

For 0.25% and 1% doped, similar phenomenon is observed from the FLIM images (Figure 2.56).

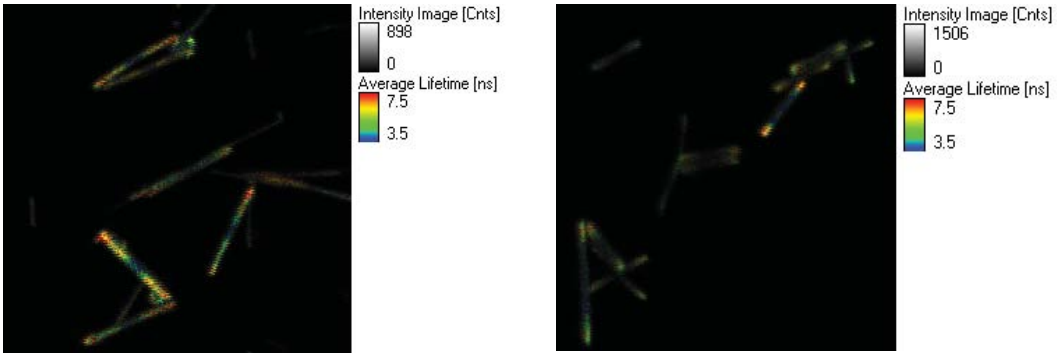

Figure 2.56: FLIM image of 0.25% (20 × 20 μm, left) and 1% (18.7× 18.7 μm, right) doped NRs, λ_{ex} = 375 nm, 400 ＜λ_{em} ＜ 450 nm, color code: average lifetime

To verify this assumption, it is necessary to investigate the distribution of **GT1** molecules within the NRs. It is known that emission intensity is proportional to the quantum yield and the intensity of light absorbed by the objects. Moreover, the quantum yield is equal to the radiative constant k_r multiplied by the lifetime τ. According to Beer's law, the absorbance is proportional to the concentration of molecules when A<2 and the intensity of light absorbed is approximatively proportional to the absorbance when A < 0.1. Therefore, by means of dividing the **GT1** emission intensity over the average decay time, we can estimate the relative concentration of **GT1** molecules within NRs.

Hence we measured the emission intensity and average decay times of **GT1** upon direct excitation on **GT1** molecules at 488 nm along the main axis of each single NR (Figure 2.57), and plot the distribution profile versus positions on a single NR. For each sample, ten different rods were analyzed.

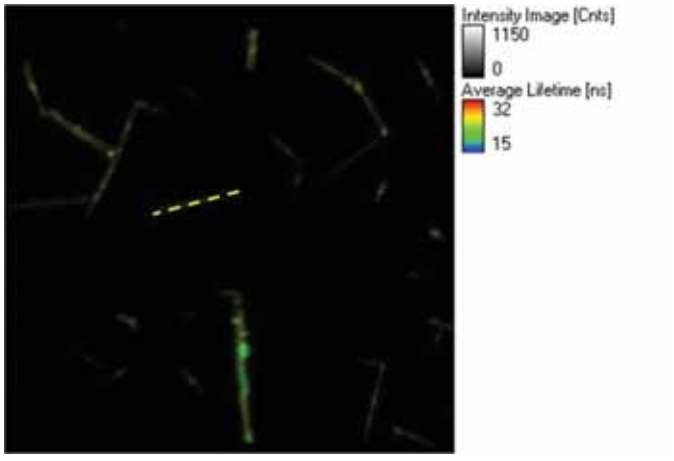

Figure 2.57: Fluorescence intensity image of 1% doped NRs (30× 30μm), λ_{ex} = 488 nm, λ_{em} >500 nm, color code: average lifetime, yellow dot line: the cross section of intensity and average lifetime.

As shown in figure 2.58, **GT1** molecules are indeed more concentrated in the middle part of NRs and then distributed among the whole rod, which validates the previous suggestion that energy transfer occurs more in the middle part of NRs due to a higher concentration of energy transfer acceptor (**GT1**) molecules.

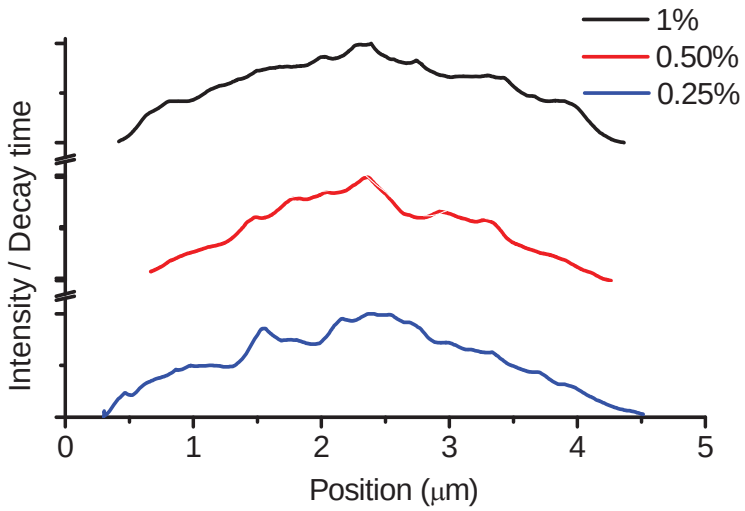

Figure 2.58: Intensity/average lifetime versus position plots for 0.25, 0.5% and 1% doped NRs, λ_{ex} = 488 nm, λ_{em} >500 nm

2.3.1.6 Spectroscopy of Individual Nanorods

To further investigate the non-homogeneous distribution of the acceptors, emission spectra on the single NRs can be a powerful tool to verify the assumption that the acceptor molecules (**GT1**) are more concentrated in the middle of the NR.

The 0.5% doped NR is excited at a single point and the emission spectrum of that certain spot is collected. Figure 2.59 clearly displays that there is more energy transfer induced green light emission in the middle part of NRs, which can only be due to more acceptors population. This observation is also demonstrated in the 0.25% and 1% doped NRs (Figure 2.60, 2.61).

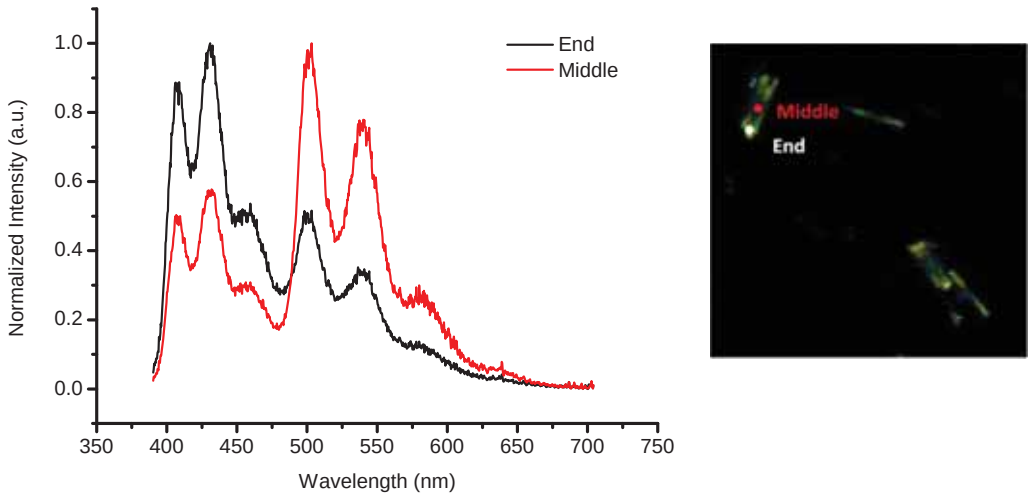

Figure 2.59: Normalized emission spectra of 0.5% doped NRs locally excited at the end part and the middle part separately, λ_{ex} = 375 nm. Inset: the corresponding FLIM image of the NRs (24 × 24 μm), λ_{ex} = 375 nm, with the emission of 400 < λ_{em} < 450 nm.

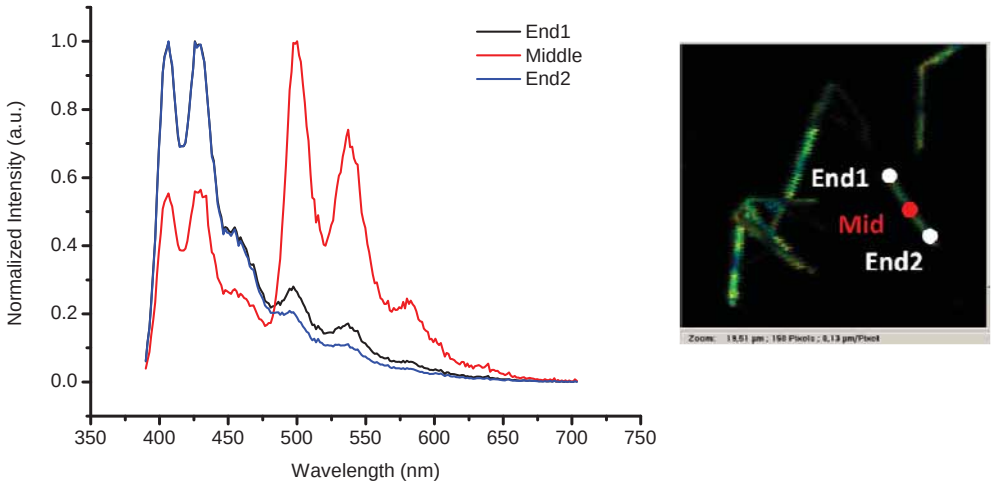

Figure 2.60: Normalized emission spectra of 0.25% doped NRs locally excited at the end part and the middle part separately, λ_{ex} = 375 nm. Inset: the corresponding FLIM image of the NRs (19.5 × 19.5 μm), λ_{ex} = 375 nm, 400 < λ_{em} < 450 nm.

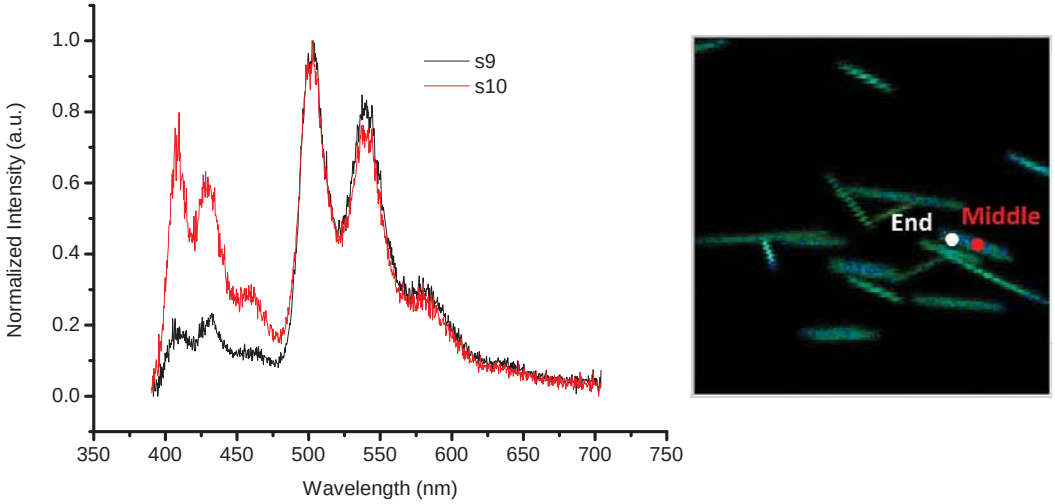

Figure 2.61: Normalized emission spectra of 1% doped NRs locally excited at the end part and the middle part separately, λ_{ex} = 375 nm. Inset: the corresponding FLIM image of the NRs (24.7 × 24.7 μm), λ_{ex} = 375 nm, λ_{em} >500 nm.

To further verify the emission color variation within single nanorod, we measured the emission intensity along the axis of nanorod of donor (400 < λ_{em} < 450 nm) and acceptor (λ_{em} >500 nm) respectively and observed the variation of emission intensity versus different positions at a single NR. For each sample, ten nanorods were analyzed to yield the average intensity versus position plot (Figure 2.62).

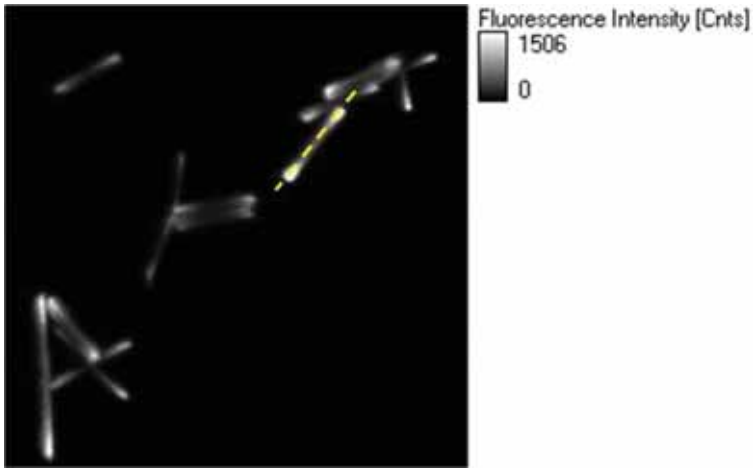

Figure 2.62: Fluorescence intensity image of 1% doped NRs (18.7× 18.7μm), λ_{ex} = 375 nm, 400 < λ_{em} < 450 nm, color code: average lifetime, yellow dot line: the cross section of intensity

As shown in figure 2.63, the different emission colors are not confined in a certain area of single nanorods as segments. In fact, the emission color is a gradient distribution in the NRs (Figure 2.64).

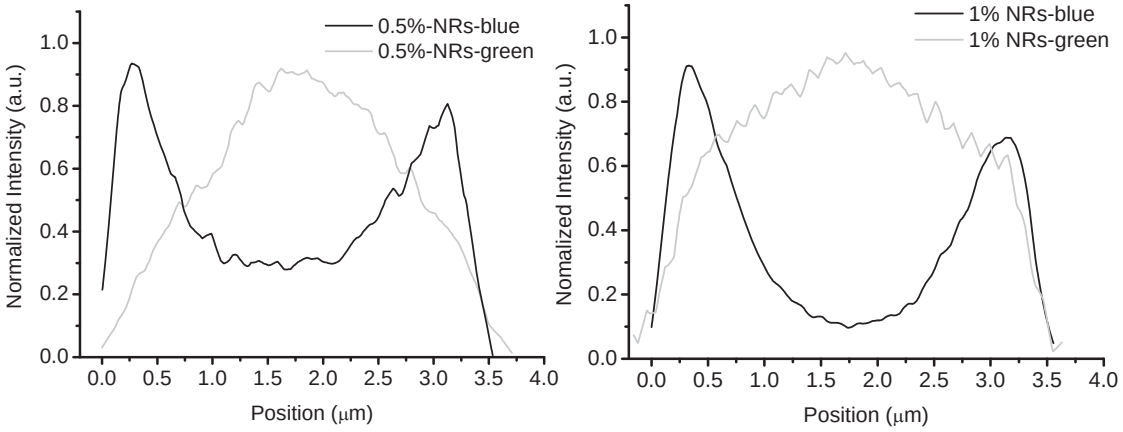

Figure 2.63: Normalized Intensity versus position plots for 0.5% (left) and 1% (right) doped NRs, 400 < λ_{em} < 450 nm for blue emission, λ_{em} >500 nm for green emission, λ_{ex} = 375 nm.

Figure 2.64: Scheme of gradient emission color of 0.5% NRs (left) and 1% NRs (right)

In contrast, while the **GT1** is diluted to 0.25%, the slope of green emission versus position profile is quite steep compared to that of 0.5% and 1% doped NRs. This shows that the sensitized **GT1** emission is concentrated in the middle of rods and no **GT1** emission is observed in the end part of NRs.

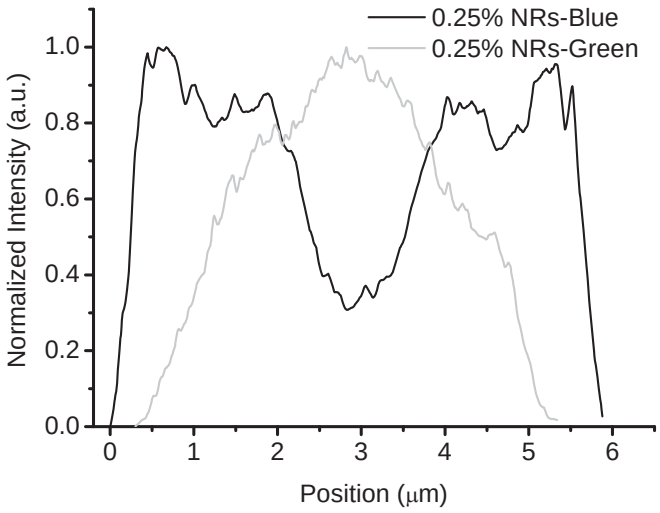

Figure 2.65: Normalized Intensity versus position plots for 0.25% doped NRs, 400 $< \lambda_{em} <$ 450 nm for blue emission, λ_{em} >500 nm for green emission, λ_{ex} = 375 nm.

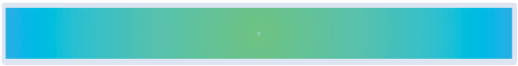

Figure 2.66: Scheme of emission color variation of 0.25% doped NRs

The CIE coordinates calculated from the emission spectra of a 0.5% doped single NR at the middle position are (0.236, 0.382), which are shifted to (0.191, 0.199) at the end position. For 0.25% doped single NR, the CIE coordinates of middle and end position are (0.226, 0.286) and (0.179, 0.140) separately. That of 1% doped single NR are (0.235, 0.391) and (0.266, 0.533) (Figure 2.66). This indicates within a 4 μm nanorod, two distinguishable colors of emission are achieved.

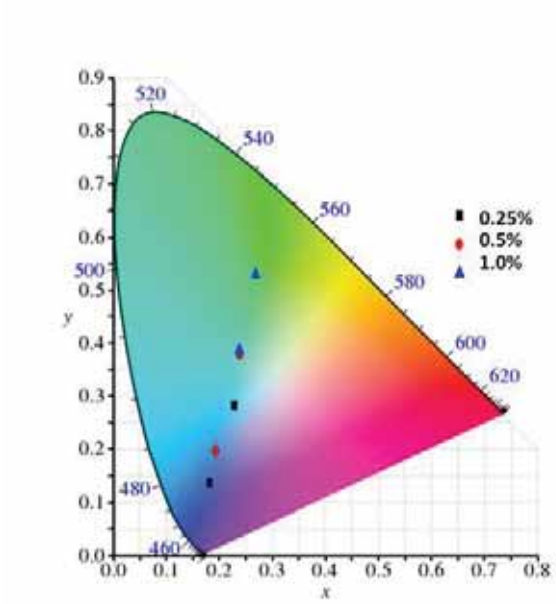

Figure 2.67: CIE 1931 chromaticity coordinates of the middle and the end position of 0.25%, 0.5% and 1% doped single NR.

2.3.1.7 Polarization

In 1% doped NRs the **B1** emits light polarized perpendicular to the long axis of the fibers (400 nm < λ_{em} < 450 nm), and *P* value varied from -0.35 to +0.40 (Figure 2.69) in agreement with pure **B1** NRs (Figure 2.46, -0.40≤*P*≤+0.35). It confirms that the self-assembly of **B1** inside the NRs is not affected by the presence of **GT1**. This is also the case in the 0.25% doped NRs (Figure 2.71, -0.40≤*P*≤+0.45).The green emission from **GT1** sensitized by **B1** displays the same angular dependence as **B1** but with a lower negative value -0.50. (Figure 2.71, λ_{ex} = 375 nm, λ_{em} >500 nm). This indicates that the sensitized **GT1** molecules are oriented at very similar way as **B1**, and the presence of **B1**-**GT1** energy transfer process.

In contrast, when **GT1** is more diluted (0.25%) the emission from **GT1** is less polarized (Figure 2.71, -0.20≤*P*≤+0.45, λ_{ex} = 375 nm, λ_{em} >500 nm).

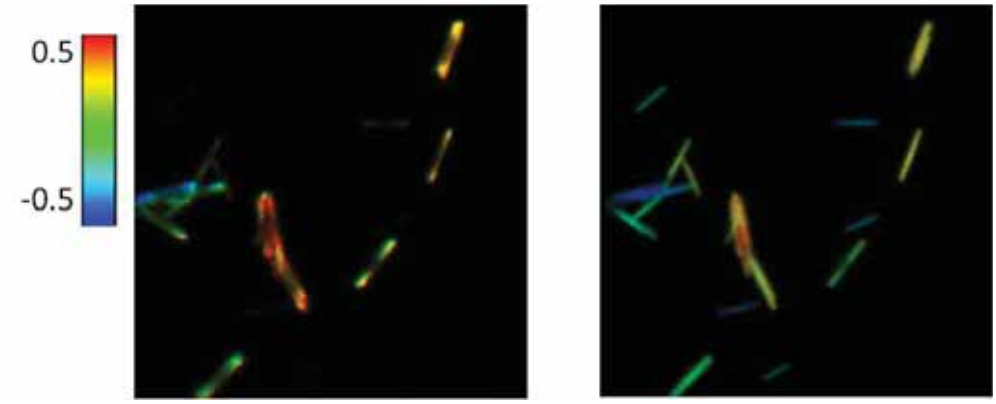

Figure 2.68: Polarization images (22.5× 22.5 μm) of 1% doped NRs: λ_{ex} = 375 nm , 400 nm < λ_{em} < 450 nm (left), λ_{em} >500 nm (right). Color code: polarization

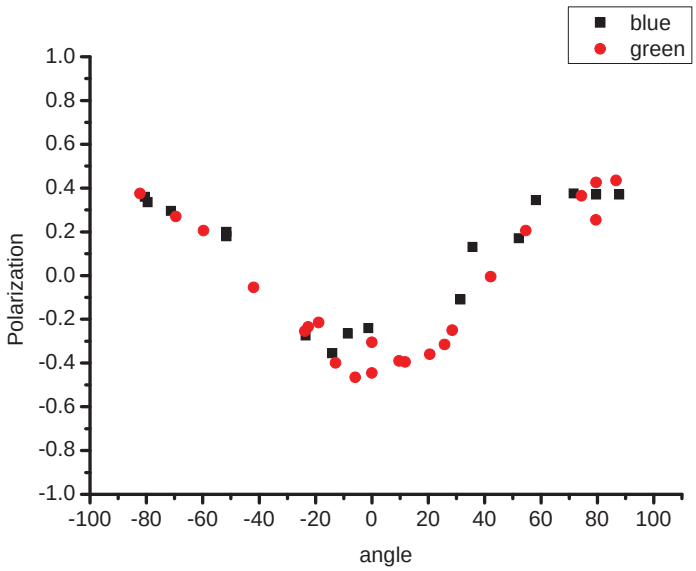

Figure 2.69: Polar plot of 1% doped NRs, λ_{ex} = 375 nm, 400 nm < λ_{em} < 450 nm (black), λ_{em} >500 nm (red).

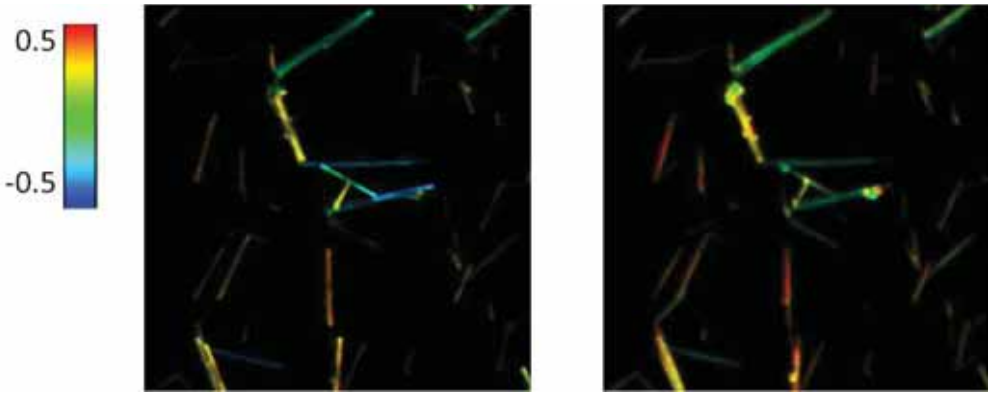

Figure 2.70: Polarization images (20 × 20 μm) of 0.25% doped NRs: λ_{ex} = 375 nm , 400 nm < λ_{em} < 450 nm (left), λ_{em} >500 nm (right). Color code: polarization

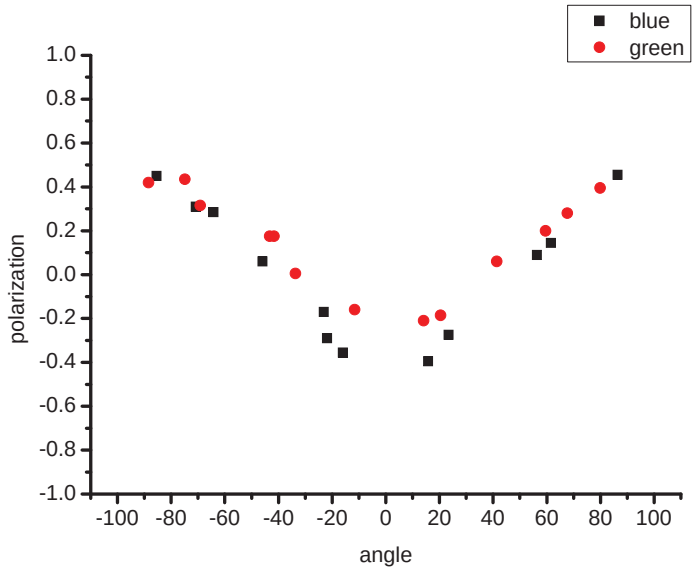

Figure 2.71: Polar plot of 0.25% doped NRs, λ_{ex} = 375 nm, 400 nm < λ_{em} < 450 nm (black), λ_{em} >500 nm (red)

To gain further insight on the polarized emission of the acceptors within the nanorods, we have also excited nanorods at 488 nm, a wavelength at which only **GT1** can absorb, and measured *P* of the resulting emission (λ_{em} > 500 nm). Additionally, in this case all the **GT1** molecules can be excited, whereas in the previous experiment the sensitization could involve all or only one fraction of the **GT1** molecules.

When the **GT1** of 0.25% doped NRs is excited directly, the emission is less polarized (-0.30≤*P*≤+0.25). It indicates **GT1** molecules are more randomly orientated in the nanorod at lower concentration. When **GT1** is present at a higher concentration of 1%, a higher *P* value (-0.22≤*P*≤+0.50) is observed. It suggests a more ordered orientation of **GT1** molecules in the nanorods under this condition.

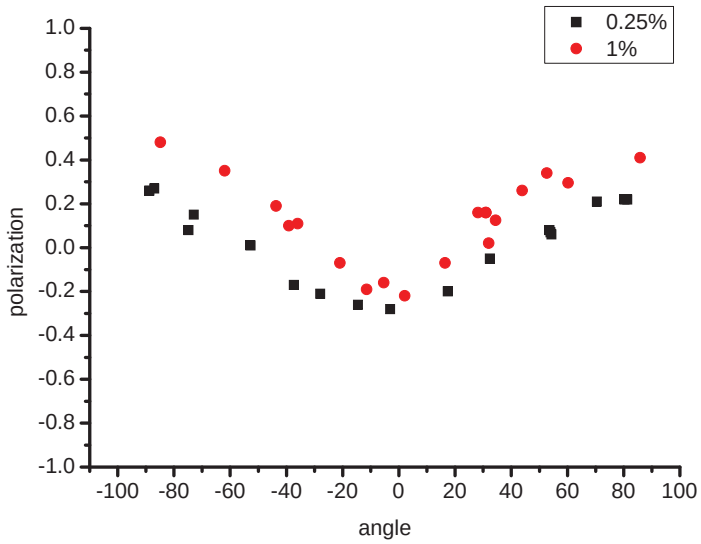

Figure 2.72: Polar plot of 0.25% (black) and 1% (red) doped NRs, λ_{ex} = 488 nm, λ_{em} >500 nm.

In 1% doped NRs, the more negative *P* value of **GT1** emission sensitized by **B1** (-0.50≤*P*≤+0.40, λ_{ex} = 375 nm) as compared to direct excitation (-0.22≤*P*≤+0.50, λ_{ex} = 488 nm) suggests that the contribution of hetero-energy transfer (**B1** to **GT1**) to orientation of polarization change is larger than homo-ET (**GT1** to **GT1**).

The variation of *P* with θ in both cases indicates that **GT1** molecules are oriented like **B1** molecules in the **B1** NRs.

2.3.2 Discussion

The nanorods derived from 2,3-methoxy-9,10-diphenylanthracene are achieved by a reprecipitation method with CTAB as a soft-template. The structured fluorescence emission spectrum and strong *P* to θ dependency indicates highly ordered molecular packing and high crystallinity of the NRs. The resemblance of the emission spectra of NRs and crystals confirms this assumption.

The addition of **GT1** as an energy transfer acceptor to the NRs yields color-tunable fluorescent nanorods. The light-harvesting and blue-emitting diphenylanthracene matrix sensitizes the green acceptors by energy transfer. The analysis by confocal microscopy of decay times and emission spectra of different positions on a single nanorod reveal there is more energy transfer occurring in the middle part of NRs. It suggests that tetracenes are not homogenously dispersed into the rods and are more concentrated in the middle of nanorods. This fact also supports the self-inducing nanorod formation mechanism.[23] First, the major proportion of **GT1** molecules solubilize in CTAB spheres due to the poor solubility in water. Then the spherical micelles induce the formation of rod-like micelles, which direct the growth of nanorod along a 1D direction. Thereby NRs with two emission colors within one single object are achieved.

The polarization study reveals that the **GT1** and **B1** display quite similar orientation. The

high degree of order at the molecular level of **B1** constituent in the nanorods is not perturbed, which is the basis for a robust self-assembled system. It also induces polarized blue emission and favors **B1→B1** exciton hopping which would contribute to the light-harvesting process.[27] The more efficient **B1→GT1** energy transfer in 1% doped NRs than 0.25% sample can be the explanation of more polarized **GT1** green emission of 1% doped NRs sensitized by **B1**.

2.3.3 Conclusion

1. Uniformly sized nanorods are fabricated in aqueous solution with assistance of CTAB as a soft template. The proposed NRs formation process is verified by the heterogeneous incorporation of less soluble dopants.
2. Although the heterogeneity of **GT1** in NRs demonstrates distinguishable color of emission in microarea, it also proves the difficulty to homogeneously dope the nanometer scaled light-harvesting matrix.
3. Confocal fluorescence microscopy plays an important role in this work. It enables us to acknowledge the heterogeneity within a several micrometer length rod from the decay times and emission spectra. It also reveals an insight of molecular packing by polarization measurement.

2.4 References

1. Haller, A.; Guyot, A. *Compt. rend.* **1904**, 138, 1251.
2. Suzuki, T.; Nagano, M.; Watanabe, S.; Ichimura,T. J. *Photochem. Photobiol. A-Chem.* **2000**, *136*, 7.
3. Adams, J. M.; Ramdas, S. *Acta Cryst.* **1979**, *B35*, 679.
4. Pu, Y.-J.; Kamiya, A.; Nakayama, K.-I.; Kido, J. *Org. Electron.* **2010**, *11*, 479.
5. Iida, A.; Yamaguchi, S. *Chem. Comm.* **2009**, 3002.
6. Jo, W. J.; Kim, K.-H.; No, H. C.; S, D.-Y.; Oh, S.-J.; Son, J.-H.; Kim, Y.-H.; Cho, Y.-K.; Zhao, Q.-H.; Lee, K.-H.; Oh,H.-Y.; Kwon, S.-K. *Synth. Mat.* **2009**, *159*, 1359.
7. Kim, S. O.; Jung, H. C.; Lee, M.-J.; Jun, C.; Kim, Y.-H.; Kwon, S.-K. *J. Polym. Sci., Part A: Polym. Chem.* **2009**, *47*, 5908.
8. Yamagishi, M.; Tominari, Y.; Takeya, J. *J. Surf. Sci. Nanotech.* **2008**, *6*, 21.
9. Tripathi, A. K.; Heinrich, M.; Siegrist, T.; Pflaum, J. *Adv. Mat.* **2007**, *19*, 2097.
10. Vinyard, D. J.; Su, S.; Richter, M. M. *J. Phys. Chem. A.* **2008**, *112*, 8529.
11. Ismail, Y. A. M.; Soga, T.; Jimbo, T. *Sol. Energy Mater. Sol. Cells.* **2009**, *93*, 1582.
12. Zhang, X.; Yuan, G.; Li, Q.; Wang, B.; Zhang, X.; Zhang,R.; Chang, J. C.; Lee, C.-S.; Lee, S.-T. *Chem. Mater.* **2008**, *20*, 6945.
13. Desvergne, J.-P.; Brotin, T.; Meerschaut, D.; Clavier, G.; Placin, F.; Pozzo, J.-L.; Bouas-Laurent, H. *New J. Chem.* **2004**, *28*, 234.
14. Fellers, T. J.; Davidson, M. W. *Introduction to Confocal Microscopy* **2007,** Olympus Fluoview Resource Center. National High Magnetic Field Laboratory.
15. Rezzonico, D.; Kwon S.-J.; Figi, H.; Kwon, O-P.; Jazbinsek, M.; Günter, P. *J. Chem. Phys.* **2008,** ***128***, 124713
16. Del Guerzo, A.; Olive, A. G. L.; Reichwagen, J.; Hopf, H.; Desvergne, J.-P. *J. Am. Chem. Soc.* **2005**, *127*, 17984.
17. Albrecht, M.; Bohne, C.; Granzhan, A.; Ihmels, H.; Pace, T. C. S.; Schnurpfeil, A.; Waidelich, M.; Yihwa, C. *J. Phys. Chem. A* **2007**, *111*, 1036.
18. (a) Birks, J.B. *Organic Molecular Photophysics* **1979**, Wiley, New York. (b) Murov, S.L.; Carmichael, I.; Hug, G. L. *Handbook of Photochemistry*, 2nd Edition, **1993** Marcel Dekker, New York.—DPA. LOW ISC
19. Wu, C. C.; Lin, Y. T.; Chiang, H. H.; Cho, T. Y.; Chen,C. W.; Wong, K. T.; Liao, Y. L.; Lee, G. H.; Peng, S. M. *Appl. Phys. Lett.* **2002**, ***81***, 577.
20. Yamaguchi, S.; Xu, C.; Yamada, H.; Wakamiya, A. *J. Org.-metal. Chem.***2005**, *690*, 5365.
21. Cazade, P.-A.; Bordat, P.; Blanc, S.; Baraille, I.; Brown, R. *Langmuir* **2008**, *24*, 2252.
22. Zhang, X.; Yuan, G.; Li, Q.; Wang, B.; Zhang, X.; Zhang, R.; Chang, J. C.; Lee, C. S.; Lee, S. T. *Chem. Mater.* **2008**, *20*, 6945.
23. Fu, H.; Xiao, D.; Yao, J.; Yang, G. *Angew. Chem. Int. Ed.* **2003**, 42, 2883.
24. Yang, B.; Xiao, J.; Wong, J. I.; Guo, J.; Wu, Y.; Ong, L.; Lao, L. L.; Boey, F.; Zhang, H.; Yang, H. Y.; Zhang, Q. *J. Phys. Chem. C* **2011**, *115*, 7924.
25. Li, Q.; Zhang, C.; Zheng, J. Y.; Zhao, Y. S.; Yao, J. *Chem. Comm.* **2012**, *48*, 85.

26. Lakowicz, J. R. *Principles of Fluorescence Spectroscopy, III Ed.*, **1999** Kluwer Academic / Plenum Press, New York.
27. Giansante, C.; Raffy, G.; Schäfer, C.; Rahma, H.; Kao, M.-T.; Olive, A. G. L.; Del Guerzo, A. *J. Am. Chem. Soc.* **2010**, *133*, 316.

Chapter 3

Nanoribbons of B16 as light-harvesting matrices

3.1 Introduction

From the work presented in previous chapter, we obtained an insight about the difficulty of sufficiently and homogeneously doping energy acceptor molecules into the matrix without damaging the nanostructure. Herein, a novel system is developed to include dopant molecules into nano-scaled structures.[1]

2,3-dihexadecyloxy **DPA** (**B16**) is known that it forms nanoribbons by recrystallization from DCM/MeOH. We use **B16** as a light-harvesting nano-scaled matrix which can be doped with green (5,12-diphenyltetracene) and orange chromophores (rubrene) and display a range of emission colors that is controllable with two or three components. Moreover, steady-state emission spectroscopy of **B16** nanoribbons containing **G16** and **R16** is exploited at different doping ratios to evaluate the energy transfer processes at the origin of color-tuning: *(i)* **B16**–to–**G16** and **B16**–to–**R16** excitation energy transfer; *(ii)* a cascade **B16**–to–**G16**–to–**R16** energy transfer.[2]

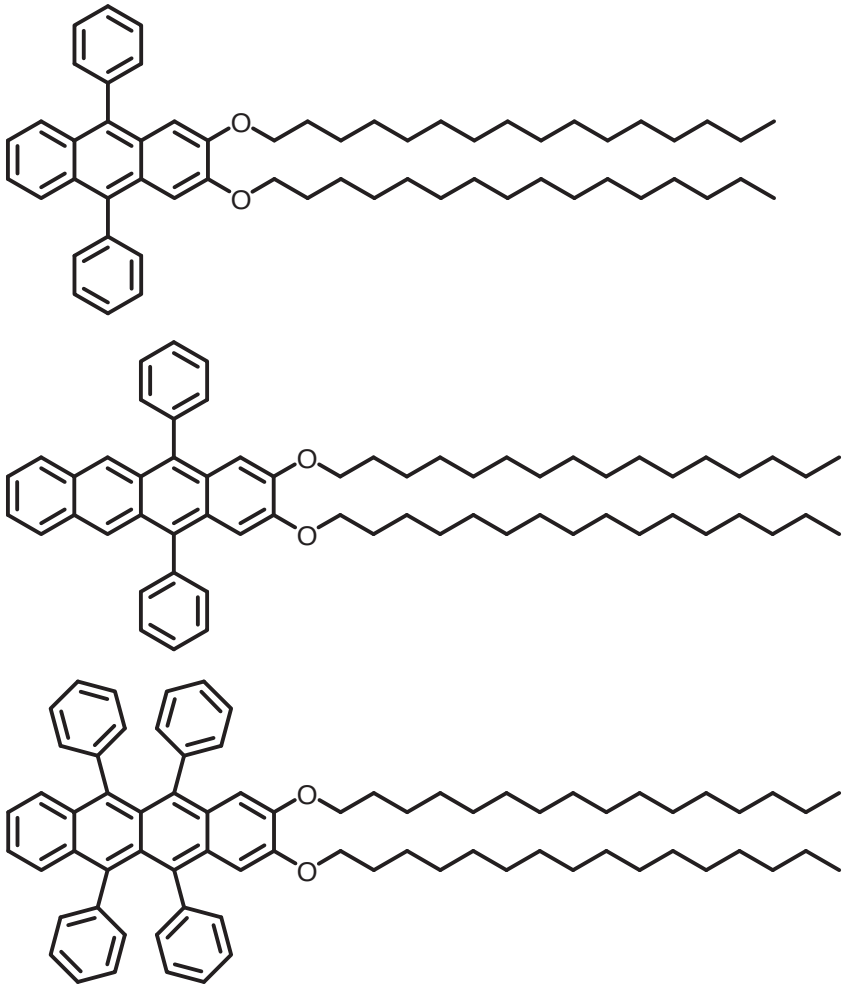

Scheme 3.1: Molecular structures of 2,3-dihexadecyloxy-9,10-diphenyl anthracene (**B16**), 2,3-dihexadecyloxy-5,12-diphenyl-tetracene (**G16**),2,3-dihexadecyloxy-5,6,11,12-tetraphenyl-tetracene (**R16**)

In THF solutions, **G16** and **R16** display green (λ_{em} = 502 nm, CIE coordinates *x*=0.262, *y*=0.631) and orange (λ_{em} = 555 nm, CIE coordinates *x*=0.470, *y*=0.525) fluorescence with quantum yields of 53% and 69%, respectively (Table 3.1)

Table 3.1: Absorption and emission properties of **B16**, **G16** and **R16** in solution and in NBs. λ^{abs} Lowest energy absorption wavelength, Extinction coefficient of absorption max $\varepsilon_{\lambda max}$, and Quantum Yield Φ_{em}, Decay Time τ, and radiative constant k_r

Compound	$\lambda^{abs}{}_{max}$ [nm]	$\varepsilon_{\lambda max}$ [$\times 10^3$ $M^{-1}cm^{-1}$]	$\lambda^{em}{}_{max}$ [nm]	Φ_{em}	τ [ns]	k_r [$\times 10^7 s^{-1}$]
B16	373	10.0	413/433	0.75	6.90	11
G16	489	8.9	502	0.53	13.8	3.8
R16	523	9.6	555	0.69	13.6	5.1
B16 NBs	375	--	440	0.40[a]	7.30	5.5

[a] Measured with integrating sphere

In our previous work,[3] **G16** and **R16** were blended with **DDOA** gel to achieve a white-light-emission gel.[4] The long alkoxy side chains allowed their incorporation into **DDOA** gel fibers without significantly altering the molecular-level order of the martrix.

3.2 Results

3.2.1 Size and shape of NanoRibbons

According to chapter 2, the **B16** micro-ribbons obtained by slow-grow crystallization method are shown to have highly polarized emission ($-0.75 \leq P \leq +0.75$) due to ordered molecular packing, but the whole process usually takes several days. In order to keep this character and accelerate the nano-structure formation, a solvent exchange method[5] is utilized to prepare the **B16** nano-ribbons.

100 μl stock solution containing **B16** (C_{B16} = 5 mM) and **G16**/**R16** (up to 0.1mM) in the good solvent DCM was quickly injected into the poor solvent MeOH (5mL). The resulting solution was allowed to ripen overnight on standing in the dark and yielded a suspension of nanoribbons. This method has very good reproducibility, proven by the fact that NBs obtained from more than 20 experiments yielded the same photophysical properties (emission spectrum, polarization of emission, lifetimes).

SEM images (Figure 3.1) show that nanoribbons are tens of μm long. The width of the NBs lies in the range of 0.5 ~ 1.0 μm. The texture of NBs is quite soft and they can be easily bended by the electron beams applied at SEM experiments. The images suggest that their thickness is similar to that of slowly recrystallized micro-ribbons of **B16**, thus about 100-200 nm as revealed by AFM in the previous chapter.

The SEM images of 1% **G16** doped NBs (Figure 3.2) reveal that, the morphology of NBs

is not influenced by the addition of small amounts of dopant.

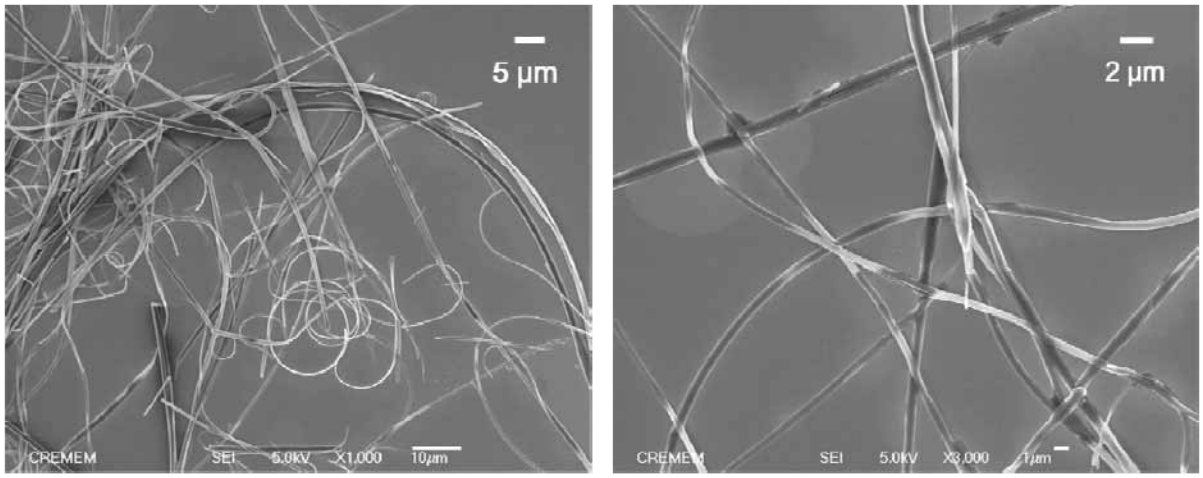

Figure 3.1: SEM images of the **B16** nanoribbons. Magnification : 1000X (left), 3000 X (right)

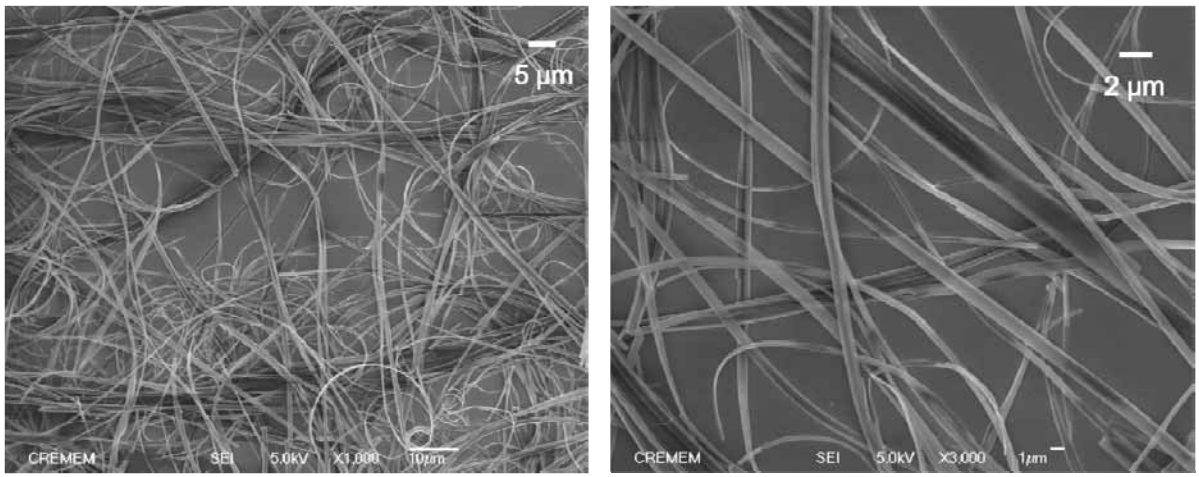

Figure 3.2: SEM images of the **B16** doped with 1% **G16** nanoribbons. Magnification : 1000X (left), 3000 X (right)

3.2.2 B16−to−G16 energy transfer

In order to investigate energy transfer process from **B16** to **G16**, 100 µL of a stock solution of **B16** (C_{B16}= 5 mM) and **G16** (C_{G16} up to 50 µM) in deoxygenated DCM is injected into 5 mL deoxygenated MeOH. After overnight ripening at r.t., the resulting nanoribbons are deposited on a quartz surface and covered by another slide for further experiments. Thereby, most of the solvent is eliminated although complete drying is not enforced. **B16** can be selectively excited due to the low absorbance ($A_{\mathbf{G16}}$) of **G16** (at λ_{ex} = 372 nm, $A_{\mathbf{B16}}$ = 0.98 for **B16** ε_{372nm} = 9844 $M^{-1}cm^{-1}$ and [**B16**] = 0.1 mM, while $A_{\mathbf{G16}} \leq 9.0\times10^{-4}$ for **G16** ε_{372nm} = 902 $M^{-1}cm^{-1}$ and [**G16**] ≤ 1 µM)

The overlap integral J_{CG} between **B16** emission and **G16** absorption, which is defined as:

$$J(\lambda) = \frac{\int_0^\infty F_D(\lambda)\varepsilon_A(\lambda)\lambda^4 d\lambda}{\int_0^\infty F_D(\lambda)d\lambda}$$

where $F_D(\lambda)$ is the emission spectrum of the donor and is dimensionless, and ε_A is the

absorption spectrum of the acceptor expressed in $M^{-1}cm^{-1}$.

The value of this overlap integral J_{BG} is sufficient to allow energy transfer to occur (Figure 3.3, $J_{BG} = 1.50 \times 10^{14}\ M^{-1}cm^{-1}nm^4$) in the nanometer scale.

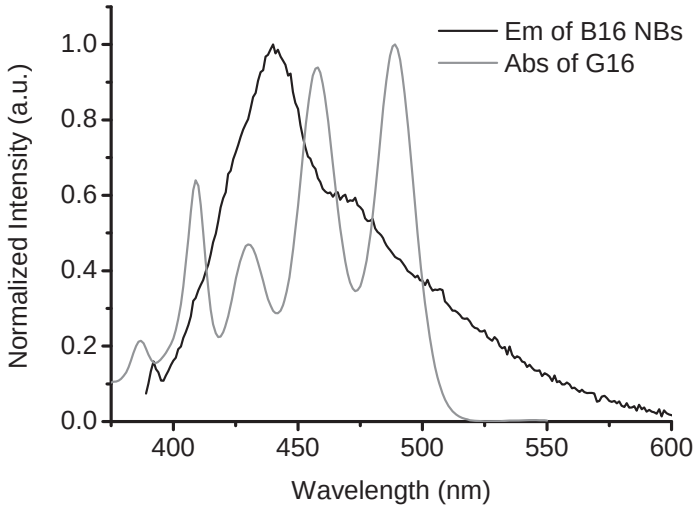

Figure 3.3: Normalized emission spectrum of **B16** nanoribbons and absorption spectrum of 10 μM **G16** in THF solution

3.2.2.1 Photophysical properties

B16 NBs doped with **G16** with concentrations of 0.1%, 0.2%, 0.5%, 0.7% and 1.0% demonstrate steadily decreasing emission of **B16** and increasing emission of **G16** (Figure 3.4) when **B16** is selectively excited. (λ_{ex} = 372 nm). The CIE coordinates vary linearly from (0.185, 0.204) to (0.304, 0.566). The color changes from blue to green, as shown in Figure 3.5.

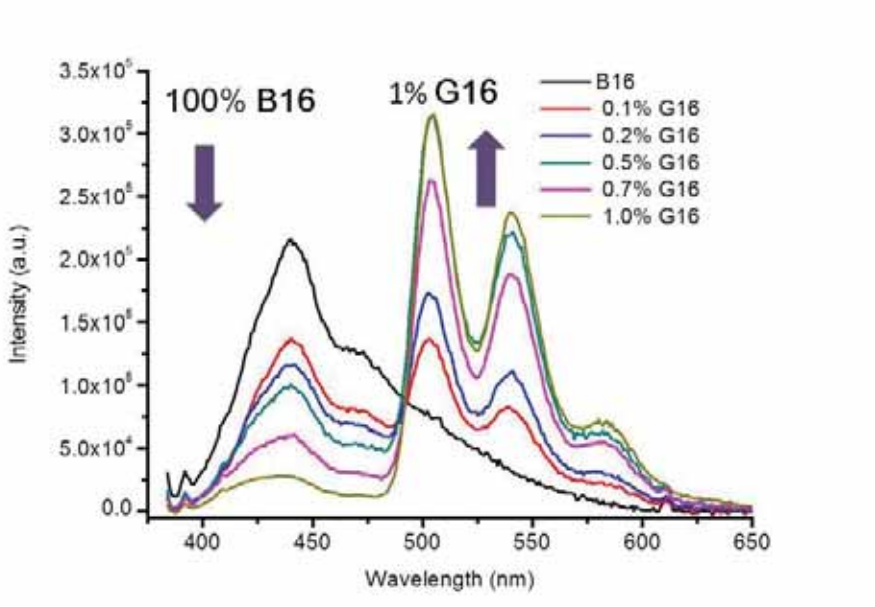

Figure 3.4: Emission spectra of **B16** NBs and doped NBs 0.1%~1% doped G16, the spectra are normalized to correspond to the Q.Y., λ_{ex} = 372 nm

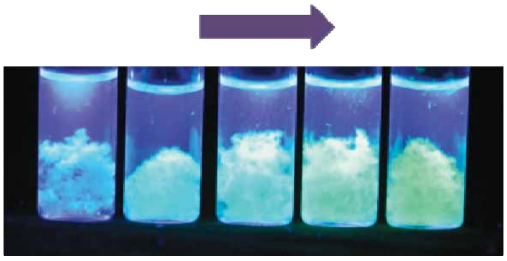

Figure 3.5: picture of **B16** NBs and NBs doped with 0.1%, 0.2%, 0.5% and 1% **G16** (from left to right) under UV irradiation (λ_{ex} = 365 nm)

We have observed an efficient photoinduced energy transfer resulting in 88% quenching of **B16** emission when 0.01 equiv of **G16** are added to the NBs (Table 3.2). By the fact that the NBs are deposited on slides for measurements, it is not possible to assure that the amount of NBs are all the same for every measurements. Therefore, the emission intensity of samples which is utilized to calculate the quenching efficiency η_Q, defined as $1 - I_{440}/I_{440}^{0}$, should be corrected with its quantum yield which is measure by integrating sphere.

The **B16** to **G16** energy transfer efficiency η_{ET} is defined as the portion of quenched donor molecules that transfers their energy to acceptors out of total quenched donors. The contribution of quantum yields of donor and acceptor are taken into account to result the following equation used to determine η_{ET}:

$$\Phi_{\text{Total}} = \Phi_D\left(1-\eta_Q\right) + \Phi_{\text{A}}\left(\eta_Q\right)\left(\eta_{ET}\right)$$

where Φ_D is the fluorescence quantum yield of **B16** NBs measured with integrating sphere in absence of **G16**; Φ_A is the quantum yield of **G16** at 460 nm in NBs, determined by specifically exciting **G16** in 1% doped NBs. The discrepancy between quenching efficiency and energy transfer efficiency indicates that a supplementary quenching process occurs upon addition of dopant (see discussion).

The radiative constant of **G16** in doped NBs is determined by combining the quantum yield and the decay time of **G16** upon specific excitation of **G16** in 1% doped NBs. Using τ = 21.6 ns, we find a radiative constant $k_r = 4.1\times10^7$ ns^{-1}, which is consistent with the radiative constant of **G16** in solution ($k_r = 3.8\times10^7$ ns^{-1}). Moreover, this 21.6 ns decay time of **G16** is clearly longer than in solution (13.8 ns), suggesting a decrease of the non-radiative constant k_{nr} due to a more rigid micro-environment[2] (k_{nr} varies from 3.4×10^7 ns^{-1} to 0.5×10^7 ns^{-1}) or other additional mechanisms with the presence of long-lived emitting species involved (which would be discussed later in the lifetime section).

Table 3.2: Energy transfer and quenching efficiencies, and quantum yields of **B16**/**G16** NBs at λ_{ex} = 372 nm

[G16]/[B16]	η_{ET}^{a}	η_Q^{b}	Φ_{ex372}^{emc}
0	--	--	0.40
0.10%	0.18	0.25	0.34
0.20%	0.37	0.42	0.36

0.50%	0.64	0.64	0.50
0.70%	0.45	0.72	0.40
1.00%	0.49	0.88	0.43

a η_{ET} is calculated by the contribution of quantum yield from donor and acceptor :

$\varphi_{\text{total}} = \varphi_{\text{d}}(1-\eta_Q) + \varphi_{\text{a}}(\eta_Q)(\eta_{ET})$, φ_{a} is 0.87

b $\eta_{\text{Q}} = 1 - I_{440}/I_{440}^{0}$, where the emission intensity (corrected with quantum yield) at 440 nm with λ_{ex} at 372 nm is indicated as I_{440} and I_{440}^{0} in the presence and in the absence of **G16**, respectively.

c Determined by intergrating sphere

From the lifetime measurements study, the fluorescence decay time of **B16** decreases in presence of **G16** (λ_{ex} = 371 nm, λ_{em} = 431 nm, Figure 6, left), while the fluorescence profile of **G16** displays a rise time upon selective excitation of **B16** (λ_{ex} = 371 nm, λ_{em} = 502 nm, Figure 6, right). These observations are a good indication for an energy transfer process from **B16** to **G16** occurring in **G16** doped nanoribbons.

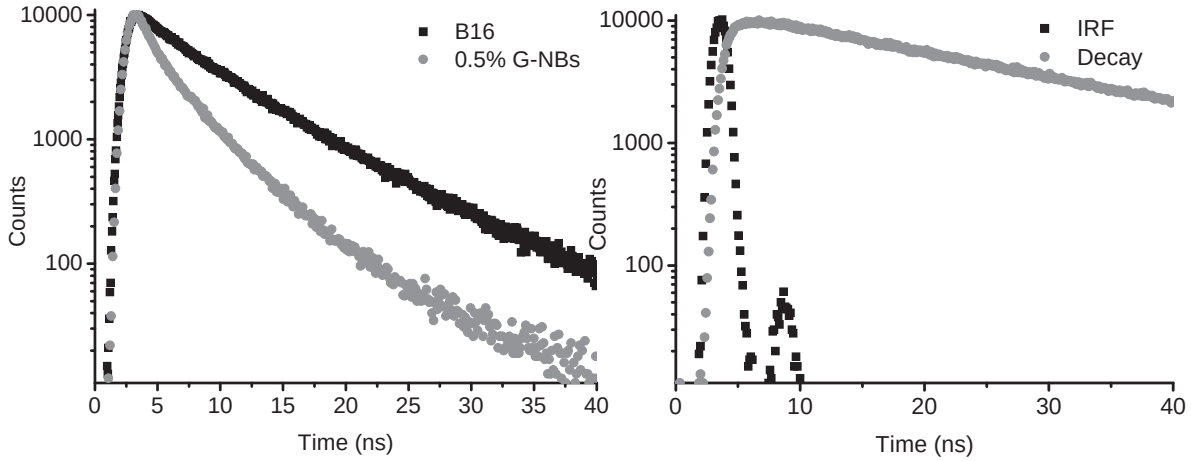

Figure 3.6: (left) Fluorescence decays of **B16** emission in NBs without (black) and with 0.5% **G16** doping (red). (λ_{ex} = 371 nm, λ_{em} = 431 nm)(right) Fluorescence decay of **G16** emission in 0.5% G-NBs.(λ_{ex} = 371 nm, λ_{em} = 502 nm) (IRF shown for clarity)

3.2.2.2 Emission spectra of single NBs

Confocal fluorescence microscopy allows us to further characterize individual nanoribbons. To prepare the samples for CFM experiments, the nanoribbons are directly drop-casted on a cover glass, and excess solvent is removed.

From chapter 2, it is known that **B16** microribbons have a good photostability. However, the dopant molecules are more fragile because they are excited tens of times more than the donors given the fact that the concentration of **G16** in the NBs is only 0.1~1% but they can emit almost the same amount of photons as other 99% **B16** molecules. (The quantum yield of doped G-NBs is very similar to B-NBs, Table 3.2)

To avoid our samples being bleached by the strong laser, the incident laser power is tested

by scanning the same area several times to see if the lifetime or emission spectra has any changes. For the laser power used in the emission spectra and lifetime measurement, it was set according to the criteria that scanning the same area two times and the lifetime of these measurements are still the same.

In order to accumulate sufficient photons and minimize photobleaching, the emission spectra are recorded by accumulating light emitted from an unscanned area (30 × 30 μm).

Samples of 0.1%, 0.2%, 0.5%, 1% and 2% **G16** doped NBs are studied under CFM. (Figure 3.7) As already observed in crystals (chapter 2), a first difference of the spectra under CFM and those of bulk-spectra resides in the observation of the 0-0 transition of **C16**. Moreover, we observed under CFM that the emission of **B16** is almost totally quenched in 1% **G16** doped NBs. With the same concentration of dopants, the emission spectrum obtained from bulk measurements (Figure 3.5) displays only 88% quenching of **B16** emission. Taking into account the photobleaching of **G16**, this difference could be rationalized if photobleaching of **G16** is assumed to occur less under the conditions of CFM than in a fluorimeter.

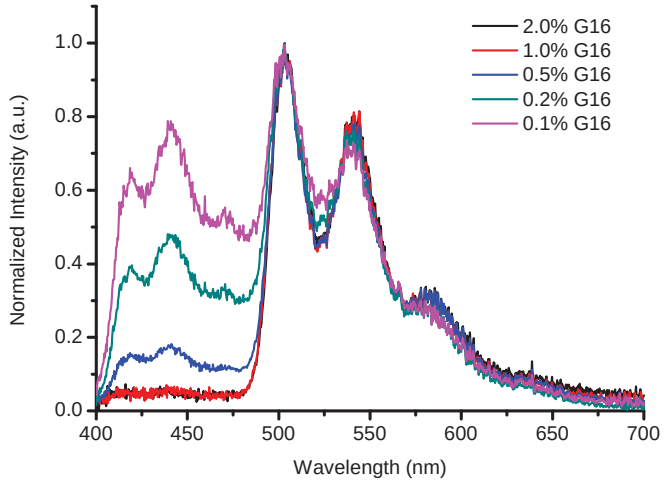

Figure 3.7: relative emission spectra at 502 nm of 0.1%, 0.2%, 0.5%, 1% and 2% **G16** doped nanoribbons, λ_{ex} = 375 nm

For each sample, five to seven different areas of NBs have been analyzed. Figure 3.8 demonstrates the similarity of the emission spectra obtained in these different areas, which indicates a very homogeneous dispersion of **G16** within the nanoribbons.

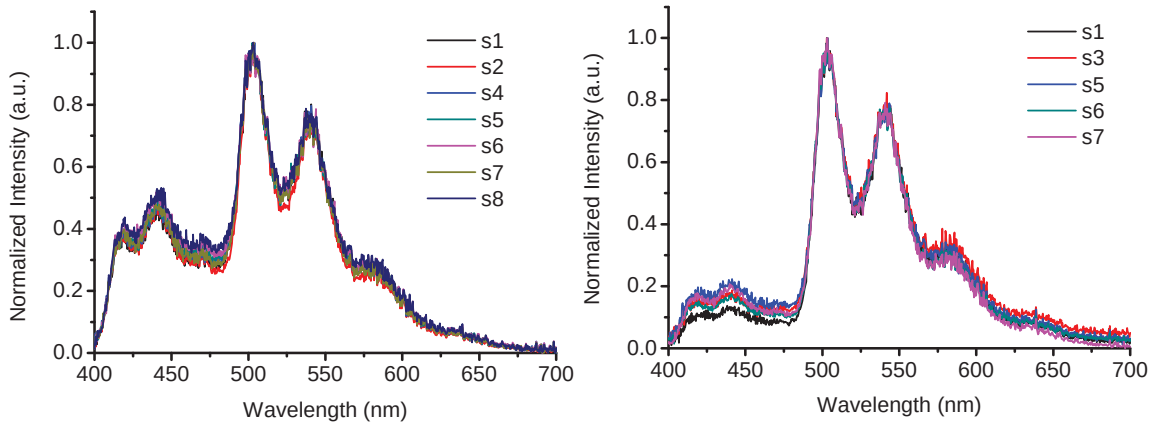

Figure 3.8: relative emission spectra at 502 nm of 0.2% (left) and 0.5% (right) **G16** doped **B16** NBs

To investigate the effect of photobleaching on the nanoribbons, 1% **G16** doped NBs is selectively excited at 375 nm with a laser power of ~30 W/cm^2, which is the same power for all of our measurement (except the power dependent experiment). An area about 5 μm length and <1 μm width of a chosen ribbon is excited continuously for 50 s (Figure 3.9 right), the emission spectra are taken by accumulating the photons emitted in each 5 s time frame. Figure 9 shows that **G16** is progressively bleached and that simultaneously the emission of **B16** is recovered. This observation straightforwardly shows that the emission of **G16** results from the sensitization of **G16** by **B16** through energy transfer.

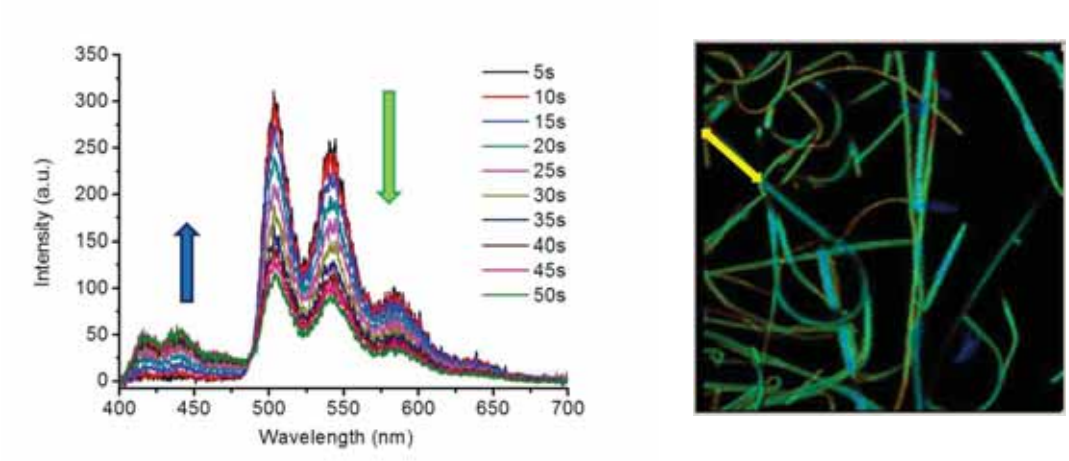

Figure 3.9: (left) Kinetic emission spectra of 1% **G16** doped NBs (power: 30 W/cm^2); (right) t the yellow arrow shows the area which was excited and where the emission was collected, λ_{ex} = 375 nm, λ_{em} >500 nm.

3.2.2.3 Polarization

The anisotropic property of the nanoribbons is revealed by emission polarization studies. In order to characterize the orientations of both donor and acceptor in mixed NBs, the emission of the donor (**B16**, 400~450 nm blue light is collected) is distinguished from emission of the acceptor (**G16**, after 500 nm green light is collected) by using band pass filters and two detectors simultaneously.

For pure **B16** nanoribbons, *P* values varying from -0.40 to +0.60 are observed. Plots of *P vs.* θ for several objects are displayed in Figure 3.10. From the polarization image (Figure 3.10, right) it appears clearly that emission is polarized perpendicularly to the main axis of the object, thus with the same trend as the slowly-grown micro-ribbons (-0.75 to +0.75, chapter 2) but smaller *P* values.

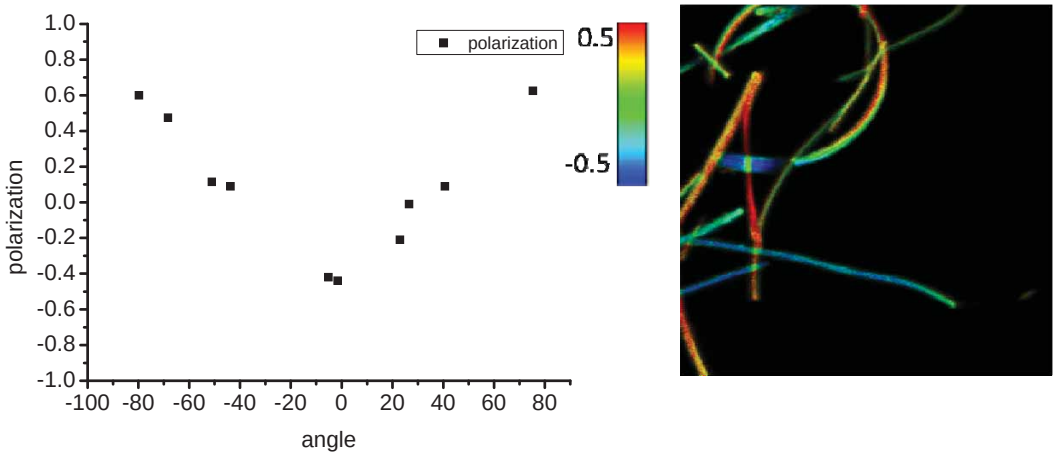

Figure 3.10: Polar plot (left) and Polarization images (30× 30 μm, right) of B16 NBs, λ_{ex} = 375 nm, λ_{em} >405 nm

In 0.5% doped NBs the *P* value of the emission of **B16** (400 nm < λ_{em} < 450 nm) varies from -0.50 to +0.50, in agreement with pure **B16** NBs (Figure 3.11). It confirms that the self-assembly of **B16** inside the NBs is not affected by the presence of **G16**. The green emission from **G16** sensitized by **B16** displays the same values and angular dependence as **B16** (Figure 3.12, λ_{ex} = 375 nm, λ_{em} >500 nm). This indicates that the sensitized **G16** molecules are oriented as the same way as **B16**.

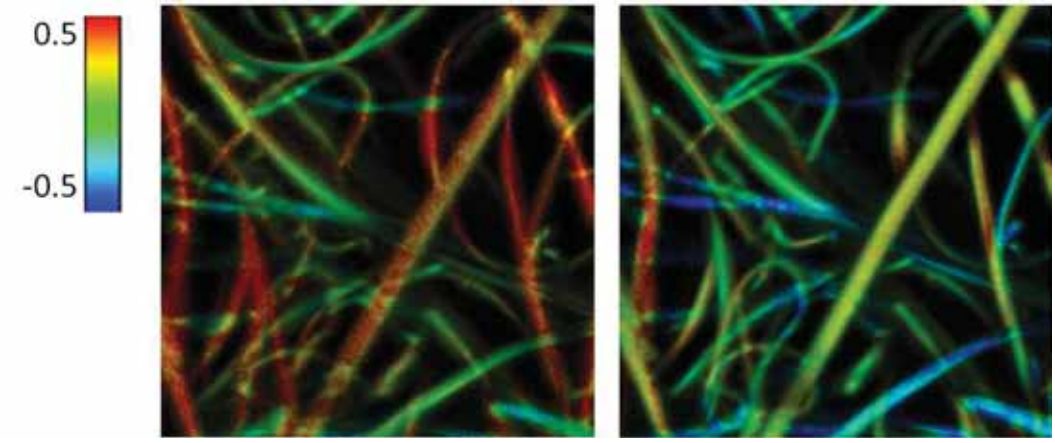

Figure 3.11: Polarization images (30× 30 μm) of 0. 5% doped NBs: λ_{ex} = 375 nm , 400 nm < λ_{em} < 450 nm (left), λ_{em} >500 nm (right). Color code: polarization.

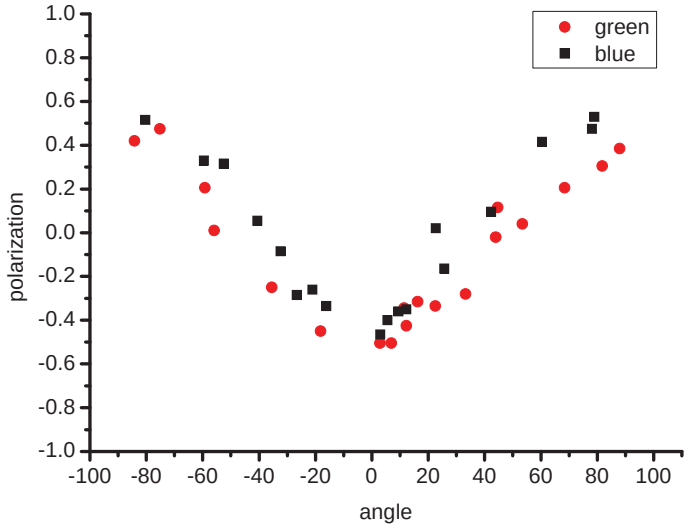

Figure 3.12: Polar plot of 0. 5% doped NBs, λ_{ex} = 375 nm, 400 nm < λ_{em} < 450 nm (black), λ_{em} >500 nm (red).

To gain further insight on the orientation of the acceptors within the nanoribbons, the NBs is excited at 488 nm, a wavelength at which only **G16** can absorb, and measured *P* of the resulting emission (λ_{em} > 500 nm). This is to assure that all the **G16** molecules can be excited, whereas in the previous experiment the sensitization could involve all or only one fraction of the **G16** molecules.

Two cases are examined with 1% and 0.2% **G16**. In 1% doped NBs, the polarization of the emission of **G16** is very similar whether **G16** is excited directly (Figure 3.13), or sensitized by **B16** (Figure 3.14, -0.50≤*P*≤+0.65). The negative *P* values also indicate that an exciton hopping occurs as efficiently when both the sensitized or directly excited **G16** excitons are involved. Furthermore, the equivalence of *P* values and their angle of the emission of **B16** and **G16** in doped NBs clearly suggest that all **G16** molecules are oriented like **B16**. This would occur if **G16** molecules were inserted in the matrix by merely replacing a **B16** molecule.

When **G16** is diluted at 0.2% and excited directly, it emits with a more positive *P* (-0.30≤*P*≤+0.70) and shows larger distribution of angular dependency behavior as compared to the sensitized emission and to the direct excitation in 1% doped NBs.

This suggests that the homo-ET **G16** → **G16** occurs les efficiently under direct excitation of diluted **G16** in 0.2% doped NBs, while in all the other cases **B16-B16** and **G16-G16** homo-ET processes occurs efficiently because of higher concentrations, resulting in more negative *P* values. This ET can be attributed to a Förster-type mechanism which is disfavored in the 0.2% G-NBs due to longer distance between chromophores.

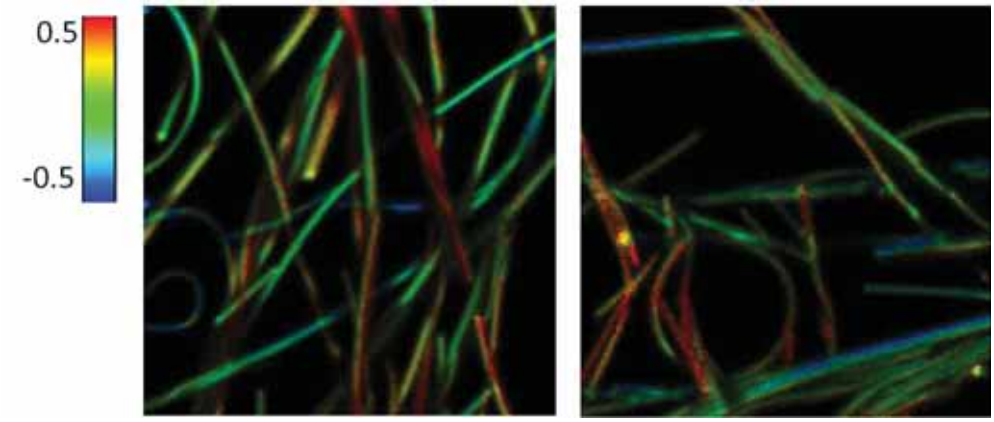

Figure 3.13: Polarization images (30 × 30 μm) of 1% **G**-NBs: λ_{em} >500 nm, λ_{ex} = 375 nm (left), λ_{ex} = 488 nm (right). Color code: polarization

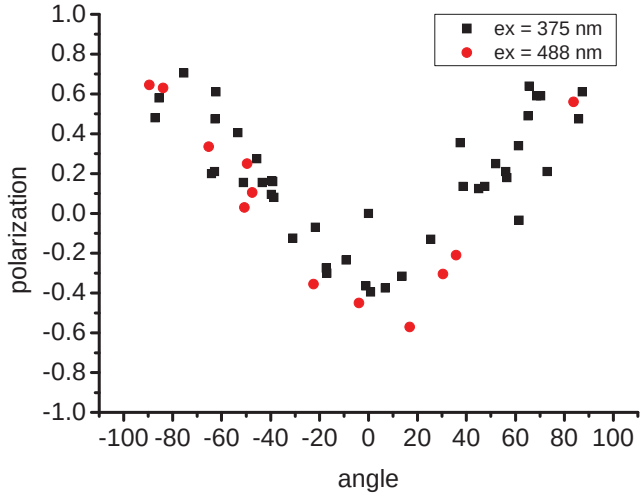

Figure 3.14: Polar plot of 1% **G**-NBs, λ_{em} >500 nm, λ_{ex} = 375 nm (red), λ_{ex} = 488 nm (black)

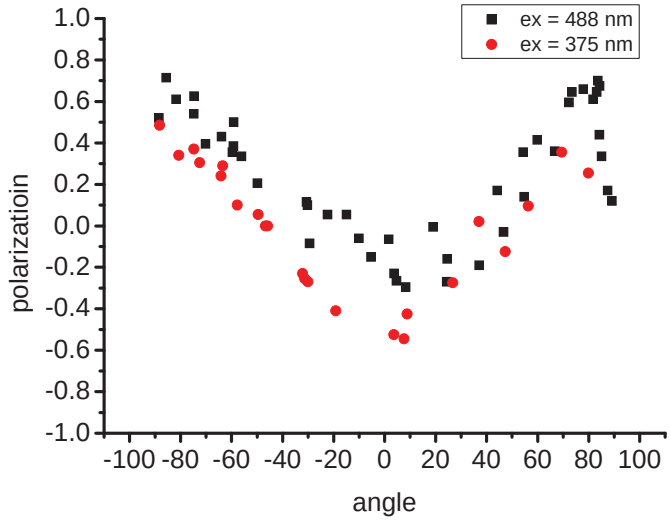

Figure 3.15: Polar plot of 0.2% **G**-NBs, λ_{em} >500 nm, λ_{ex} = 375 nm (red), λ_{ex} = 488 nm (black)

3.2.2.4 Decay Times

The FLIM image of **B16** emission reveals excited state decays on several timescales. In a first approximation, tri-exponential functions have been used to fit the accumulated decays and values of 2.8, 6.2 and 19.0 ns have been obtained. In doped NBs, the decay times of **B16** emission become much shorter than in pure **B16** NBs (Figure 3.16). Figure 3.17 shows that with the addition of **G16**, **B16** emission decay times decrease down to 1.6, 3.8 and 11.8 ns (for 0.5% **G16**-NBs).

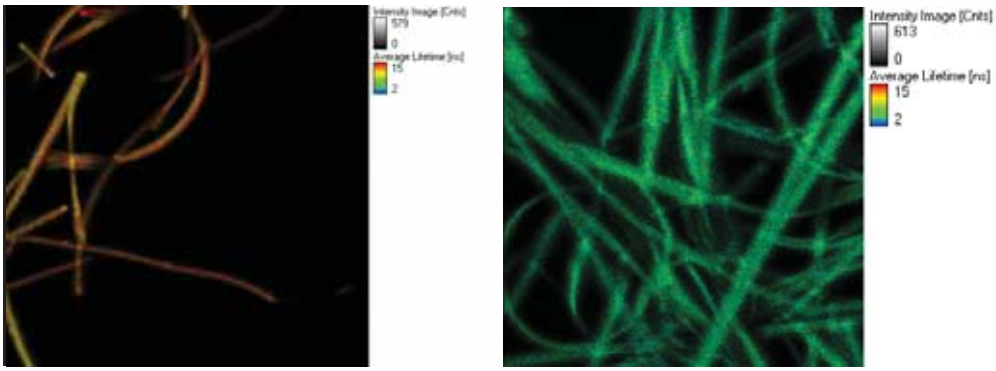

Figure 3.16: FLIM image of **B16** NBs (40 × 40 μm), λ_{ex} = 375 nm, λ_{em}> 405 nm (left); 0.1% **G16**-NBs (30 × 30 μm), λ_{ex} = 375 nm, 400 < λ_{em} < 450 nm (right), color code: average lifetime

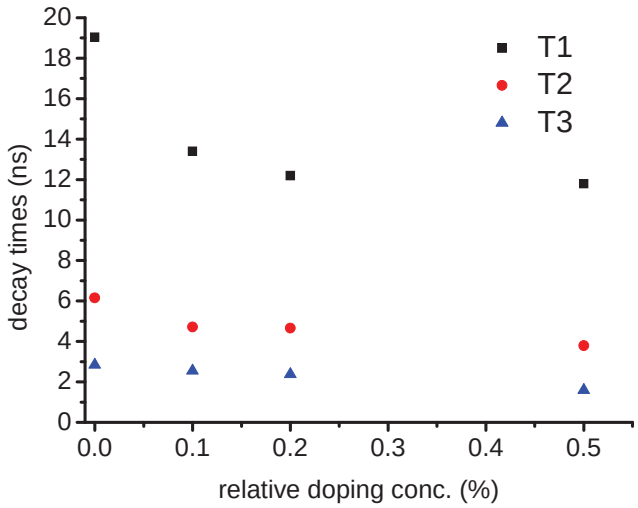

Figure 3.17: Three decay times of **B16** obtained by tri-exponential fitting versus doping concentrations λ_{ex} = 375 nm, 400 < λ_{em} < 450 nm

The emission decay times of **G16** molecules within 1% and 0.2% **G16** doped NBs (Figure 3.18) are also investigated using tri-exponential fittings on each pixel. The results of each image are analyzed according to distributions of decay times (similar to Figure 3.19). In both cases, the fluorescence of **G16** in the NBs rises with time upon selective excitation of **B16** with distribution of τ around weighted mean values of 0.24 ns and 1.76 ns for 1% and 0.2% **G16** doping respectively. For 1% **G16**-NBs, the emission decay of **G16** occurs with the same decay time as when **G16** is directly excited (τ = 20 ns and 38 ns, λ_{ex} = 488 nm, Figure 3.19)

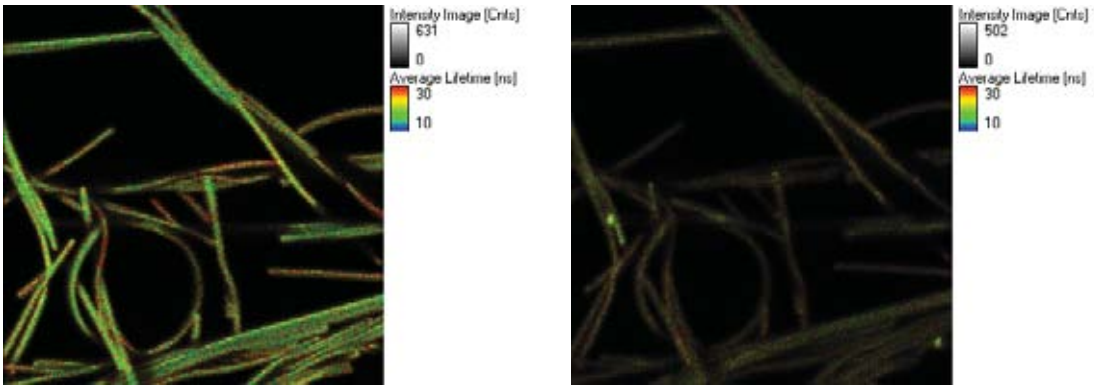

Figure 3.18: FLIM image of 1% **G**-NBs (30 × 30 μm), λ_{em} >500 nm, λ_{ex} = 375 nm (left), λ_{ex} = 488 nm (right), color code: average lifetime (left)

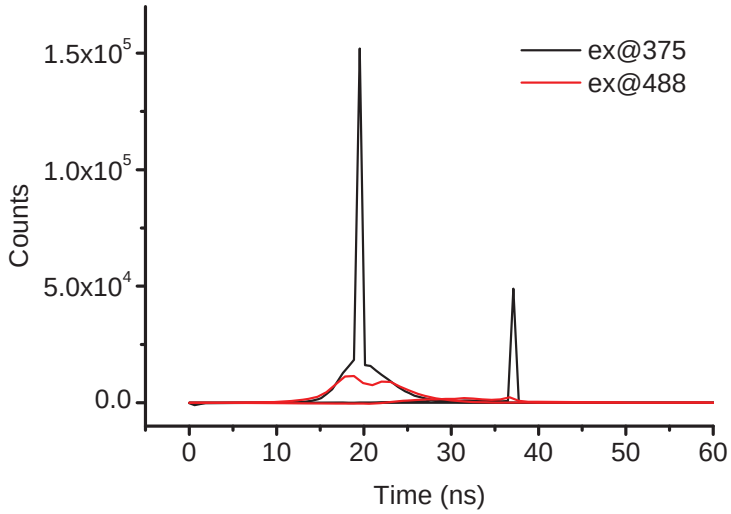

Figure 3.19: Decay times distributions of 0.2% **G**-NBs, λ_{em} >500 nm, λ_{ex} = 375 nm (black), λ_{ex} = 488 nm (red)

In contrast, when **G16** is diluted to 0.2% doping (Figure 3.20), one of the emission decays of **G16** is slower upon sensitization by **B16** then upon direct excitation of **G16** (τ = 53 ns, λ_{ex} = 375 nm; 34ns, λ_{ex} = 488 nm, Figure 3.21).

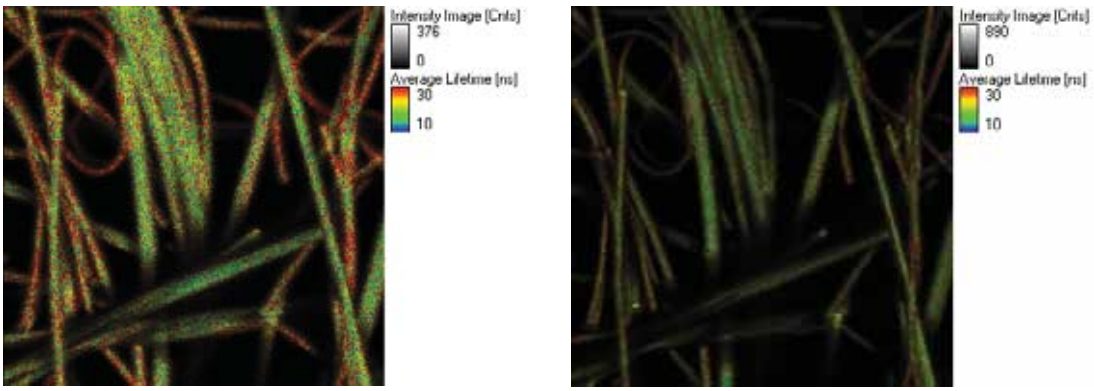

Figure 3.20: FLIM image of 0.2% **G**-NBs (30 × 30 μm), λ_{em} >500 nm, λ_{ex} = 375 nm (left), λ_{ex} = 488 nm (right), color code: average lifetime (left)

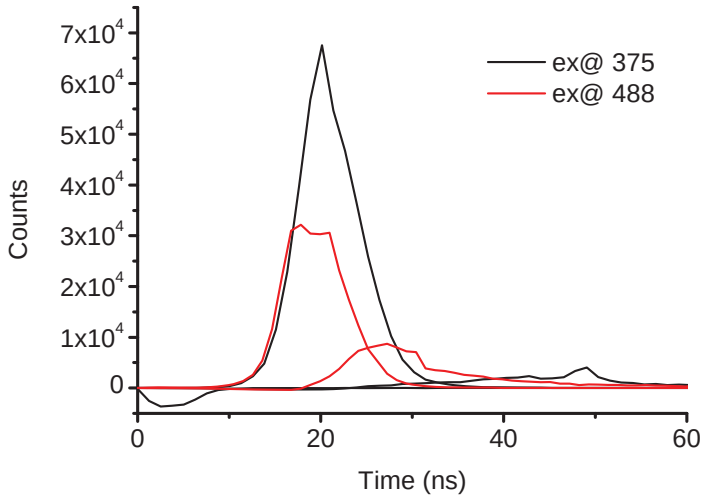

Figure 3.21: Decay times distributions of 0.2% **G**-NBs, λ_{em} >500 nm, λ_{ex} = 375 nm (black), λ_{ex} = 488 nm (red)

This slowest decay component of sensitized emission of **G16** cannot be explained unless a supplementary mechanism is involved. Indeed, the decay time of **G16** is limited by the intrinsic lifetime of the compound, which in solution is k_r^{-1} = 26.3 ns. Burdett and Bardeen reported a delayed fluorescence decay time of 55 ns for tetracene films,[6] which agrees with our experimental data. It is reasonable to attribute this long-lived component to the delayed fluorescence resulting from triplet-triplet annihilation.

Figure 3.22 shows the **G16** emission decay of 1% **G16**-NBs by CFM, which displays a long-lived tail. Recent studies of crystalline rubrene and diphenyl-tetracene films have shown that emission decay tails can be fitted as t^{-2} under certain conditions.[7-9] The dynamic fluorescence behaviour in crystalline rubrene and diphenyl-tetracene films was rationalized by a combination of singlet exciton splitting and triplet-triplet fusion. Indeed, a singlet exciton localized on one tetracene can form two triplet excitons localized on two adjacent tetracenes, which can annihilate at a slower pace and regenerate a singlet.[9-11]

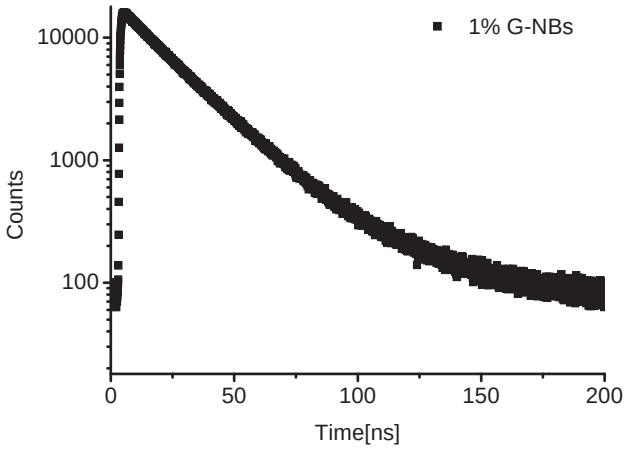

Figure 3.22: Fluorescence decay of **G16** emissions in 1% **G16**-NBs, λ_{ex} = 375 nm, λ_{em} >500 nm

According to Ryasnyanskiy and Biaggio's description of TT annihilation,[12] when $t \ll \tau_T$,

the resulting delayed fluorescence follows the power law $(1 + T_0\gamma t)^{-2}$, where τ_T is the triplet lifetime, T_0 is the initial triplet density, and γ is a bimolecular interaction rate.

The decay has thus been fitted with an exponential component for 10 < t < 50 ns, and since in our case the contribution of first exponential decay is not negligible at t > 50 ns, it is taken into account into our tail fitting. Therefore, the formula utilized to fit the tail (t > 100 ns) is the following:

$$y = A_1 \exp(-t/\tau_1) + A_2(1 + B_1 t)^p + y_0$$

However, due to the facts that the covariance between A_2 and B_1 is very significant and the value of $B_1 t$ is much larger than 1, the formula is then simplified to:

$$y = A_1 \exp(-t/\tau_1) + A_2(t)^p + y_0$$

A1 and τ1 are determined first by the mono-exponential fitting of the decay with 10 < t < 50 ns. In a second fit with 100 < t < 200 ns and fixed values for A1 and t1, the other parameters are fitted freely. However, the background (y0~80 counts) appeared to be overestimated by simply considering the pre-pulse background value. This can be due to a slightly too high laser repetition rate (5 MHz) with respect to the decay length (slightly longer than 200 ns). The value of y0 also influences the value of p obtained by fitting, and therefore we estimated p with a range of fixed values of y0. It results that the p value can vary from − 1.5 < p < −2.5 with the background varying from 40 to 70 counts. The data set y0 > 70 is eliminated due to the too high deviation of fitting residuals (the max. residual of y0 > 70 = 3.68, higher than the reasonable value ±3.0, and yielded a p value up to 4). This range of p values is in agreement with the −2 value that is proposed for the long-lived emission tail resulting from a delayed fluorescence induced by triplet fusion. As shown in Figure 3.x, with y0 = 59 counts and τ1 = 22.1 ns, the data fitting can be achieved with a curve with p = −2.0.

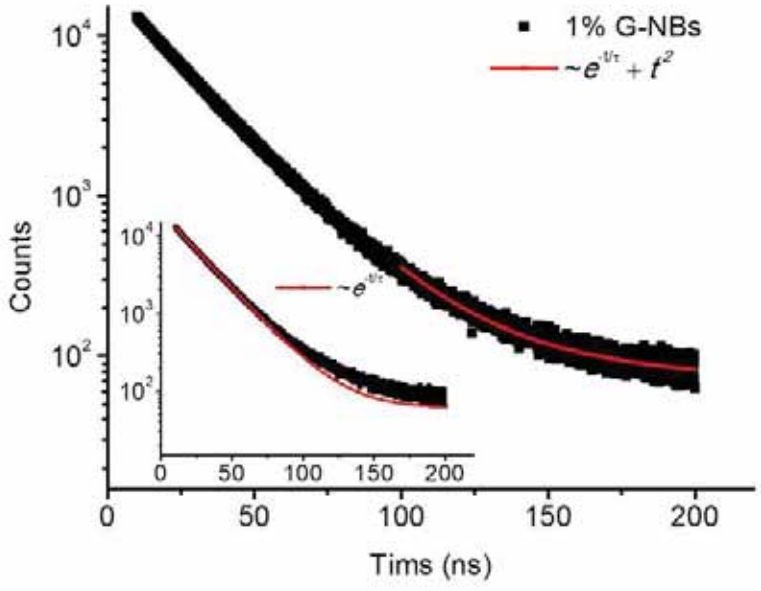

Figure 3.23: G16 Emission decay measured for 1% **G16**-NBs. The red line represents a t^{-2} power law + exponential fit after 100 ns. The inset corresponds to the same data. The red line is the exponential decay exp (-t/τ), with τ ~22 ns (value obtained from a fit from 10 ns ~ 50 ns).

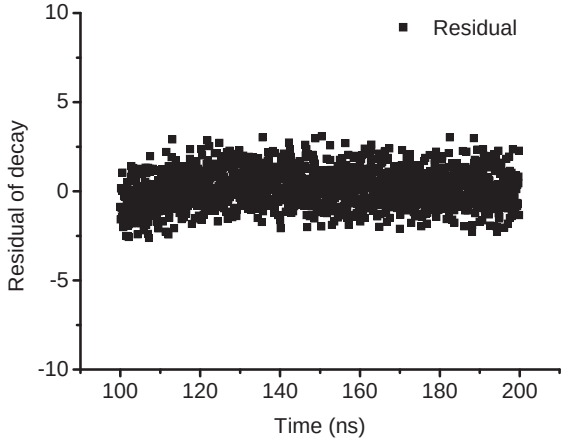

Figure 3.24: The residual of **G16** emission decay fit with power law

To gain further insights about this TT-annihilation phenomenon, the correlation between this slow decay component and the concentration of excited states is investigated.

To increase the triplet excited state concentration, two methods are applied: the increase of the dopant concentration inside the nanoribbons and the increase of the excitation power. The results previously shown already indicated a difference of **G16** longest emission decay time depending on the concentration of dopant (0.2% and 1% doped NBs). Therefore, further investigation is performed in the following section.

3.2.2.5 Concentration effect

The relation between triplet concentration and decay times is investigated in additional blended NBs with 2%, 5%, 10% 15% and 20% **G16**.

Figure 3.25 displays the normalized emission spectra of blended **G16**-NBs. It shows that the **G16** emission band at 502 nm is clearly red-shifted and the ratio of two emission bands changed. It probably results from reabsorption by **G16** of the emission of **G16**, which increases with concentration of **G16**, whereas aggregation of **B16** should have resulted in a shift of all the bands.

The spectra and the decay times of 15% and 20% doped NBs are identical (Figure 3.25, 3.26), suggesting that that the energy transfer within the doped NBs is complete or that at such a high concentration of **G16** the two molecules do not completely blend. Due to this doubt, the 20% blend was not further investigated.

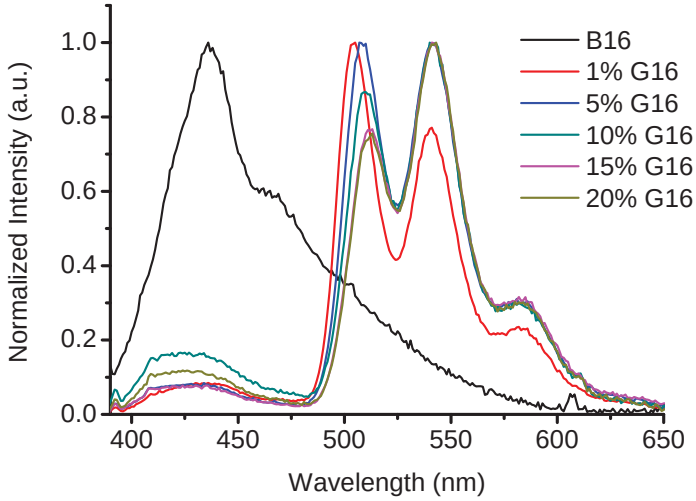

Figure 3.25: Normalized emission spectra of 0%, 1%, 5%, 10%, 15% and 20% blended **G**-NBs; λ_{ex} = 372 nm

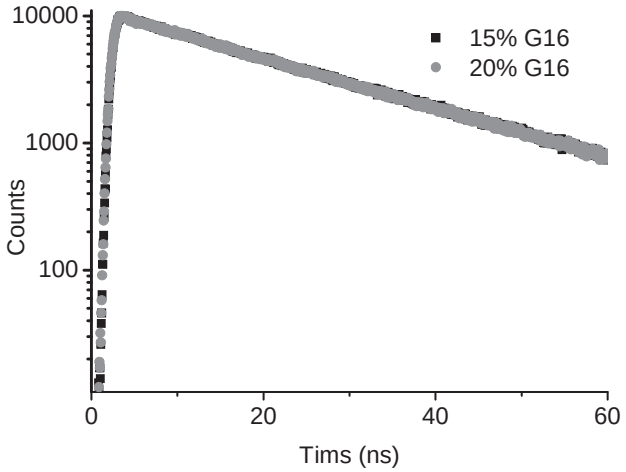

Figure 3.26: Fluorescence decays of 15% (black) and 20% (red) **G16**-NBs; λ_{ex} = 371 nm, λ_{em} = 502 nm. (Further decay is truncated for clarity)

The morphology of blended NBs is influenced by a large amount of doping (>1%). From Figure 3.27 it appears that the population of "big" micro-ribbons with diameters ~ 1μm becomes majority with increasing the [**G16**]. Furthermore, the FLIM images also show that the average lifetime decreases with the increase of **G16** concentration. Detailed analysis of the decay times of **G16** emission is carried out next.

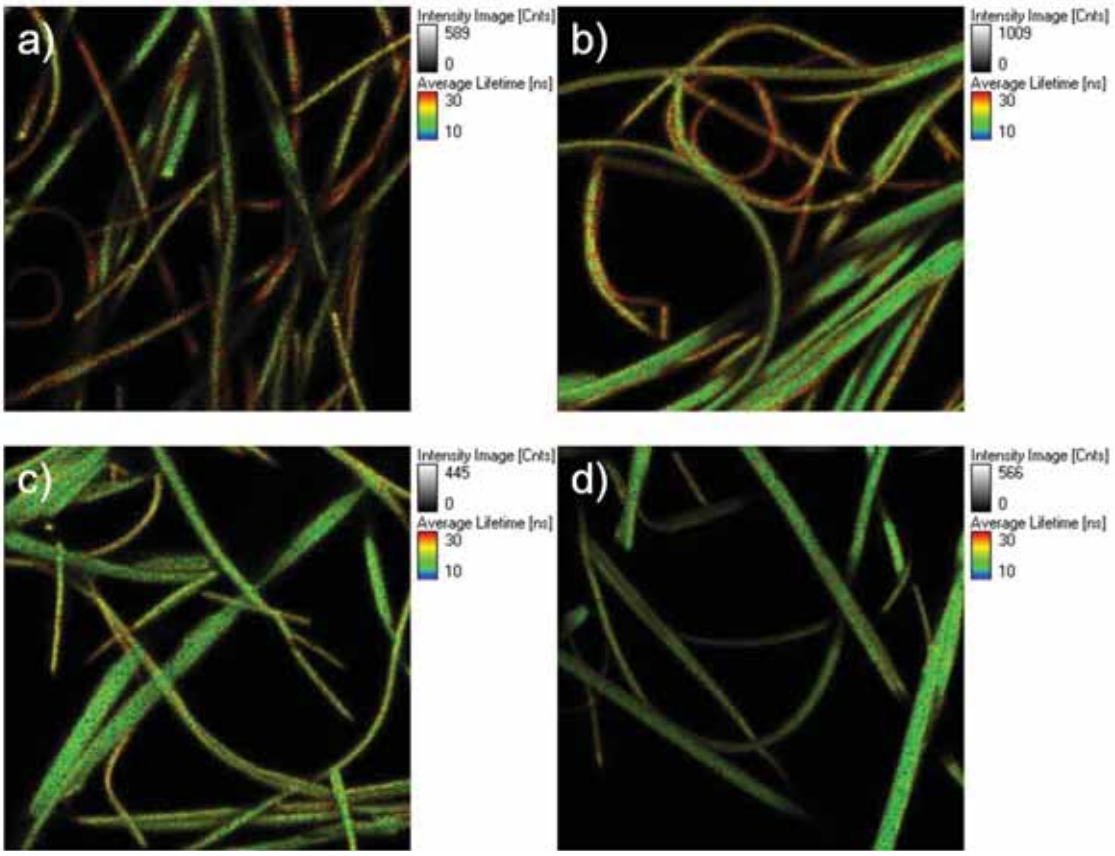

Figure 3.27: FLIM images of 1%, 5%, 10% and 15% doped **G**-NBs (a, b, c, d, respectively, 30 × 30 μm), λ_{ex} = 375 nm, λ_{em} >500 nm, color code: Average lifeitme

Figure 3.28 shows that the rise time of **G16** fluorescence decreases with increasing doping concentration of **G16**, indicating a more efficient energy transfer process with a higher population of **G16** molecules within the nanoribbons.

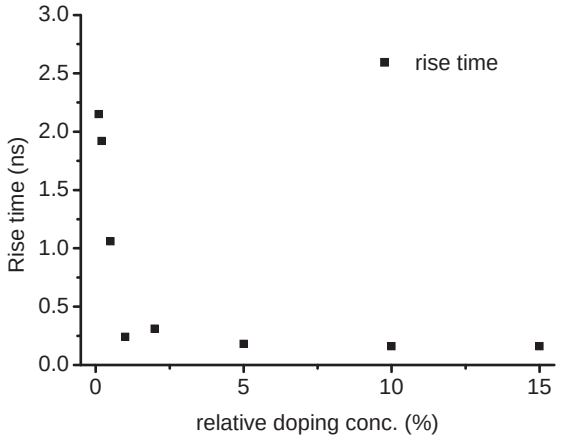

Figure 3.28: Rise times of **G16** emission versus doping concentrations, λ_{ex} = 375 nm, λ_{em} >500 nm

The decays have been approximated with a tri-exponential function in order to carry out the same type of analyses both on decays obtained by accumulation of fluorescence on a sample area, and for FLIM with fittings performed on each pixel (in FLIM, exponential fittings are the only option). The decay time of 20 ns (T2) slightly decreased with [**G16**] from

0.1% to 10%, but not for the 15% sample. In addition, the slowest decay time (T1) evidently decreases with the increase of **G16** concentration, and the corresponding pre-exponential factor (A1) increases (Figure 3.29). Considering that almost all excited states of **B16** are rapidly quenched with such high concentrations of **G16**, the excited state properties must result exclusively from singlet or triplet **G16** excited states. The acceleration of the decay process can reasonably be expected for a biexcitonic **G16-G16** annihilation process, since it would be favored by a higher concentration of **G16** triplet states. Moreover, the increase of the proportions of delayed fluorescence would also be related to the increase of the concentration of **G16** triplet excitons.

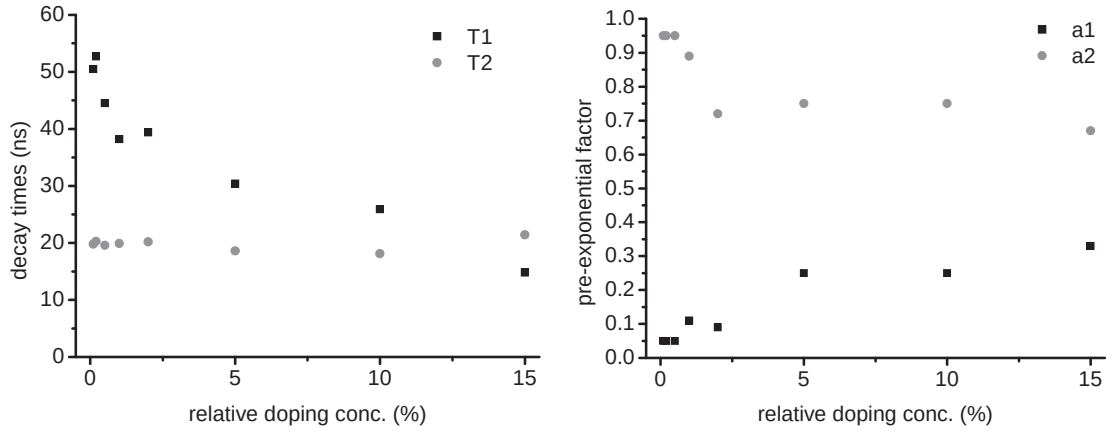

Figure 3.29: decay times (left) and corresponding pre-exponential factor (right) of **G16** emission versus doping concentrations, λ_{ex} = 375 nm, λ_{em} >500 nm

3.2.2.6 Excitation power effect

The second method that was used to analyze the effect of the concentration of excitons in NBs was to perform the decay times measurement with increasing incident excitation power, 1% **G16** doped nanoribbons were thus studied under CFM. During acquisition, a continuous light N_2 gas flow is applied to reduce the photo-bleaching resulting from the use of higher than usual laser power. Under our experimental conditions, the photo-bleaching effect was verified and less than 5% with the largest incident power density applied. The absence of oxygen due to continuous N_2 blowing also results in a 10% increase of the decay times under the excitation power (~30 W/cm^2) used in air.

The incident laser power was measured by a power meter positioned just before the objective lens, and the resulting power density was calculated as an average power per square centimeter. Decay times are obtained by fitting FLIM images with a tri-exponential function on the accumulated decays. Figure 3.30 shows that the slowest decay component (T1) decreases with the increase of excitation power density, whereas the corresponding pre-exponential factor increases. Thus, the same trend is observed as in the case of an increase of the dopant concentration, supporting the attribution of the longest decay to a biexcitonic process. In addition, these experiments show that T2 decreases slightly with incident power density. This could be attributed to the appearance of singlet-singlet annihilation processes or

other biexcitonic mechanism at high power densities. Such processes could also explain the decrease of T1, whereas the increase of A1 with increasing power density indicates the correlation between the long process and the exciton density.

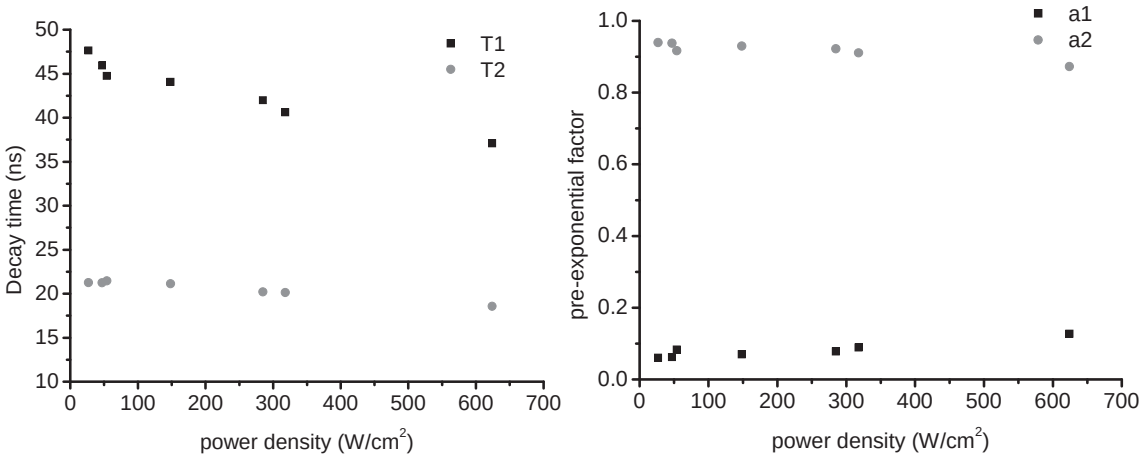

Figure 3.30: decay times (left) and corresponding pre-exponential factor (right) of **G16** emission versus incident power density, λ_{ex} = 375 nm, λ_{em} >500 nm

3.2.2.7 Size effect

The detailed analyses of the FLIM data of **G16** doped NBs was performed with some iterations. The FLIM image (Figure 3.31) reveals that the average lifetime is longer in thinner nanoribbons. In order to verify the origin of this long average lifetime, the tail of the time-resolved fluorescence of each pixel of the image is fitted with a bi-exponential function without rise time (tail-fitting is started after the complete rise of fluorescence). To increase the contrast of the image, the fraction of the slowest component is displayed using the ratio of the normalized pre-exponential factors a1/(a1+a2) (Figure 3.32). When calculating this image, in order to compensate for the weak photon count at each pixel, not only the pixels are binned (from 1×1 to 2×2), but also the fitting parameters were varied in a narrow value fork. The upper and lower limits for the decay time values were optimized *a posteriori* after analysing the decay fittings described below, and were set to the values of the decay times of thin and wide ribbons, respectively (e.g. 44 and 48 ns for T1).

Figure 3.32 clearly demonstrates that the thinner ribbons have a higher contribution of the delayed fluorescence component (color code: red, high fraction), and the FWHM of these red ribbons lies in a range of 500-700 nm (intensity fitted with Gaussian Amplitude function, Figure 3.32, right a). In contrast, less delayed fluorescence (color code: blue, low fraction) occurs in the wider ribbons that have a FWHM of about 900-1200 nm (Figure 3.31, right b).

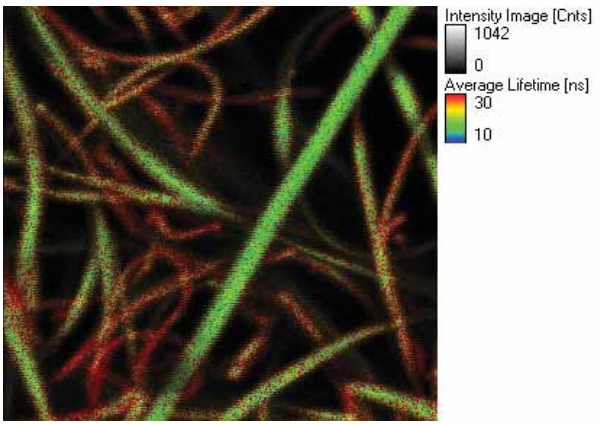

Figure 3.31: FLIM image of 0.5% **G16** doped NBs (30 × 30 μm), λ_{ex} = 375 nm , λ_{em} >500 nm

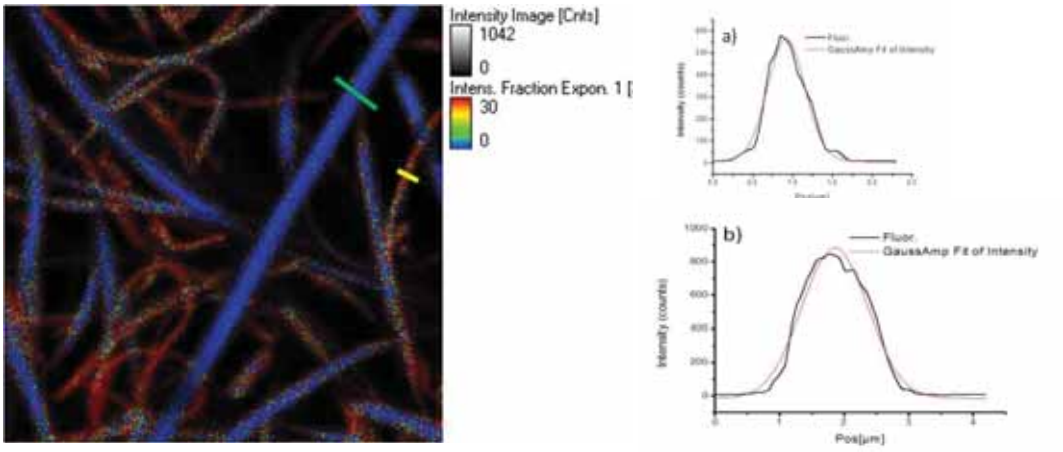

Figure 3.32: FLIM image of 0.5% **G16** doped NBs (30 × 30 μm), Color-code: fraction of the slowest decay (blue < 5%, red > 15%), λ_{ex} = 375 nm , λ_{em} >500 nm (left); a) Intensity of the thin NB (yellow mark), b) Intensity of the big NB (green mark)

As a result of this observation, the previously described FLIM images were re-processed. The nanoribbons are separated into two groups according to their diameter measured in the FLIM images: type A NBs have a width <0.8 μm and type B > 0.8 μm. For each images obtained at different dopant concentration and incident power, the cumulated decays of type A and B ribbons were analyzed separately.

Figure 3.33 shows that both A and B ribbons emission decay with a similar, [**G16**]-independent T2 decay time (Figure 3.30). The decay time of the delayed fluorescence (T1) is slower in thin (type A) than in wider type B NBs, especially at low doping concentrations ([**G16**] < 5%, Figure 34). However, with the increase of [**G16**] the decay time difference between A and B decreases, when [**G16**] reaches 15%, T1 of B NBs is even slower than the T1 of A. This trend can also be seen in the corresponding pre-exponential factor (A1). A1 of A is slightly higher than A1 of B, whereas this is clearly inverted for [**G16**] = 15%. This shows that at low doping ([**G16**]<5%), more triplet states are present in thinner NBs (width< 0.8 μm) and that the triplet fusion is slower than in wider NBs. This trend is inverted when [**G16**] reaches 15%.

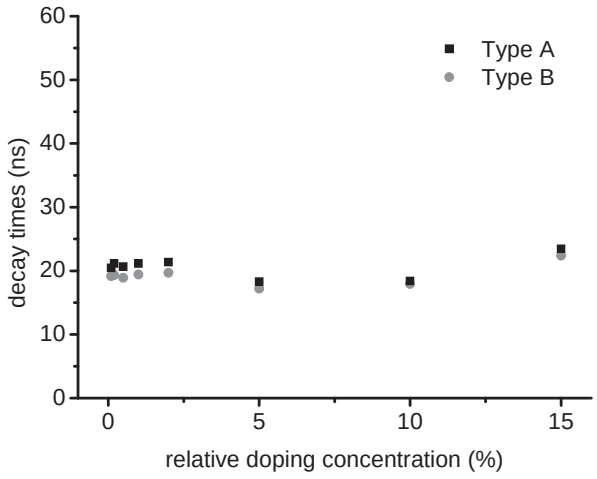

Figure 3.33: decay time of **G16** emission versus doping concentrations, λ_{ex} = 375 nm, λ_{em} >500 nm

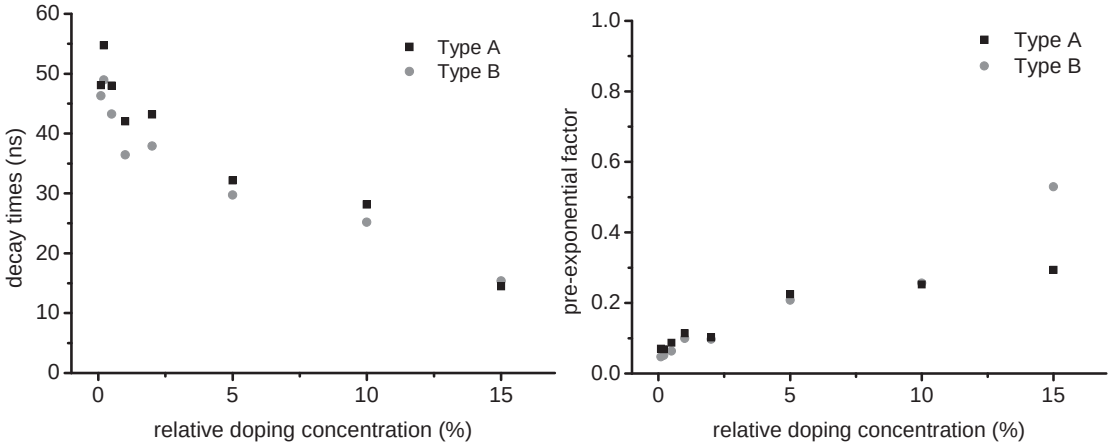

Figure 3.34: The slowest decay times (T1, left) and corresponding pre-exponential factor (right) of **G16** emission of nanoribbons versus doping concentrations, λ_{ex} = 375 nm, λ_{em} >500 nm

The same analysis is applied on the decays of **G16** emission at variable incident power density. Figure 3.35 shows that T2 only slightly decreases with the excitation power, but in the same way in both cases A and B. The slowest decay time T1 of both A and B display a similar trend, *i.e.* a decrease with increasing incident power (Figure 3.36, left). In most cases, the pre-exponential factor of T1 (A1) is larger in type B than in type A NBs, but this is inverted at the largest excitation power used (~620 W/cm^2) (Figure 3.36, right). In both cases studied, the highest concentration of triplet **G16**'s induces thus an inversion of the behaviour observed at the lowest doping and power.

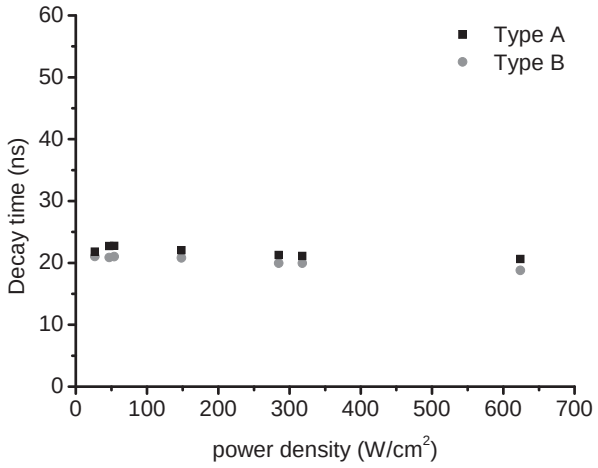

Figure 3.35: The second slow decay time (T2) of **G16** emission versus incident power density, λ_{ex} = 375 nm, λ_{em} >500 nm

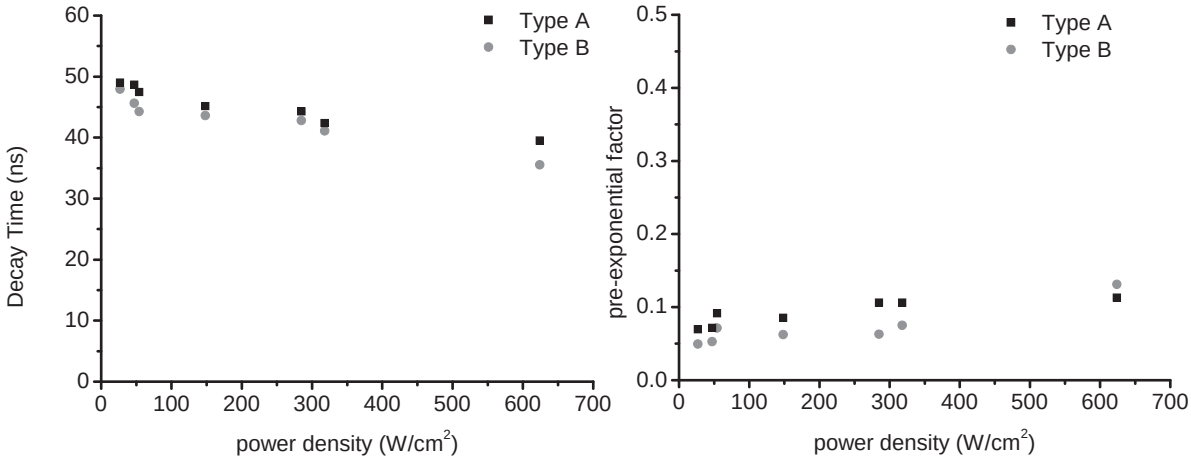

Figure 3.36: The slowest decay times (T1, left) and corresponding pre-exponential factor (A1, right) of **G16** emission of nanoribbons versus incident power density, λ_{ex} = 375 nm, λ_{em} >500 nm

3.2.2.8 Discussion

1. Energy transfer :

As a dopant, **G16** displays a very homogeneous dispersion and highly ordered molecular packing with other **B16** molecules inside the **B16** NBs. The polarization study indicates that tetracene incorporation occurs by "replacing" a **B16** molecule in the native structure. This incorporation and dispersion of the acceptors in the donor matrix is favored by structural and chemical similarity such as compatible chain length between **G16** and **B16**, and that these aspects are fundamental to achieve efficient energy transfer.[13]

From the quantum yield of **B16** NBs and **G16** inside the NBs, we calculated the percentage of quenched **B16** molecules transferring their energy to **G16** (η_{ET}). For instance in 1% G-NBs, 49% of quenched **B16** sensitize **G16** molecules. This is very high compared to **DDOA-DHOT** gel system published previously (η_{ET} =54%)[13] in which the energy transfer overlap integral J_{AT} is 1.8 times larger than in the nanoribbons J_{BG} (J_{AT} =2.3×10^{14} M^{-1}cm^{-1};

J_{BG} = 1.28×10^{14} M^{-1}cm^{-1}).

From the point of view of quenching efficiency η_Q, it reveals that about 250 molecules of **B16** are quenched by a single **G16** molecule at lower doping concentration (Table 3.2, 0.1% **G16** doped NBs). This high number results not only from direct energy transfer from the closest donors, but also suggests involvement of exciton migration.[13]

The exciton diffusion length of 9,10-diphenyl anthracene is 5.5 nm in polystyrene film,[14] with a critical Föster radius R_0 = 2.34 nm.

Indeed, at a distance of R_0 = 2.86 nm between **B16** and **G16**, the energy transfer efficiency is 50%. R_0 is defined as:

$$R_0 = 0.0211\left(n^{-4}\kappa^2\Phi_D J(\lambda)\right)^{1/6}$$

Where Φ_D is the donor fluorescence quantum yield, κ^2 is the orientation factor, and n is the refractive index. The R_0 value has been obtained assuming κ^2 = 1 (fluorescence polarization microscopy suggests that a **G16** molecule takes the place of a **B16** molecule in G-NBs.[2]

This value for the nanoribbons of **B16** is calculated based on the crystal structure of DPA derivatives in chapter 2, in which it is observed that the emission dipoles, along the diphenyl axis of the molecule, are almost parallel to each other, J_{BG} = 1.28×10^{14} M^{-1}cm^{-1}, and the refractive index of diphenyl anthracene for doped NBs is estimated at 1.698.[15]

In the polarization section, the presence of **G16-G16** homo-energy transfer process is proposed. To verify this suggestion, we calculated the energy transfer overlap integral J_{GG} = 7.09×10^{13} M^{-1}cm^{-1}, giving a critical Föster radius R_0 = 2.95, 3.71 nm (κ^2= 1, 4, respectively). (Φ_D is 87% measured by specifically exciting **G16** molecules in 1% G-NBs with an integrating sphere). The next step is to estimate the average distance between **G16** molecules in G-NBs. The crystal structure data of **B8** is taken to approximate the distances in **B16**. For 1% doped G-NBs, we assumed one **G16** is located at the center of 99 **B16** molecules which fill about 88.2 nm^3, resulting in a sphere with the radius about 2.76 nm. It suggests that the nearest distance of two **G16** molecules would be at least 5.52 nm in a perfectly homogeneous dispersion matrix, which is much larger than the critical Föster radius R_0 (2.95 and 3.71 nm). Under this condition, the **G16-G16** energy transfer efficiency is calculated by the following equation: $E = 1/[1 + (r/R_0)^6]$, which is about 2% and 8% (R_0 = 2.95 and 3.71 nm, respectively). However, we still can observe this homo-ET process in 1% G-NBs (see polarization data), suggesting that the dispersion of **G16** may not be perfectly homogeneous.

2. Delayed fluorescence :

The TCSPC measurements and FLIM analysis by CFM reveal the presence of delayed fluorescence of **G16** emission. The power law fitting of this tail of emission decay suggested this component is due to the delayed emission from singlet states that have been formed through triplet-triplet fusion.[12]

The origin of **G16** triplet excited states can be attributed to several processes: intersystem conversion (ISC) from **G16** singlet state, energy transfer from **B16** triplet states or singlet fission of **G16**.

By increasing the doping amount of **G16** in NBs and the excitation power density, we create more **G16** excited states that favor triplet-triplet annihilation or even singlet-singlet annihilation[16] in the system.

In both experiments the relative amplitude of the delayed fluorescence (presented as the pre-exponential factor of the longer decay time) is demonstrated to be positively correlated to both [**G16**] and incident power density. These facts indicates that when the population of ***G16** increases, the contribution of delayed fluorescence also increases, suggesting the bi-excitonic origin of the process. In agreement, the increase of triplet states population accelerates the annihilation process and thus the kinetics of delayed fluorescence.

The detailed analysis of the correlation of the nanoribbons size and the decay times reveals that at low doping condition ([**G16**] < 5%), nanoribbons with diameter < 0.8 μm end to have a larger contribution of delayed fluorescence, which indicates a larger population of triplets. However, the kinetics of the annihilation is slower than in bigger NBs. This indicates that one or several properties that distinguish wide and thin ribbons influences differently the triplet formation and triplet fusion processes. Wider fibers are more intensely emissive, thus probably also thicker, and thus have a smaller surface to volume ratio. Moreover, images reveal that wider fibers are straight, while thinner fibers are more bended. This could be related to a larger crystallinity of the larger ribbons, and maybe the presence of more defects in the smaller ribbons. These results thus suggest that triplet state formation is favored due to less crystallinity and/or more defects and/or rather at the surface of the ribbon. In addition, the triplet fusion is accelerated in ribbons with opposite properties, thus higher crystallinity and/or less defects and/or rather in the core of the ribbon. It is assumed that no diffusion of the molecules occurs.

When **[G16]** > 5%, tetracene aggregation and partial demixing of **B16** and **G16** can be expected. This had been previously observed in **DDOA** organogels blended with high proportions of the tetracene **DDOT**. At 15% [**G16**], we observed a much higher population of triplet states, but also accelerated kinetics of triplet fusion and probably some singlet-singlet annihilation. The inversion of the behaviour of thin and wide ribbons is however difficult to interpret and requires a more detailed analysis. It could be of interest indeed to pursue a close investigation on the origin of the high population of triplet states.

To further analyze the contribution of triplet-triplet annihilation mechanism on the fluorescence decay times, we assume that the excited state behavior of **G16** in 1% doped G-NBs can be described by the following kinetics and differential equations:

$$\frac{dS^*}{dt} = -(k_{\mathrm{r}} + k_{\mathrm{ic}} + k_{\mathrm{isc}} + k_{\mathrm{sf}} + k_{\mathrm{ss}})S^* + k_{\mathrm{TS}}\mathrm{T}^{*2}$$

$$\frac{dT^*}{dt} = -k_{\mathrm{T}}\mathrm{T}^* - k_{\mathrm{TS}}\mathrm{T}^{*2} - k_{\mathrm{TT}}\mathrm{T}^{*2} + (k_{\mathrm{isc}} + 2k_{\mathrm{sf}})S^*$$

Where k_{r} is the radiative decay rate, k_{ic} is the internal conversion rate, k_{isc} is the

intersystem crossing rate, k_{sf} is the singlet fission rate, k_{ss} is the singlet-singlet annihilation rate, k_T is the triplet decay rate for an isolated triplet, k_{TS} and k_{TT} are the triplet-triplet annihilation rates to generate a singlet excited state (k_{TS}) or not (k_{TT}).

To model our experimental data, these two equations are numerically solved in Matlab software to yield the singlet and triplet populations as a function of time with several approximations: 1. The triplet lifetime of tetracene in solution is several hundred μs and can be neglected here[17] (the time range of **G16** emission decay t is 200 ns, $t \ll \tau_T$); 2. Since **G16** molecules are doped into the **B16** matrix with concentration only 1% and a high quantum yield, the probability of singlet-singlet annihilation should also be negligible (see also discussion above); 3. It is assumed that all the triplet excited states are generated from singlet excited states via intersystem crossing or singlet fission; 4. The studies of the polarization of the emission of **G16** described previously in this chapter have suggested that the **G16** molecules which are sensitized by **B16** are identical to those excited directly. Considering also that no spectral change is observed whether sensitizing **G16** or directly exciting the dopant, we assume that the radiative constant of **G16** does not change in the NBs ($k_r = 3.8\times10^7$ s^{-1}); 5. The sensitization of **G16** by **B16** occurs fast and mostly from the singlet, thus without considering sensitization by **B16** triplets. With these approximations, several models are proposed to fit the experimental data.

Model 1: As mentioned previously, the ~20 ns decay of **G16** emission in NBs can be due to the rigidity of the micro-environment, which leads to a very small k_{ic} and hence the longer decay time (~20 ns) than that in solution (13.8 ns). To verify this plausible effect, we adapt $k_{ic} = 0$, $k_r = 3.8\times10^7$ s^{-1}, $k_{isc} = 1.1\times10^7$ s^{-1},[8] $k_{TS} = 4.6\times10^{-11}$ cm^{-3} s^{-1},[8] $k_{TT} = 9.0\times10^{-11}$ cm^{-3} s^{-1}.[8] The triplet related rate constants k_{isc}, k_{TS}, k_{TT} and taken from the literature of 5,12-diphenyltetracene,[8] but it should be noted that the alkoxy chain substituents of **G16** would alter the energy level of HOMO, LUMO and thus some of these constants.

As shown in Figure 3.37, the generated curve fits the experimental data well, suggesting a good chance for the occurrence of this mechanism. This model will be further examined later together with other models.

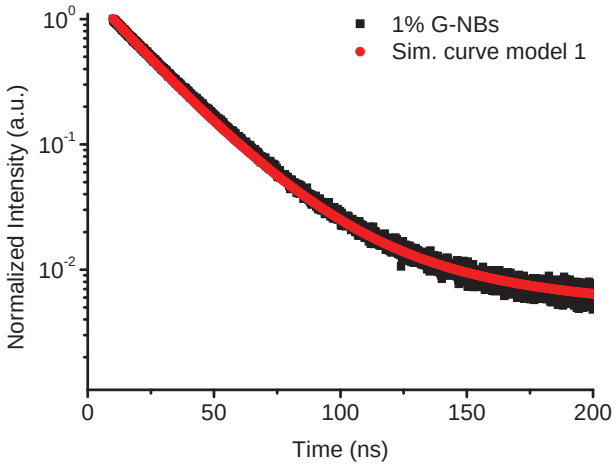

Figure 3.37: Experimental data of **G16** emission decay (black, λ_{ex} = 375 nm, λ_{em} >500 nm) and the simulated fluorescence decays of **G16** generated by the kinetic model 1 (red).

One thing that should be noticed is that the presence of T-T annihilation process not only influences the long-lived emission tail, but also contributes to lengthen the first decay component (Figure 3.38), thus resulting in an apparent decay time in NBs (21.6 ns, measured by specific excitation of **G16** molecules of 1% G-NBs in the bulk) which is much longer than in solution (13.8 ns). It can also explain why this ~20 ns decay times T2 shows a dependency on power density and concentration of **G16**.

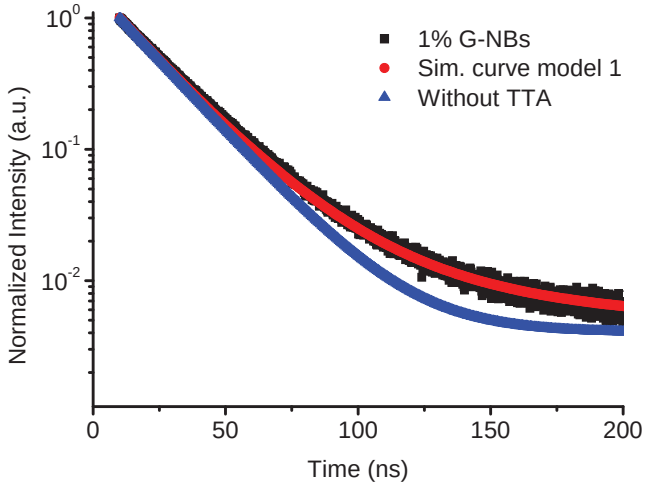

Figure 3.38: Experimental data of **G16** emission decay (black, λ_{ex} = 375 nm, λ_{em} >500 nm) and the simulated fluorescence decays of **G16** generated by the kinetic model 1 with (red) and without TT- annihilation process (blue).

Model 2: Besides k_r does not change, we assume the singlet excited state decay time ($k_{fl} = k_r + k_{ic} + k_{isc}$) of **G16** in 1% G-NBs is also the same as that in solution (k_{fl} =13.8 ns^{-1}). Which means if k_{ic} decreases, k_{isc} has to be increased to keep k_{fl} as a constant. Instead of taking the value of biexcitonic parameters from literature, k_{TS} and k_{TT} are determined by numerically solving the systems for various values to fit the experimental

data. The parameters applied here $k_r = 3.8\times10^7\ s^{-1}$, $k_{ic} = 0$, $k_{isc} = 3.4\times10^7\ s^{-1}$, and the value obtained for triplet dynamics are $k_{TS} = k_{TT} = 2.0\times10^{-10}\ cm^{-3}\ s^{-1}$. Literature values for these two parameters vary by at least an order of magnitude,[6,8] and our values l lie within these ranges.

Figure 3.39 shows the simulated curve generated from this model can also fit the experimental data.

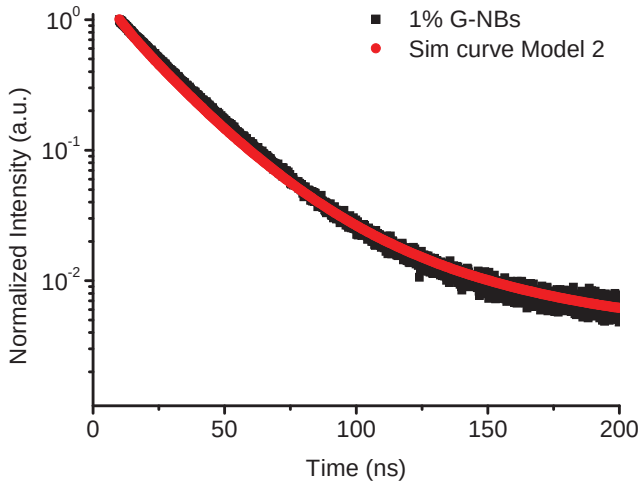

Figure 3.39: Experimental data of **G16** emission decay (black, λ_{ex} = 375 nm, λ_{em} >500 nm) and the simulated fluorescence decays of **G16** generated by the kinetic model 2 (red).

Model 3: In this model, most of the assumptions are the same as model 2 (k_{fl} =13.8 ns^{-1} and is kept as a constant; $k_r = 3.8\times10^7\ s^{-1}$ and it does not change; k_{TS} and k_{TT} are determined by data fit). However, we introduce the singlet fission process into this model, giving $k_{fl} = k_r + k_{ic} + k_{isc} + k_{sf}$. The data are fit with fixed parameters $k_r = 3.8\times10^7\ s^{-1}$, $k_{isc} = 1.1\times10^7\ s^{-1}$.[8] k_{ic} and k_{sf} are also determined by numerically solving the system, the decrease of k_{ic} leads to the increase of k_{sf}. The values obtained are $k_{ic} = 9.1\times10^6\ s^{-1}$, $k_{sf} = 1.4\times10^7\ s^{-1}$, $k_{TS} = 1.0\times10^{-10}\ cm^{-3}\ s^{-1}$ and $k_{TT} = 1.5\times10^{-10}\ cm^{-3}\ s^{-1}$. As shown in figure 3.40, the experimental data can be fit by the generated curve of model 3 with acceptable quality, indicating the presence of singlet fission process cannot be easily ruled out.

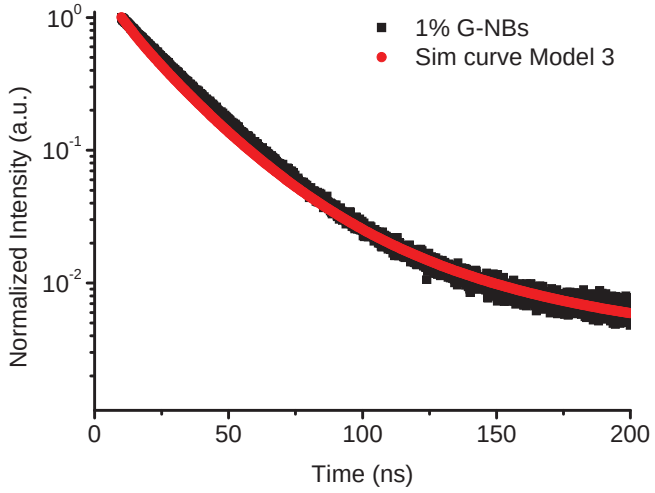

Figure 3.40: Experimental data of **G16** emission decay (black, λ_{ex} = 375 nm, λ_{em} >500 nm) and the simulated fluorescence decays of **G16** generated by the kinetic model 3 (red).

Model 4: The k_{sf} term is also introduced in this model. Instead of keeping k_{fl} as a constant, we assume that k_r, k_{isc} and k_{ic} are the same as in solution and do not change when k_{sf} is introduced. The data are fit with fixed parameters $k_r = 3.8\times10^7\ s^{-1}$, $k_{isc} = 1.1\times10^7\ s^{-1}$,[8] $k_{ic} = 2.3\times10^7\ s^{-1}$, $k_{TS} = 5.0\times10^{-10}\ cm^{-3}\ s^{-1}$,[6] $k_{TT} = 2.0\times10^{-10}\ cm^{-3}\ s^{-1}$.[6] k_{sf} is determined by numerically solving the system. The values obtained are $k_{sf} = 1.4\times10^7\ s^{-1}$.

Figure 3.41 shows the simulated curve generated from this model agrees the experimental data.

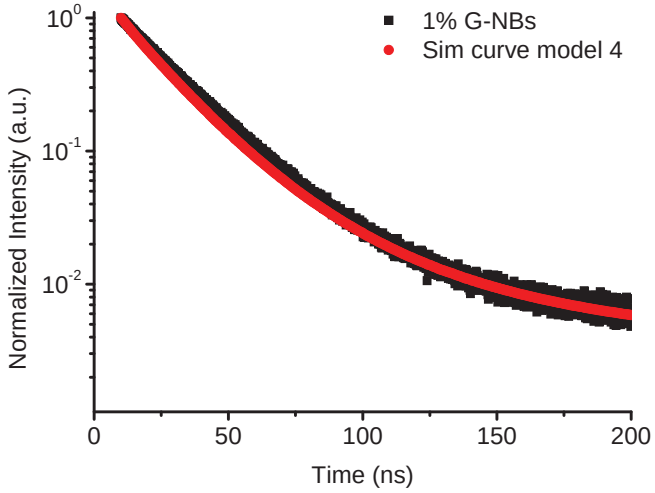

Figure 3.41: Experimental data of **G16** emission decay (black, λ_{ex} = 375 nm, λ_{em} >500 nm) and the simulated fluorescence decays of **G16** generated by the kinetic model 4 (red).

In order to examine these three models, we simulated the excitation power effect using the conditions mentioned above respectively and compared with the experimental data. To simplify the condition, we assume only the excited state density will vary with excitation

power and neglect other possible effects such as the presence of singlet-singlet annihilation or the possible variation in the biexcitonic parameters.

Figure 3.42 shows the initial intensity of **G16** emission (S_0) in 1% G-NBs at different excitation power density recorded with CFM, it appears linear when the power density under 300 W/cm^2. Therefore, we take the data of power density within this range to process the simulation.

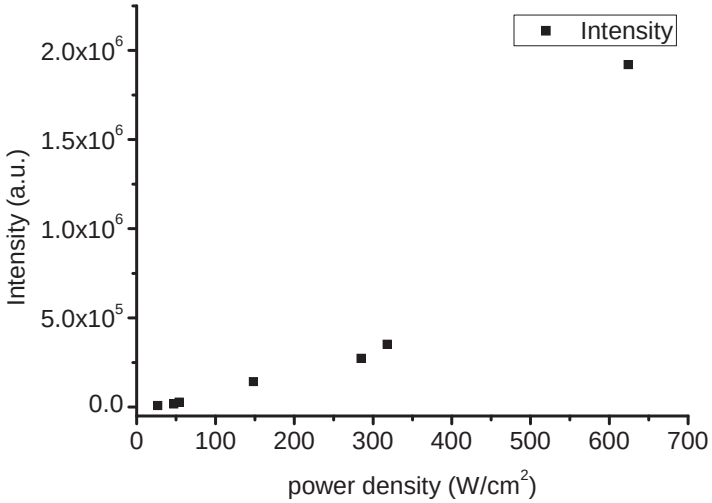

Figure 3.42: Initial intensity versus excitation power density, λ_{ex} = 375 nm, λ_{em} >500 nm

The decay profiles shown in Figure 3.43 displays an acceleration of the whole decay especially in the tail after 100 ns with increase of excitation density. Compared with the experimental data, the simulated decays of model 1 (Figure 3.44a) shows no change before 100 ns and only little difference between 150 and 300 W/cm^2; whereas model 2, 3 and 4 show the acceleration of whole decay with the increase of excitation power density from 30 W/cm^2 to 150 W/cm^2. However, model 2 and 3 shows a small difference of decays between 150 and 300 W/cm^2 (Figure 3.44b, c). Model 4 qualitatively reproduces the best the acceleration trend of the experimental data (Figure 3.44d), suggesting this kinetic scheme might be the most adated to illustrate the **G16** excited state behaviour in 1% G-NBs.

The reason of none of our models can quantitatively reproduce the experimental data can be attributed to several aspects. The most important one is the presence of heterogeneity, defects and other complications in our system. It makes our models insufficient to describe the full photophysical behavior of the **G16** in nanoribbons due to its neglect of defects and trapping sites. However, with this simulation exercise we demonstrated that the assumption that only the decrease of k_{ic} resulting the apparent slow decay times (~20 ns) is not sufficient enough to explain our data, and the singlet fission process is still a plausible mechanism to generate triplet excited states from singlet excited states.

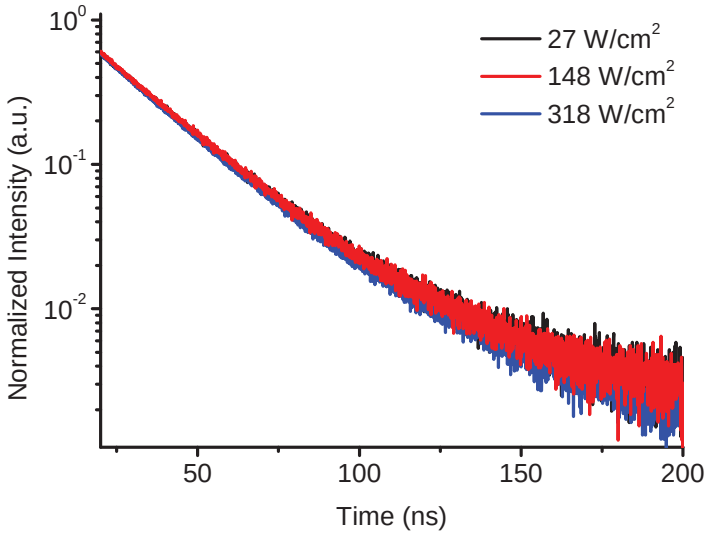

Figure 3.43: The **G16** fluorescence decays from 1% G-NBs at different excitation densities: 27 (black), 148 (red), and 318 W/cm^2, λ_{ex} = 375 nm, λ_{em} >500 nm.

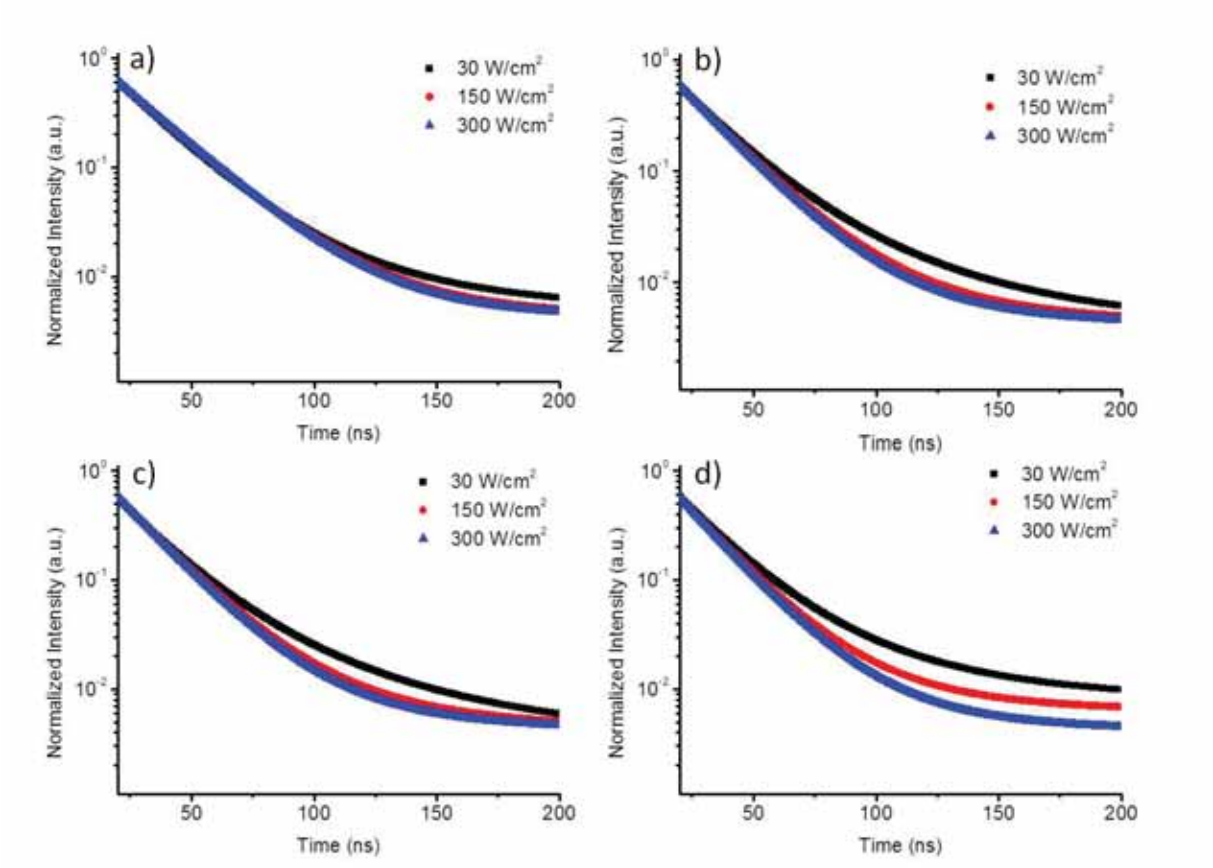

Figure 3.44: Simulated fluorescence decay generated by kinetic models 1 (a), 2 (b), 3 (c) and 4 (d) respectively and the excitation densities 30 (black), 150 (red), and 300 W/cm^2. The rise of fluorescence decays are emitted for the clarity.

In order to obtain a further insight about singlet fission process, it would be ideal to simulate the concentration effect by using our proposed models due to the fact that the increase of dopant concentration does not only increase the excited state density but also

increases the probability to have the “pair” of excitation sites where can accommodate the two triplet excitations generated via singlet fission, which means k_{sf} is increased. However, to introduce of more dopants into the **B16** nanoribbons suggests higher probability to have defects and heterogeneity in the matrices. As mentioned previously, these complications make it very difficult to describe the excited states behaviours with the kinetic schemes we proposed. This is the reason why we did not perform the simulation of concentration effects.

In conclusion, this system provides an interesting tuneable nano-system for the investigation of fundamental photophysical processes and the parameters that influence them. Triplet fusion is currently of interest in order to optimize the performances of purely organic electroluminescent devices, such as OLED’s. Singlet fission is a phenomenon that could be of high importance for future applications in photovoltaics. The optimization of these nano-systems with high concentrations of tetracenes could provide a tool to investigate such a process, already observed in pure tetracene solid state systems.

3.2.3 B16−to−R16 energy transfer

Similar to the previous section, investigation of energy transfer from **B16** to **R16** has been conducted on 100 μL of a stock solution of **B16** (C_{B16}= 5 mM) and **R16** (C_{R16} up to 100 μM) in deoxygenated DCM is injected into 5 mL deoxygenated MeOH. The resulting solution was allowed to ripen overnight on standing in the dark and yielded a suspension of nanoribbons. **B16** can be selectively excited due to the low absorbance ($A_{\mathbf{R16}}$) of **R16** (at λ_{ex} = 372 nm, $A_{\mathbf{B16}}$ = 0.98 for **B16** ε_{372nm} = 9844 $M^{-1}cm^{-1}$ and [**B16**] = 0.1 mM, while $A_{\mathbf{R16}} \leq 5.2\times10^{-3}$ for **R16** ε_{372nm} = 2600 $M^{-1}cm^{-1}$ and [**R16**] ≤ 2 μM)

The overlap integral J_{BR} between **B16** emission and **R16** absorption is J_{BR} = 2.46 $\times10^{14}$ $M^{-1}cm^{-1}nm^4$ (Figure 3.45), about 1.6 times of J_{BG} and thus sufficient for energy transfer to occur also in the nanometer scale.

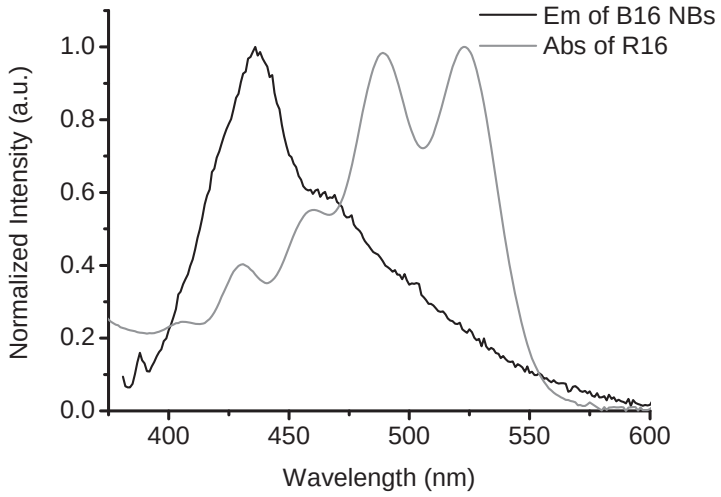

Figure 3.45: Normalized emission spectrum of **B16** nanoribbons and absorption spectrum of 10 μM **R16** in THF solution

3.2.3.1 Morphology of R16 doped NBs

SEM images of 2% **R16** doped NBs (Figure 3.46) display very similar shape and sizes of nanoribbons as **B16** NBs, clearly indicating the morphology of NBs is not influenced by the addition of small amount of **R16** molecules. However, some amorphous aggregates are observed in figure 3.47 besides the nanoribbons.

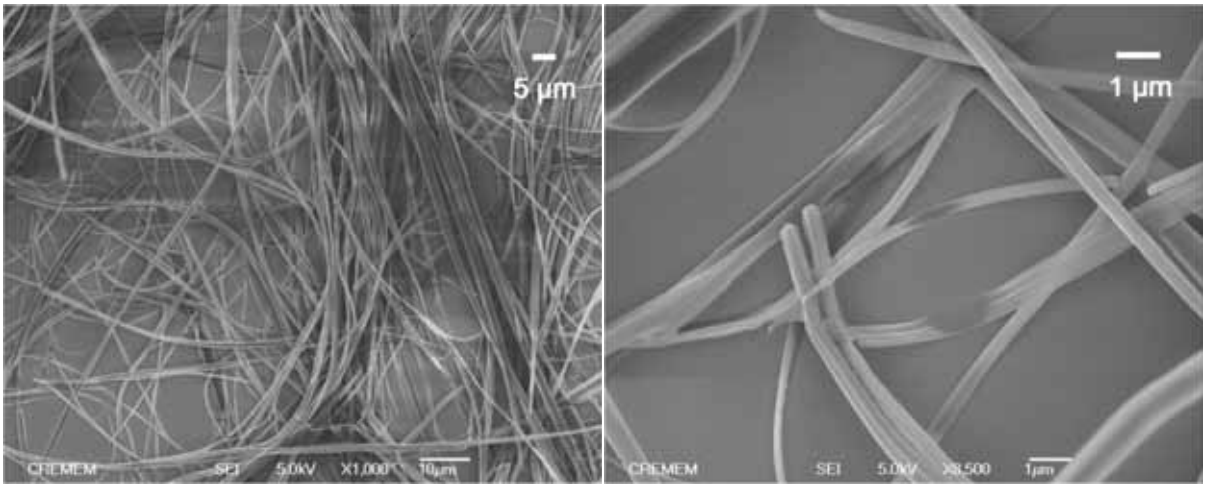

Figure 3.46: SEM image of 2% **R**-NBs. Magnification : 1000X (left), 8500 X (right)

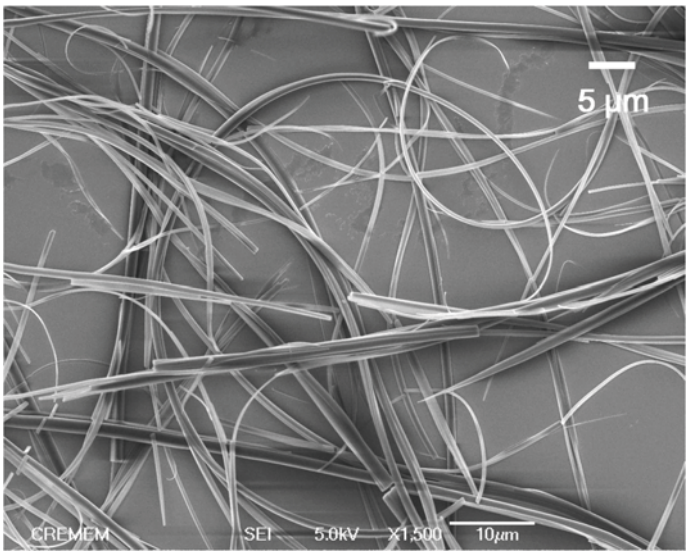

Figure 3.47: SEM image of 2% R-NBs. Magnification : 1500X

3.2.3.2 Photophysical properties

B16 NBs doped with **R16** with concentrations of 0.1%, 0.2%, 0.5%, 0.7% and 1.0% demonstrate steadily decrease of **B16** emission and increase of **R16** emission (Figure 3.48) when **B16** is selectively excited. (λ_{ex} = 372 nm). The CIE coordinates vary linearly from (0.185, 0.204) to (0.389, 0.424).

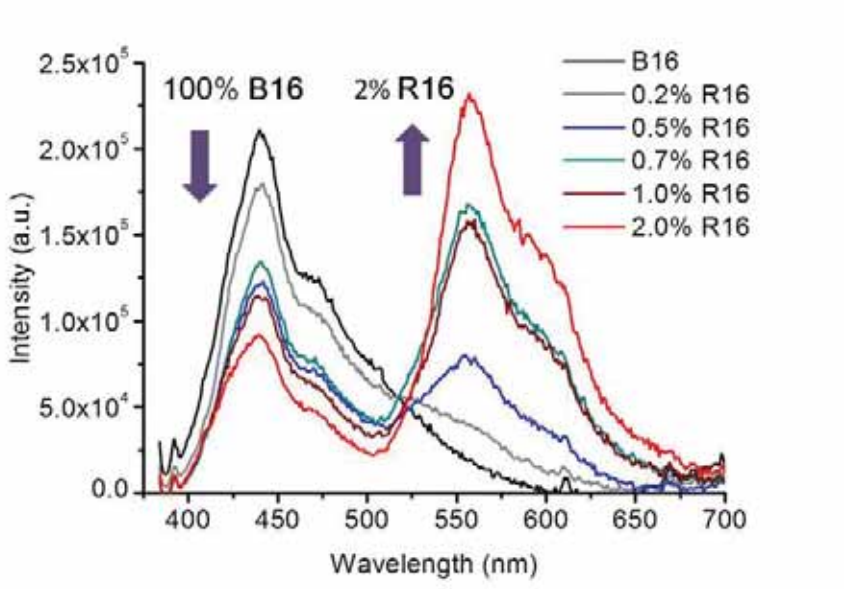

Figure 3.48: Emission spectra of **B16** NBs with 0.2%~2% doped **R16,** intensity is corresponding to Q.Y., λ_{ex} = 372 nm

An efficient energy transfer is observed resulting in 68% quenching of **B16** emission when 0.02 equiv of **R16** are added to the NBs (Table 3). The **B16** to specifically exciting energy transfer efficiency η_{ET} is calculated with the contribution of quantum yields of donor and acceptor by the same formula as pervious section:

$$\Phi_{\text{Total}} = \Phi_D\left(1-\eta_Q\right) + \Phi_{\text{A}}\left(\eta_Q\right)\left(\eta_{ET}\right)$$

where Φ_D is the fluorescence quantum yield of **B16** NBs in absence of **R16**; Φ_A is the quantum yield of **R16** in NBs, determined by specifically exciting **R16** in 2% doped NBs at 460 nm with intergrating sphere. The Φ_A value measured is only 25%. A radiative constant of **R16** in doped NBs is determined by combining the quantum yield the decay time of **R16** upon excitation of **R16** in 2% doped NBs (18.2 ns). We find a radiative constant $k_r = 1.4 \times 10^7$, which is relatively low compared to the radiative constant of **R16** in solution ($k_r = 5.1\times10^7$). This fact can be attributed to the following reasons: 1. **R16** molecules in doped NBs are photo-bleached by the light source during quantum yield acquisition; 2. the presence of non-emissive species formed by **R16** molecules (for example due to aggregation).

Figure 3.49 shows the effect of photo-bleaching on **R16** molecules by specific excitation of **R16** in 2% doped NBs at 460 nm and then the resulting fluorescence intensity at 556 nm is monitored simultaneously under the same set up as quantum yield measurements. During 360 s, 30% emission is photo-bleached, which indicates the effect of photo-bleaching is not the only process contributing to the estimation of k_r.

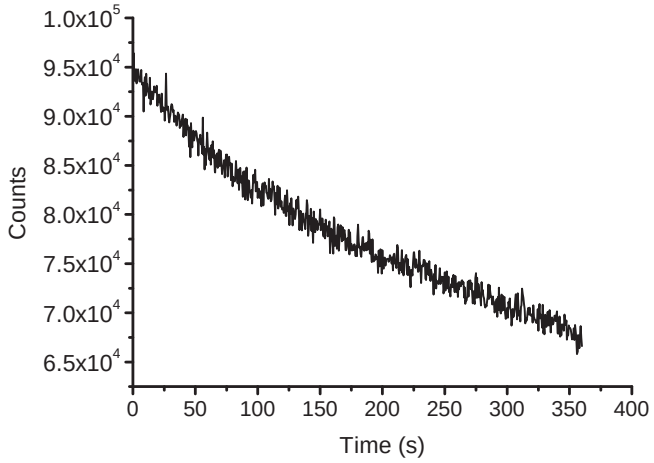

Figure 3.49: Emission intensity at 556 nm of 2% **R16** doped NBs versus irradiation time, λ_{ex} = 460 nm

The assumption that **R16** non-emissive species form is also supported by the fact that in a **B16-G16** system, a ~30% lower quenching efficiency η_Q is measured whereas the energy transfer efficiency η_{ET} is similar with the same amount of dopants and the overlap integral J_{BR} is 1.6 times J_{BG} (take 1% doped NBs as example: **G16** system η_Q = 0.88, η_{ET} = 0.49; **R16** system η_Q = 0.53, η_{ET} = 0.51).

According to the previous section, the radiative constant k_r of **G16** doped in NBs is in agreement with the radiative constant of **G16** in solution. Therefore, an assumption that the k_r of **R16** molecules doped in the NB is also consistent with the k_r of **R16** in solution ($k_r = 5.1\times10^7$) is made to calculate the "real" Φ_A. The resulting Φ_A value is 92.8%, which is applied to the formula for further η_{ET} calculation.

Table 3.3: Energy transfer and quenching efficiencies, and quantum yields of R-NBs at λ_{ex} = 372 nm

[**R16**]/[**B16**]	$\eta_{ET}{}^a$	$\eta_Q{}^b$	$\Phi_{ex372}{}^{emc}$
0	--	--	0.40
0.20%	1.00	0.09	0.45
0.50%	0.47	0.31	0.41
0.70%	0.47	0.50	0.42
1.00%	0.51	0.53	0.44
1.50%	0.45	0.61	0.41
2%	0.49	0.68	0.44

a η_{ET} is calculated by the contribution of quantum yield from donor and acceptor :

$$\varphi_{total} = \varphi_d(1-\eta_Q) + \varphi_a(\eta_Q)(\eta_{ET})$$

b $\eta_Q = 1 - I_{440}/I_{440}{}^0$, where the emission intensity (corrected with quantum yield) at 440 nm with λ_{ex} at 372 nm is indicated as I_{440} and $I_{440}{}^0$ in the presence and in the absence of **R16**, respectively.

c. Determined by intergrating sphere

The fluorescence decay time of **B16** decreases in presence of **R16** (λ_{ex} = 371 nm, λ_{em} = 431 nm, Figure 3.50, left), while the fluorescence of **R16** rises upon selective excitation of **B16** (λ_{ex} = 371 nm, λ_{em} = 556 nm, Figure 3.50, right). These observations account for the energy transfer process from **B16** to **R16** occurring in **R16** doped nanoribbons.

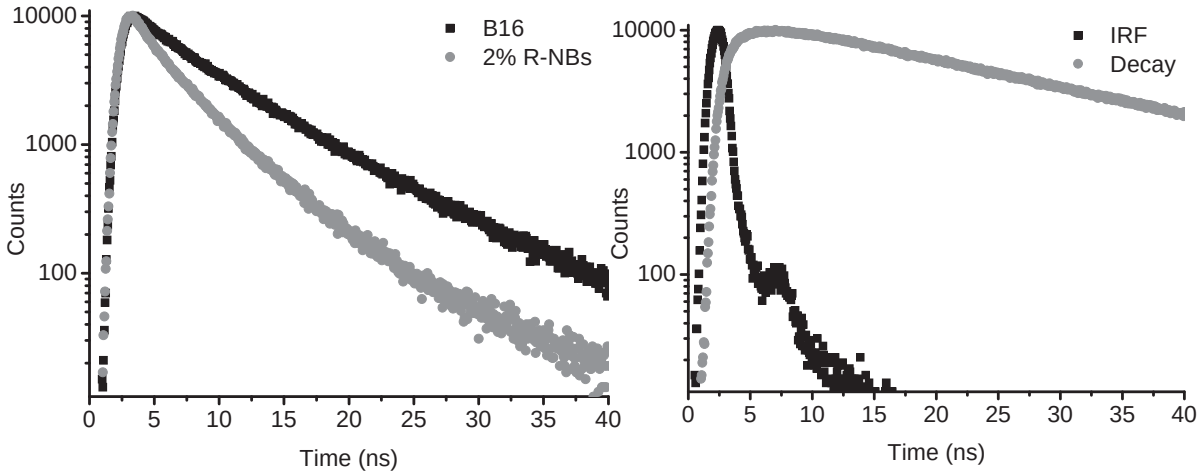

Figure 3.50: (left) Fluorescence decays of **B16** NBs (black) without and with 2% **R16** doping (gray). (right) Fluorescence decay of 2% **R16** in **B16** NBs.(λ_{ex} = 371 nm, λ_{em} = 556 nm) (IRF shown for clarity)

3.2.3.3 Emission spectra of single NBs

In order to accumulate sufficient photons and minimize photobleaching, the emission spectra are recorded by accumulating light emitted from an area (30 × 30 μm).

Samples of 0.2%, 0.5%, 0.7%, 1% and 2% **R16** doped NBs are investigated under CFM (Figure 3.51). As already observed in previous section, the difference of the spectra under CFM and those of bulk-spectra resides in the observation of the 0-0 transition of **B16**. The CIE coordinates vary linearly from (0.234, 0.245) (0.2% doped NBs) to (0.389, 0.424) (2% doped NBs). Interestingly, the CIE coordinates for 0.5% **R16** doped NBs emission is that of white light (0.319, 0.347), (Figure 3.52) nearly matching the standard daylight fluorescent illuminant (0.314, 0.345).

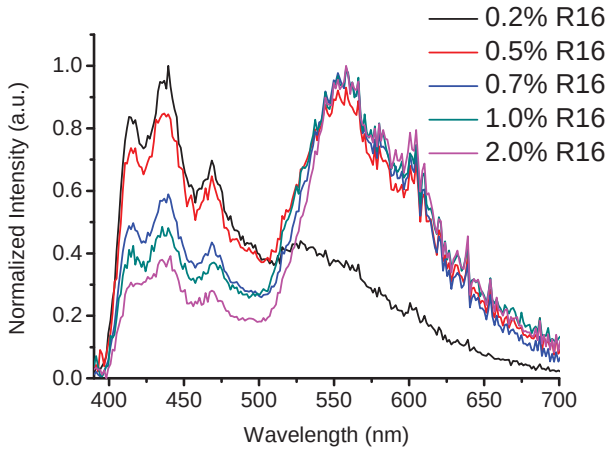

Figure 3.51: Normalized emission spectra at 556 nm of 0.2%, 0.5%, 0.7%, 1% and 2% **R16** doped nanoribbons, λ_{ex} = 375 nm

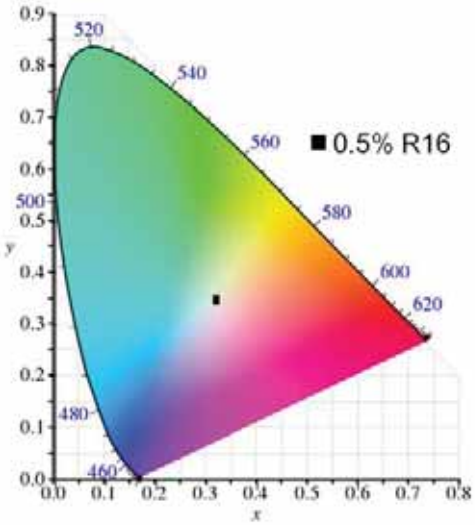

Figure 3.52: Picture of sample vial with 0.5% **R16** doped NBs under UV light, λ_{ex} = 365 nm (left); CIE 1931 chromaticity coordinates of 0.5% **R16** doped NBs: x = 0.319, y = 0.347 (right)

For each sample, more than five different areas have been analyzed. Figure 3.53 demonstrates some differences of the emission spectra obtained in these different areas, which indicates the dispersion of **R16** molecules doped in NBs is not as homogeneous as **G16**.

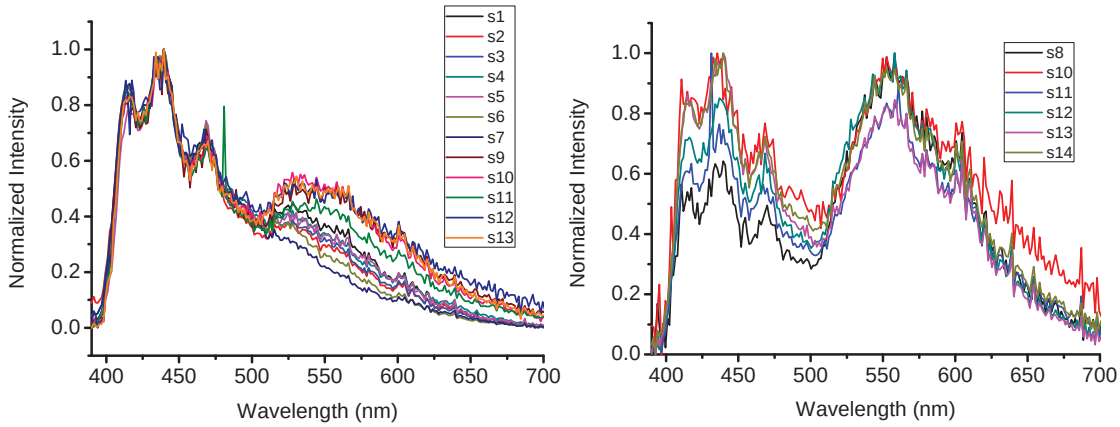

Figure 3.53: Normalized emission spectra of 0.2% (left) and 0.5% (right) **R16** doped **B16** NBs

3.2.3.4 Polarization

In 0.5% **R16** doped NBs, the P value of the emission of **B16** (400 nm < λ_{em} < 450 nm) varied from -0.60 to +0.45 in agreement with pure **B16** NBs (Figure 3.54), confirming that the self-assembly of **B16** inside the NBs is not seriously affected by the presence of **R16**. The orange emission from the **R16** components in the 0.5% NBs is less polarized than **B16** (-0.50 to +0.35, Figure 3.55) when sensitized by **B16** (λ_{ex} = 375 nm, λ_{em} >500 nm), indicating the sensitized **R16** molecules populated inside the NBs are slightly less oriented than **B16**.

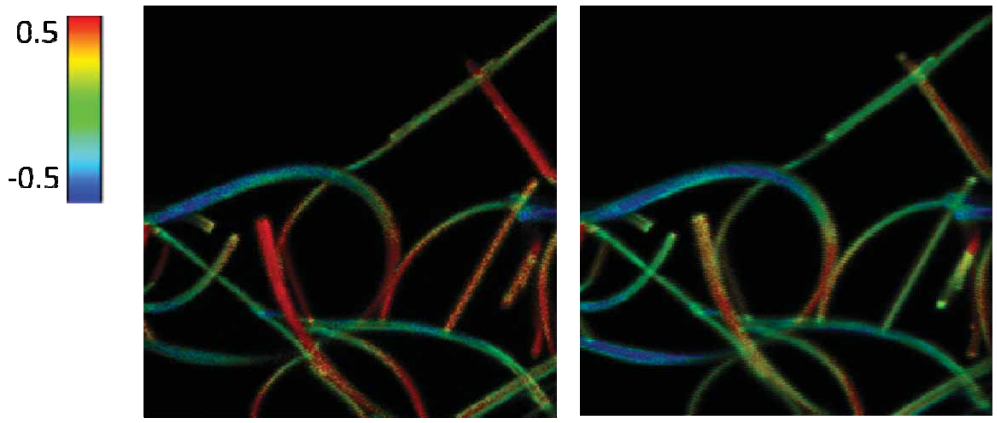

Figure 3.54: Polarization images (30 × 30 μm) of 0.5% R-NBs: λ_{ex} = 375 nm , 400 nm < λ_{em} < 450 nm (left), λ_{em} >500 nm (right). Color code: polarization

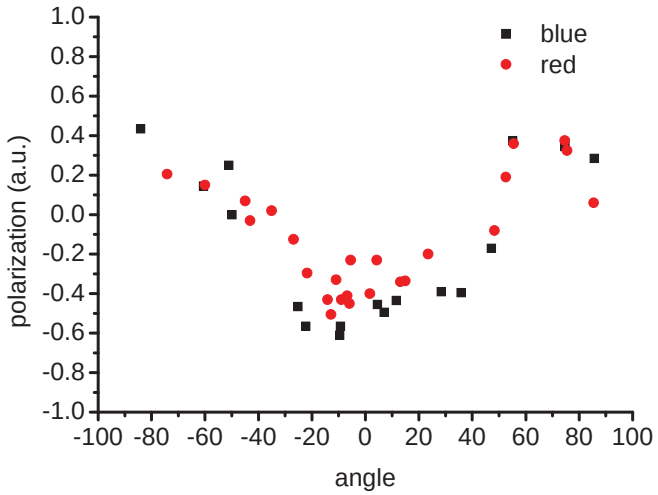

Figure 3.55: Polar plot of 0.5% R-NBs, λ_{ex} = 375 nm, 400 nm < λ_{em} < 450 nm (black), λ_{em} >500 nm (red).

In the previous experiment the sensitization could involve all or only one fraction of the **R16** molecules. In order to assure all the **R16** molecules are excited, directly excitation on the **R16** molecules in nanoribbons at 488 nm is performed to gain further insight on the polarized emission of the acceptors. Two cases are examined with 1% and 0.2% **R16**. In 1% doped NBs, the emission of **R16** is much less polarized (-0.20≤*P*≤0.20, Figure 3.57) compared to the emission of **R16** sensitized by selectively excited at **B16** (-0.40≤*P*≤0.60, Figure 3.57). It suggests that the hetero-ET **B16→R16** is more efficient than homo-ET **R16→R16** due to the more negative *P* value**.**

When **R16** is diluted at 0.2% and excited directly, it always emit with a positive *P* (-0.1≤*P*≤0.5, Figure 3.58) and the polarization of emission is almost independent of the orientation θ of the nanoribbons as compared to the sensitized emission (-0.40≤*P*≤0.60) and to the direct excitation in 1% doped NBs. Similar as **G16**-NBs, this suggests that the homo-ET **R16 → R16** occurs les efficiently under direct excitation of diluted **R16** in 0.2% doped NBs, while in all the other cases **B16-B16** and **R16-R16** homo-ET processes occurs efficiently because of higher concentrations, resulting in more negative *P* values.

This ET can be attributed to a Förster-type mechanism which is disfavored in the 0.2% **R16**-NBs due to a higher distance between chromophores.

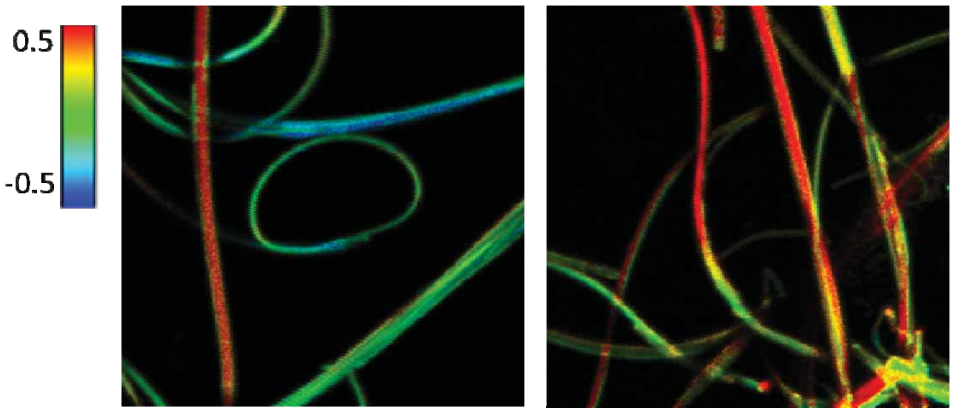

Figure 3.56: Polarization images (30 × 30 μm) of 1% R-NBs: λ_{em} >500 nm, λ_{ex} = 375 nm (left), λ_{ex} = 488 nm (right). Color code: polarization-

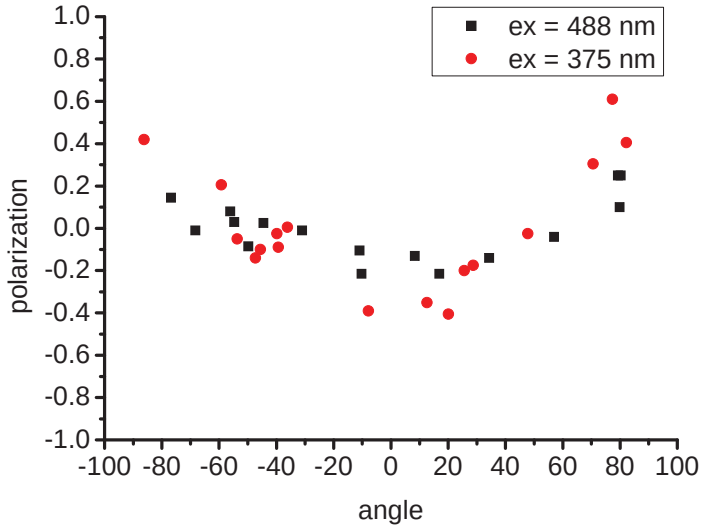

Figure 3.57: Polar plot of 1% R-NBs, λ_{em} >500 nm, λ_{ex} = 375 nm (red), λ_{ex} = 488 nm (black)

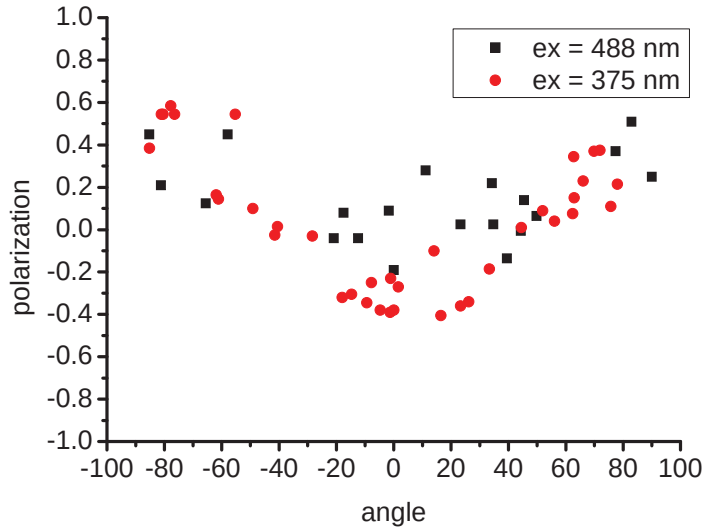

Figure 3.58: Polar plot of 0.2% R-NBs, λ_{em} >500 nm, λ_{ex} = 375 nm (red), λ_{ex} = 488 nm (black)

3.2.3.5 Decay Times

Similar to **B16-G16** system, the FLIM images of **B16** emission of 0.5% **R16** doped white light system reveals excited state decays on several timescales. First, tri-exponential functions have been used to fit the decays and values of 2.1, 4.4, 11.0 ns. These decay times of **B16** emission in doped **R16**-NBs are much shorter than pure **B16**-NB (Figure 3.59). Figure 3.60 shows that with the addition of **R16** in NBs, **B16** emission decay times decrease.

The fluorescence of **R16** rises with time upon selective excitation of **B16** with a distribution of τ around a weighted mean value of 1.1 ns (λ_{ex} = 375 nm, λ_{em} > 500 nm; Figure 3.53), which is in the same order as the fastest decay time of **B16** emission (2.0 ns).

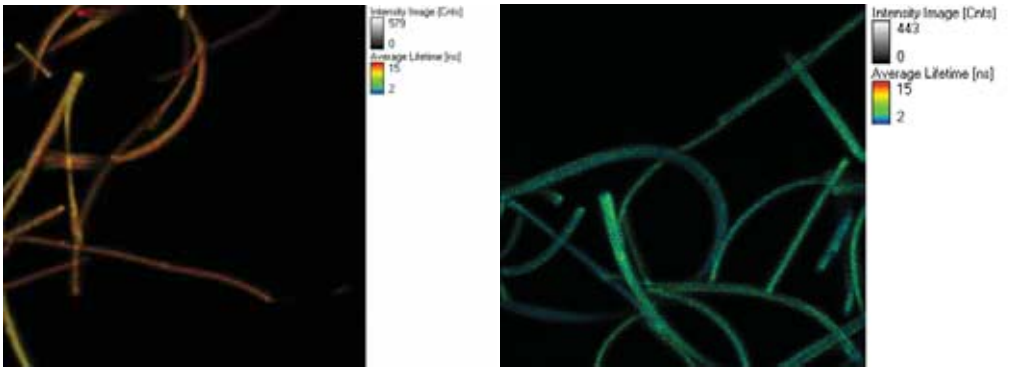

Figure 3.59: FLIM image of **B16** NBs (40 × 40 μm), λ_{ex} = 375 nm, λ_{em}> 405 nm (left); 0.5% **R16** doped NBs (30 × 30 μm), λ_{ex} = 375 nm, 400 < λ_{em} < 450 nm (right), color code: average lifetime

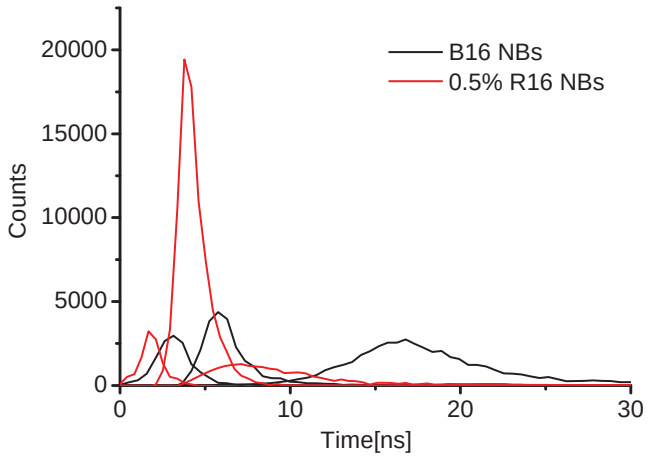

Figure 3.60: Decay times distributions of **B16** NBs (black) and 0.5% **R16** doped NBs (red), 400 < λ_{em} < 450 nm, λ_{ex} = 375 nm

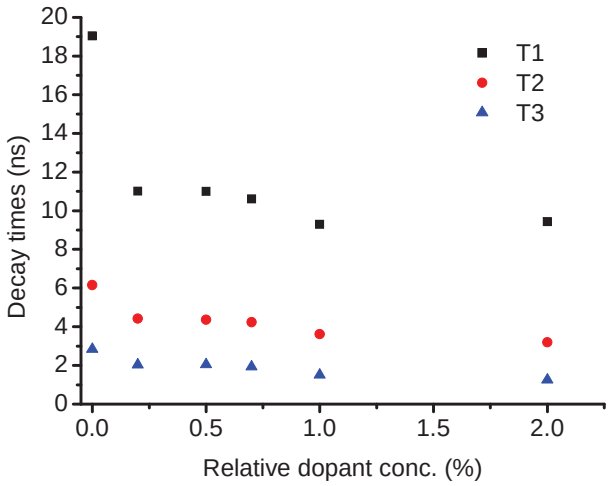

Figure 3.61: Three decay times of **B16** obtained by tri-exponential fitting versus doping concentrations [**R16**], λ_{ex} = 375 nm, 400 $< \lambda_{em} <$ 450 nm

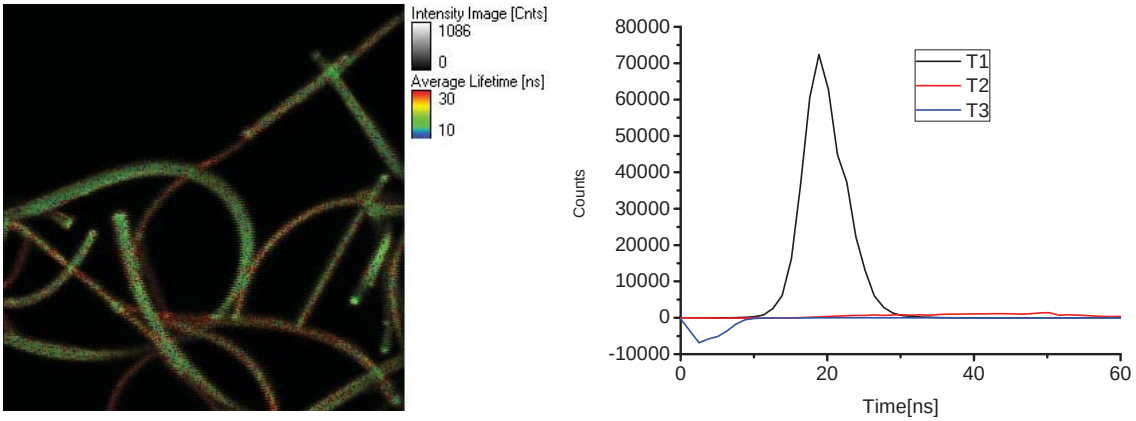

Figure 3.62: FLIM image of 0.5% **R16** doped NBs (30 × 30 μm), λ_{ex} = 375 nm , λ_{em} >500 nm

The emission decay times of **R16** molecules within 1% and 0.2% **R16** doped NBs are investigated using tri-exponential fittings on each pixel. Unlike **B16-G16** system, the decay times of **R16** emission upon selective excitation are not influenced by the dopant concentration. In both cases, the fluorescence of **R16** rises and decays with the same kinetics as when **R16** is directly excited (for 1% τ =18 ns and 42 ns; for 0.2% τ =18 ns and 38 ns, λ_{ex} = 488 nm, Figure 3.64, 3.66)

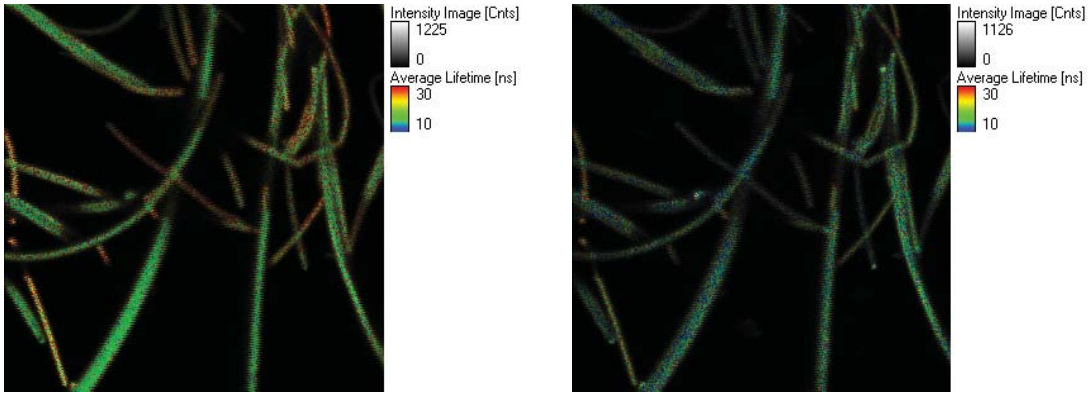

Figure 3.63: FLIM image of 1% **R16** doped NBs (30 × 30 µm), λ_{em} >500 nm, λ_{ex} = 375 nm (left), λ_{ex} = 488 nm (right), color code: average lifetime (left)

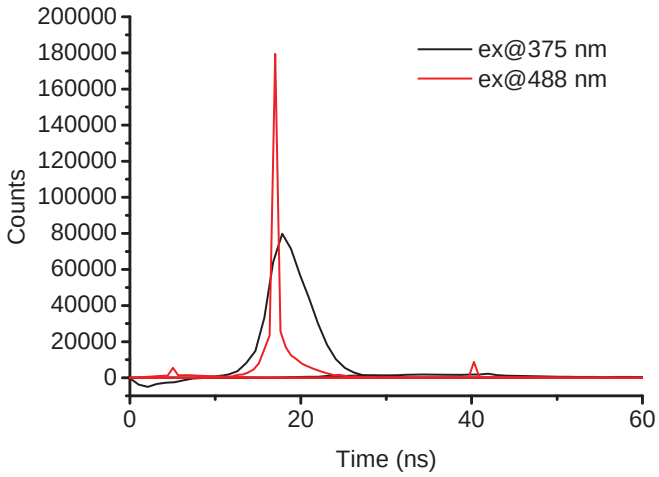

Figure 3.64: Decay times distributions of 0.2% **R16** doped NBs, λ_{em} >500 nm, λ_{ex} = 375 nm (black), λ_{ex} = 488 nm (red)

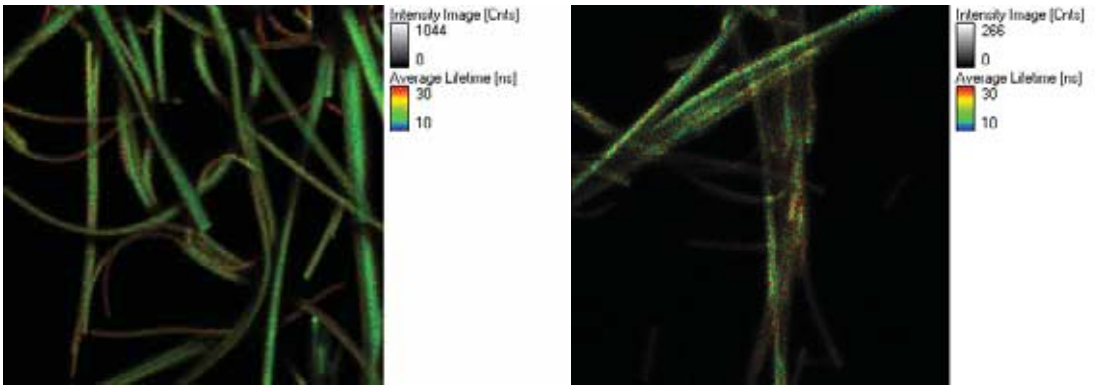

Figure 3.65: FLIM image of 0.2% **R16** doped NBs (30 × 30 µm), λ_{em} >500 nm, λ_{ex} = 375 nm (left), λ_{ex} = 488 nm (right), color code: average lifetime (left)

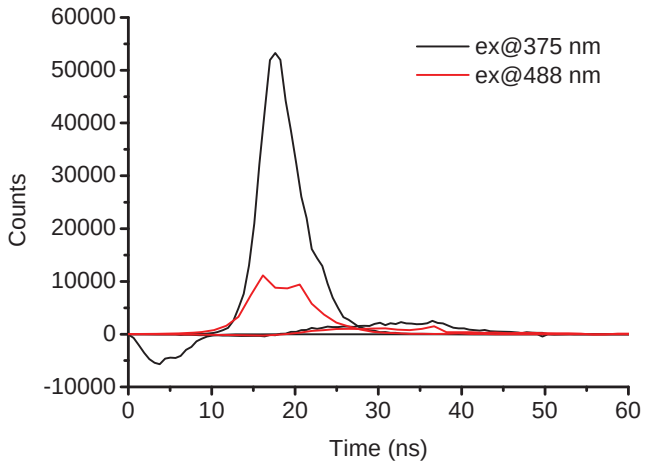

Figure 3.66: Decay times distributions of 0.2% **G16** doped NBs, λ_{em} >500 nm, λ_{ex} = 375 nm (black), λ_{ex} = 488 nm (red)

Figure 3.67 shows the **R16** emission decay of 1% R-NBs by CFM, which also shows a long-lived tail in the nanoribbon's emission decay profile. The decay has thus been fitted with an exponential component for 10 < t < 50 ns, and the contribution of first exponential decay is also taken into account into our tail fitting. The formula utilized to fit the tail (t > 100 ns) is described at previous section:

$$y = A_1 \exp(-t/\tau_1) + A_2(t)^p + y_0$$

A_1, τ_1 and y_0 are decided by the mono-exponential fitting for 10 < t < 50 ns, and the rest parameters are fit freely by the software.

The background values are also decided following the same procedures mentioned in the previous tetracene section. As shown in Figure 3.69, with y_0 = 86 counts, τ_1 = 18.9 ns, a well-fitting curve of the power p=−2.0 can be achieved, indicating the long-lived emission tail is thus consistent with delayed fluorescence being induced by TT-annihilation.

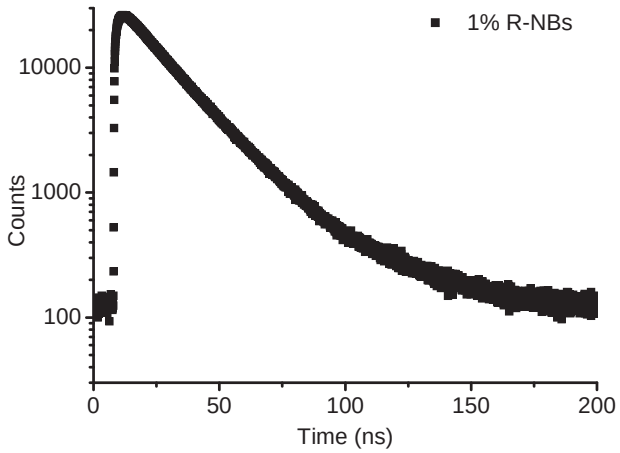

Figure 3.67: TCSPC measurements of **R16** emissions in 1% R-NBs, λ_{ex} = 375 nm, λ_{em} >500 nm

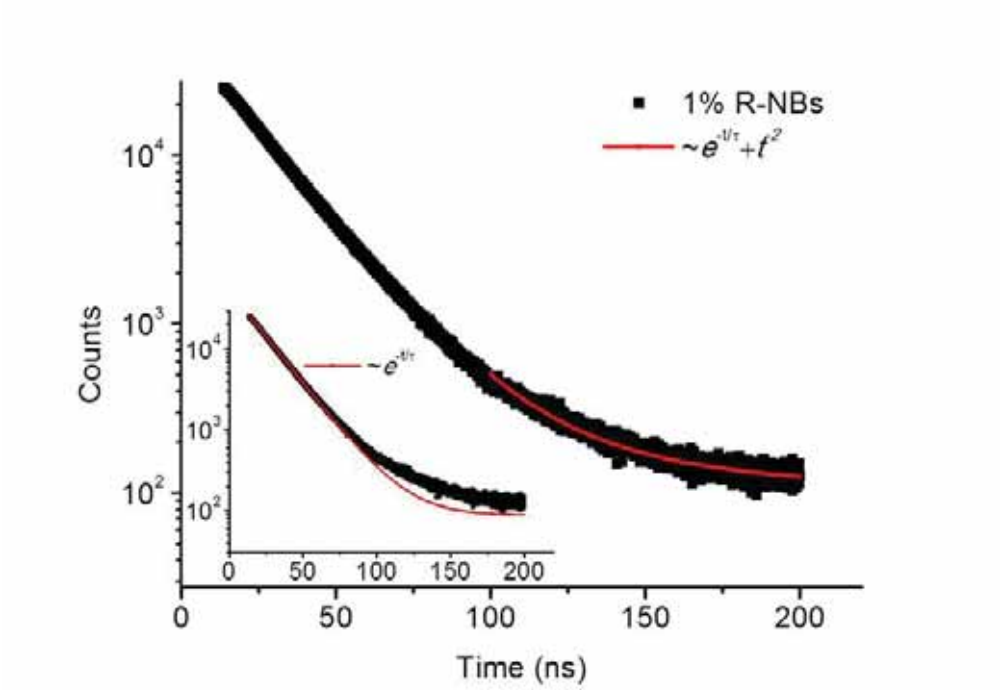

Figure 3.68: R16 Emission decay measured for 1% R-NBs. The red line represents a t^{-2} power law + exponential fit after 100 ns. The inset is a semi-log plot of the same data. The red line is exponential decays exp (-t/τ), with τ ~19 ns (fit from 10 ns ~ 50 ns).

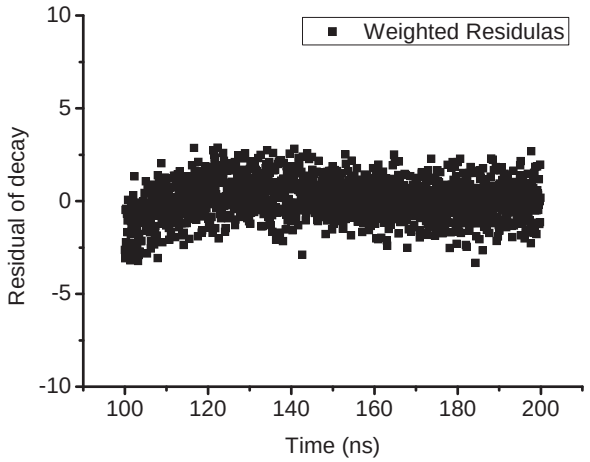

Figure 3.69: The residual of **R16** emission decay fit with power law

Detailed analysis of the **R16** emission decay times is shown in the following to help us obtain more information. Due to the presence of non-emissive **R16** aggregates at 2% R-NBs, further concentration experiments are not performed. The decays have been approximated with a tri-exponential function in order to carry out the same type of analyses both on decays obtained by accumulation of fluorescence on a sample area, and for FLIM with fittings performed on each pixel.

Figure 3.70 shows that the rise time of **R16** fluorescence decreases with increasing doping concentration of **R16**, suggesting a more efficient energy transfer process with a higher population of **R16** molecules within the nanoribbons.

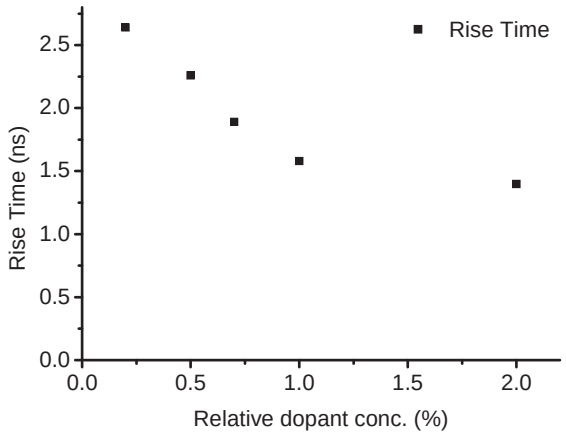

Figure 3.70: Rise times of **R16** emission versus doping concentrations, λ_{ex} = 375 nm, λ_{em} >500 nm

The slowest decay time (T1) first slightly increases with the increase of **R16** concentration, and then decreases again. This fluctuation is also seen in **B16-G16** system with 0.1%~1% dopants. The corresponding pre-exponential factor (A1) also varied with an opposite trend (Figure 3.71), even though the contribution of T1 is quite small (<5%). In contrast, the decay time about 18 ns (T2) is independent of [**R16**]. These observations show that even the contribution of this delayed fluorescence component is really low, there is still some correlation between this slowest decay times T1 and [**R16**].

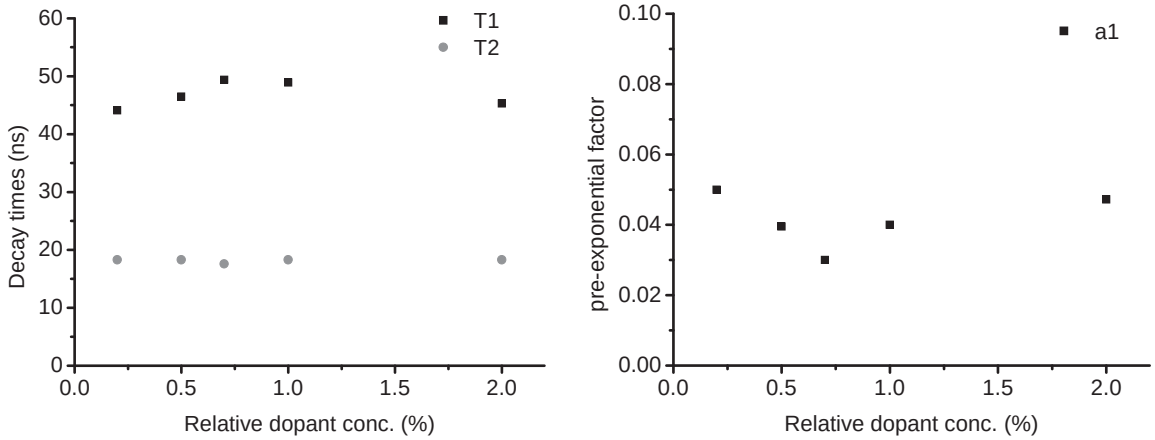

Figure 3.71: decay times (left) and corresponding pre-exponential factor (right) of **R16** emission versus doping concentrations, λ_{ex} = 375 nm, λ_{em} >500 nm

3.2.3.6 Power effect

Although the **R16** concentration increasing analysis was not carried out for more than 2% **R16** doped in the NBs, another option that was used to analyze the effect of the concentration of excitons in NBs was to perform the decay times measurement with increasing incident excitation power. 2% **R16** doped nanoribbons were thus studied under CFM. During acquisition, a continuous light N_2 gas flow is also applied to reduce the photo-bleaching

resulting from the use of higher than usual laser power. The effect of photo-bleaching was verified and was less than 5% with the largest incident power density applied. This largest incident power density applied in **R16**-NBs system is only 50% of G16-NBs, indicating the **R16** molecules doped in the NBs are more fragile than **G16** molecules.

The slowest decay component (T1) is shown to decrease with the increase of incident power density (Figure 3.72), whereas the corresponding pre-exponential factor does not display a well-defined trend with different incident power density. This T1 acceleration is small but it suggests the attribution of the longest decay to a biexcitonic process. Additionally, this experiment shows that T2 doesn't vary with the incident power density.

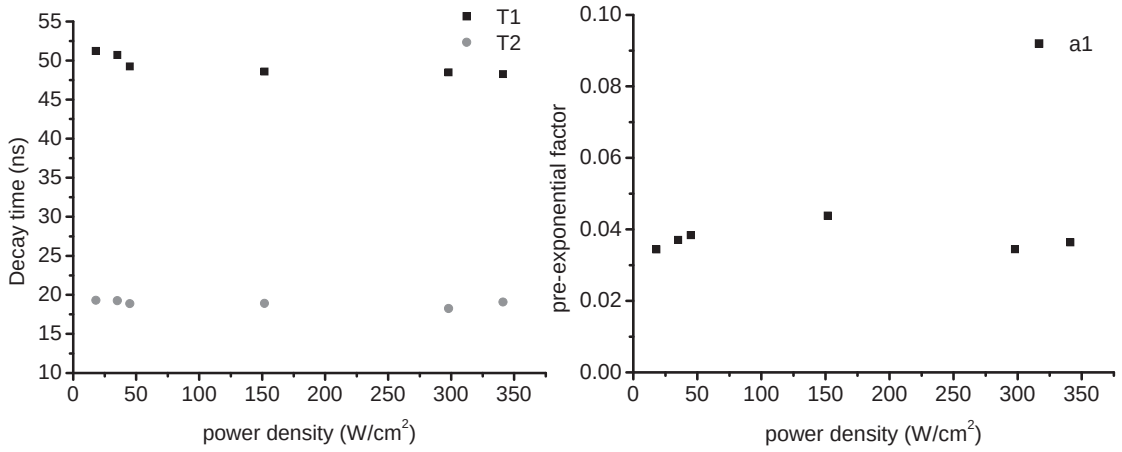

Figure 3.72: decay times (left) and corresponding pre-exponential factor (right) of **R16** emission versus incident power density, λ_{ex} = 375 nm, λ_{em} >500 nm

3.2.3.7 Size effect

The detailed analyses of the FLIM images of **R16-N**Bs (Figure 3.61) reveals a similar trend as G-NBs that the average lifetime is longer in thinner nanoribbons, although the difference is not as obvious as **G16**-NBs. Again, in order to verify the origin of this long average lifetime, the previously described FLIM images were processed. Each pixel of the image is fitted with a bi-exponential function with neglect of the rise time to display the fraction of the slowest component by the ratio of normalized pre-exponential factor a1/(a1+a2) (Figure 3.73). Similarly, to increase the contrast and overcome the insufficient photons for a good fit, the fitting parameter were set with the upper and lower limit calculated from cumulated decay fitting.

Figure 3.73 demonstrates that the thinner ribbons have a higher contribution of the delayed fluorescence component (color code: red, higher fraction), and the FHWM of these red ribbons lies in a range of 500-700 nm (intensity fitted with Gaussian Amplitude function, Figure 3.73 right a). In contrast, less delayed fluorescence (color code: blue, lower fraction) occurs in the wider ribbons that have a FWHM of about 1000 nm (Figure 3.73 right b). This finding suggests that more triplets are formed in the thinner ribbons. Due to the fact this slowest decay time (T1) is not shown obviously dependent of dopant concentration and

incident power density, further detailed analysis of those two experiments with different size of NBs is not carried out.

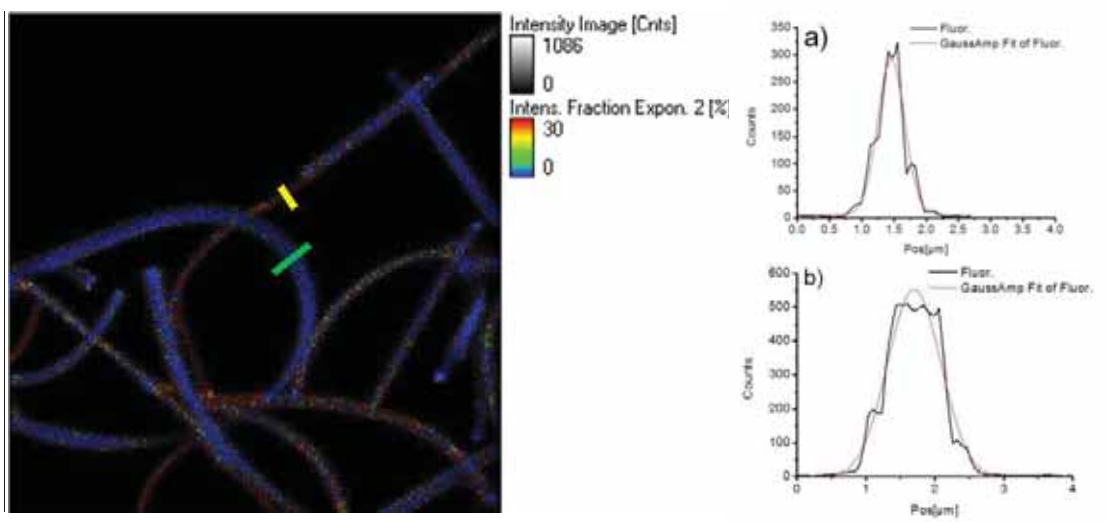

Figure 3.73: FLIM image of 0.5% **R**-NBs (30 × 30 µm), Color-code: fraction of the slowest decay (blue < 5%, red > 25%) λ_{ex} = 375 nm , λ_{em} >500 nm (left); a) Intensity of the thin NB (yellow mark), b) Intensity of the big NB (green mark) (right)

3.2.3.8 Discussion

1. Energy transfer :

Although with similar molecular structure, the dispersion of **R16** population in the NBs is not as homogeneous as **G16**. The polarization studies also reveal that while **B16** and **G16** display a similar preferential orientation, **R16** is oriented but with more disorder. The bulky phenyl substitution groups disfavoured the "insertion" of rubrenes into tightly packed **B16** matrix. The **R16** molecules could have a tendency to partially self-aggregate,[3] which is observed in the SEM image.

From the quantum yield of **B16** NBs and "theoretical" Q.Y. of **R16** inside the NBs, we calculated that for 1% doped R-NBs, 51 out of 100 quenched **B16** molecules transfer their energy to **R16** (η_{ET}). This value is relatively low compared to G-NBs system (η_{ET} =49%) with a overlap integral J_{BG} being only 55% of J_{BR} (J_{BR} =2.31×10^{14} M^{-1}cm^{-1}; J_{BG} = 1.28×10^{14} M^{-1}cm^{-1}).

The analysis of the quenching efficiencies η_Q, reveal that about 90 molecules of **B16** are quenched by a single **R16** molecule at the lower doping concentration (Table 3.3, 0.2% R-NBs). This number result not only from direct energy transfer from the closest donors, but also suggests involvement of exciton migration.[13] However, it is still relatively low compared to G-NBs system.

The value at which the energy transfer efficiency from **B16** to **R16** is 50% of R_0 = 2.95 nm, assuming κ^2 = 2/3 (with the assumption that **R16** molecules are less orderly oriented in R-NBs, suggested by the polarization study). This critical Föster radius of R-NBs is higher than that of G-NBs (2.86 nm), which is not consistent with previous results that the energy transfer

efficiency of G-NBs system is high than R-NBs. The quenching efficiency and energy transfer efficiency of R-NBs system seems to be underestimated due to the fact that **R16** tends to self-aggregate.

At a composition of 0.5% R16, while exciting at 375 nm, the light-harvesting and blue-emitting **DPA** matrix sensitizes the red rubrene acceptor by partial energy transfer process **B16 → R16**, and a two component polarized ($-0.5 \leq P \leq +0.5$) white light emission is achieved.

To verify the presence of **R16**-**R16** homo-energy transfer, we calculated the energy transfer overlap integral $J_{RR} = 8.78 \times 10^{13}$ $M^{-1}cm^{-1}$, giving a critical Föster radius $R_0 = 2.75$, 2.89 nm ($\kappa^2 = 2/3$, $\Phi_D = 0.69$ (Q.Y. in solution) or 0.93 (theoretical Q.Y. in NBs)). With the model constructed by **B8**'s crystal structure, the theoretical distance between two **R16** molecules in 1% doped R-NBs is at least 5.52 nm. It is much larger than the critical Föster radius R_0 (2.75 and 2.89 nm). The resulting **R**-**R** homo-energy transfer efficiency $E = 1/[1 + (r/R_0)^6]$ is around 2% (for both R_0 values), which is less than **G**-**G** homo ET in G-NBs system (2% and 8%). It is consistent with the results of polarization studies under specifically excitation on the dopants. For 0.2% R-NBs, $-0.1 \leq P \leq 0.5$; whereas for 0.2% G-NBs, $-0.3 \leq P \leq 0.7$. As a reminder, positive values of P are expected in the absence of energy transfer processes upon excitation with linearly polarized light due to photoselection processes. The negative values of P tend to result from energy transfer processes. In R-NBs, negative P values are observed at higher doping only (1% of R16).

2. Delayed fluorescence :

The FLIM image and TCSPC measurement reveals the existence of one slow decay component of **R16** emission. This tail of emission decay can also be fitted with t^{-2} power law,[10] indicating a bi-excitonic process is involved.

Due to the presence of non-emissive rubrene aggregations at 2% R-NBs, further concentration experiments are not performed. But the slow decay time still displays dependency with incident power density, suggesting excited states density does influence this component. Compared with G-NBs system, the delayed fluorescence is less favoured in R-NBs. However, the direct comparison of the two systems is compromised due to a less precise knowledge of **R16** within the nanoribbons due to the aforementioned partial self-aggregation.

The simulation of **R16** decay profile in 1% R-NBs by kinetic models was not carried out due to the lack of time. However, the further analysis of delayed fluorescence may lead us to gain more insight about the whole picture of these mechanisms.

3.2.4 G16−to−R16 energy transfer

In order to extend the tuning of colors in NBs, and furthermore to study energy transfer processes from **G16** to **R16** in a matrix, three components nanoribbons were made. 100 μL of a stock solution of **B16** (C_{B16}= 5 mM), **G16** (C_{G16} = 50 μM) and **R16** (C_{R16} up to 100 μM) in deoxygenated DCM was injected into 5 mL deoxygenated MeOH and allowed to ripen on standing overnight at room temperature. Even in this three-components system, the selective excitation of **B16** is guaranteed by the low absorbance of the dopants (at λ_{ex} = 372 nm, $A_{\mathbf{B16}}$ = 0.98 for **B16** ε_{372nm} = 9844 $M^{-1}cm^{-1}$ and [**B16**] = 0.1 mM, while $A_{\mathbf{G16}}+A_{\mathbf{R16}} \leq 6.1\times10^{-3}$ for **G16** ε_{372nm} = 902 $M^{-1}cm^{-1}$ and **R16** ε_{372nm} = 2600 $M^{-1}cm^{-1}$) and the emission of **G16** at 502 nm does not overlap with the emission of the other components. The spectral overlap between **G16** and **R16** is J_{GR} = 3.8 × 10^{14} $M^{-1}cm^{-1}nm^4$ (Figure 3.74), even higher than those between the anthracene and the tetracenes.

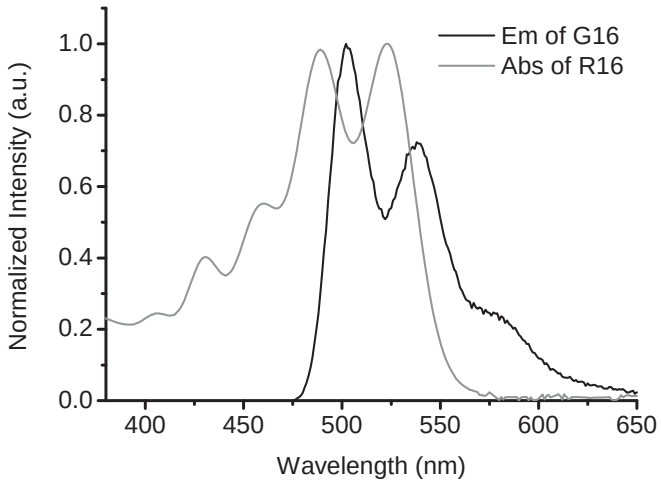

Figure 3.74: Normalized emission spectrum of 10 μM **G16** in THF solution and absorption spectrum of **R16** in THF solution

3.2.4.1 Morphology of 3 components nanoribbons

SEM images of 1% **G16** + 2% **R16** doped NBs (Figure 3.75) show the ribbon-like morphology as **B16** NBs, clearly indicating the morphology of NBs is not influenced by the addition of small amount of dopants. One thing should be noted is that no amorphous aggregates were observed in SEM experiments, even though there is also 2% **R16** doped in the NBs.

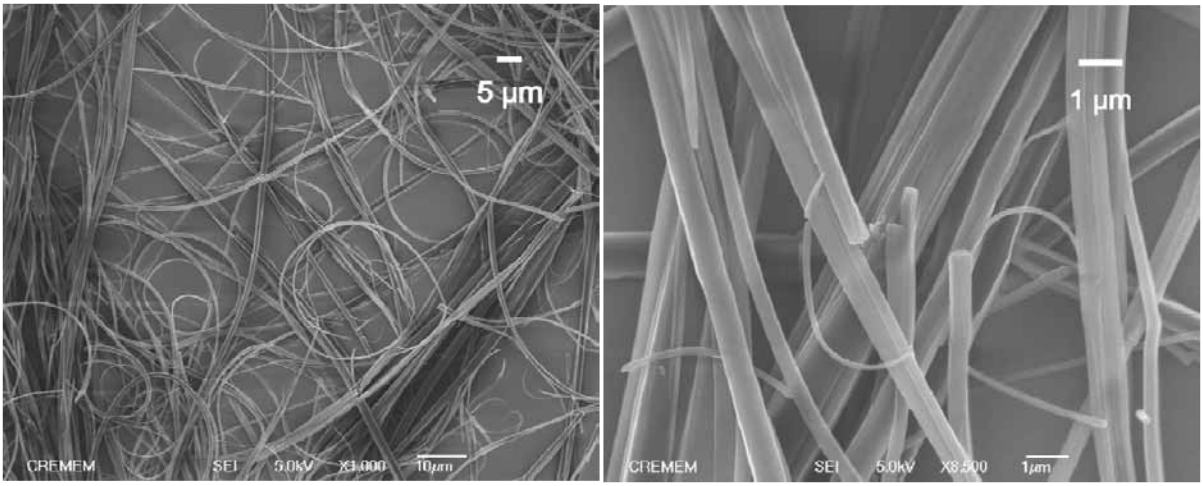

Figure 3.75: SEM image of the 1% **G16** + 2% **R16** doped nanoribbons. Magnification : 1000X (left), 8500 X (right)

3.2.4.2 Photophysical properties

B16 NBs doped with 1% **G16** and **R16** with concentrations of 0.5%, 1.0%, 1.5% and 2.0% demonstrate the sensitized emission of **G16** is reduced with the addition of **R16**, while the emission of **R16** gradually increases. It suggests that the presence of **R16** reduces the probability of **G16** excited states to be populated (Figure 3.76).

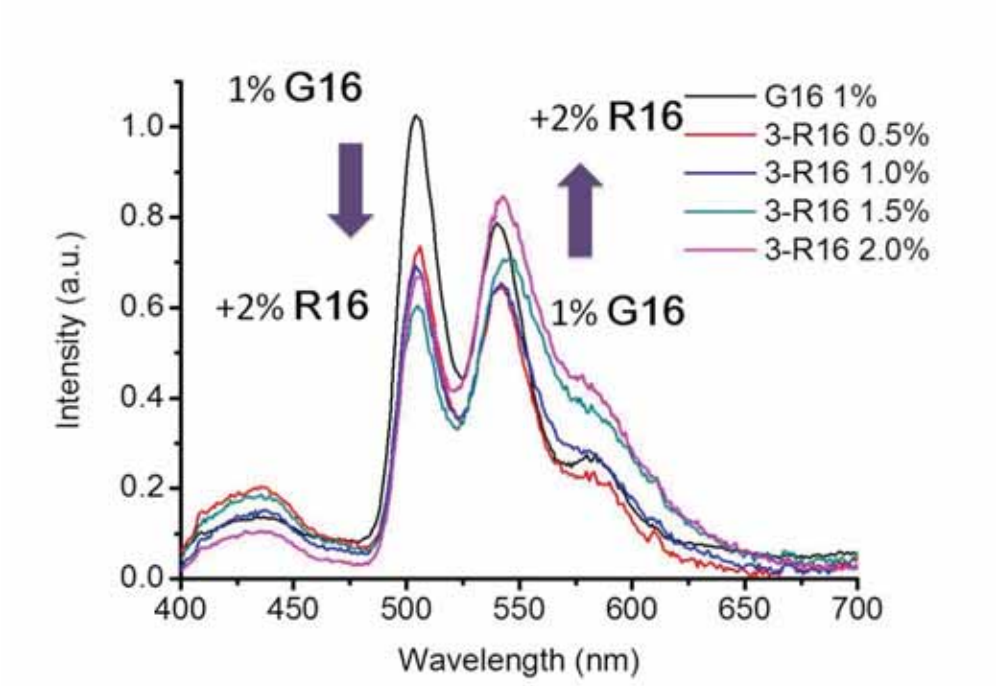

Figure 3.76: emission spectra of 1% **G16** + 0%, 0.5%, 1.5%, and 2% **R16** doped nanoribbons, intensity is corresponding to Q.Y., λ_{ex} = 372 nm

Table 3.4: quantum yields of 3-NBs at λ_{ex} = 372 nm

[**R16**]/[**B16**]	ϕ_{ex372}^{em}
0	0.40
0.50%	0.33
0.70%	0.37
1.00%	0.33
1.50%	0.39
2%	0.40

The fluorescence decay time of **G16** at 502 nm decreases from 20.12 ns to 18.85 ns in presence of 2% **R16** (λ_{ex} = 371 nm, λ_{em} = 502 nm, Figure 3.77, left). In contrast, the decay time of fluorescence at 580 nm increases from 19.13 to 23.3 ns, with a faster rise time < 1 ns. (Figure 3.77, right)

While in the **R**-NBs, the emission at 580 nm is due only to **R16**, in the three-component system it is due to both **G16** and **R16** yielding a multi-exponential decay profile. Thus, the emission profile does not allow a precise determination of **R16** emission lifetime. However, the findings of varied emission spectra and decay times account for a further energy transfer process from **G16** to **R16** upon selectively excitation of **B16** in the three-component nanoribbons.

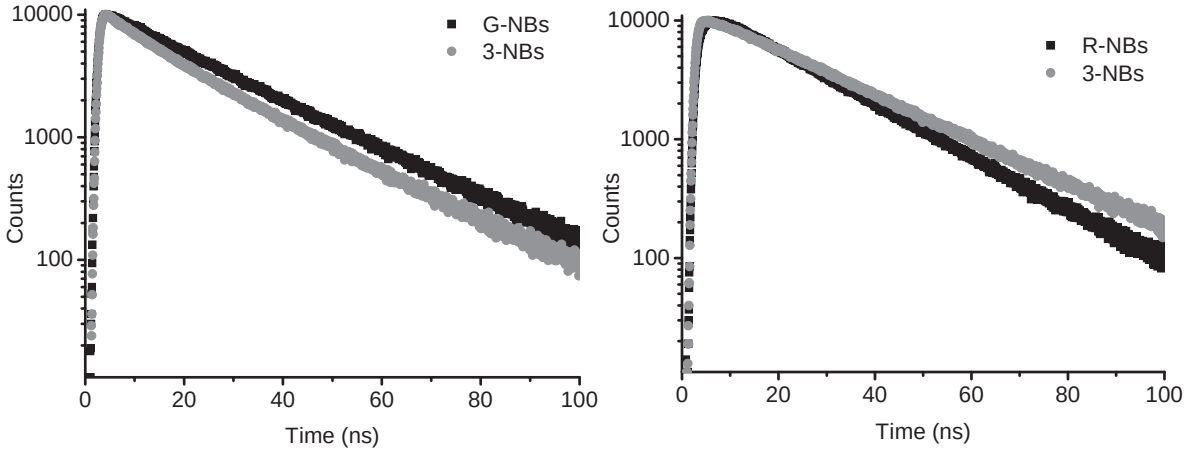

Figure 3.77: Fluorescence decays (λ_{ex} = 371 nm, λ_{em} = 502 nm) of **B16** + 1% **G16** NBs (black) without and with (red) 2% **R16** (left) ; Fluorescence decay of **B16** +2% **R16** NBs (black) without and with (red) 1% **G16**(right) (λ_{ex} = 371 nm, λ_{em} = 580 nm)

3.2.4.3 Emission spectra of single NBs

The emission spectra are collected by accumulating light emitted from an area (30 × 30 μm) to avoid photobleaching.

Samples of 0.5%, 1.0%, 1.5% and 2% **R16** doped in 1% **G16** NBs are investigated under

CFM (Figure 3.78). The emission of **B16** is almost totally quenched in the samples all concentration. The CIE coordinates vary linearly from (0.316, 0.540) (0.5% doped 3 component NBs) to (0.383, 0.538) (2% doped NBs).

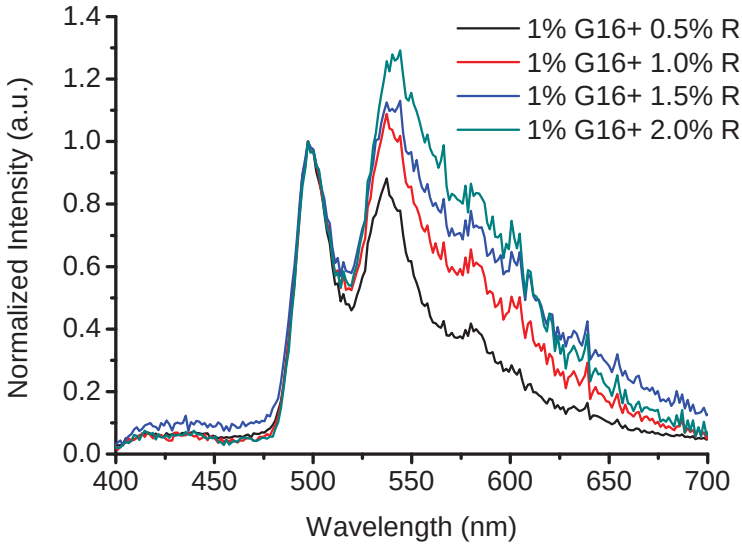

Figure 3.78: relative emission spectra at 502 nm of 1% **G16** + 0.5%, 1.5%, and 2% **R16** doped nanoribbons, λ_{ex} = 375 nm, the emission intensity are normalized to 1at 502 nm.

For each sample, three to five different areas of NBs have been analyzed. Figure 3.79 demonstrates the similarity of the emission spectra obtained in several different areas, indicating the dispersion of acceptors within the nanoribbons is quite homogeneous.

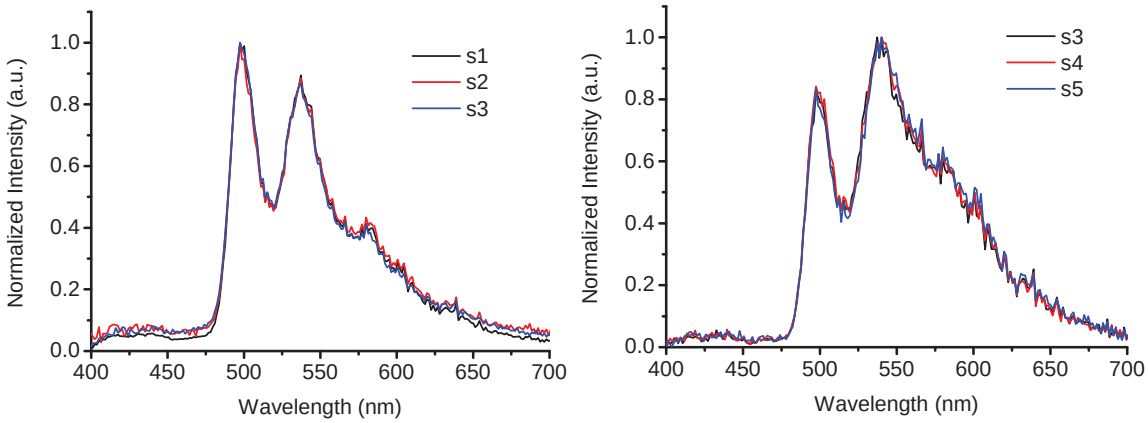

Figure 3.79: Normalized emission spectra of 1% **G16** + 0.5% (left) and 2% (right) **R16** doped **B16** NBs

3.2.4.4 Polarization

Two cases are examined with 1% **G16** + 2% and 0.5% **R16**.

In the 2% 3-NBs, the green/orange emission from the teracenes sensitized by **B16** display the same values (-0.60 to +0.70, Figure 3.81) (λ_{ex} = 375 nm, λ_{em} >500 nm) but shows larger distribution of angular dependency behavior as compared to the **B16** emission and sensitized tetracene emission from one acceptor systems. (Figure 3.14 1% G-NBs and Figure 3.57 1%

R-NBs) When the tetracenes of 2% 3-NBs are excited directly, the emission is almost all positive polarized (Figure 3.81, -0.15≤*P*≤+0.60). This character is more like R-NBs system.

When **R16** is diluted at 0.5% and all the acceptors are excited directly, the emission polarization varies on a larger value scale (-0.40≤*P*≤+0.65) (Figure 3.83). These differences in behaviour suggest that in the 0.5% 3-NBs, where the **G16** emission is more dominant, the ET processes **G16→G16** occur efficiently under direct excitation of the tetracenes yielding quite positive and negative *P* values, while in the 2% 3-NBs the **G16→R16** and **R16→R16** processes might be overall less efficient thus resulting in less negative *P* values.

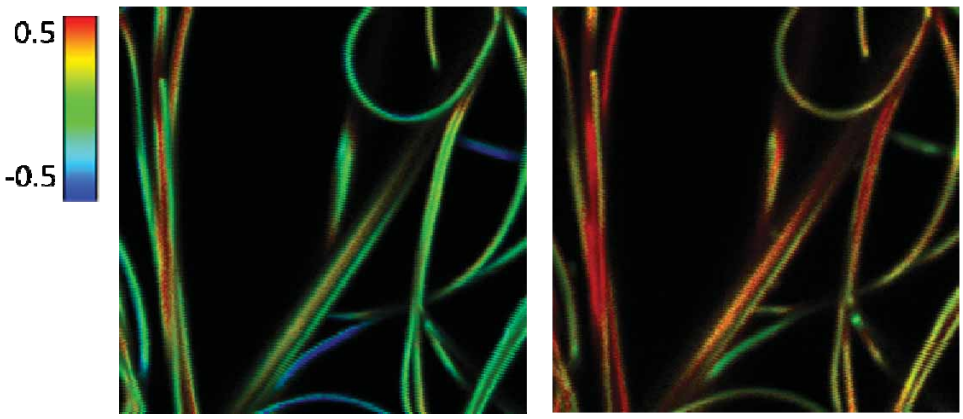

Figure 3.80: Polarization images (30× 30 μm) of 1% **G16**+ 2% **R16** NBs: λ_{em} >500 nm, λ_{ex} = 375 nm (left), λ_{ex} = 488 nm (right). Color code: polarization

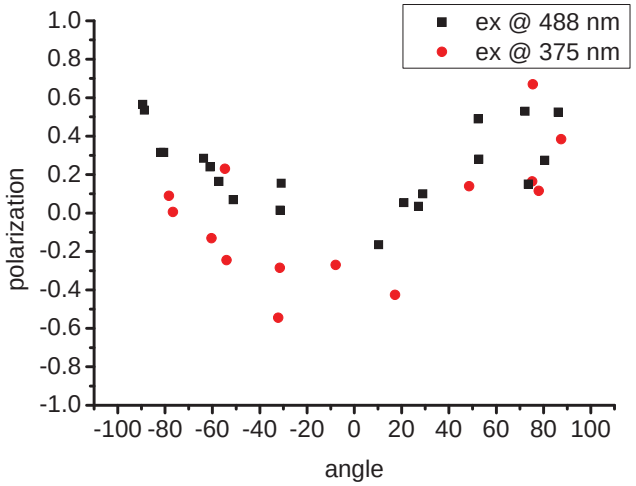

Figure 3.81: Polar plot of 2% 3-NBs, λ_{em} >500 nm, λ_{ex} = 375 nm (red), λ_{ex} = 488 nm (black)

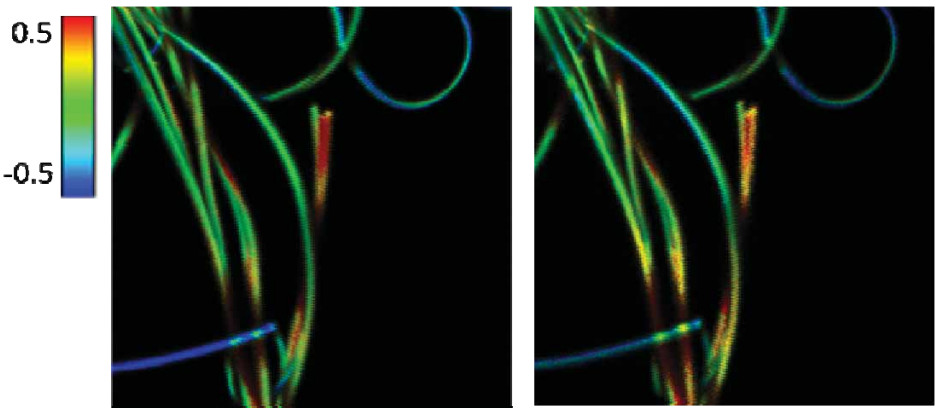

Figure 3.82: Polarization images (30 × 30 μm) of 1% **G16**+0.5% **R16** NBs: λ_{em} >500 nm, λ_{ex} = 375 nm (left), λ_{ex} = 488 nm (right). Color code: polarization

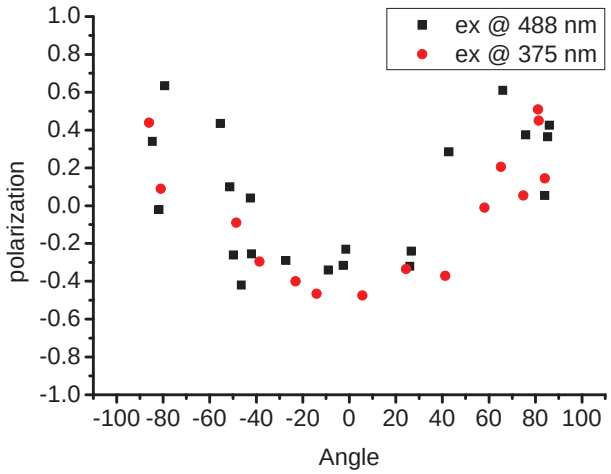

Figure 3.83: Polar plot of 0.5% 3-NBs, λ_{em} >500 nm, λ_{ex} = 375 nm (red), λ_{ex} = 488 nm (black)

3.2.4.5 Discussion

With a spectral overlap between **G16** and **R16** being higher than those between **B16** and tetracenes (J_{GR} = 3.8 × 10^{14} $M^{-1}cm^{-1}nm^4$), the **G16-R16** distance where energy transfer efficiency is 50% (R_0) is 3.73 nm by assuming **G16** and **R16** molecules relative randomly dispersed in NBs (κ^2 = 2/3). It makes the energy transfer possible at low **G16** and **R16** loads.

The emission spectra and emission decay times analysis clearly display the existence of **G16-R16** energy transfer process upon selectively excitation of **B16**. Besides supporting the **G16-R16** ET assumption, the polarization study also reveals the sensitized tetracenes emission is not strongly depolarized during these energy transfer processes.

The efficient intra-nanofiber energy transfer processes are resulting from the high degree of molecular-level order that results from self-assembly and promotes favorable donor-donor and donor-acceptor dipole alignment. Thus, excitation energy can be directly transferred to the acceptors by coulombic energy transfer. Moreover, exciton hopping over **B16** molecules contributes further to the light-harvesting process. The possible energy transfer processes in three component **B16 G16 R16** nanoribbons are sketched in scheme 3.2.[2]

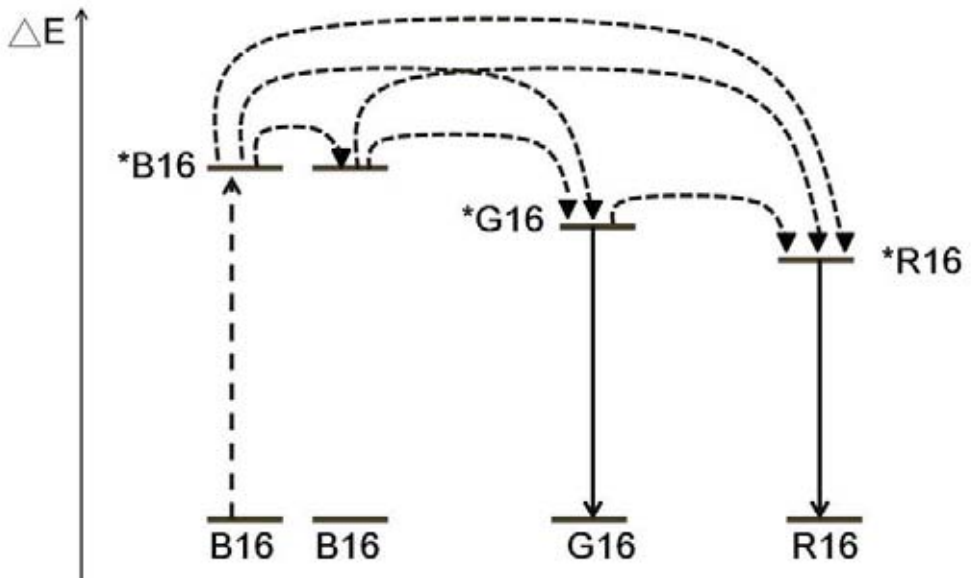

Scheme 3.2: Energy level diagram showing the photophysical processes (absorption: dashed line, radiative decay: solid line, energy transfer process: dotted line) of **B16 G16 R16** three-component system. For clarity, non-radiative decays are not shown.

3.3 Conclusion

1. The nanoribbons of **DPA** derivative **B16** is demonstrated as a highly efficient blue-emitting and light-harvesting matrix for hosting **G16** and **R16** tertacene derivatives in low doping concentration. Similarity of molecular structures favors co-assembling of these three components: all are linear acenes, compatible length of two alkoxy side chains.

The homogeneous dispersion of the acceptors, within the range of maximum 2% equivalents each, is suggested by the steady variation of the spectral properties of the NBs with increasing doping concentrations of the tetracenes. This property yields color-tunable fluorescent nanoribbons system, showing controllable blue, green, orange and white-light emission. The CIE coordinates can be fine-tuned, by adapting the proportions of **B16**, **G16** and **R16**, within the range of values determined by the extreme concentrations of **G16** and **R16** tested (Figure 3.84).

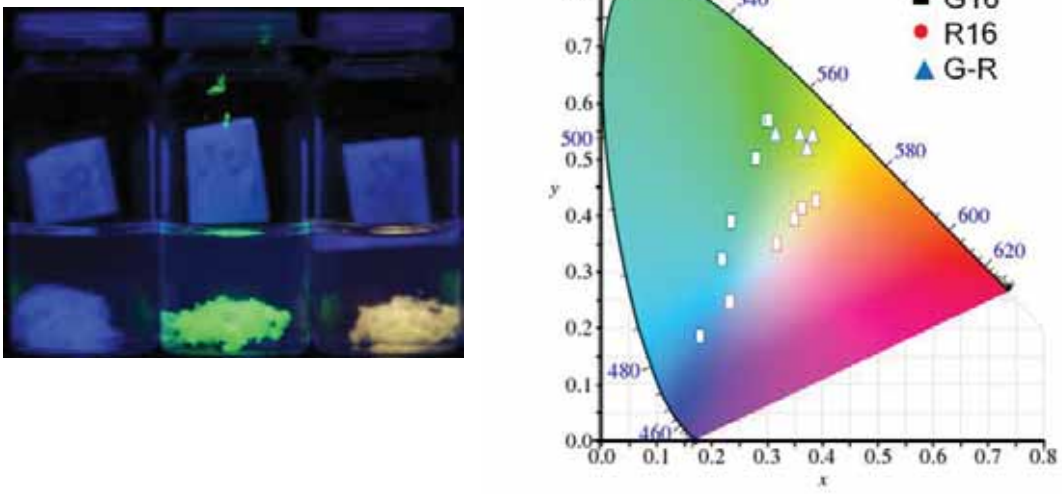

Figure 3.84: Picture of sample vials with **B16**, 1% G-NBs and 2% R-NB (from left to right) under UV light, λ_{ex} = 365 nm (left); CIE 1931 chromaticity coordinates

2. The micro-spectroscopy studies reveal that the nanoribbons individually emit light and the photophysical properties are similar is all the ribbons. The acceptor molecules are thus quite homogeneously dispersed into the ribbons. The efficient energy transfer allows sensitization of acceptor molecules by **B16** donors, while the low absorbance of **G16** and **R16** ensures absence of emission re-absorption. Self-assembly is thus an efficient method to accurately blend multiple components into highly organized and anisotropic nanostructures.

3. The emitted colors result from the sensitization of these components upon UV excitation, exploiting the partial excitation energy transfer from the selectively excited blue-emitting matrix towards the green and orange emitters.

As expected for a Förster-type energy transfer mechanism, **B16** should sensitize **R16** more efficiently than **G16** due to a better spectral overlap. However, the presence of some extend of non-emissive aggregated species does not allow us precisely determined the "real" amount of **R16** molecules doped inside the NBs. The resulted differences of energy transfer efficiency between **G16** and **R16** are not very large and when blended in a three-component system, **G16** and **R16** compete to receive excitation energy from **B16**.

4. The delayed fluorescence of **G16** and **R16** sensitized by **B16** is revealed and characterized by CFM. The reason of they are not clearly revealed by bulk measurement might be following reasons: 1. the power of LED light sources is much lower than the laser of the CFM. 2. The time to accumulate enough counts for analysis in same area is several minutes, which is much longer than CFM analysis (0.6 ms per pixel). It might suggest some larger photo-bleaching. 3. The emission-absorption-reemission mechanism alters the apparent kinetics in the bulk measurements.

The tails of **G16** and **R16** emission profile measured by CFM are well fitted with a t^{-2} power law, suggesting that a triplet-triplet annihilation process is involved. The slowest decay time of **G16** obtained by tri-exponential fitting is shown to be dependent with the excited state density, indicating the involvment of bi-molecular process such as ^{3}T-^{3}T or ^{1}S-^{1}S annihilation.[16] From the simulation of **G16** excited states behaviors, it is found that ^{3}T-^{3}T annihilation is also involved in the second slow decay process, resulting a ~20 ns decay time (measured by selectively excitation upon **G16** in 1% G-NBs) which is much longer than the lifetime in solution (13.8 ns). In high doping concentrations (15% of **G16**), the reduction of the decay times suggests a larger contribution from bimolecular proceses involving singlets, such as ^{1}S-^{1}S annihilation or singlet fission.

Detailed analysis of the FLIM images of G-NBs reveals that the thinner NBs (<0.8μm) exhibit more triplet excited states, and that in the thicker NBs the recombination occurs faster. It can be suggested that a more ordered molecular orientation favors this bi-molecular process induced emission in the large ribbons. Furthermore, this delayed fluorescence of rubrene emission in R-NBs does not contribute as much as tetracene emission in G-NBs. Given the fact that **R16** molecules are less orderly oriented inside nanoribbons, the assumption of ordered molecular packing favors delayed fluorescence might be more solid.

5. This light-harvest color-tuning nanoribbon matrix is a very good system to study photophysical processes such as TT-annihilation, SS-annihilaiton or even singlet fission. Indeed, several paramteres can be tuned such as the nature and the excited state density of the tetracenes, the mean distance between tetracenes and a quite fixed orientation between the molecules. This can be achieved while keeping the tetracenes highly emissive, whereas in 'pure' tetracene systems the emission is very weak and highly influenced by the presence of impurities.[18]

3.4 References

1. Zhao, Y. S.; Fu, H.; Peng, A.; Ma, Y.; Xiao, D.; Yao, J. *Adv. Mater.* **2008**, *20*, 2859.
2. Giansante, C.; Schäfer, C.; Raffy, G.; Del Guerzo, A. *J. Phys. Chem. C* **2012** DOI: 10.1021/jp3073188
3. Giansante, C.; Raffy, G.; Schäfer, C.; Rahma, H.; Kao, M.-T.; Olive, A. G. L.; Del Guerzo, A. *J. Am. Chem. Soc.* **2010**, *133*, 316.
4. (a)Yang, X.; Lu, R.; Xue, P.; Li, B.; Xu, D.; Xu, T.; Zhao, Y. *Langmuir* **2008**, *24*, 13730; (b) Vijayakumar, C.; Praveen, V. K.; Ajayaghosh, A. *Adv. Mater.* **2009**, *21*, 2059; (c) Abbel, R.; van der Weegen, R.; Pisula, W.; Surin, M.; Leclère, P.; Lazzaroni, R.; Meijer, E. W.; Schenning, A. P. H. J. *Chem. Eur. J.* **2009**, *15*, 9737.
5. Kim, D. H.; Lee, D. Y.; Lee, H. S.; Lee, W. H.; Kim, Y. H.; Han, J. I.; Cho, K. *Adv. Mater.* **2007**, *19*, 678
6. Burdett, J. J.; Muller, A. M.; Gosztola, D.; Bardeen, C. J. *J. Chem. Phys.* **2010**, *133*, 144506.
7. Singh-Rachford, T. N.; Castellano, F. N. *J. Phys. Chem. A* **2008**, *112*, 3550.
8. Roberts, S. T.; McAnally, R. E.; Mastron, J. N.; Webber, D. H.; Whited, M. T.; Brutchey, R. L.; Thompson, M. E.; Bradforth, S. E. *J. Am. Chem. Soc.* **2012**, *134*, 6388.
9. Kepler, R. G.; Caris, J. C.; Avakian, P.; and Abramson, E. *Phys. Rev. Lett.* **1963**, *10*, 400.
10. Hall, J. L.; Jennings, D. A.; McClintock, R. M. *Phys. Rev. Lett.* **1963,** *11*, 364.
11. Pope, M.; Swenberg, C. *Electronic Processes in Organic Crystals and Polymers* **1999**, Oxford University Press.
12. Ryasnyanskiy, A.; Biaggio, I. *Phys. Rev. B* **2011**, *84*, 193203.
13. Del Guerzo, A.; Olive, A. G. L.; Reichwagen, J.; Hopf, H.; Desvergne, J.-P. *J. Am. Chem. Soc.* **2005**, *127*, 17984.
14. Renschler, C. L.; Faulkner, L. R. *J. Am. Chem. Soc.* **1982**, *104*, 3315.
15. MSDS of 9,10-diphenylanthracene, CAS: 1499-10-1
16. Larsen, J.; Brüggemann, B.; Polívka, T.; Sundström, V.; Åkesson, E.; Sly, J.; Crossley, M. J. *J. Phys. Chem. A* **2005**, *109*, 10654.
17. (a) Burgdorff, C.; Ehrhardt, S.; Löhmannsröben, H.-G. *J. Phys. Chem.* **1991**, *95*, 4246; (b) Müller, A. M.; Avlasevich, Y. S.; Müllen, K.; Bardeen, C. J. *Chem. Phys. Lett.* **2006**, *421*, 518.
18. Desvergne, J.-P.; Del Guerzo, A.; Bouas-Laurent, H.; Belin, C.; Reichwagen, J.; Hopf, H. *Pure Appl. Chem.* **2006**, *78*, 707.

Chapter 4

Organogelators of 9,10-disubstituted anthracenes

4.1 Introduction

During the last decades, thermo-reversible physical gels generated from low molecular weight organic gelators (LMOG) and an organic solvent have been investigated actively.[1-3] Organogelators can indeed induce unique properties to the resulting soft material[4] and self-assemble to create supramolecular networks of extended nano-objects. Whether in gels or in crystals, the solvent-mediated intermolecular interactions play a critical role.[5,6] This was demonstrated in studies investigating the impact of different solvents on the morphology of the structures formed.[7] Within the same environment however, a molecule tends to reproduce a determined morphology, while polymorphism can be observed when conditions are altered.[5,8] The following work draws our attention on the particular behaviour of an organogelator producing two different, selectable morphs in the same environment.

2,3-didecyloxyanthracene (**DDOA**) has been exploited extensively as a super-gelator, in particular of alcohols and polar solvents such as DMSO. In particular, the soft organogel displayed blue fluorescence which could act as a light-harvesting matrix and be color-tuned by controllable sensitization of tetracene derivatives through efficient energy transfer processes.[9] The design and properties of **DDOA** inspired the following gelators: **DDPEA**, **DCNA**, **F17** and **PT** (Scheme 4.1).

We designed and synthesized these organogelators based on the skeleton of **DDOA**. In addition, to achieve the highly emissive gels, the chosen substituent moieties were all known to give a high quantum yield with regular anthracene. For 9,10-diphenylethynylanthracene (**DPEA**) and 9,10-dicyanoanthracene (**DCA**), which have reported fluorescence quantum yields of 0.85[10] and 0.9[11] respectively. In addition, **DPEA** has been widely used as a fluorophore in the solid state, in organic light emission diodes,[12-14] in chemiluminescent light sources[15-17] and as molecular probes.[18] While the non-substituted **DPEA** adopts a herringbone packing in crystals,[19-21] **DDPEA** is expected to pack differently due to the alkoxy chains.

DCA, a chromophore has excellent electron-acceptor properties, widely used in electron transfer studies.[22] With the electron-donating alkoxy chains modification at 2 and 3 positions of **DCA** core, **DCNA** is expected to exhibit the intramolecular charge-transfer character in the excited state, which would be revealed by solvent polarity effect on its fluorescence. Additionally, it's known that solvent−gelator interactions play a key role in mediating organogel formation and ultimately determine the properties of the gel. By means of investigating the solvent effect of **DCNA** gel emission, we can thus probe the interactions between solvent and the **DCNA** gelators.

9,10-diphenyl-anthracene **(DPA)**, which has been mentioned in chapter 2 that exhibits a fluorescence quantum yields of 0.88,[23] has been chosen as a chormophore moiety of novel organogelator. However, it is known that 2,3-decyloxy-9,10-diphenylanthracene (**B10**) and 2,3-hexadecyloxy-9,10-diphenylanthracene (**B16**) can form micro- or nano-ribbons (chapter 2 and 3) but no gel can be obtained with **B10** or **B16** in any organic solvent.

As this molecule can be chemically tailored, we suggested adapting its structure by adding specific functions in order to modulate the solubility of the molecule and foster the

supramolecular assembly. Fluorinated chains are chosen as the side substituents because they are known to display an extreme hydrophobic and lipophobic nature.[24] Additionally, it has been reported that the perfluorinated alkyl-terminated dendritic molecules induced hexagonal supramolecular structures.[25,26] Besides linear perfluoroalkyl chains, branched perfluoroalkyl chains (fluorous ponytails) are also selected. Horvá and Rábai reported that the presence of fluorous ponytails substituents of the phosphine ligands made their Rhodium-phosphine complex soluble in perfluorocarbons and insoluble in toluene at r.t..[27,50] It interests us to investigate the organogel fabrication in perfluorinated solvents.

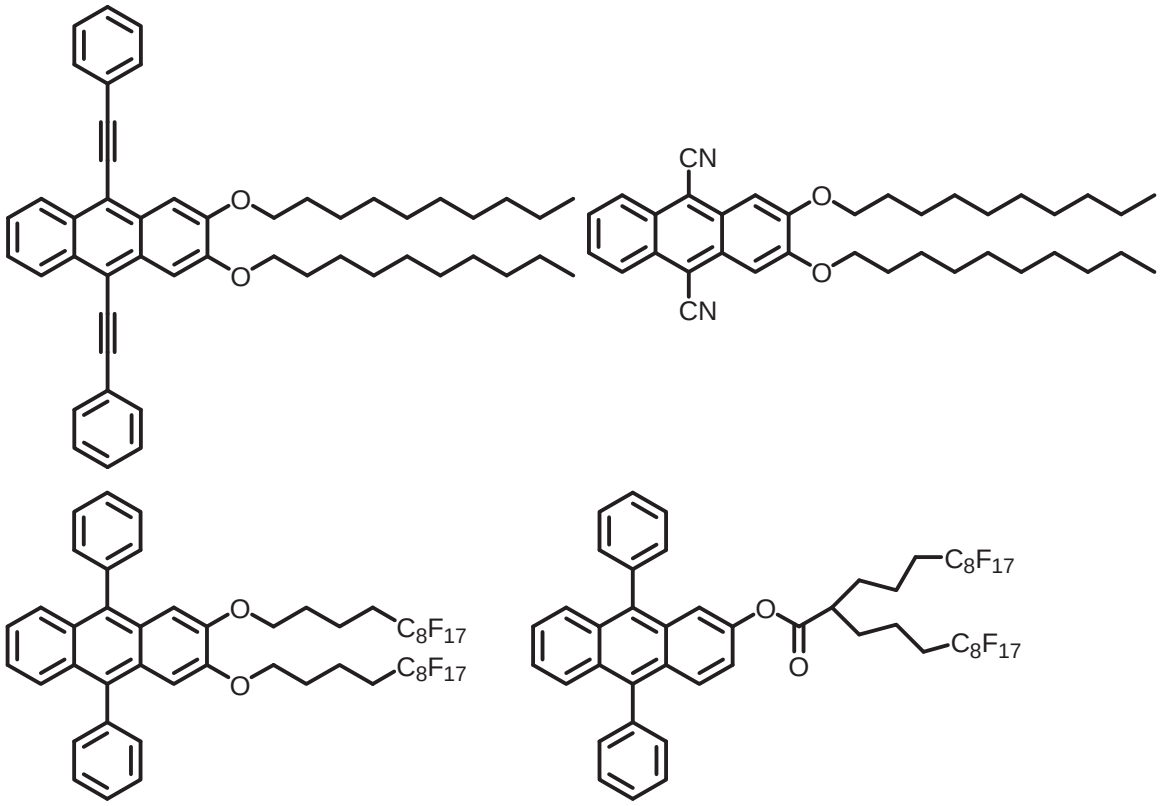

Scheme 4.1: Molecular structures of 2,3-didecyloxy-9,10-diphenylethynyl anthracene (**DDPEA**), 2,3-didecyloxy-9,10-dicyano anthracene (**DCNA**), 2,3-diperfluoro-alkoxy-9,10-diphenyl anthracene (**F17**) and 2-perfluoro-ester-9,10-diphenyl anthracene (**PT**)

4.1.1 Synthesis

All anthracene derivatives synthesized systems were obtained starting from 2,3-*bis*-decyloxy-anthraquinone, which was prepared by known procedures[28] and is a precursor to 2,3-*bis*-decyloxy-anthracene (**DDOA**). Scheme 4.2 shows the reaction sequences used to get the 9,10-dicyano- and 9,10-*bis*-phenylethinyl-**DDOA**.

The systems of **DDPEA** were prepared directly from the anthraquinone, the corresponding Grignard-reagent was prepared first from phenylacetylene and *n*-butyl lithium. The quinone was added under iced cooling and the resulting twofold alcohol was reduced directly with tin(II)-chloride to achieve 42% yield. The second reaction pathway for **DCNA** involves reduction of the quinone to **DDOA** as previously reported[29] and bromination with

tetra-*n*-butyl-ammonium-tribromide (TBATB). Copper(I)-cyanide was used in boiling DMF as a cyanide source to yield **DCNA** with 76%. The synthetic route is first designed by Dr. Christian Schäfer and further repeated and fine-tuning the productive yield by me.

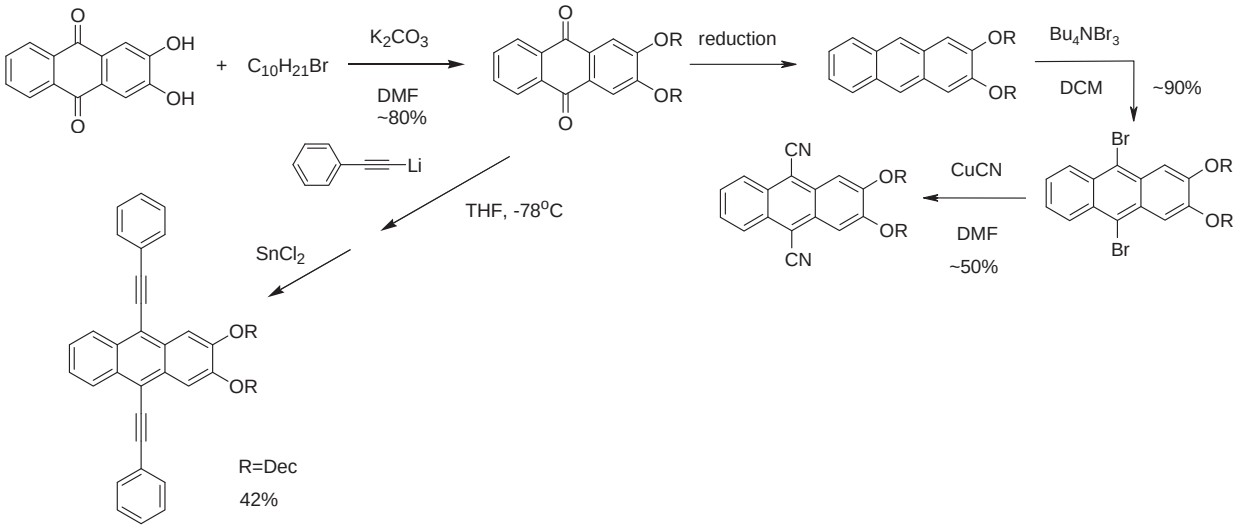

Scheme 4.2: synthetic route for **DDPEA** and **DCNA**

All compounds were compared with **DDOA** regarding absorbance and fluorescence (Table 4.1) in THF solutions (1×10^{-5} M).

As expected, the substitution at 9,10-positions causes a red shift for all compounds compared to **DDOA,** the elongation of dipole moment sufficiently tuned the emission wavelength. A more conjugated substituent induces a larger red shift.

The fluorescence quantum yields of these derivatives are highly improved, although the improvement in **DCNA** is not very big. This improvement is mainly due to the increase of radiative constant k_r, suggesting that the efficient intersystem crossing (ISC) of anthracene from the singlet excited state to the second triplet state[30] is successfully suppressed by extending the conjugation at 9,10- position of anthracene.

Table 4.1: Absorption and emission properties of **DDOA** and derivatives in solution. λ^{abs}, λ^{em} , Extinction coefficient of absorption max $\varepsilon_{\lambda max}$, and Quantum Yield Φ_{em}, Decay Time τ, and radiative constant k_r

	$\lambda^{abs}{}_{max}$ (nm)	$\varepsilon_{\lambda max}$ ($M^{-1}cm^{-1}$)	$\lambda^{em}{}_{max}$ (nm)	Φ_{em}	τ[ns]	k_r [$\times10^8 s^{-1}$]
DDOA	358	7020	409	0.24[a]	6.6	0.36
DDPEA	462	37300	475	0.64[b]	3.6	1.80
DCNA	404	16800	449	0.29[a]	6.5	0.45
F17	372	8600	413	0.75[a]	6.5	1.15

PT	375	11000	414	0.73 [a]	6.7	1.10

[a] 9,10-Diphenyl-anthracene in cyclohexane as reference in solution.

[b] Perylene in cyclohexane as reference in solution.

All the experiments were measured in THF solution.

4.1.2 Gelation of organic solvents

These organogelators dissolution were attempted in fourteen boiling solvents (Table 4.2), such as alcohols, polar solvents and alkanes, and subsequently allowed to cool in a small tube at room temperature to verify the formation of organogels. Typically, 1-3 mg of solid was dissolved in 1 mL of argon-degassed solvent under sonication and subsequent heating. The inverted tube tests (ITT), reported in Table 1, show that **DDPEA** forms gels upon cooling at room temperature in short-chain alcohols such as ethanol, 2-propanol and *n*-butanol at concentrations of 2.5, 3.0 and 2.2 mM, respectively. Lower concentrations did not lead to gel formation. **DCNA**, which has a slightly higher quantum yield than **DDOA**, behaves quite similar regarding the gelation abilities. It can gelate most of the solvent both polar (EtOH, ACE) and non polar (several linear alkanes) at a concentration less than 3.0 mM, which make **DCNA** a very good matrix for organogel solvent polarity study.[31] (Fluorinated chain substituted compounds **F17** and **PT** are discussed in other section.)

Table 4.2: Gelation tests in various solvents. Lower concentrations of compounds did not change observation, or induced loss of gelation property.

	Compound	mmol/L (mg/mL)
Solvent	**DDPEA**	**DCNA**
Methanol	**P**[b] 1.6(1.1)	**P**[b] 3.3 (1.8)
Ethanol	**G** 2.46(1.7)	**G** 5.5 (3.0)
2-propanol	**G** 3.03(2.1)	**CP** 2.4 (1.3)
n-butanol	**G** 2.17(1.5)	**CP** 3.7 (2.0)
n-hexanol	**CP** 3.76(2.6)	**CP** 5.0 (2.7)
n-octanol	**CP** 4.78(3.3)	**CP** 3.7 (2.0)
n-decanol	**S** 2.75(1.9)	**G** 4.4 (2.4)
n-hexane	**S** 1.6(1.1)	**G** 2.6 (1.4)
n-nonane	**S** 3.62(2.5)	**G** 3.7 (2.0)
n-tetradecane	**S** 4.2(2.9)	**G** 5.2 (2.8)

Cyclohexane	**S** 3.33(2.3)	**G** 3.0 (1.6)
Acetone	**P**[b] 3.62(2.5)	**G** 6.8 (3.7)
DMF	**S** 1.6(1.1)	**CP** 3.7 (2.0)
DMSO	**PG** 3.76(2.6)	**CP** 5.2 (2.8)

[a] S = clear solution, P = Precipitate, CP = cloudy precipitate, G = gel, PG = partial gel

[b] Compound doesn't dissolve in boiling solvent.

The gelation tests grant us an insight about the self-assembly properties of **DDPEA** and **DCNA**, further characterization of gels are carried out and demonstrated in following sections.

4.2 Kinetic selection between organogel fibers and nano-ribbons of 2,3-didecyloxy-9,10-bisphenylethynyl-anthracene

The first section is the study of unusual polymorphism of **DDPEA** gel. The variation of its photophysical properties reveals that the **DDPEA** gel readily evolves into another more thermally stable state with time.

4.2.1 Photophysical properties

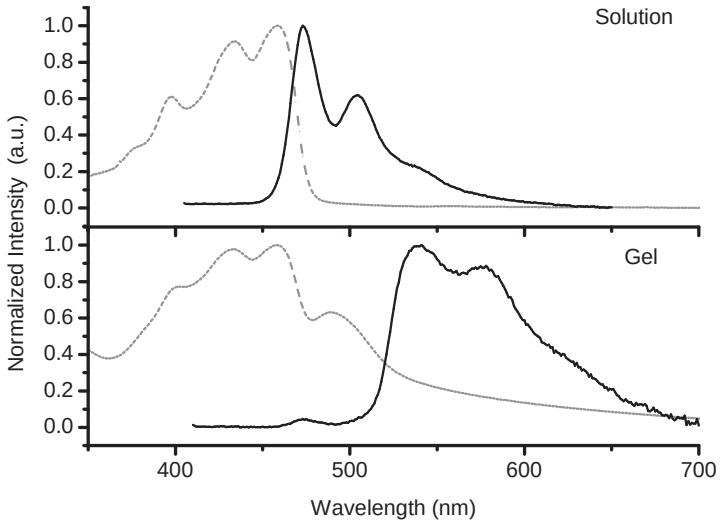

Figure 4.1: Absorption (gray dash line) and emission (black full line) spectra of **DDPEA** in *n*-butanol solution (1.0×10^{-5} M, top) and 'fresh' **DDPEA** gel (3.0×10^{-3} M in *n*-butanol, bottom), λ_{ex}= 402 nm (room temperature).

The absorption and emission spectra of a 'fresh' **DDPEA** gel (3.0×10^{-3} M in *n*-butanol), measured less than 1 hour after dissolution of the solid and cooled to room temperature in air, are shown in Figure 4.1 along with those of the **DDPEA** monomers (1.0×10^{-5} M in *n*-butanol). The monomers exhibit three resolved absorption bands at 398, 434 and 459 nm. In the gel, these three bands become less resolved and a new band emerges at 489 nm (Figure 4.1). A similar red-shifted absorption was previously described for aggregates of **BPEA**.[13]

The emission spectrum of the monomer exhibits a clear vibronic structure, with λ_{max} = 475 nm and a second band at 504 nm. In contrast, the emission intensity of the **DDPEA** gel drops to 8% quantum yield (obtained with an integration sphere) and the spectrum displays two less-resolved bands (λ_{em} = 535 and 580 nm), which are red-shifted by more than 60 nm with respect to that of the monomer. This red-shift is reminiscent of J-aggregate formation. The contribution to the emission of molecularly dissolved **DDPEA** in the gel is difficult to assess uniquely based on this spectrum, since the aggregated state absorbs at the wavelengths corresponding to the first two vibronic bands of the monomer emission. It can thus not be excluded. To correlate absorption and emission characteristics, the **DDPEA** gel was excited at the four absorption peaks (402, 433, 458 and 489 nm). The emission spectra (Figure 4.2)

essentially preserved the same emission bands, but with varying proportions of the two main bands. The proportion of the lower energy 580 nm band is the highest when exciting in the lower energy absorption band at 489 nm, and also when exciting at the highest energy (402 nm). Meanwhile, the first band is most significant when exciting at 458 and 433 nm.

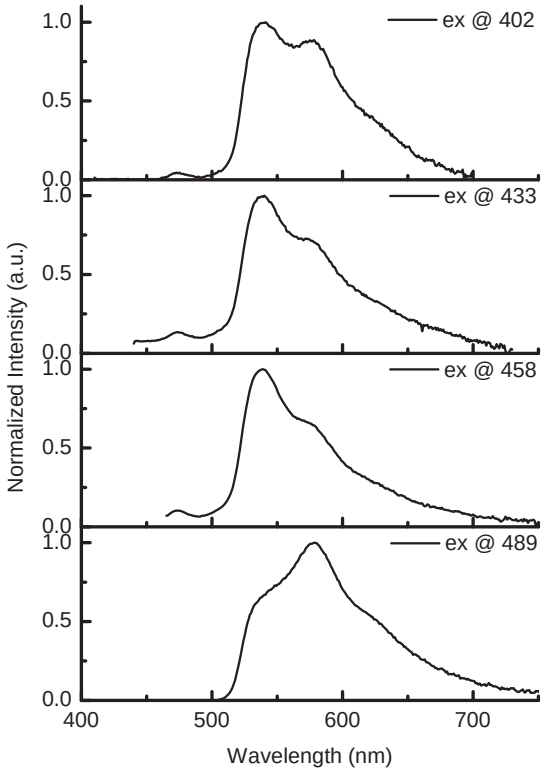

Figure 4.2: Emission spectra of **DDPEA** gel (3.0×10^{-3} M in *n*-butanol,) , λ_{ex}= 402, 433, 458, 489 nm .

Table 4.3: Emission lifetime of the **DDPEA** sample [a]

	Bulk							CFM	
	475 nm	535 nm		580 nm		618 nm		>405 nm	
	τ / ns	Rel. Amp.	τ / ns	Rel. Amp.	τ / ns	Rel. Amp.	τ / ns	Rel. Amp.	τ / ns
Monomer	3.55								
Fresh gel		0.68	3.54	-0.34	2.73				
		0.32	5.88	1.28	5.64			0.90	4.16
				0.06	26.9			0.10	9.33
Aged gel		0.45	0.4			-0.07	0.3	0.21	0.78
		0.55	3.58	0.71	2.78	0.74	2.73	0.73	2.51
				0.29	5.48	0.33	5.86	0.06	6.25

[a] All measurements were carried out at room temperature. The concentration of gel sample in *n*-butanol is 3.0×10^{-3} M. Monomer sample is 1.0×10^{-5} M solution in THF. Bulk samples excited at 455 nm with a nanoled. CFM samples excited at 375 nm with a ps pulsed laser.

Time-resolved fluorescence at the two emission peaks (Table 4.3) was performed to further

attribute the origin of these features. When comparing decays at 535 and 580 nm, one of the decay times is almost identical with a value between 5.6 and 5.9 ns. This component constitutes most of the emission at 580 nm. Additionally, the shorter decay component at 535 nm is in the range of the risetime measured for the emission at 580 nm. This suggests a link between both kinetic processes, although the decay time at 535 nm matches also the one of the monomer in solution (3.55 ns). Finally, a weak but quite long-lived contribution (27 ns) is observed at 580 nm only.

4.2.2 Kinetic evolution of the gel

The most original behaviour of this **DDPEA** gel resides in its kinetic evolution. Several experiments were performed in order to characterize the meta-stability of the system. The characteristic low energy absorption of the gel at 500 nm was monitored while increasing and subsequently decreasing slowly the temperature (0.5 K steps with 1 minute stabilization). The gels also diffract light, contributing partially to the change in transmission at 489 and 500 nm. This experiment (Figure 4.3) reveals that the gel melting is not reversible and that the gel formation does not occur under these slow-cooling conditions, in contrast to a fast-cooling (Figure 4.1).

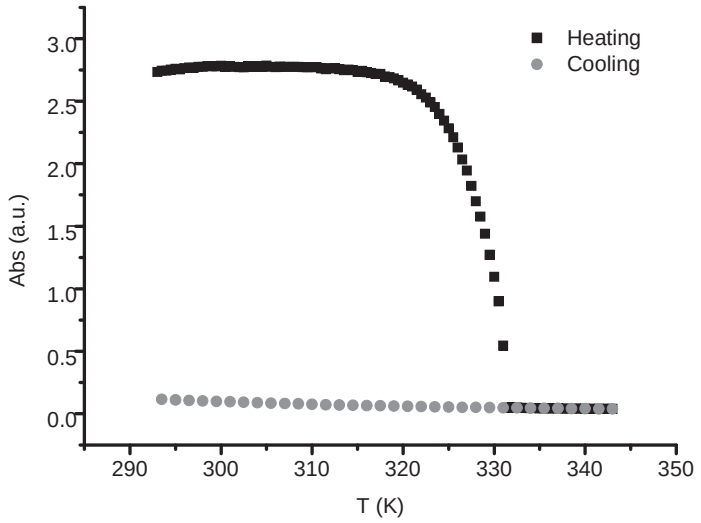

Figure 4.3: Temperature dependence of the aggregation-induced absorption band (500 nm) of the **DDPEA** gel (3.0×10^{-3} M) in *n*-butanol.

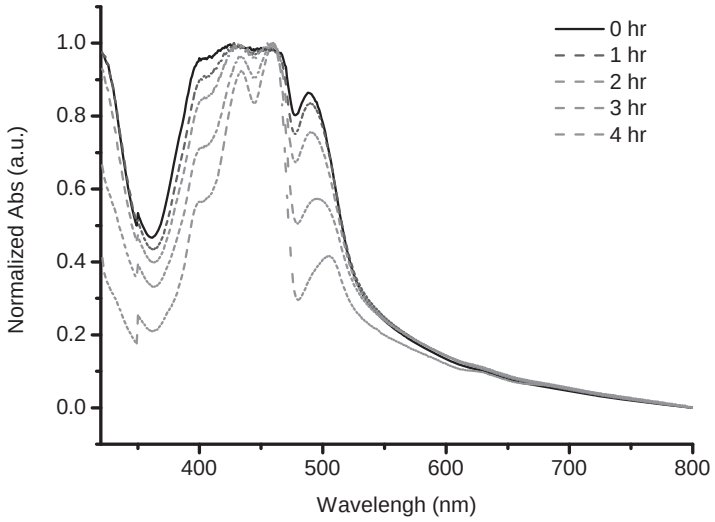

Figure 4.4: Time-dependent absorption spectra of **DDPEA** gel (3.0×10^{-3} M in *n*-butanol)

Kinetic aspects are thus decisive in the formation of the gel, but also in its maturation. Indeed, absorption spectra evolve over four hours at *r.t.*, as shown in Figure 4.4 for one-hour intervals. The first spectrum was recorded just after gel formation and displays the typical band at 489 nm. During the first two hours, the resolution of the vibronic structure increased and the proportions of the different peaks varied. While during that initial phase the lowest energy absorption remained at 489 nm, after three hours this band was red-shifted and reached 500 nm after four hours. The relative intensities of the bands were also affected by the phase separation occurring over time, clearly observed by naked eyes after four hours. Hence, the resolved peaks at 433 and 458 nm could be suspected as monomer absorptions, albeit the complete analysis of the data does not support this as a unique attribution.

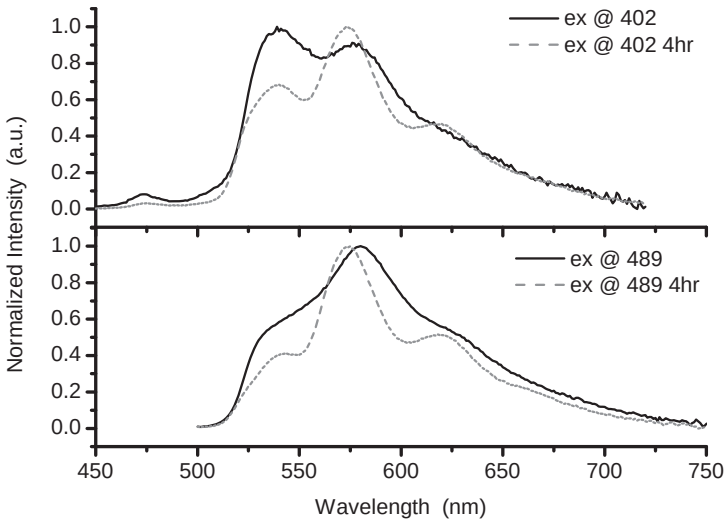

Figure 4.5: Emission spectra comparison of 'fresh' **DDPEA** gel (3.0×10^{-3} M in *n*-butanol) and aged sample (the same sample aging for 4 hr) excited at 402 nm (top), 489 nm (bottom) separately.

The emission spectra of the sample aged for four hours were compared with those of the 'fresh' gel state. The proportions of the lower energy bands are significantly increased in the

aged sample, and the emission maximum at λ_{ex} of 489 nm is shifted from 580 nm to 573 nm (λ_{em} = 575 nm when λ_{ex} = 402 nm). Furthermore, the 620 nm shoulder grew into an obvious band after aging. The decay times of the aged sample (Table 4.3) are quite different from the 'fresh' gel state. Indeed, at 580 nm the rise time (2.7 ns) and the longer lifetime components (26 ns) are no longer observed, while a dominant decay of 2.78 ns adds to the ~5.5 ns component. The same decay times are observed at 618 nm, but interestingly a risetime of 0.3 ns is observed that could be correlated to the short decay time of 0.4 ns measured at 535 nm. At this wavelength, an additional decay of 3.6 ns coincides with earlier observations in the 'fresh' gel.

Since doubts subsist about the presence of monomer, we have performed an additional experiment with a higher concentration of gelator to further favour gel formation. Indeed, a 4 mM gel can be formed upon cooling of the solution at room temperature, although it can easily phase-separate, especially under application of a shear. In this gel, the absorption spectrum also displays a more intense band at 500 nm, slightly red-shifted as compared to the band at 489 nm that is observed in the 3 mM gel. An increased light scattering is also present.

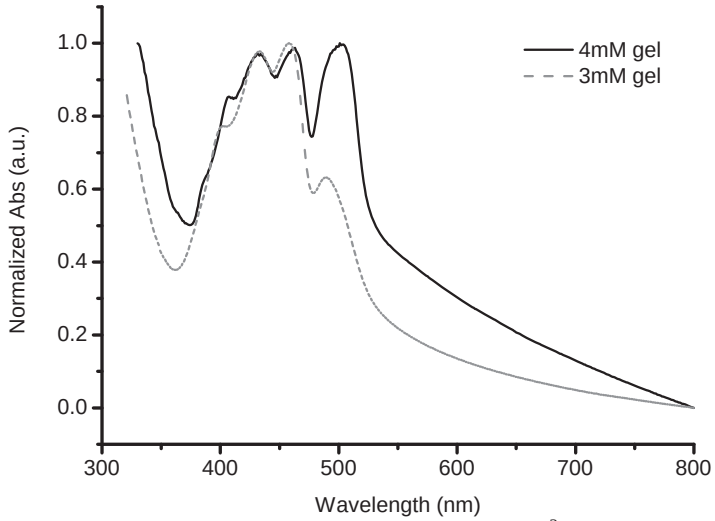

Figure 4.6: Absorption spectra of 'fresh' **DDPEA** gel in 3.0×10^{-3} M (gray dash line) and 4.0×10^{-3} M (black full line) in *n*-butanol

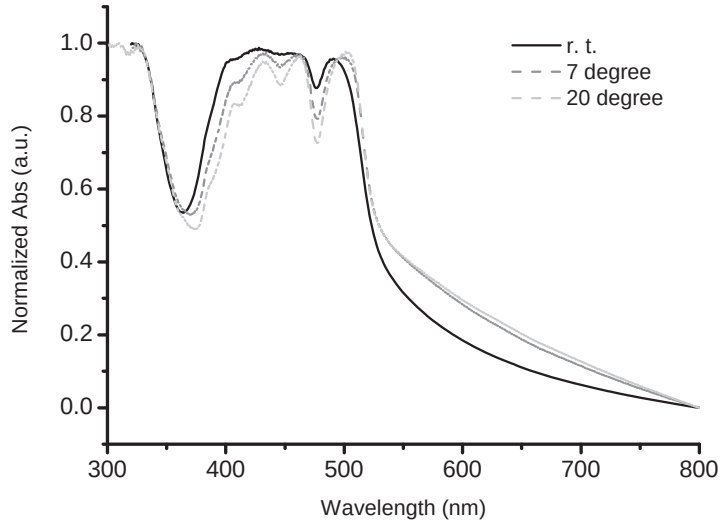

Figure 4.7: Absorption spectra of a 'fresh' **DDPEA** gel (4.0×10^{-3} M in *n*-butanol) and subsequent treatment at 7°C and 20°C.

A more precise observation of the kinetic evolution of the 4 mM sample reveals that the 489 nm absorption is an intermediate before obtaining the final aggregate absorbing at 500 nm. This is shown when comparing a gel obtained by quick air-cooling at room temperature (λ_{abs} = 489 nm), a further cooling of the gel at 7 °C (λ_{abs} evolves to 500 nm) and a slow reheating of the same sample at 20 °C (λ_{abs} = 500 nm).

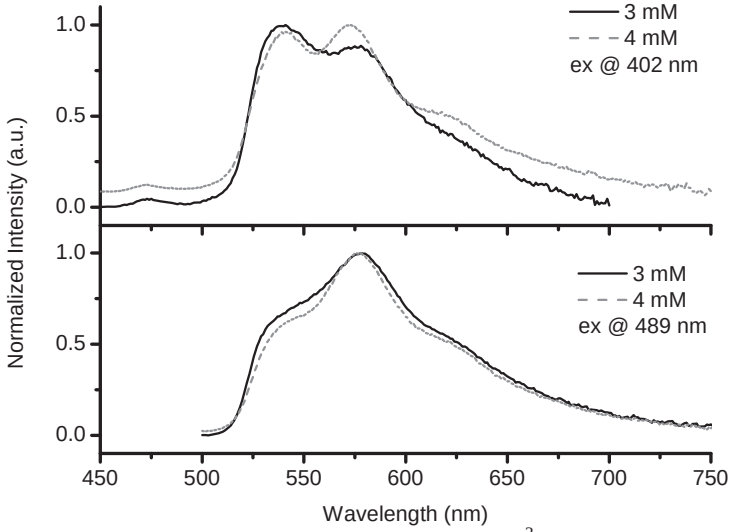

Figure 4.8: Emission spectra of 'fresh' **DDPEA** gel in 3.0×10^{-3} M (gray dash line) and 4.0×10^{-3} M (black full line) in *n*-butanol

In the emission spectra, the 4 mM gel at room temperature (Figure 4.8) displays a higher proportion of the 580 nm band and the shoulder at 620 nm appears more clearly. The vibronic structure is also more resolved in the 4 mM sample than in the fresh 3 mM gel. Both absorption and emission properties tend thus to suggest similarities between the 4 mM gel and the aged 3 mM samples.

4.2.3 Confocal Fluorescence Microscopy

Confocal fluorescence microscopy (CFM) is the technique of choice to study the change in morphology of the **DDPEA** gel, since it can be performed both in a solvated organogel and on xerogels (desolvated organogel). The FLIM images (Figure 4.9a) show that the fresh **DDPEA** 3 mM organogel sample is composed of a network of interlaced fibers, which are not terminated and have a width that is lower or similar to the optical diffraction limit (230 nm). Similar observations had been made with other organogels, as for example **DDOA** mentioned in the introduction. If the air-drying of the sample is allowed to occur within few minutes, the nanofibers are preserved and deposit flat on the glass slide (Figure 4.9b). No dissolved monomer remains under these conditions. In contrast, when the solvent is kept the sample ages and stiffer, wider fibers appear. These are more reminiscent of nano-ribbons or nano-crystals, although the images cannot clearly establish their thickness and shape. Thus, after two hours both nanofibers and nano-ribbons are present in the same area of the sample

(Figure 4.9c). Interestingly, a fiber seems to merge with a ribbon on the top-left side of the image. A very clear transformation is observed after four hours of ripening. Indeed, in Figure 4.9d only ribbons are detected.

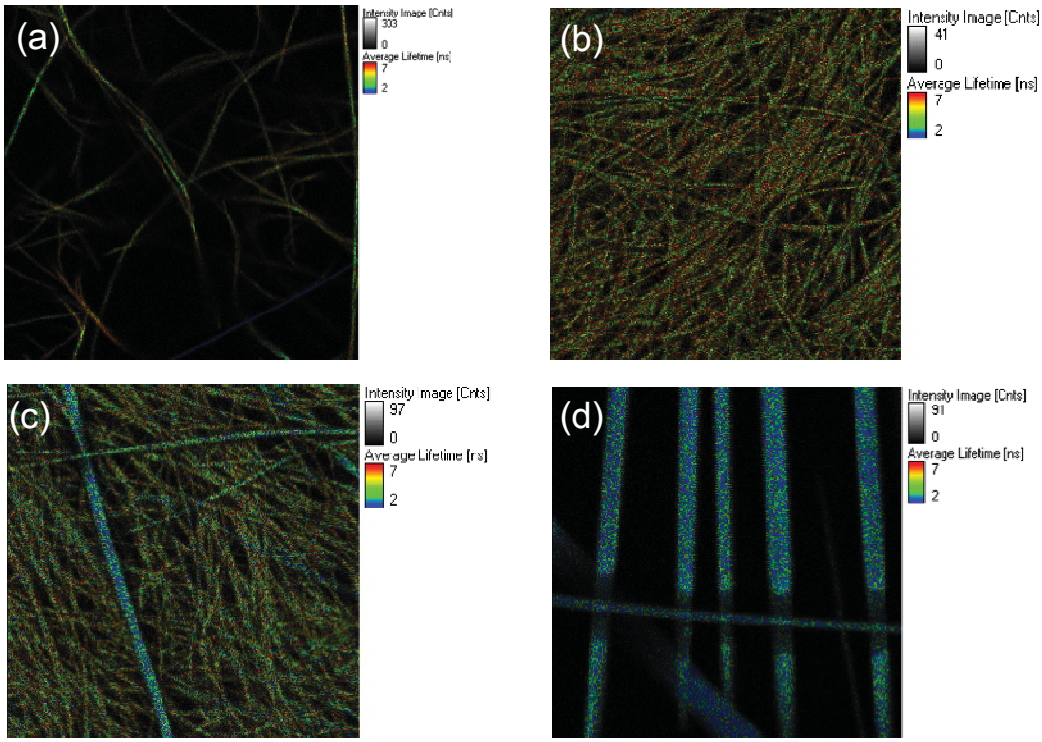

Figure 4.9: FLIM images (a: 40 × 40 μm; b,c,d: 30 × 30 μm) of 3 mM **DDPEA** in *n*-butanol at *r.t.*, λ_{ex} 375 nm, λ_{em} > 405 nm (color code: average decay time): (a) solvated gel fibers (organogel); (b) non-aged sample air-dried (typical widths of fibers ≤230nm); (c) sample aged for 2hr in *n*-butanol and then dried; (d) sample aged for 4hr in *n*-butanol and then dried.

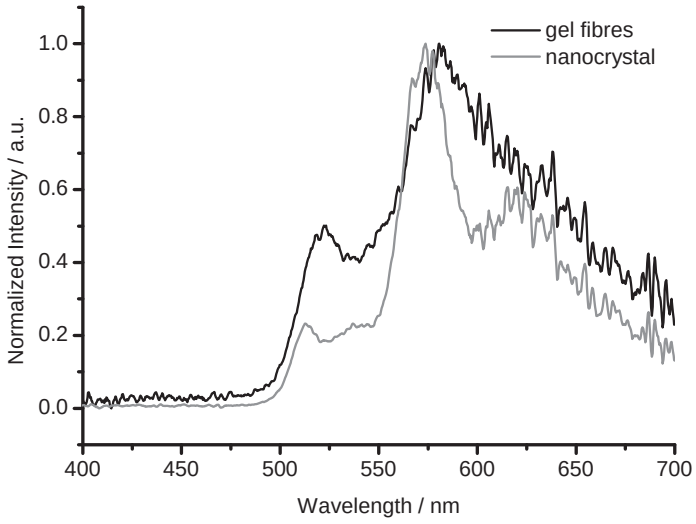

Figure 4.10: Average spectra obtained by confocal fluorescence microscopy of several single objects (λ_{ex} 375 nm): (black full line) dry organogel fibers, areas similar to Figure 9b; (gray full lines) dry crystal-like objects, areas similar to Figure 9d

The fluorescence spectra and the emission decays of single nano-objects can be analyzed

by CFM. Figure 10 shows the typical spectra of two types of objects, obtained on areas similar to Figure 9b and Figure 9d. They reveal that the larger objects are at the origin of two low energy emission bands, corresponding to those at 573 and 620 nm obtained in the bulk measurements (a higher energy band is weak). In contrast, the nanofibers display a more intense emission at 535 nm and a maximum which corresponds to the 580 nm band in the bulk measurements. The evolution of the emission spectra in the bulk is thus clearly related to the transition from nano-fibers to larger objects. This is also confirmed by the analysis of the fluorescence decays. Although not performed in the same conditions as in the bulk (in CFM λ_{ex}: 375 nm and λ_{em} > 405 nm), the analyses of the fluorescence images revealed longer decay-times in nanofibers as compared to nano-crystals, in agreement with the bulk measurements. Indeed, the most significant decay time in nanofibers is 4.2 ns (90% relative amplitude), while it is 2.5 ns in the nanocrystals (73%). The FLIM images also clearly show that when both types of objects are present simultaneously (Figure 4.9c), the larger object's emission is shorter-lived (blue color-code).

4.2.4 Discussion

DDPEA organogels can be formed by air-cooling a *n*-butanol solution to room temperature. However, this soft material constituted of a network of nanofibers entrapping the solvent is metastable and evolves over time. Confocal fluorescence microscopy shows indeed that the nanofibers transform into larger objects, reminiscent of ribbons or nano-crystals, and the material turns thereupon into a non-homogeneous dispersion of objects. This evolution can be attributed to an 'Ostwald ripening'and occurs within hours in a 3 mM sample, and is further favoured at 4 mM of **DDPEA**. UV-visible absorption and fluorescence spectroscopies have shown that this morphological evolution is inducing, or is due to, a change of the aggregation of the gelator molecules. Indeed, the absorption and the emission are characterized by a strong red-shift as compared to the molecule in solution. This indicates the formation of J-type aggregates, as already observed for **BPEA** molecules in crystals.[17] These J-aggregates are not necessarily the only type of molecules present in the nano-objects, but they are at the origin of most of the emission. Besides direct excitation, their sensitization can occur by energy transfer and/or exciton hopping.

More precisely, three spectral and photophysical signatures can be distinguished in the different samples studied, although the emissions partially overlap and a more complex situation might be present. We thus propose a photophysical scheme for both nanofibers and nanoribbons (Scheme 4.3). First, some monomer appears to be present in the fresh 3 mM gel. Although almost no emission is observed below 500 nm, as would be expected for the monomer, this can be due to reabsorption of the emission by the aggregates. The third vibronic band of the monomer however can contribute to the emission at 535 nm, with a lifetime of 3.6 ns. This emission is weaker in the more concentrated and aged samples, and is not expected in the dry samples observed by CFM. The absorption bands at 433 and 458 nm are nevertheless still intense in the aged and concentrated samples, although the relative

intensities of monomer and aggregate absorption bands could be affected by some inhomogeneities in the sample due to phase separation. This does nevertheless not exclude the possibility that a first type of aggregate, M-agg, is present and displays absorption bands similar to those of the monomer. These M-agg would emit at similar wavelengths as the monomer and sensitize the lower energy J-aggregates, thus being responsible for the risetimes observed by time-resolved fluorescence in nano-fibers and –ribbons.

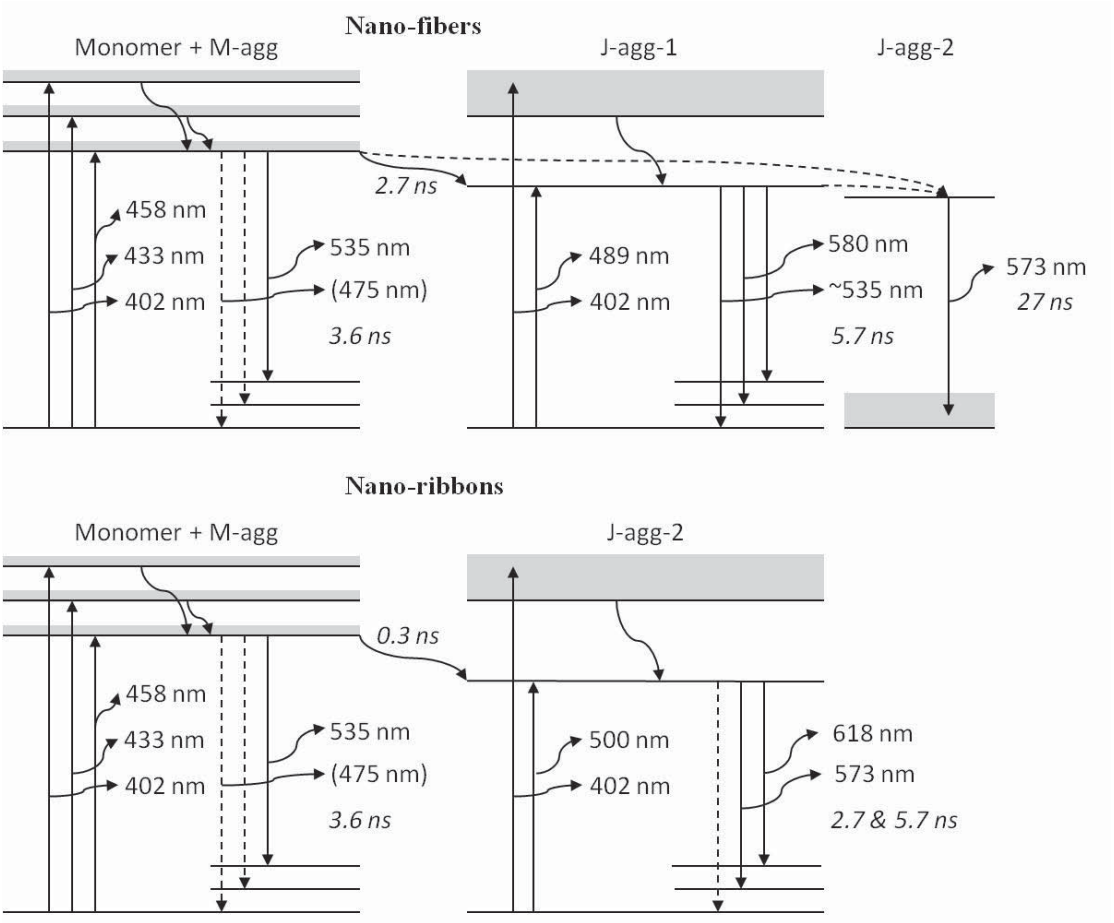

Scheme 4.3: Photophysical pathways in nano-fibers (fresh gel, top) and nano-ribbons (aged sample, bottom). Straight arrows are optical transitions. Dashed arrows indicate transitions that are not clearly observed in the spectra. Gray boxes indicate uncertainties on energy of the state.

As mentioned, J-aggregates are most probably responsible for the two other spectral features, which are characteristic of the two morphs. The differences in energies of the transitions can indicate a coupling of dipoles with different strengths, linked tentatively to two different packing geometries. J-agg-1 absorbs at 489 nm, contributes mostly to the emission at 535 nm and 580 nm with a decay time of 5.7 ns and is formed in the fresh gel, while it is less present in aged samples. J-agg-2 is mostly observed in the aged sample, where it absorbs at 500 nm and emits essentially at 573 and 618 nm with two decay times of 2.7 and 5.7 ns. The correspondence of lifetimes of J-agg-1 and J-agg-2 would be a coincidence in this case. J-agg-2 could also be responsible for the weak long-lived emission at 580 nm in the gel (Scheme 4.3). The main bands at 580 and 573 nm are attributed to the second vibronic band

of the aggregates. The 0-0 transition in J-agg-2 is indeed weak. In both gels and aged sample, the correspondence of risetimes of J-agg-1 and J-agg-2 emission and one decay time at 535 nm, attributed to M-agg, suggests that the latter photosensitizes partially the J-aggregates. This process would be favoured by the overlap of the emission of M-agg and the absorption of the J-aggregates and would explain the absence of emission by M-agg. Further studies are nevertheless necessary to attribute the process to a Förster-type energy transfer mechanism. Several other energy transfer processes can occur in nanofibers and nanoribbons, including exciton hopping (homo-transfers) or energy transfer to non-emissive traps.[13,27] The shorter decay- and rise-times in the nano-ribbons indicate that these processes are more efficient in the larger structures than in the nanofibers. Furthermore, the difference in decay times of J-agg-2 in the two morphs could be linked to the existence of homo-transfer in the ribbons, leading efficiently to the transport of excited states to shorter-lived traps. In contrast, the J-agg-2 are present in lesser quantities in the nano-fibers, thus ‘diluted’, do not undergo homo-transfer and trapping and thus emit with long lifetimes. Further studies are also necessary to confirm these mechanisms.

The experiments at different ripening times and concentration of gelator indicate that J-agg-2 is the most thermodynamically favoured packing, while J-agg-1 is kinetically favoured and trapped in the fresh gel state. The current experimental data do not yield the molecular packing, but clearly indicate that a rearrangement of the intermolecular interactions occurs. This could be due to the bulkiness of the substituents, both in positions 2,3 and in positions 9,10 of the anthracene. Interestingly, this change in packing not only influences the local structure of the nano-objects, but also induces a whole morphological change of the material. Thereupon, as suggested by CFM (Figure 4.9c), nanofibers seem to merge into nanoribbons or nanocrystals.

4.3 Effect of solvent in DCNA Gels

The formation of an organogel is both the result of the gelator-gelator interactions and gelator-solvent interactions.[32–34] However, the mechanism of molecular assembly in different solvents remains largely unknown. The interactions of solvent and gelator molecules govern the process of gelation and the physical behavior of the resulting gels. Therefore, key information on gel assembly is needed with respect to gelation in different solvents to reveal the relationship between solvent-gelator interactions during gelation.[35-42] Furthermore, in previous studies the solvent polarity effect investigation are focused on the hydrogen-bonding efficiency in organogels,[43] and their discoveries are mainly based on the mechanism that polar solvents interact with the gelators strongly and thus weaken the H-bonding between the gelators. van Esch *et al.* found that the thermal stability of the bis-urea organogels increases with the polarity of the solvent.[44] In their system, both H-bonding and solvophobic interactions exist in the gels. However, solvent effects on organogels only driven by van der Waals interactions are rarely reported.[45] Our organogelator **DCNA**, which is derived from **DCA**, exhibit a good gelation ability of both polar and nonpolar solvents (Table 4.2) via van del Waal interactions, is expected to be a good candidate to perform the solvent effect investigation on the organogels.

4.3.1 Solvent effect in solution

To verify the solvent polarity dependency of the spectroscopic properties of **DCNA** in solution, 1×10^{-5} M **DCNA** was studied in 10 different solvents. Figure 11 shows a very small red shift and a variation of the vibrational structure in the absorption spectra with increasing the solvent polarity, indicating little ground state interaction between **DCNA** and solvent molecules. In fluorescence spectra of **DCNA**, strong red shift and the loss of vibronic structure in different solvents are observed (Figure 4.12). These results suggest that **DCNA**-solvent interaction stabilized the lowest singlet excited state much more than the ground state, indicating that the charge-transfer character is more evident in the excited state than that in the ground state. This fact can be further shown at Figure 4.13, which displays linear dependency of the maximum of emission spectrum the resulting Stokes shift with solvent polarity.

The solvent polarity here we adopted is the Lippert-Mataga[46,47] solvent polarity parameter Δf, which is defined as the following equation :

$$\Delta f = [(\varepsilon^2 - 1)/(2\varepsilon + 1)] - [(n^2 - 1)/(2n^2 + 1)]$$

Where ε is the dielectric constant of solvent, and n is the refractive index of solvent.

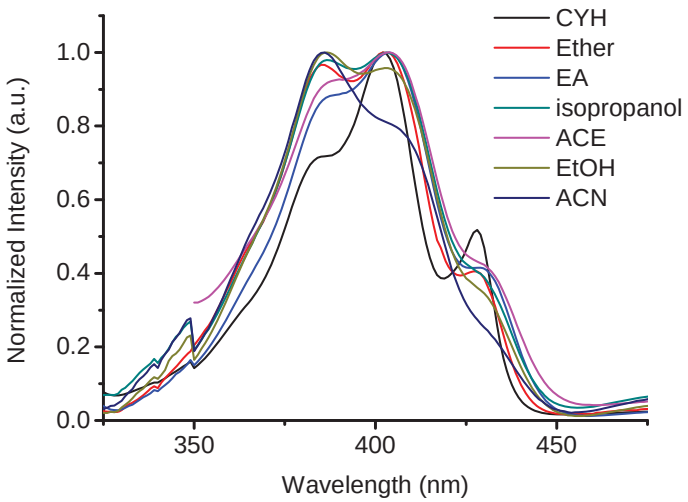

Figure 4.11: Normalized absorption spectra of **DCNA** solution in different solvents (1×10^{-5} M)

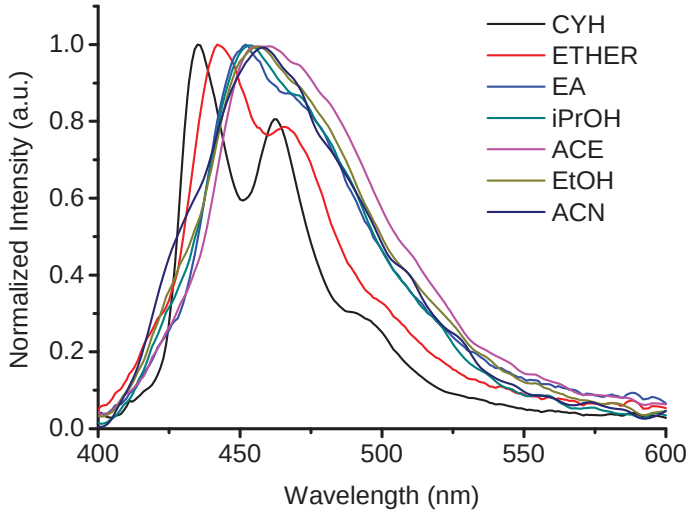

Figure 4.12: Normalized emission spectra of **DCNA** solution in different solvents (1×10^{-5} M), λ_{ex}= 402 nm

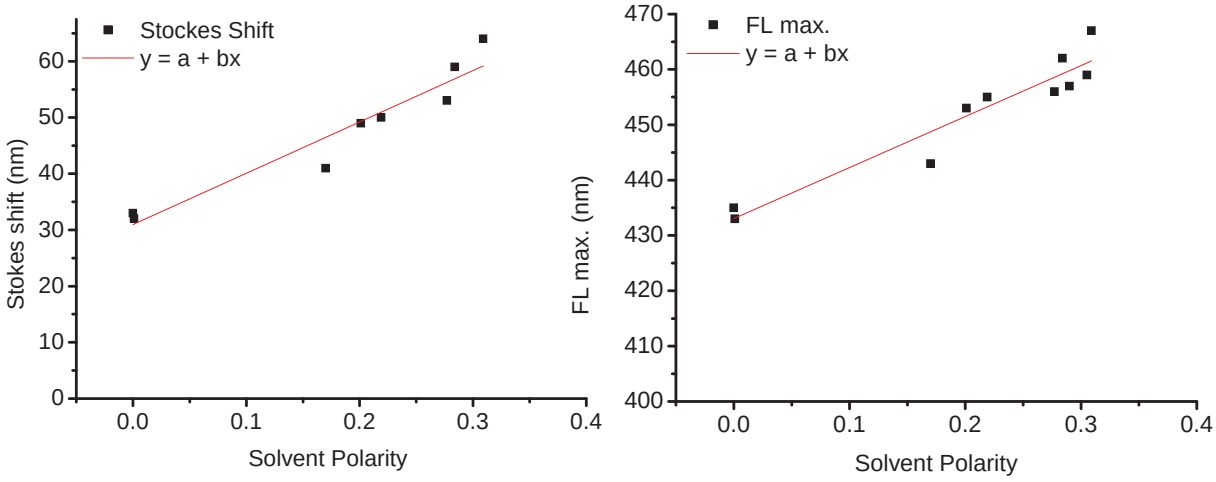

Figure 4.13: Stokes shifts (left) and FL max. (right) of **DCNA** (1.0 x10^{-5} M) in different solvents versus solvent polarity derived from the Mataga scale

DCNA emission decay in most of these solutions can be represented by bi-exponential functions except that of cyclohexane sample. Table 4.4 reveals that the slower decay times, which are named as T1, are all between 6.2 ns and 6.8 ns. They are similar to the mono-exponential decay time of **DCNA** emission in CYH, which can be attributed to the decay from ^{1}S to the ground state. On the other hand, the faster decay time T2 (~2.5 ns) only appears in a more polar environment with a contribution about 10%. Due to the major contribution of the fluorescence decay resides in T1 (from 86%~92%), we approximately use T1 and quantum yield of **DCNA** in these solvents to estimate the radiative constant kr_1. It is revealed that kr_1 for most of the samples are similar to the kr of CYH sample ($5.3\times10^7 s^{-1}$), further supported our suggestion.

The presence of T2 can be due to several possibilities: first, small aggregates of **DCNA** molecules formed in the polar solvent; second, the formation of exciplex between **DCNA** and solvent molecules. The first assumption can be verified by further experiments with lower **DCNA** concentrations. The second assumption, **DCNA**/ solvent exciplex formation might be able to be excluded due to the fact that 9,10-dicyanoanthracene is known to form exciplex with aromatic compound as stilbene[48] and hexamethylbenzene.[49] In this case, the probability of **DCNA**/solvent exciplex formation should be low.

Table 4.4: Quantum Yield Φ_{em}, Decay Time τ of **DCNA** solutions in different solvents with solvent polarity derived from Mataga scale

Solvent	$\triangle f$	Φ_{em}[a]	Rel. Amp.1	τ1 [ns]	Rel. Amp.2	τ2 [ns]	kr_1 ($\times10^7 s^{-1}$)
CYH	0	0.32	--	6.0	--	--	5.3
Ether	0.17	0.26	0.91	6.6	0.09	2.5	3.9
EA	0.20	0.28	0.92	6.4	0.08	2.5	4.4
*i*PrOH	0.28	0.35	0.88	6.8	0.12	2.6	5.1
ACE	0.28	0.26	0.92	6.2	0.08	2.5	4.2
EtOH	0.29	0.35	0.86	6.6	0.14	2.4	5.3
ACN	0.31	0.35	0.86	6.6	0.14	2.5	5.3

[a] Measure with 9,10-diphenyl anthracene in THF as a reference

4.3.2 Photophysical properties of Gel

From the gelation test of **DCNA** (Table 2), we found out that **DCNA** can gelate several solvent regardless of the polarity. However, according to Olea *et al.*'s work,[33] **DCA** tends to form exciplex with electron-donating solvent molecules. To simplify the gel-solvent polarity system study, cyclohexane (CYH) and acetone (ACE) are selected to process further investigation.

For the absorption spectra in solution and gel, we observed a new band emerging at 449 nm in the gel state. There is a significant red shift from solution to gel in fluorescence spectra, more than the solvent effect between CYH and ACE. The absorption and emission spectra of **DCNA** in CYH and ACE solutions display the loss of vibronic structure in both cases, and a red shift (~25 nm) in fluorescence (Figure 14). On the other hand, except the loss of vibronic structure of absorption spectra of ACE gel, the spectral features are quite similar in CYH and ACE gel.

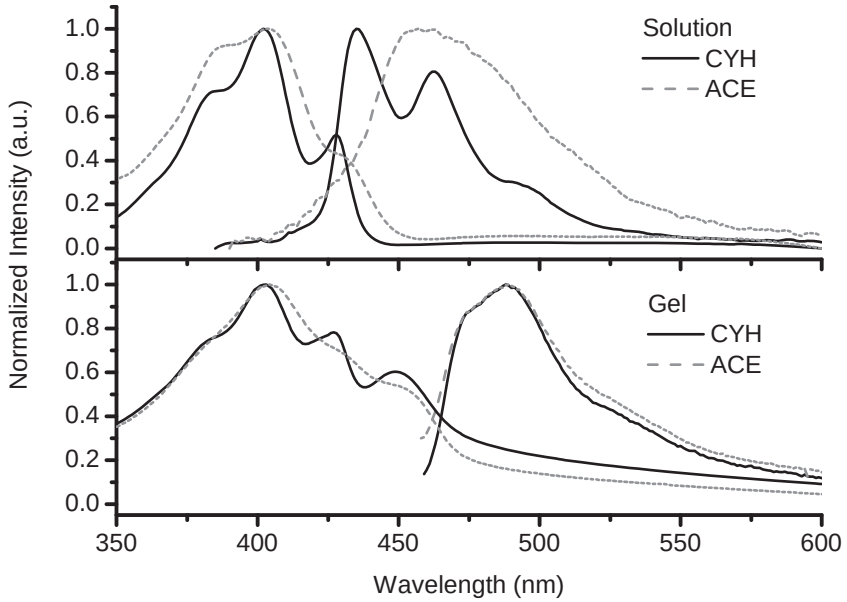

Figure 4.14: Normalized absorption and emission spectra of **DCNA** in cyclohexane (black full line), acetone (gray dash line) (1.0×10^{-5} M, top) and **DCNA** gel (bottom) (4.6×10^{-3} M in CYH, 7.0×10^{-3} M in ACE) λ_{ex}= 402 nm for soln.; λ_{ex}= 449 nm for gel

In the previous section, we have seen that the emission spectra of gels can differ when exciting at different wavelength, which reveals several types of aggregates in the gel. Therefore, **DCNA** gel in CYH and ACE are excited at three absorption peaks (403, 427 and 449 nm) in order to correlate the absorption and emission characteristics.

The emission spectra of CYH gel (Figure 4.15, left) exhibit the same emission bands (474, 488nm), but with varying proportions of the two main bands. The proportion of the lower energy 488 nm band is the highest when exciting in the lower energy absorption band at 449 nm. Meanwhile, the first band is most significant when exciting at 403 and 427 nm. For ACE gel, the emission spectra do not show any variation with varied excitation wavelength.

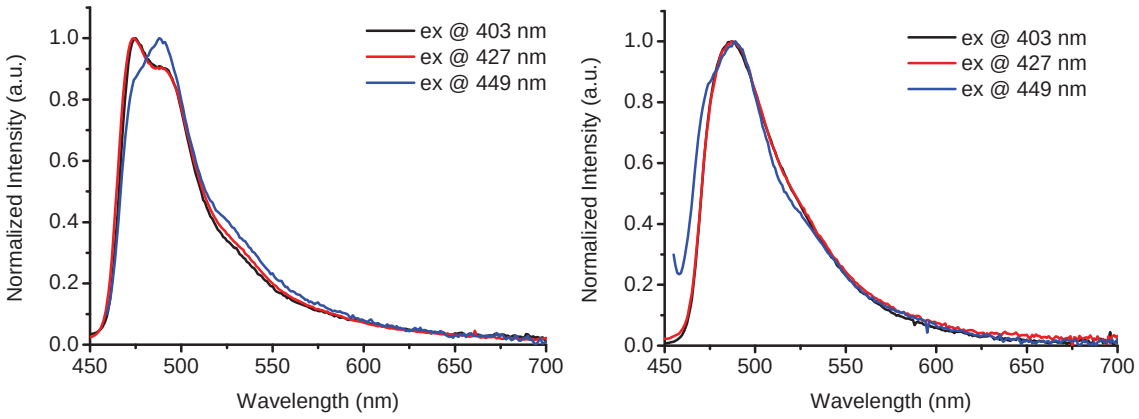

Figure 4.15: Emission spectra of **DCNA** gel (4.6×10^{-3} M in CYH, left; 7.0×10^{-3} M in ACE, right), λ_{ex}= 403, 427 and 449 nm.

4.3.3 Confocal Fluorescence Microscopy

Confocal fluorescence microscopy reveals the differences of morphology and lifetime in CYH and ACE gels. The width of gel fibres is measured by fitting the intensity profile with Gaussian amplitude function. The width of **DCNA** gel fibers in CYH (4.6 mM) is about 500 nm (statistical value from tens of fibers). For **DCNA** in ACE gel, the width of gel fiber is 800~ 1000 nm, much wider than the CYH gel fibers. The FLIM images of gels show excited decays can be fitted by tri-exponential functions (Figure 4.16). The decay times of ACE gel are evidently longer than that of CYH gel (Figure 4.17).

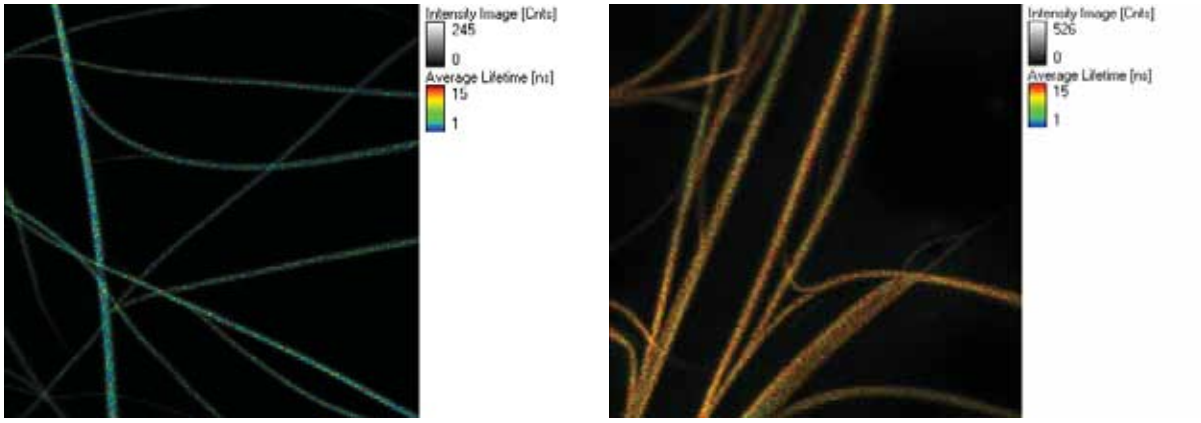

Figure 4.16: FLIM images of 4.6 mM **DCNA** gel in CYH (left), 7.0 mM gel in ACE (right), λ_{ex} =375 nm, λ_{em} >405 nm (40 × 40 μm) (color code: average decay time)

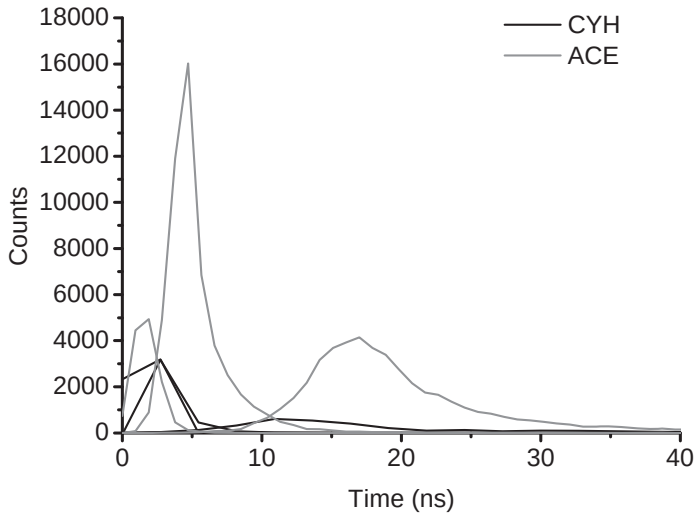

Figure 4.17: Decay times distributions of **DCNA** in CYH gel (black) and **DCNA** in ACE gel (red), λ_{em} >405 nm, λ_{ex} = 375 nm

4.3.4 Kinetic evolution of gel

To further differentiate the CYH and ACE gels, the characteristic low energy absorption of the gel at 449 nm was monitored while increasing and subsequently decreasing slowly the temperature (0.5 K steps with 1 minute stabilization). The light diffracted by gels also partially contributed to the variation in transmission at 449 nm especially in the case of ACE gel. The behaviour of CYH gel observed in this kinetic gel formation study is more “gel-like” (Figure 4.18). When the temperature is lower than 293 K, the absorption at 449 nm significantly increases, suggesting the gel formation occurred below the certain temperature. On the other hand, ACE gel displays a relatively slow and small variation during heating and especially cooling process. Even being heated to 333 K, the absorption of ACE gel sample at 449 nm is still quite high (Abs ~0.6, Figure 4.19), indicating the presence of aggregation species. The maximum temperature applied is set at 333K by the limitation of boiling point of ACE and CYH. During the cooling process of ACE gel, the absorption at 449 nm did not increase much below 305 K till 288 K, indicating the re-formation of aggregation is not complete and slower than that of CYH gel.

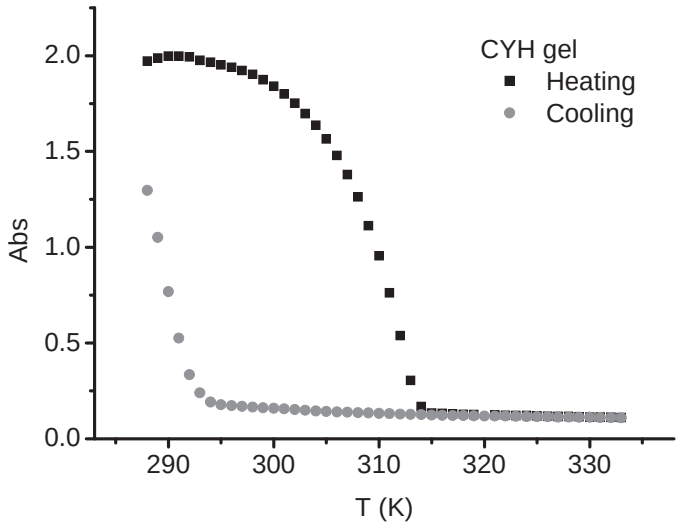

Figure 4.18: Temperature dependence of the aggregation-induced absorption band (449 nm) of the **DCNA** gel (4.6×10^{-3} M) in CYH.

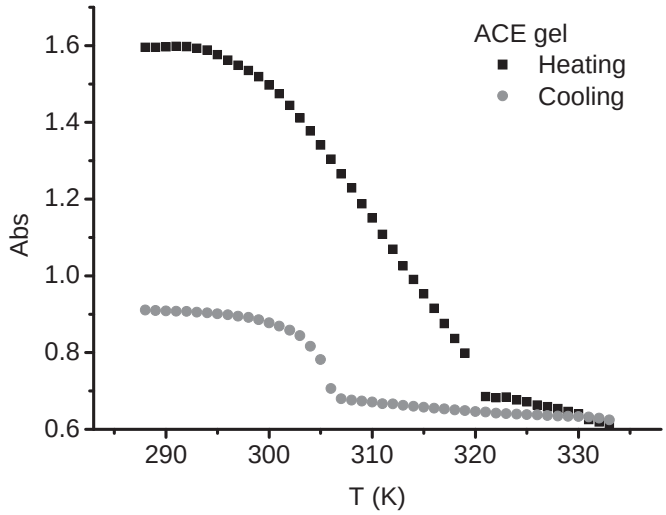

Figure 4.19: Temperature dependence of the aggregation-induced absorption band (449 nm) of the **DCNA** gel (7.0×10^{-3} M) in ACE.

4.3.5 Discussion

DCNA monomer emission displays sensibility to polar environments, the position and vibronic structure of the emission spectrum show a strong dependence on the solvent while the ground state absorption shows much less solvent sensitivity.

Once **DCNA** forms a gel, the emission of gels in CYH and ACE unexpectedly behaves quite similar to each other, suggesting the influence of gelator-gelator interaction on photophysical behavior is much stronger than gelator-solvent interaction. Furthermore, the red-shift of emission and of the absorption spectra in both CYH and ACE gel indicate the formation of J-aggregates. This aggregation-induced red-shift emission does not display solvent polarity sensitivity.

Table 4.5: photophysic properties of **DCNA** in solution and in gel state.

	solvent	λ^{abs}_{0-0} (nm)	λ^{em}_{0-0} (nm)	Stokes shift (nm)	Φ_{em}	τ (ns)	k_r ($\times 10^7 s^{-1}$)
soln	CYH	428	435	33	0.32	6.03	5.3
	ACE	430	462	59	0.26	5.54	4.5
gel	CYH	449	474[a]	25	0.09	6.43	1.4
	ACE	452	484	32	0.12	6.75	1.8

[a]: λ_{ex}= 403 nm

Since the photophysical properties do not allow us to straightforwardly differentiate CYH and ACE gel, further investigation was carried out by CFM and kinetic gel formation study. Although the molecular packing of both gels are still unknown from current experimental results, we can reckon that in ACE gel is more ordered than CYH gel according to the slower fibers growing process revealed by kinetic gel formation study. Also, the emission spectrum of ACE gel suggests it's a more thermo-dynamic favored aggregation form, given the fact that the same emission spectrum can be obtained by exciting CYH gel at the lowest absorption band 449 nm. CFM study clearly demonstrated that the gel fibers are thicker in ACE gel than CYH gel.

4.4 Fluorinated side chain substituted DPA

The photophysical properties measurement of this part of work is attributed to the under-graduated student Jenny Debaere. Although it is not a complete study, these preliminary results still can give us an insight about 9,10-diphenylanthracene derivatives' behavior as organogelators.

4.4.1 Synthesis

The synthetic route for the perfluorinated chain substituted **DPA** derivatives is different than the synthetic route of other **DPA** derivatives described in chapter 2.

In case of the poor solubility of perfluoro chains substituted anthraquinone, the order of attached phenyl ring and side chains are reversed in both the synthetic route of **F17** and **PT**. The general synthetic schemes are similar for **F17** and **PT**. First, phenyl lithium was attached to the dimethoxyanthraquinone/monomethoxy anthraquinone and the resulting hydroxy groups were removed with hydrogen iodide as a reducing reagent in boiling ether. BBr_3 was then applied to demethylate the methoxy protecting group to yield dihydroxy/monohydroxy dipheylanthracene. For **F17**, the hydroxyl groups were deprotonated with potassium carbonate in DMF and the perfluorobromide was added to get the 2,3-diperfluoroalkoxy-9,10-diphenylanthracene (**F17**).

For **PT**, the 2-hydroxy-DPA was esterificated with branched-ponytailed-perfluoro acid under DCC, DMAP condition to yield the final product **PT**. All final products were purified by column chromatography on silica gel.

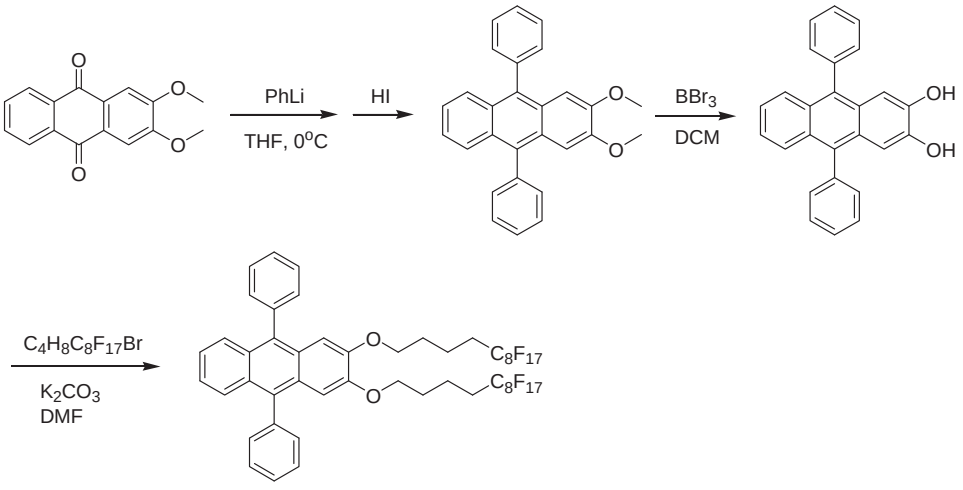

Scheme 4.4: synthetic route for **F17**

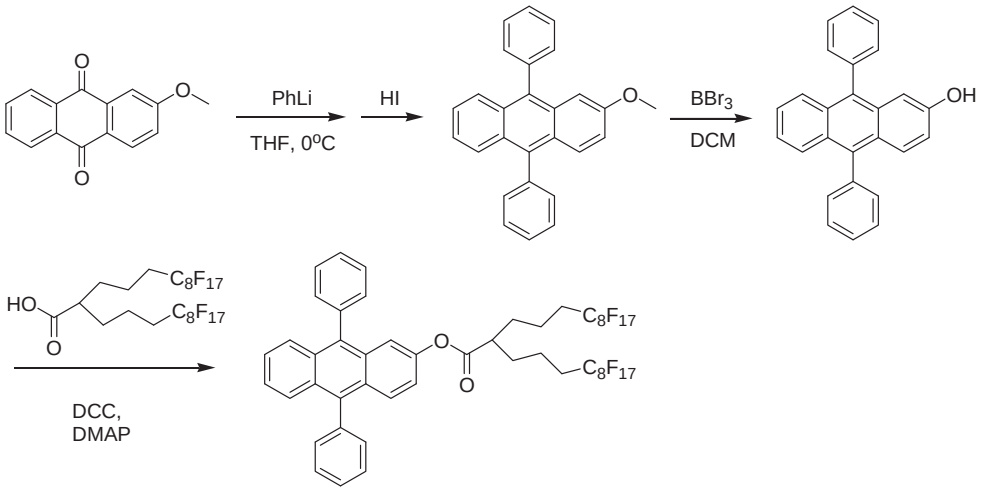

Scheme 4.5: synthetic route for **PT**

4.4.2 Gelation test

Twelve boiling solvents were used for gelability test of **F17** with inverted tube test (ITT). Besides the solvents tested in the previous section, some fluorinated solvents such as try-fluoroethanol (TFE) and perfluoro-decaline (FC-72) are also tested here (Table 4.6). Given the fact that we don't have much amount of **PT** compound, only the solvents tested with **F17** give positive results were further tested with **PT**. Unfortunately, no solvent can be successfully gelated by **F17** and **PT**. Only the polar solvents DMSO and *n*-octanol lead to promising formation of nano-structures.

Table 4.6: Gelation tests in various solvents. Lower concentrations of compounds did not change observation, or induced loss of gelation property.

	Compound	mmol/L (mg/mL)
Solvent	**F17**	**PT**
methanol	**P** 3.43(4.5)	--
ethanol	**P** 2.39(3.13)	--
2-propanol	**P** 2.40(3.15)	--
n-butanol	**S** 2.52(3.3)	--
n-octanol	**P.G.** 3.92 (5.1)	**P.G.** 3.78 (4.95)
n-hexane	**S**3.36(4.4)	--
cyclohexane	**S**2.85(3.73)	--
DMF	**P**2.40 (3.14)	--

DMSO	**P.G.** 3.7 (4.8)	**P.G.** 4.34 (5.7)
TFE (trifluoroethanol)	**P.G.** 3.8 (4.9)	**P**3.44 (4.5)
FC-72 (perfluorodecalin)	**P**[b]3.7 (4.7)	**P**[b]4.32 (5.7)

[a] S = clear solution, P = Precipitate, CP = cloudy precipitate, G = gel, PG = partial gel

[b] Compound doesn't dissolve in boiling solvent.

4.4.3 Photophysical properties

Even though the gelation test didn't give results as we expected, the partial-gels in *n*-octanol for both gelators were further characterized to grant us an insight about their self-assembly process.

Figure 4.20 displays the absorption and emission spectra of **F17** and **PT** in solution and in the gel state, the slightly red-shifted absorption and emission for both gelators suggest the presence of weak dipolar coupling or stabilization of the excited state by weak interactions. Additionally, the emission spectrum profile of is also changed, the $v_{0\text{-}1}$ band becomes more prominent in the gel state. Generally speaking, these two molecules behave quite similar to each other. It suggests that 2- or 2, 3- positions modification does not influence the photophysical properties of the **DPA** chromophore.

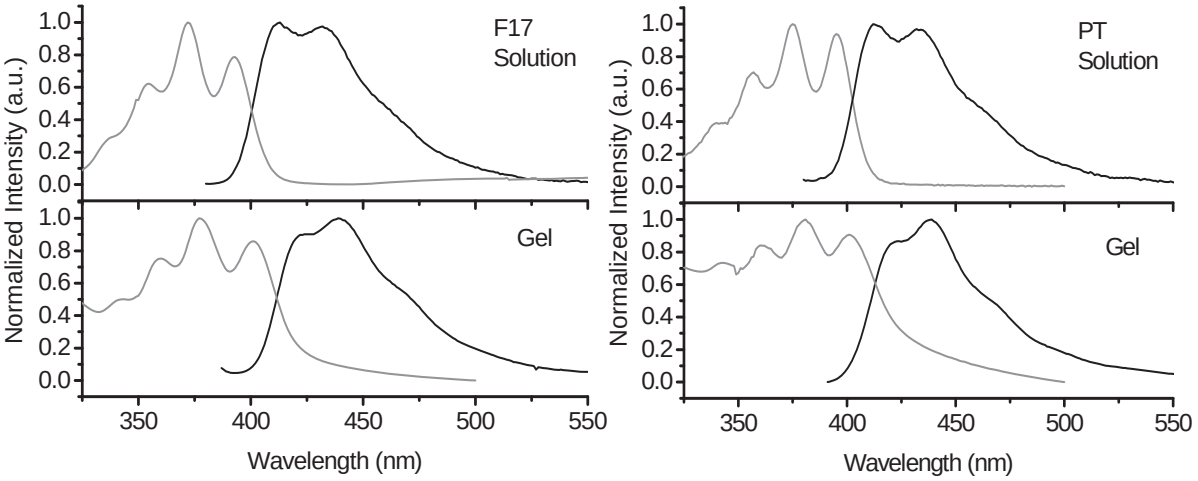

Figure 4.20: (left) Absorption (gray line) and emission (black line) spectra of **F17** in THF solution (1.0×10^{-5} M, top) and **F17** gel (4.0×10^{-3} M in *n*-octanol, bottom), λ_{ex}= 372 nm (room temperature).(Right) Absorption and emission spectra of **PT** in THF solution (1.0×10^{-5} M, top) and **PT** gel (4.0×10^{-3} M in *n*-octanol, bottom), λ_{ex}= 375 nm (room temperature).

4.4.4 Morphology of the Gel

From the pictures (Figure 4.21a and b) we can see that the **F17** gel is more transparent and the **PT** gel is more opaque. It suggests that the size of micro-structures of **PT** gel is larger

than that of **F17** gel. And these so-called partial-gels are highly viscous solutions (Figure 4.21c and d).

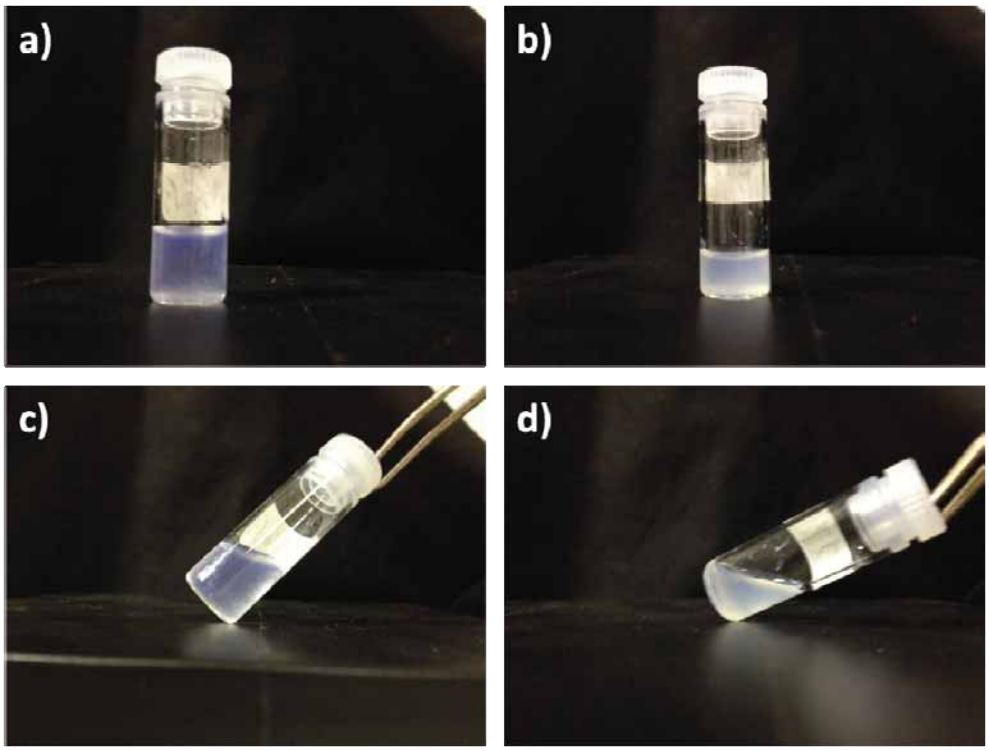

Figure 4.21: Macroscopic pictures of **F17** and **PT** gels in *n*-octanol

The micro-structures of both suspensions are revealed by CFM. Figure 4.22 shows that the **F17** gel sample is composed of stiff and crystalline fibers with width about 700-800 nm, given the fact they are less bended than other gels studied in this chapter.

On the other hand, **PT** gel has a smaller diameter about 500-600 nm. The size between fibers is also more homogeneous for **PT** gel. The emission decay time of both nanofibers can be expressed with a bi-exponential function (Figure 4.22).

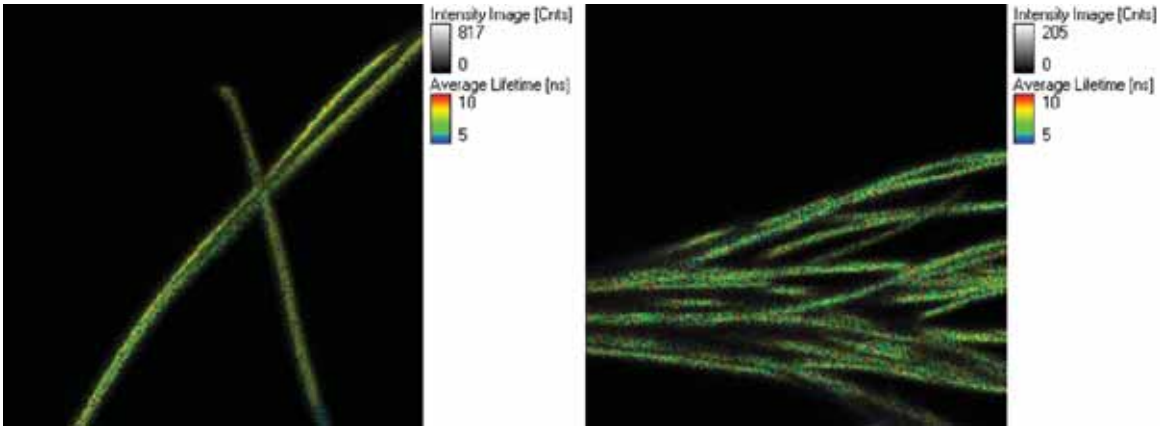

Figure 4.22: FLIM images of **F17** (left), **PT** (right) 4 mM gel in *n*-octanol, λ_{ex} =375 nm, λ_{em} >405 nm (30×30 μm) (color code: average decay time)

Although the diameter of **PT** gel fibers is thinner than that of **F17** gel fibers, the **PT** fibers

tend to entangle with each other and spread in the end, yielding pony-tail like micro-structure. It also explains the opacity of **PT** gel from macroscopic view (Figure 4.23).

Due to the microstructures of both gels are three-dimensional, in order to obtain a clear picture of micro-structures of **PT** gel, transmission images are taken with a CCD camera. This pony-tail shape stricture is more evident under optical microscopy. The most interesting thing is that the pony-tails are everywhere in **PT** gels, even though the size of some are bigger (more fibers involved), some are smaller (less fibers involved).

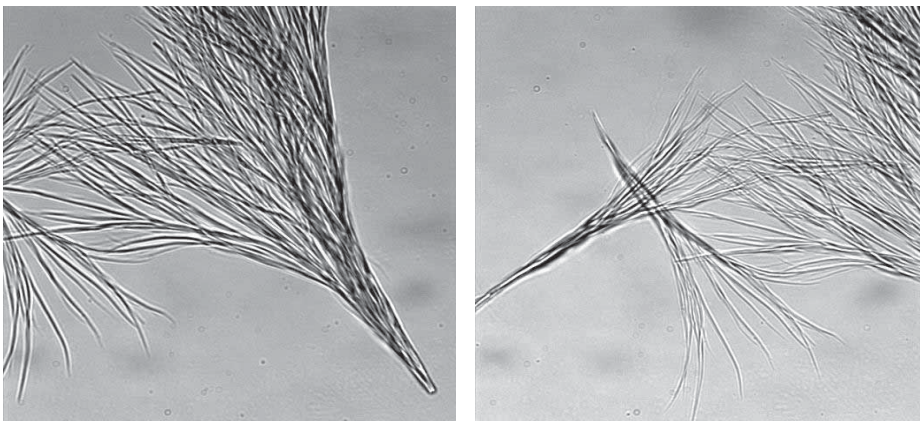

Figure 4.23: Transmission images of **PT** gel 4 mM in *n*-octanol (80×80 μm)

4.4.5 Discussion

Compared with 2,3-didecyloxy-9,10-diphenyl anthracene (**B10**), **F17** and **PT** are shown to exhibit similar photophysical properties in the monomer state (Table 4.7)
However, while self-assemble micro-structures are formed, the 2-ester-ponytail substituted **DPA** derivative **PT** is shown with quantum yield only half of that of **B10** microribbons, in the mean time that **F17** nanofibers exhibit the same quantum yield as **B10**. The decay times of both **F17** and **PT** (T1 and T2) are longer than **B10**, suggesting the radiative constants of **F17** and **PT** are smaller than that of **B10**.

Table 4.7: Photophysic properties of **DPA** derivatives in solution and in solid state

	Compound	λ^{abs}_{max} (nm)	λ^{em}_{max} (nm)	Φ_{em}	τ1, τ2 (ns)	k_r ($\times 10^8 s^{-1}$)
Soln	**F17**	372	413.433	0.75 [a]	6.5,--	1.1
	PT	375	414.434	0.73 [a]	6.7,--	1.1
	B10	373	413,433	0.77 [a]	7.0,--	1.1
Gel	**F17**	377	439	0.43 [b]	5.6, 8.8	--
	PT	381	439	0.20 [b]	3.8, 10.1	--
Micro-ribbons	**B10**	380	443	0.42 [b]	2.9, 5.6	--

[a] Measured with **DPA** in cyclohexane as reference

[b] Measured with integrating sphere

Table 4.8: Photophysical properties of **DPA** derivatives in solid state

	Compound	Rel, Amp. 1	τ_1 (ns)	Rel, Amp. 2	τ_2 (ns)
Gel	**F17**	0.27	8.8	0.73	5.6
	PT	0.34	10.4	0.66	4.2
Micro-ribbons	**B10**	0.20	5.6	0.80	2.9

4.5 General Discussion and Conclusion

1. **DDPEA** self-assembles into nanofibers in n-butanol, but in the presence of solvent, this kinetically favoured morph ripens and transforms into larger objects, reminiscent of nano-ribbons or nano-crystals. This polymorphism has rarely been reported for a compound at fixed environmental conditions (solvent concentration and temperature), and illustrates that organogels could be kinetically favoured meta-stable states. Further studies will inform us on the advantages of the gel state over the nano-crystalline state, as well as on the exploitation of this polymorphism in nanomaterials for photonic applications.

2. **DCNA** in solution displays environment sensitivity due to its charge-transfer characteristic excited state. Nevertheless, the gelator-gelator interaction dominates the photophysical behaviour in the gel state. The **DCNA** gel does not sense the solvent polarity with the optical properties. CFM and kinetic studies, show that the gel formation process in ACE and CYH are quite different. Indeed, **DCNA** in CYH displays typically organogel behaviour with well-defined melting temperature and gelation temperature, whereas the ACE gel fibres are more crystalline.

3. **DPA** derivatives are shown to have very good quantum yield and photo-stability in the solid state. In order to make uniformly sized nano-structures, we synthesized two **DPA**-based organo gelators with perfluorinated alkyl chains. These chains induce a new supramolecular interactions. **F17** is designed based on the 2,3-substituted alkoxy substituent strategy, which is demonstrated to adopt the good photophysical performance as other **DPA** crystals reported at chapter 2. On the other hand, **PT** is synthesized by esterification at 2- position of **DPA** with a perfluoro-ponytail-mono acid.[50] The quantum yield of fluorescence of **PT** gel is only 20%, which is not very good compared with other **DPA** derivatives. The most interesting fact is that **PT** gel fibers tend to entangle together to yield ponytail-like microstructures. The photophysical properties indicate that organization of 2,3-alkyl chain substituted **DPA** molecules in the solid state favors radiative decay process. The perfluorinated chain designs open new prospectives to tune microstructures.

   9,10-substituted **DDOA** derivatives are synthesized and investigated as novel organo gelator candidates. The elongation of anthracene conjugation by introducing modification at 9,10 positions successfully tunes the molecular photophysical properties such as the emission quantum yield, as well as absorption and emission wavelengths. Furthermore, the self-assembly character of these gelators is also altered by the substituents. The dicyano-substituted **DCNA** is shown to have best gelation performance, but the quantum yield is only slightly higher than that of **DDOA**. The good self-assembling ability of **DDPEA** can be attributed to the π-π stacking facilitated by the almost coplanar aromatic parts interaction, which is suggested according to the **BPEA** crystal structure shown in

Figure 4.24. (For **BPEA** crystal, the angle between the plane of anthracene and that of the substituents is 0.26°, and the π-π stacking distance is about 3.46 Å.[51]) In addition, the formation of J aggregates also indicates **DDPEA** molecules are nicely aligned in the gel state.

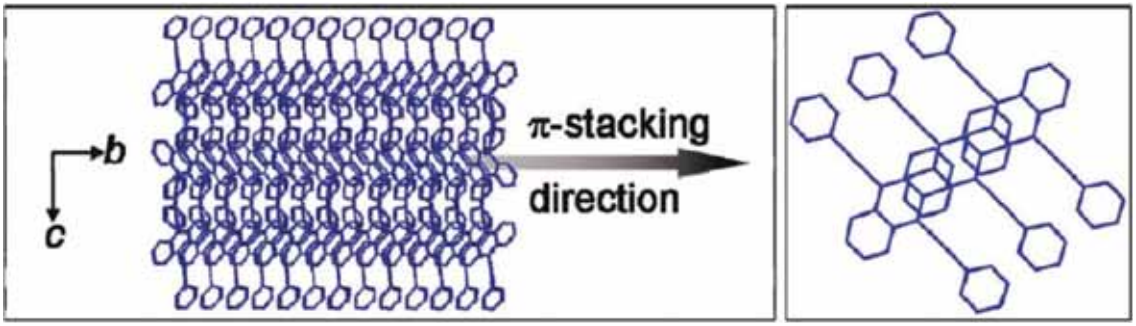

Figure 4.24[51] : crystal structure of BPEA

DPA derivatives which adopt the 2,3-alkoxy chains skeleton display strikingly high quantum yield both in solution and in the aggregated state. However, no organogel can be obtained with this unit. In previous chapters, it is shown that **DPA**s can form crystals and polarized emission nanostructures, suggesting the self-assembly ability of **DPA** is very good. Therefore, to attribute the reason of no organogel formation with **DPA**s, the crystal structure of **B8** and **DHpOA** (2,3-diheptoxy anthracene) are compared (Figure 4.25). As shown in figure 4.25, the substituted alkyl chains of **B8** are disordered and seriously twisted; whereas the chains of **DHpOA** are uni-directional packed. It suggests that it might take time for the alkyl chains of **DPAs** to be oriented, which is not favoured in the kinetically stable gel state.

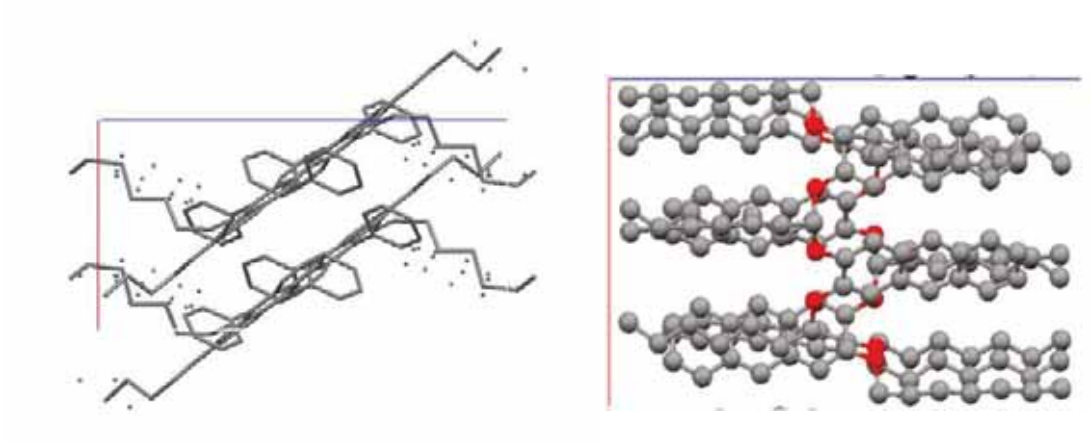

Figure 4.25: molecules orientation in crystal structure of **B8** (left) and **DHpOA**[52]

4.6 References

1. Terech, P.; Weiss, R. G. *Chem. Rev.*, **1997**, *97*, 3133
2. Estroff, L. A.; Hamilton, A. D. *Chem. Rev.*, **2004**, *104*, 1201
3. (a) Ajayaghosh, A.; George, S. J. *J. Am. Chem. Soc.*, **2001**, *123*, 5148. ; (b) Babu, S. S.; Kartha, K. K.; Ajayaghosh, A. *J. Phys. Chem. Lett.*, **2010**, *1*, 3413. ; (c) Kartha, K. K.; Babu, S. S.; Srinivasan, S.; Ajayaghosh, A. *J. Am. Chem. Soc.*, **2012**, *134*, 4834
4. (a) Gu, W.; Lu, L.; B. Chapman, G.; G. Weiss, R. *Chem. Commun.* **1997**, 543. ; (b) J. H. Hafkamp, R.; P. A. Kokke, B.; M. Danke, I.; P. M. Geurts, H.; E. Rowan, A.; C. Feiters, M.; J. M. Nolte, R. *Chem. Commun.* **1997**, 545.
5. Kuang, G.-C.; Teng, M.-J.; Jia, X.-R.; Chen, E.-Q.; Wei, Y. *Chem. Asian J.*, **2011**, *6*, 1163.
6. Hirst, A. R.; Coates, I. A.; Boucheteau, T. R.; Miravet, J. F.; Escuder, B.; Castelletto, V.; Hamley, I. W.; Smith, D. K. *J. Am. Chem. Soc.*, **2008**, *130*, 9113.
7. (a) Zhu, P.; Yan, X.; Su, Y.; Yang, Y.; Li, J. *Chem. Eur. J.*, **2010**, *16*, 3176. ; (b) Cui, J.; Shen, Z.; Wan, X. *Langmuir* **2009**, *26*, 97
8. (a) van der Laan, S.; Feringa, B. L.; Kellogg, R. M.; van Esch, J. *Langmuir* 2002, *18*, 7136. ; (b) Gopal, A.; Varghese, R.; Ajayaghosh, A. *Chem. A. J.*, 2012, DOI:10.1002/asia.201200410
9. (a) Giansante, C.; Raffy, G.; Schäfer, C.; Rahma, H.; Kao, M.-T.; Olive, A. G. L.; Del Guerzo, A. *J. Am. Chem. Soc.*, **2010**, *133*, 316.; (b) Del Guerzo, A.; Olive, A. G. L.; Reichwagen, J.; Hopf, H.; Desvergne, J.-P. *J. Am. Chem. Soc.*, **2005**, *127*, 17984.
10. Porrès, L.; Holland, A.; Pålsson, L.-O.; Monkman, A.; Kemp, C.; Beeby, A. *Journal of Fluorescence* **2006**, *16*, 267.
11. Reddy, G. S.; Chen, H.-Y.; Chang, I-J. *J. Chi. Chem.Soc.* **2006**, *53*, 1303
12. Zhu, A.; White, J. O.; Drickamer, H. G. *J. Phys. Chem. A.*, **2002**, *106*, 9209.
13. Zhao, Y. S.; Xu, J.; Peng, A.; Fu, H.; Ma, Y.; Jiang, L.; Yao, J. *Angew.Chem. Int. Ed.*, **2008**, *47*, 7301.
14. Giménez, R.; Piñol, M.; Serrano, J. L. *Chem. Mater.*, **2004**, *16*, 1377.
15. Maulding,D. R.; Zweig, A. *U.S. Patent* 3729426, **1973**.
16. Nakatsuji, S.; Matsuda, K.; Uesugi,Y.; Nakashima, K.; Akiyama, S.; Fabian W. *J. Chem. Soc., Perkin Tran*s. *1*, **1992**, 755.
17. Li, B.; Miao,W.; Cheng, L. *Dyes Pigm.*, **2000,** *46*, 81.
18. Cicerone, M. T.; Blackburn, F. R.; Ediger, M. D. *J. Chem. Phy.*, **1995,** *102***,** 471
19. Karl, N.; Marktanner, *J. Mol. Cryst. Liq. Cryst.*, **2001,** *355*, 149.
20. Dimitrakopoulos,C. D. ; Malenfant, P. R. L. *Adv. Mater.*, **2002,***14*, 99.
21. Wang, C.; Liu, Y.; Ji, Z.; Wang, E.; Li, R.; Jiang, H.; Tang, Q.; Li, H.; Hu, W. *Chem. Mater.*, **2009**, *21*, 2840.
22. (a) Vauthey, E. *J. Phys. Chem. A* **1997**, *101*, 1635.(b) Hasegawa, E.; Brumfield, M. A.; Mariano, P. S.; Yoon, U. C. *J. Org. Chem.***1988**, *53*, 5435. (c) Baciocchi, E.; Giacco, T. D.; Elisei, F.; Gerini, M. F.; Guerra, M.; Lapi, A.; Liberali, P. *J. Am. Chem. Soc.* **2003**, *125*, 16444.

23. Suzuki, T. ; Nagano, M. ; Watanabe, S. ; Ichimura, T. *J. Photochem. Photobiol. A-Chem.* **2000**, *136*, 7.
24. De Luca, G.; Liscio, A.; Melucci, M.; Schnitzler, T.; Pisula, W.; Clark, C. G.; Scolaro, L. M.; Palermo, V.; Mullen, K.; Samori, P. *J. Mater. Chem.* **2010**, *20*, 71.
25. Jung, H. T.; Kim, S. O.; Hudson, S. D.; Percec, V. *Appl. Phys. Lett.* **2002**, *80*, 395.
26. Hudson, S. D.; Jung, H. T.; Percec, V.; Cho, W. D.; Johansson, G.; Ungar, G.; Balagurusamy, V. S. K. *Science* **1997**, *278*, 449.
27. Horváth, I. T.; Rábai, J. *Science* **1994**, *266*, 72.
28. Desvergne, J.-P.; Brotin, T. ; Meerschaut, D.; Clavier, G. ; Placin, F.; Pozzo, J.-L.; Bouas-Laurent, H. *New J. Chem.*, **2004,** *28*, 234
29. Pozzo, J.-L.; Clavier, G. M.; Colomes, M.; Bouas-Laurent, H. *Tetrahedron* **1997**, *53*, 6377.
30. Fukumura, H.; Kikuchi, K.; Koike, K.; Kokubun, H. *J. Photochem. Photobiol. A: Chem.* **1988**, *42*, 283.
31. Olea, A. F.; Worrall, D. R.; Wilkinson, F.; Williams, S. L.; Abdel-Shafi, A. A. *Phys. Chem. Chem. Phys.* **2002**, *4*, 161.
32. Jeong, Y.; Hanabusa, K.; Masunaga, H.; Akiba, I.; Miyoshi, K.; Sakurai, S.; Sakurai, K. *Langmuir*, **2005**, *21*, 586.
33. Pham, Q. N.; Brosse, N.; Frochot, C.; Dumas, D.; Hocquet, A.; Jamart-Gregoire, B. *New J. Chem.*, **2008**, *32*, 1131.
34. Hirst, A. R.; Coates, I. A.; Boucheteau, T. R.; Miravet, J. F.; Escuder, B.; Castelletto, V.; Hamley, I. W.; Smith, D. K. *J. Am. Chem. Soc.***, 2008**, *130*, 9113.
35. Zhu, G.; Dordick, J. S. *Chem. Mater.* **2006**, *18*, 5988.
36. Xue, P.; Lu, R.; Yang, X.; Zhao, L.; Xu, D.; Liu, Y.; Zhang, H.; Nomoto, H.; Takafuji, M.; Ihara, H. *Chem – Eur. J.* **2009**, *15*, 9824.
37. Bielejewski, M.; Łapiński, A.; Luboradzki, R.; Tritt-Goc, J. *Langmuir* **2009**, *25*, 8274.
38. Zhu, P.; Yan, X.; Su, Y.; Yang, Y.; Li, J. *Chem – Eur. J.* **2010**, *16*, 3176.
39. Huang, X.; Terech, P.; Raghavan, S. R.; Weiss, R. G. *J. Am. Chem. Soc.* **2005**, *127*, 4336.
40. Wang, R.-Y.; Liu, X.-Y.; Narayanan, J.; Xiong, J.-Y.; Li, J.-L. *J. Phys. Chem. B* **2006**, *110*, 25797.
41. Li, J.-L.; Liu, X.-Y. *J. Phys. Chem. B* **2009**, *113*, 15467.
42. Brinksma, J.; Feringa, B. L.; Kellogg, R. M.; Vreeker, R.; van Esch, J. *Langmuir* **2000**, *16*, 9249.
43. (a) Wilder, E.A.; Spontak, R. J.; Hall, C. K. *Mol. Phys.* **2003**, *101*, 3017. (b) Xue, P. C; Lu, R.; Yang, X. C.; Zhao, L.; Xu, D. F.; Liu, Y.; Zhang, H.; Nomoto, H.; Takafuji, M.; Ihara, H. *Chem. Eur. J.* **2009**, *15*, 9824. (c) Bielejewski, M.; Lapinski, A.; Luboradzki, R.; Tritt-Goc, J. *Langmuir*, **2009,** *25*, 8274. (d) Zhu, P. L.; Yan, X. H.; Su, Y.; Yang Y.; Li, J. B. *Chem. Eur. J.* **2010**, *16*, 3176.
44. Brinksma, J.; Feringa, B. L.; Kellogg, R. M.; Vreeker, R.; van Esch, J. *Langmuir*, **2000,** *16*, 9249
45. Wu, Y.; Wu, S.; Zou, G.; Zhang, Q. *Soft Matter.* **2011**, *7*, 9177.

46. Lippert, E. *Z. Naturforsch* **1955**, *10a*, 541.
47. Mataga, N.; Kaifu, Y.; Koizumi, M. *Bull. Chem. Soc. Jpn*. **1956**,*29*, 465.
48. Lewis, F. D.; Dykstra, R. E. *J. Photochem. Photobio. A: Chem.* **1989**, *49*, 109.
49. Gould, I. R.; Young, R. H.; Mueller, L. J.; Farid, S. *J. Am. Chem. Soc.* **1994**, *116*, 8176.
50. Loiseau, J.; Fouquet, E.; Fish, R. H.; Vincent, J.-M.; Verlhac, J.-B. *J. Fluor. Chem.* **2001**, *108*, 195.
51. Wang, C.; Liu, Y.; Ji, Z.; Wang, E.; Li, R.; Jiang, H.; Tang, Q.; Li, H.; Hu, W. *Chem. Mater*. **2009**, *21*, 2840.
52. Olive, A. G. L.; Raffy, G.; Allouchi, H.; Léger, J.- M.; Del Guerzo, A.; Desvergne, J.-P. *Langmuir* **2009**, *25*, 8606.
53. Adams, J. M.; Ramdas, S. *Acta Cryst. Sec. B* **1979**, *35*, 679.

General conclusion and perspectives

9,10-disubstituted anthracene derivatives with 2,3-dialkoxy chains are shown to be able to self-assemble into nano-scaled structures: nanorods, nanoribbons and nanofibers.

9,10-diphenylanthracene derivatives are shown to exhibit excellent photophysical properties in the solid state. This work shows that the chain length allows to tune the molecular packing and the size of the aggregates. Indeed, the crystals of short side chain derivatives exhibit an exceptional quantum yield (**B1**: 0.97, **B2**: 0.86, **B4**: 0.90) and all the derivatives have anisotropic blue emission ($-0.75 \leq P \leq 0.75$). The increase of the chain length not only reduces the macroscopic size of the needle/fiber-like crystals, but also alters the molecular packing in the crystals. With decyl and hexadecyl chains (**B10**, **B16**), microribbons are formed instead of crystals. This simple design can be used to favor nanostructuration of 9,10-substituted anthracenes.

The downsizing of crystals could also be achieved by another method. In order to turn to good account the photophysical behaviors of **B1** in the solid state, uniformly sized anisotropic nanorods (length: 4 μm, width: 300-400 nm) are fabricated via a soft template method with the assistance of the surfactant (CTAB). This method was shown to allow the doping of **B1** nanorods. These can thus be used as a light-harvesting matrix that co-assembles with a specifically designed green emitting tetracene (**GT1**) to yield tunable dual-color emitting single nanorods. The color tuning in this binary nanorods is achieved through partial excitation energy transfer that can be controlled by the amount of doping. This soft templating method does nevertheless not allow the homogeneous dispersion of **GT1** molecules within the nanorod matrix and induces an unusual dual-color emission in single rods.

This non-homogeneous distribution of dopants in the nano-scaled matrices can be overcome by the nanoribbons system based on **B16**. The **B16** nanoribbons display an anisotropic blue emission, and its morphology is not influenced by the addition of small amount of dopants molecules (1% e.q. for green emitter **G16**; 2% e.q. for red emitter **R16**). The similarity between the structures of **B16**, **G16** and **R16**, as well as the nano-ribbon formation mechanism favors the homogeneous dispersion of acceptors, as revealed by CFM studies, and thus yields controllable color-tuneable two-component (**B16**—**G16**, **B16**—**R16**) and three-component (**B16**—**G16**—**R16**) nano-scaled systems. This color-tuning property can thus be provided with anthracenes and tetracenes yielding a partial excitation energy transfer from the blue-emitting component to the green/red-emitting components. In a three-components system, a cascade energy transfer process is achieved by **B16** to **G16**, **B16** to **R16** and **B16** to **G16** to **R16**. This dispersion method allows also to induce the anisotropy of the sensitized green and red emission. Additionally, a delayed fluorescence of **G16** and **R16** sensitized by **B16** is revealed and characterized by CFM, suggesting the presence of a triplet-triplet annihilation process. This system provides thus also an interesting tuneable nano-system for the investigation of fundamental photophysical processes and the parameters that influence them. Triplet fusion and singlet fission are phenomena that could be optimized in these nano-systems with a controlled assembly of tetracenes.

Self-assembly of other 9,10-substituted anthracene derivatives was also attempted by using a 2,3-disubstitution with alkoxy chains. It appeared with the most elongated substituent in **DDPEA** (9,10-bisphenylethylnyl-DDOA) that an organogel could be formed, which also displays a unusual polymorphism. The **DDPEA** gel fibers can evolve into another more thermally stable crystal-like structure within few hours. The attempt to form nanofibers with a solvent-sensitive emission did not succeed when a dicyano-substituted anthracene **DCNA** was used. Indeed, whereas in solution the charge-transfer excited state emits with a solvent-dependent behaviour, the gelator-gelator lead to solvent-independent J-aggregate emission in the gel state. **DPA** organogelatation was attempted by introducing new supramolecular interactions with with perfluorinated alkyl chains **F17** and **PT**. Although no gel can be formed with these moleules, nanocrystals and unusual microstructures were observed in suspension.

The studies of nanostructures based on 9,10-substituted anthracenes not only fulfilled the expectation drawn in the beginning, but also opened up new perspectives which can be explored with the assistance of the powerful tool CFM. These are some topics that could be further investigated:

1. From the chapter 2, dibutyloxy DPA derivative **B4** is shown to exhibit polymorphism in the crystal. Detailed investigation of the polymorphism of **B4** can allow us to utilize this character to construct different shapes and sizes of nanostructures and study their photophysical properties.
2. So far, it is known that the diphenylanthracene nanostructure systems all exhibit polarized emission, it would be very promising in devices to align these nanorods and nanoribbons in a single direction. For instance, the nanomaterials could be embedded into polymers and then stretched to apply a force to align these nanostructures.
3. Besides energy transfer, other photophysical behaviors can also be investigated in the DPA nano-scaled systems. Up-conversion, which can occur between DPA and Ruthenium complexes, is quite attractive.
4. With the experience accumulated in fabricating anthracene nanostructures, tetracene derivatives or even pentacenes can be the next targets to be constructed as nanomaterials. It can also allow us to obtain a better understanding of the triplet formation and triplet-triplet annihilation processes in sensitized **G16** and **R16** in **B16** nanoribbons.
5. The polymorphism of **DDPEA** gel can be further study by adding dopants into the gels. To monitor the photophysical behavior of dopants with the variation of **DDPEA** fibers to crystal can provides us more information on this ripening process.

Chapter 5

Experimental Section

5.1 Materials

Commercially available chemicals were used without further purification. Anhydrous solvents, such as absolute ethanol, chlorobenzene, DMSO and DMF were used as received. Dichloromethane, toluene and acetonitrile were distilled over calcium hydride (CaH_2). Tetrahydrofuran (THF) and diethyl ether were dried over sodium/benzophenone and distilled immediately before use. Petroleum ether (PET) with a boiling range of 40-60°C was used.

5.2 Thin-layer chromatography and column

The thin-layer chromatography was performed on Merck 60 silica plate F254. The plates are visualized under UV at 254 nm and 365 nm. The column chromatography was performed on silica gel (silica gel Merck, particle size of 63-200 microns, 230-400 mesh or size from 40 to 63 microns).

5.3 Nuclear magnetic resonance (NMR)

The ^{1}H and ^{13}C NMR spectra were recorded by Bruker Avance 300 (^{1}H: 300 MHz, ^{13}C: 75 MHz). Chemical shifts δ are expressed relative to tetramethylsilane (TMS) using the residual signals of deuterated solvents ($CDCl_3$, CD_2Cl_2, D_2O, d_6-DMSO, CD_3OD) as internal reference. The coupling constants are calculated in Hertz (Hz). For the assignment of signals, the following abbreviations are used: s = singlet, d = doublet, t = triplet, q = quartet, dd = doublet doublet, m = multiplet.

5.4 Mass Spectrometry

The mass spectra were produced by the Centre of Study and Structural Analysis Organic Molecules (CESAMO) at the University Bordeaux I. The impact spectra (EI) (E = 70 eV) and LSIMS + (E = 35 keV) were performed on a spectrometer Micromass VG Autospec-Q. Electrospray spectra were performed on a spectrometer Varian Saturn-4D. HRMS measurements were performed using a QStar mass spectrometer (Applied Biosystems) equipped with an ESI source and a time-of-flight detector.

5.5 Fluorescence spectroscopy

Fluorescence spectra were obtained on a Horiba Jobin-Yvon Fluorolog spectrofluorimeter, using a 1×1-cm cuvette in a right-angle configuration and exciting with a Xenon lamp of 450 W. Lifetimes have been recorded by time-correlated single photon counting, exciting with nanoled. The detector used is HAMAMATSU 928P PMT in single photon counting mode.

5.6 Absorption spectroscopy

The instrument we used to perform absorption spectra and kinetic absorption study is a Varian Cary 5000 spectrophotometer whose wavelength range extends from 170 to 3300 nm equipped with a temperature controller.

5.7 Atomic force microscope

AFM measurements have been performed with a CP-R Thermomicroscope Atomic Force Microscope operated in tapping mode. Samples have been prepared by spin-coating a freshly prepared solution of NRs on freshly cleaved mica.

5.8 Scanning electron microscope

The SEM is a JEOL JSM-6700F field emission scanning electron microscope (FESEM) capable of SEI resolutions down to 1 nm and magnification of x25 to x650,000. Samples were prepared by drop casting materials on ITO/glass surface, dried in vacuum overnight. Before measurement, samples were vacuum evaporated Pt on the surface.

5.9 Confocal fluorescence microscope

The CFM is a Picoquant Microtime 200 based on an inverted IX71 from Olympus. The Ti–Sa laser chain includes a Coherent Mira and a frequency doubler and affords pulses of 4–6 ps at 4.75 MHz. The 375 nm diode laser was used as an excitation light source in all the energy transfer experiments, which gives pulses of ~70 ps at 5 MHz. The orientation of the linearly polarized excitation light can be controlled with a Babinet Soleil compensator.

The beam is coupled into the microscope via a polarization maintaining optical fiber and is injected by 90° reflection on a 80% T/20% R spectrally flat beam splitter in the microscope. A high numerical aperture objective was used (100× UPLSAPO, NA 1.4), and oil was in contact with the 170 micron thick coverslips that support the sample. The emission is collected by transmission through the same beam splitter and a long pass/band pass interferential filter before being focused on a pinhole 50 μm (for most of the samples: 405 nm LP filter; for energy transfer sample: 425/50 nm BP filter for blue-emitting donors, 500 nm LP for green/red-emitting acceptors). The emission is then detected by a steady-state CCD-spectrometer (Andor) or time-resolved avalanche photodiodes (MPD). When specified, parallel and perpendicular components of the emitted light have been split by using a polarizing beam splitter and two Glan-Thompson polarizers before the MPD detectors. The room is thermostated at 23°C with air-conditioning.

The spectra obtained with the Andor system were intensity corrected by measuring suitable reference solutions (9,10-diphenylanthracene, fluorescein and $[Ru(bpy)_3Cl_2]$) that cover the whole spectral range and using reference spectra recorded in Horiba Jobin-Yvon

Fluorolog. The avalanche photodiodes are used in the time-correlated single photon counting mode, yielding time-resolved data provided in the TTTR mode (each photon is correlated to the excitation pulse and to the sample scanning time). Fluorescence lifetime microscopy (FLIM) images were obtained using the Symphotime fitting software, which performs a multi-exponential fitting (one, two, or three exponentials depending on the sample) at each pixel. A distance of 100 nm between each pixel and an acquisition time of 0.6 ms per pixel have been used for due to the balance of time and resolution.

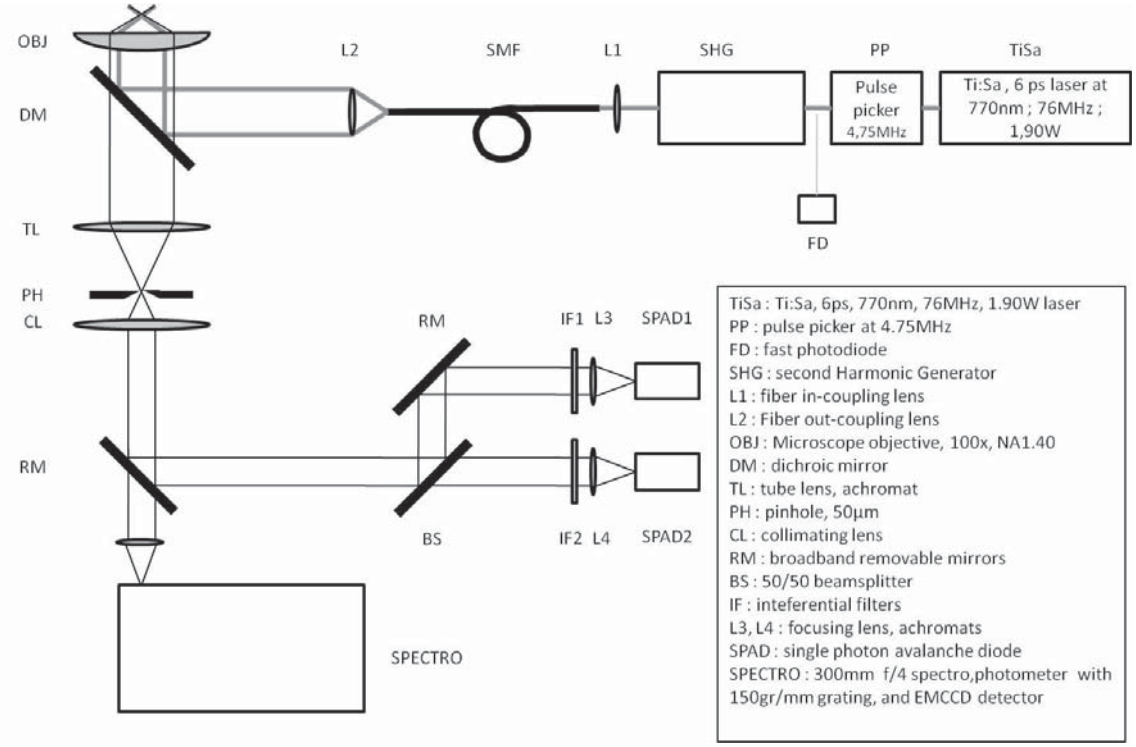

Scheme 5.1: scheme of confocal fluorescence microscopy set-up

5.10 IRF (Instrument Response Function)

The instrumental response function (IRF) is in general used to de-convolute the emission decays. In our instrument, the IRF depends on the wavelength of the light detected. However, since a broad spectral range is generally used to detect sufficient photons at each pixel, the IRF cannot be determined with precision.

Our experience reflects well the tech-note supplied by the manufacturer (Pico-Quant) on the IRF of the SPADs measured with a LED laser at different wavelengths.

Table 5.1: IRF at different wavelength

Wavelength (nm)	IRF, FWHM (ps)	Laser pulse, FWHM (ps)
375	140	45
405	154	55
470	71	56
635	83	66
670	49	32

Due to this limitation, the fluorescence decays were tail-fitted starting at 200 ps.

5.11 2,3-dimethoxy-9,10-diphenylanthracence (1/B1) nanorod fabrication

The condition of **B1** nanorods formation is quite critical, besides the presence of surfactant which is shown in the chapter 2, other factors such as the concentration of stock **B1** solution, solvent for stock solution and the temperature of the aqueous solution were all optimized from trials. Herein we listed the conditions that were tested and the results. For screening the samples, we used the epi-fluorescence microscopy with a 375 nm LED as light source and a CCD camera.

1. Temperature effect

We tested the different temperatures of the aqueous solution with fixed [**B1**] = 5 mM in THF, [CTAB] = 0.4 mM. As shown in figure 5.5a, most of the objects are amorphous aggregates. When the aqueous solution temperature was increased to 60˚C, more rod-like structures were found than that in r.t. (Figure 5.5b). In 100˚C, most of the structures are rod-like. But the sizes between the rods are quite different, the big ones have a length ~10 μm and a width ~500 nm; the small ones have a length in the range of 2-3μm and a width ~200 nm (Figure 5.5c). It shows that the higher temperature leads to more ordered molecular packing, which can be attributed to the better solubility of the organic components in the aqueous solution to allow the nanostructures time to grow. However, we failed in reproducing the same experimental results. From figure 5.5d, we found that the big rods become shorter and wider, and the amount of small rods decreased a lot. This leads us to continue modifying the conditions.

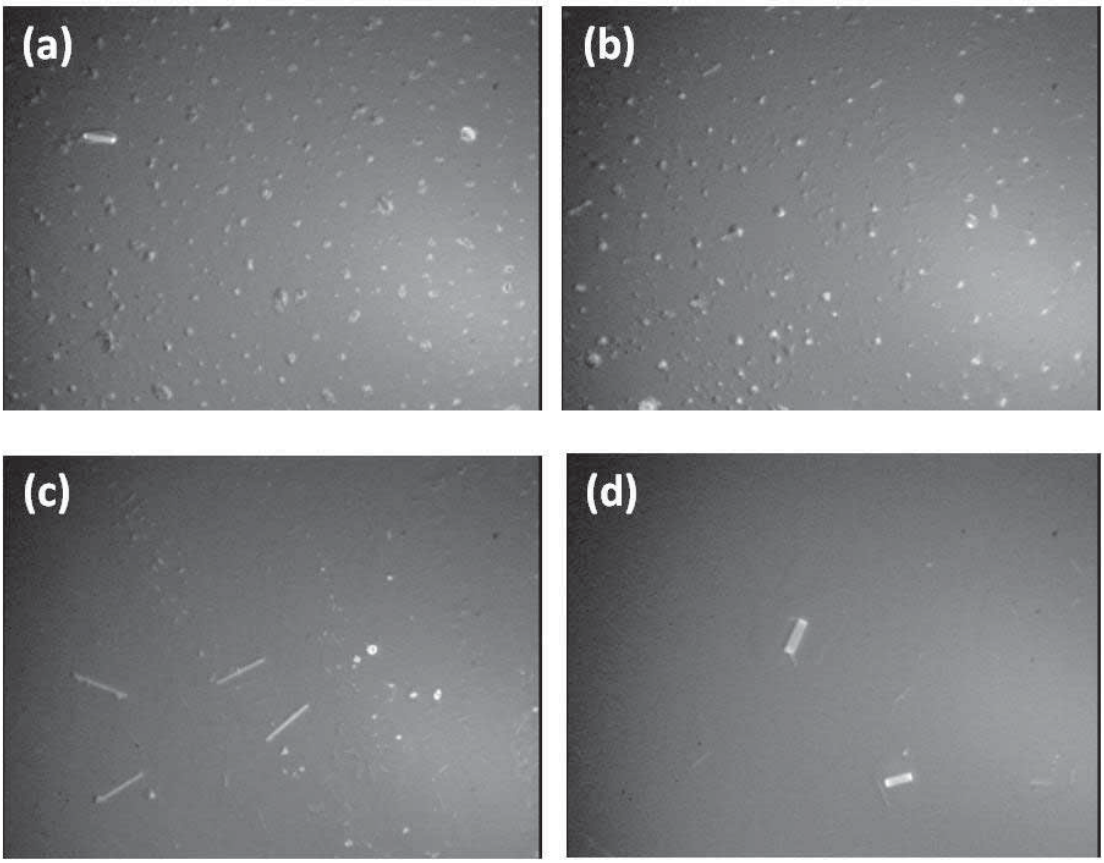

Figure 5.5: The epi-fluorescene images of NRs (a) r.t., (b) 60˚C, (c) 100˚C and (d) 100˚C (the same experiment carried out in the next day), image size: 80 μm × 80 μm (roughly)

2. Solvent effect

From the conclusion drawn in the temperature effect, we increased the [CTAB] from 0.4 mM to 1 mM in order to increase the solubility of **B1** in an aqueous solution. In the mean time, we also tested different solvents. Figure 5.6a is the sample from the THF stock solution, and b is the sample from DMSO. In DMSO, the amount of big rods is much larger than that in THF.

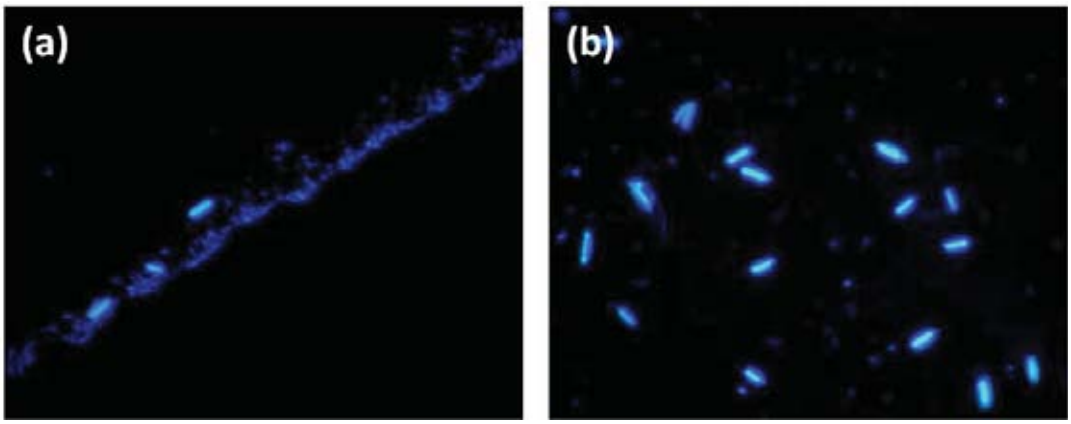

Figure 5.6: The epi-fluorescene images of NRs (a) THF (b) DMSO, image size: 100 μm × 100 μm

In the mean time, we also tried to add dopants into nanorods to tune the photophysical properties. The dopant used here is a red-emitter 2,3-dimethoxy rubrene (**R1,** Figure 5.7), which was synthesized by Dr. Christian Schäfer. We tested the doping experiments with both THF and DMSO. In the THF system, the rod-like morphology is seriously influenced by the

addition of dopants (Figure 5.8c, d) and the energy transfer efficiency is low (Figure 5.9). However, most of the **R1** molecule did not even co-assemble with **B1** in the DMSO system.

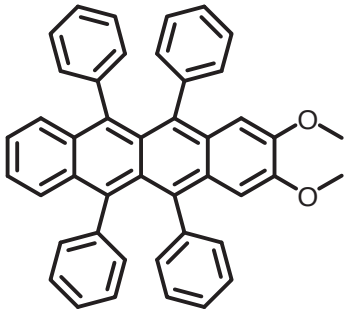

Figure 5.7: molecular structure of **R1**

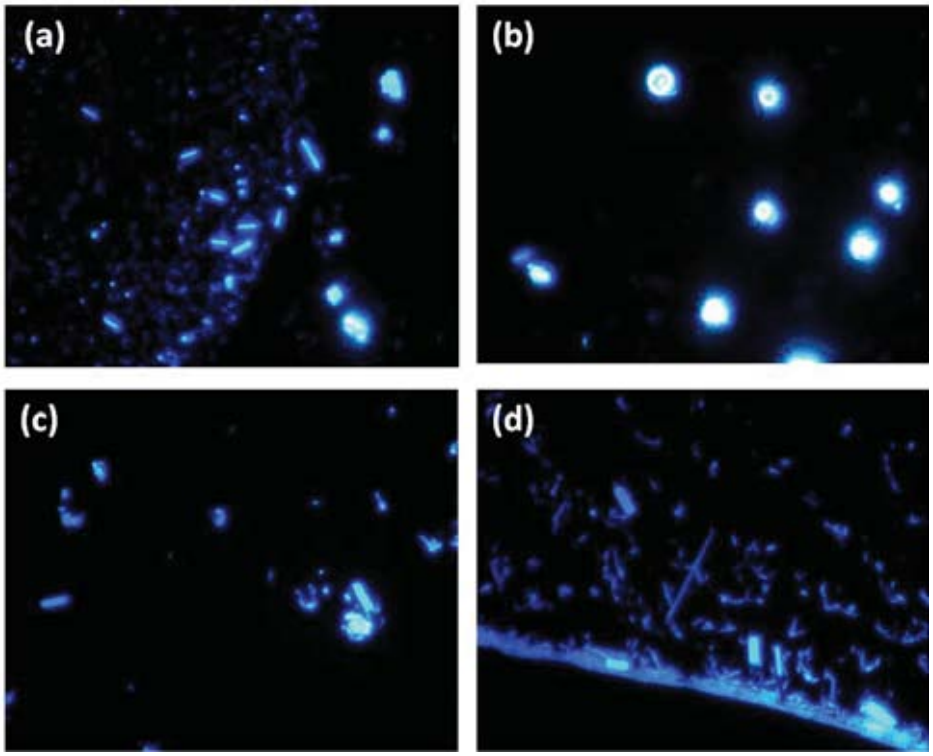

Figure 5.8: The epi-fluorescene images of NRs (a) 0.5% **R1** in THF, (b) 1% **R1** in THF, (c) 0.5% **R1** in DMSO and (d) 1% **R1** in DMSO, image size: 100 μm × 100 μm

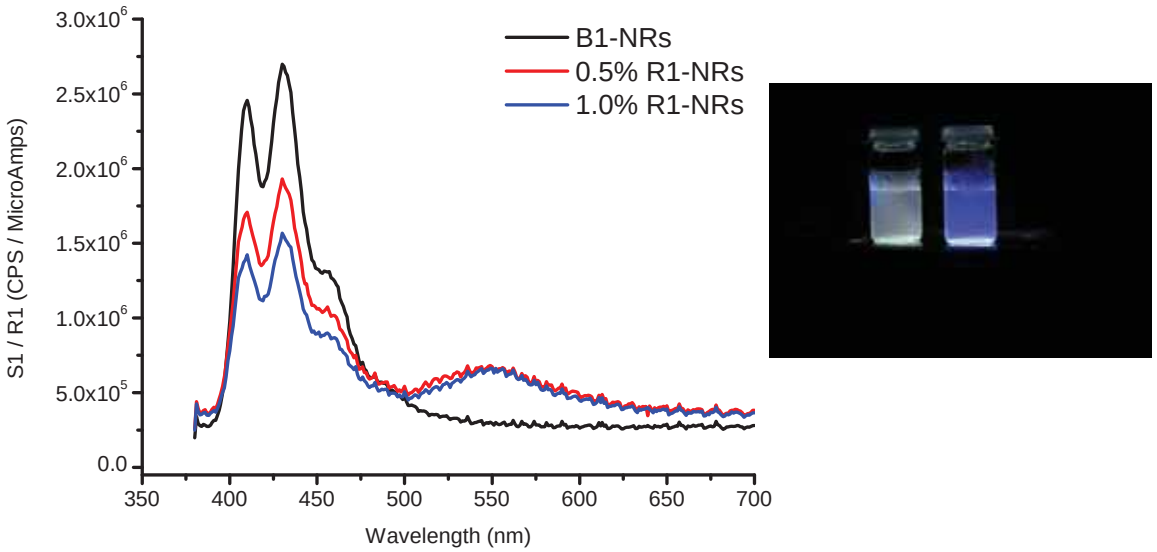

Figure 5.9: (Left)emission spectra of **B1**-NRs doped with 0.5% and 1% **R1**; (right) pictures of **B1** NRs and 1% **R1**-NRs under UV excitation (λ_{ex}= 365 nm)

After we successfully fine-tuned the condition (chapter 2-2), **R1** was also tested the doping of B1 rods under the conditions described in chapter 2 ([**B1**] = 0.5 mM in THF/ACN (1:1, v/v), [CTAB]=0.25 mM, 100 ˚C). As shown in the microscopy image in Figure 5.10, most of the **R1** molecules seem to form amorphous aggregates with **B1** and do not lead to nice rods. However, optimization of the experimental conditions might lead to white light-emitting nanorods (see fluorescence spactra and photographies in Figure 5.9).

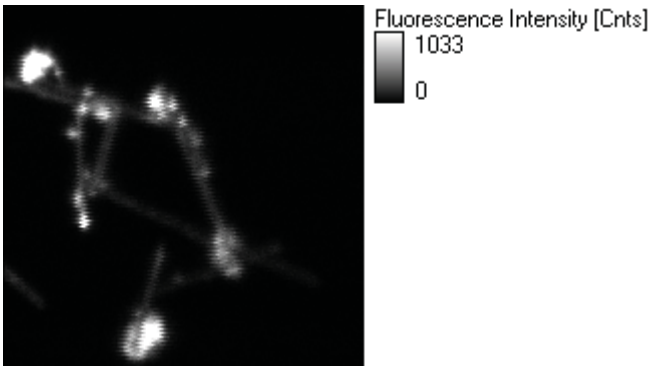

Figure 5.10: Fluorescence Intensity image of 1.5% **R1**-NRs, (14.4 × 14.4 μm), λ_{ex} = 375 nm, λ_{em} >500 nm

In summary, the nanostructure fabrication takes efforts and every experimental parameter should be taken into account. Furthermore, the addition of dopants can strongly affect the original morphology of the nano-scaled matrices.

5.12 The growth of 7/B16 nanoribbons

To gain a further insight of the **B16** nanoribbons formation mechanism, a video of **B16** NBs formation was taken by CCD camera under optical transmission mode. The selected images are displayed in the following Figures. After injection of **B16** stock solution of DCM into MeOH, the first minute was needed to search the whole area and to locate visible objects. Figure 5.11a is the first image taken and the rest of the images were recorded in a range of the first 30 s. It shows that this nanoribbons formation process is quite fast.

As shown in figure 5.11, the ribbons were grown from seeds. First, it took some time for the nucleation process, next, the molecules started to assemble and the ribbons growth took place.

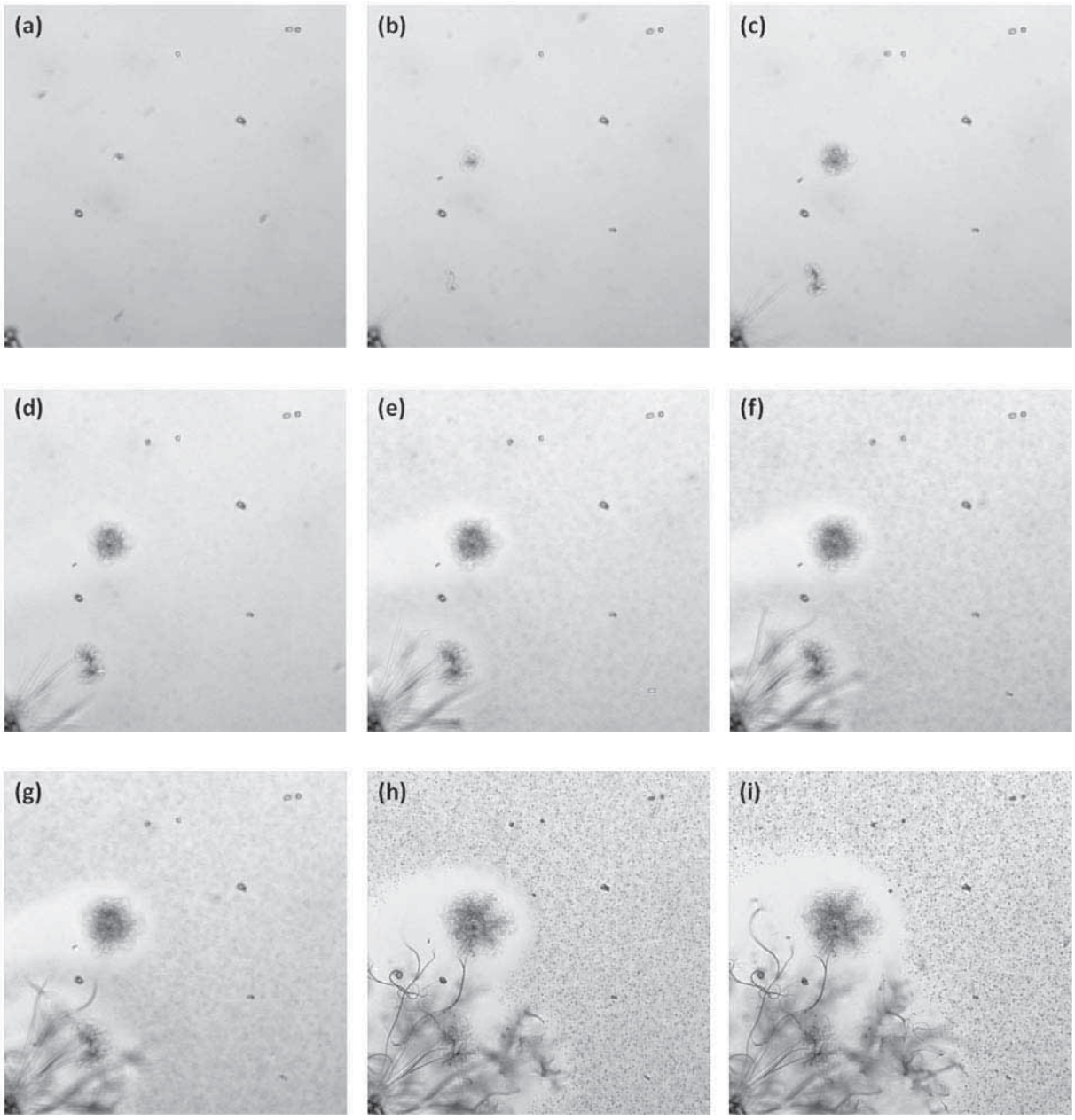

Figure 5.11: (a)-(f) are recorded in first 10 s, (g)-(i) are taken at 12, 23 and 30 s, image size: 400 × 400 μm

5.13 Synthesis

General procedure for 2,3-dialkyloxy-9,10-diphenyl-anthracenes:

0.5 mmol 2,3-dialkyloxy-anthraquinone were dissolved/suspended in 25 mL THF under argon and cooled down in an ice bath. PhLi (1.8 M in cyclohexane/Et_2O 7:3, 5 equiv.) was added dropwise and the solution stirred in the melting ice bath for 18 h. Afterwards, the reaction was given in NH_4Cl-solution and extracted with Et_2O several times. The combined org. layers were washed with water and brine, dried over $MgSO_4$ and the solvent was removed in vacuo. The residue was dissolved in Et_2O, heated to reflux and HI (57% in H_2O, 1 mL per 0.15 mmol quinone) was added dropwise. The reaction stirred at reflux for another 15 min, was allowed to cool down and given into $Na_2S_2O_5$-solution. The product was extracted with DCM. The org. layer was washed with water and brine, dried over $MgSO_4$ and the solvent was removed in vacuo. The product was isolated by column chromatography on silica gel and crystallized from DCM/MeOH to obtain it as a colorless solid if necessary.

2,3-dimethoxy-9,10-diphenyl-anthracene (**1/B1**):

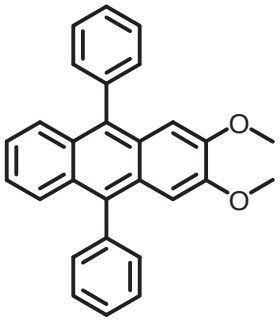

Yield: 87%.

^{1}H-NMR ($CDCl_3$, 300 MHz): δ(ppm) = 3.74 (s, 6 H, CH_3), 6.88 (s, 2 H, ArH), 7.27 (m, 2 H, ArH), 7.45-7.65 (m, 12 H, ArH). ^{13}C-NMR ($CDCl_3$, 300 MHz): δ(ppm) = 55.47 (OCH_3), 103.88 ($C_{Ar}H$), 124.21 ($C_{Ar}H$), 126.45 ($C_{Ar}H$), 126.84 ($C_{Ar,q}$), 127.40 ($C_{Ar}H$), 128.53 ($C_{Ar}H$), 129.12 ($C_{Ar,q}$), 131.15 ($C_{Ar}H$), 134.88 ($C_{Ar,q}$), 139.46 ($C_{Ar,q}$), 149.44 ($C_{Ar,q}$). HRMS (ESI, positive ions): calc. for $[C_{28}H_{22}O_2+Na]^+$: 413.1512; measured: 413.1509.

2,3-diethoxy-9,10-diphenyl-anthracene (**2**/**B2**):

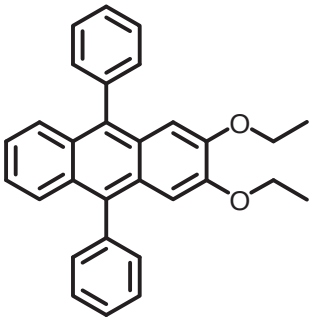

Yield: 88%.

^{1}H-NMR ($CDCl_3$, 300 MHz): δ(ppm) = 1.40 (t, ^{3}J=7.0 Hz, 6 H, CH_3), 3.94 (q, ^{3}J=7.0 Hz, 4 H, OCH_2), 6.88 (s, 2 H, ArH), 7.26 (m, 2 H, ArH), 7.45-7.65 (m, 12 H, ArH). ^{13}C-NMR ($CDCl_3$, 300 MHz): δ(ppm) = 14.33 (CH_3), 63.87 (OCH_2), 105.05 ($C_{Ar}H$), 124.06 ($C_{Ar}H$), 126.43 ($C_{Ar}H$), 126.89 ($C_{Ar,q}$), 127.31 ($C_{Ar}H$), 128.47 ($C_{Ar}H$), 129.01 ($C_{Ar,q}$), 131.20 ($C_{Ar}H$), 134.66 ($C_{Ar,q}$), 139.54 ($C_{Ar,q}$), 148.97 ($C_{Ar,q}$). HRMS (ESI, positive ions): calc. for $[C_{30}H_{26}O_2+Na]^+$: 441.1825; measured: 441.1823.

2,3-dibutyloxy-9,10-diphenyl-anthracene (**3**/**B4**):

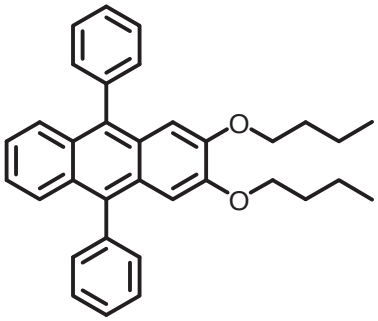

Yield: 50%

^{1}H-NMR ($CDCl_3$, 300 MHz): δ(ppm) = 0.92 (t, ^{3}J=7.3 Hz, 6 H, CH_3), 1.43 (m, 4 H, CH_2), 1.75 (m, 4 H, CH_2), 3.87 (t, ^{3}J=6.5 Hz, 4 H, OCH_2), 6.87 (s, 2 H, ArH), 7.26 (m, 2 H, ArH), 7.45-7.65 (m, 12 H, ArH). ^{13}C-NMR ($CDCl_3$, 300 MHz): δ(ppm) = 13.83 (CH_3), 19.19 (CH_2), 30.71 (CH_2), 68.08 (OCH_2), 105.18 ($C_{Ar}H$), 124.02 ($C_{Ar}H$), 126.43 ($C_{Ar}H$), 126.94 ($C_{Ar,q}$), 127.29 ($C_{Ar}H$), 128.47 ($C_{Ar}H$), 128.98 ($C_{Ar,q}$), 131.20 ($C_{Ar}H$), 134.63 ($C_{Ar,q}$), 139.60 ($C_{Ar,q}$), 149.36 ($C_{Ar,q}$). HRMS (ESI, positive ions): calc. for $[C_{34}H_{34}O_2+Na]^+$: 497.2451; measured: 497.2428.

2,3-dihexyloxy-9,10-diphenyl-anthracene (**4/B6**):

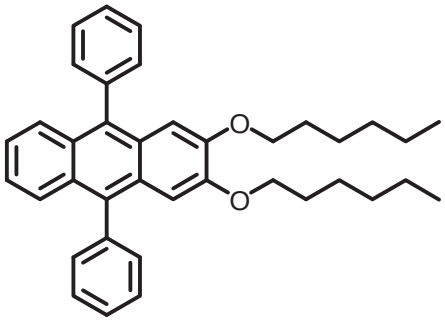

Yield: 52%.

^{1}H-NMR ($CDCl_3$, 300 MHz): δ(ppm) = 0.88 (t, ^{3}J=6.8 Hz, 6 H, CH_3), 1.20-1.45 (m, 12 H, CH_2), 1.75 (m, 4 H, CH_2), 3.85 (t, ^{3}J=6.6 Hz, 4 H, OCH_2), 6.85 (s, 2 H, ArH), 7.25 (m, 2 H, ArH), 7.44-7.64 (m, 12 H, ArH). ^{13}C-NMR ($CDCl_3$, 300 MHz): δ(ppm) = 14.01 (CH_3), 22.58 (CH_2), 25.65 (CH_2), 28.67 (CH_2), 31.55 (CH_2), 68.38 (OCH_2), 105.15 ($C_{Ar}H$), 124.02 ($C_{Ar}H$), 126.43 ($C_{Ar}H$), 126.93 ($C_{Ar,q}$), 127.30 ($C_{Ar}H$), 128.48 ($C_{Ar}H$), 128.97 ($C_{Ar,q}$), 131.20 ($C_{Ar}H$), 134.62 ($C_{Ar,q}$), 139.59 ($C_{Ar,q}$), 149.34 ($C_{Ar,q}$). HRMS (ESI, positive ions): calc. for $[C_{38}H_{42}O_2+Na]^+$: 553.3077; measured: 553.3089.

2,3-dioctyloxy-9,10-diphenyl-anthracene (**5/B8**):

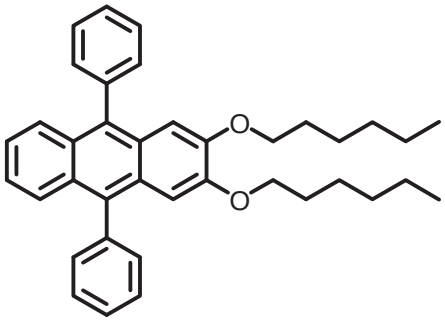

Yield: 62%.

^{1}H-NMR ($CDCl_3$, 300 MHz): δ(ppm) = 0.93 (t, ^{3}J=6.7 Hz, 6 H, CH_3), 1.25-1.50 (m, 20 H, CH_2), 1.81 (m, 4 H, CH_2), 3.90 (t, ^{3}J=6.6 Hz, 4 H, OCH_2), 6.91 (s, 2 H, ArH), 7.28 (m, 2 H, ArH), 7.49-7.69 (m, 12 H, ArH). ^{13}C-NMR ($CDCl_3$, 300 MHz): δ(ppm) = 14.08 (CH_3), 22.64 (CH_2), 25.99 (CH_2), 28.73 (CH_2), 29.25 (CH_2), 29.33 (CH_2), 31.78 (CH_2), 68.37 (OCH_2), 105.19 ($C_{Ar}H$), 124.01 ($C_{Ar}H$), 126.41 ($C_{Ar}H$), 126.93 ($C_{Ar,q}$), 127.28 ($C_{Ar}H$), 128.46 ($C_{Ar}H$), 128.97 ($C_{Ar,q}$), 131.19 ($C_{Ar}H$), 134.62 ($C_{Ar,q}$), 139.60 ($C_{Ar,q}$), 149.36 ($C_{Ar,q}$). HRMS (ESI, positive ions): calc. for $[C_{42}H_{50}O_2+Na]^+$: 609.3703; measured: 609.3733.

2,3-didecyloxy-9,10-diphenyl-anthracene (**6/B10**):

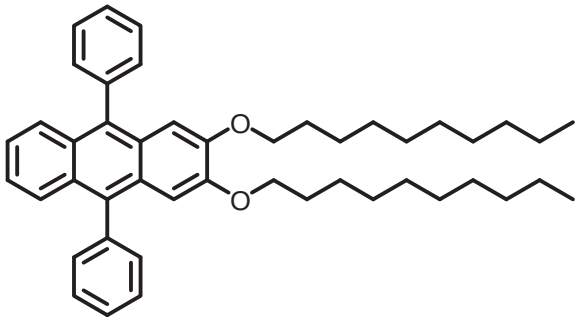

Yield: 35%.

^{1}H-NMR ($CDCl_3$, 300 MHz): δ(ppm) = 0.87 (t, ^{3}J=6.7 Hz, 6 H, CH_3), 1.20-1.45 (m, 28 H, CH_2), 1.74 (m, 4 H, CH_2), 3.84 (t, ^{3}J=6.6 Hz, 4 H, OCH_2), 6.84 (s, 2 H, ArH), 7.24 (m, 2 H, ArH), 7.45-7.65 (m, 12 H, ArH). ^{13}C-NMR ($CDCl_3$, 300 MHz): δ(ppm) = 14.11 (CH_3), 22.69 (CH_2), 25.98 (CH_2), 28.71 (CH_2), 29.34 (CH_2), 29.39 (CH_2), 29.55 (CH_2), 29.61 (CH_2), 31.91 (CH_2), 68.38 (OCH_2), 105.18 ($C_{Ar}H$), 124.01 ($C_{Ar}H$), 126.43 ($C_{Ar}H$), 126.93 ($C_{Ar,q}$), 127.29 ($C_{Ar}H$), 128.47 ($C_{Ar}H$), 128.97 ($C_{Ar,q}$), 131.20 ($C_{Ar}H$), 134.61 ($C_{Ar,q}$), 139.58 ($C_{Ar,q}$), 149.34 ($C_{Ar,q}$). HRMS (ESI, positive ions): calc. for $[C_{46}H_{58}O_2+Na]^+$: 665.4329; measured: 665.4324.

2,3-dihexadecyloxy-9,10-diphenyl-anthracene (**7/C16**):

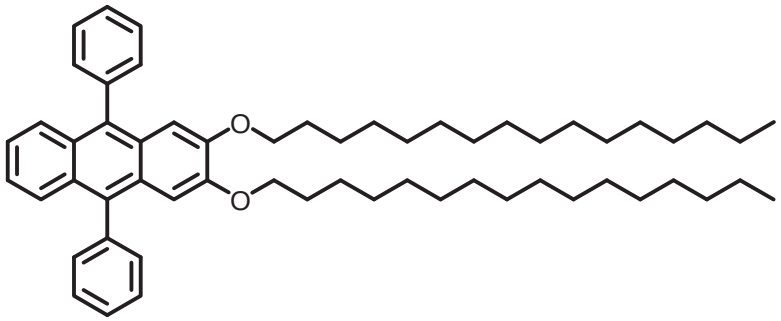

Yield: 50%

^{1}H-NMR ($CDCl_3$, 300 MHz): δ(ppm) = 0.87 (t, ^{3}J=6.7 Hz, 6 H, CH_3), 1.20-1.45 (m, 52 H, CH_2), 1.74 (m, 4 H, CH_2), 3.84 (t, ^{3}J=6.6 Hz, 4 H, OCH_2), 6.84 (s, 2 H, ArH), 7.24 (m, 2 H, ArH), 7.44-7.64 (m, 12 H, ArH). ^{13}C-NMR ($CDCl_3$, 300 MHz): δ(ppm) = 14.12 (CH_3), 22.69 (CH_2), 25.99 (CH_2), 28.72 (CH_2), 29.37 (CH_2), 29.41 (CH_2), 29.62 (CH_2), 29.67 (CH_2), 29.72 (CH_2), 31.92 (CH_2), 68.39 (OCH_2), 105.16 ($C_{Ar}H$), 124.01 ($C_{Ar}H$), 126.43 ($C_{Ar}H$), 126.93 ($C_{Ar,q}$), 127.29 ($C_{Ar}H$), 128.47 ($C_{Ar}H$), 128.97 ($C_{Ar,q}$), 131.21 ($C_{Ar}H$), 134.62 ($C_{Ar,q}$), 139.59 ($C_{Ar,q}$), 149.34 ($C_{Ar,q}$).

HRMS (ESI, positive ions): calc. for $[C_{58}H_{82}O_2+Na]^+$: 833.6207; measured: 833.6166.

Perfluoro long chain:[2]

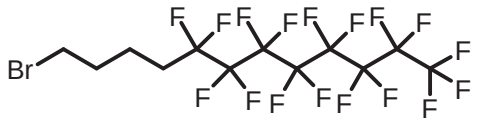

A mixture of 1.24 g (2.6 mmol)

5,5,6,6,7,7,8,8,9,9,10,10,11,11,12,12,12-heptadecafluorododecanol, 7 ml concentrated hydrobromic acid, 1.3 ml concentrated sulphuric acid, 0.1 g tetrabutylammonium hydrogensulphate and 7 ml benzene is stirred for 10 hours under reflux. Water is then added carefully and the mixture is extracted three times with Et_2O. The combined organic phases are washed with brine, dried over Na_2SO_4 and evaporated under reduced pressure. The crude product is purified by column chromatography on silica gel (eluent: DCM).

Yield: Quantitative

^{1}H-NMR (400 MHz, $CDCl_3$): δ = 1.74-1.70 (m, 2H, CH_2); 1.90-1.97 (m, 2H, CH_2); 2.06-2.15 (m, 2H, CH_2); 3.41 ppm (t, ^3J = 6.7 Hz, 2H, $BrCH_2$).

2,3-Bis-(5,5,6,6,7,7,8,8,9,9,10,10,11,11,12,12,12-heptadecafluoro-dodecyloxy)-9,10-diphenyl -anthracene **(F17)** :

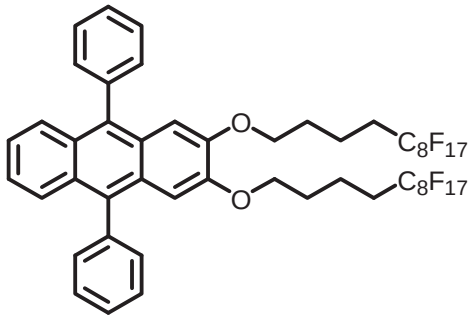

To a DMF solution (15 mL) containing 2,3-dihydroxy-9,10-diphenylanthracene (170 mg, 0.47 mmol) and potassium carbonate (330 mg, 2.39 mmol) 12-Bromo-1,1,1,2,2,3,3,4,4,5,5,6,6,7,7,8,8-heptadecafluoro-dodecane (1.3 g, 2.34 mmol) was added. The reaction was stirred at 80°C overnight. Afterward, the reaction was added to 50 mL of water and extracted with dichloromethane. The organic layer was washed over water, dried with $MgSO_4$.The solvent was removed in vacuo. The product was isolated by column chromatography on silica gel (eluent dichloromethane (DCM)/pentane, 1:4)

Yield: 65%

^{1}H-NMR ($CDCl_3$ 300 MHz): δ(ppm) = 1.81 (m, 4 H, CH_2), 2.11 (m, 2 H, CH_2), 3.86 (t, ^3J=6.6 Hz, 4 H, OCH_2), 6.84 (s, 2 H, ArH), 7.24 (m, 2 H, ArH), 7.45-7.65 (m, 12 H, ArH). ^{13}C-NMR ($CDCl_3$): δ(ppm) = 17.21 (CF_3), 28.32 (CF_2), 30.04 (CF_2), 30.67 (CH_2), 30.97 (CH_2), 67.59 (OCH_2), 105.23 ($C_{Ar}H$), 124.24 ($C_{Ar}H$), 126.48 ($C_{Ar}H$), 126.86 ($C_{Ar,q}$), 127.42 ($C_{Ar}H$), 128.54 ($C_{Ar}H$), 129.15 ($C_{Ar,q}$), 131.18 ($C_{Ar}H$), 134.86 ($C_{Ar,q}$), 139.49 ($C_{Ar,q}$), 148.96 ($C_{Ar,q}$). LRMS (MARDI m/z): calc. for [$C_{50}H_{32}F_{34}O_2$]: 1310.19; measured: 1310.20.

2-ester-fluorous ponytailed-9.10-diphenylanthracene **(PT):**

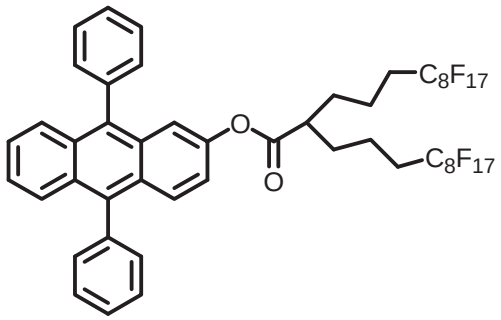

2-hydroxy-9,10-diphenyl anthracene (53mg, 0.15 mmol), dicyclohexylcarbodiimide (DCC, 38 mg, 0.18 mmol), 4,4-Dimethylaminopyridine (22.3mg, 0.18 mmol) and perfluoro-alkyl-carboxylic acid (150mg, 0.15 mmol)were given in 10 mL THF and 20 mL DCM under r.t.. The reaction was kept stirred overnight at r.t.. Afterwards, the mixture was filtered out the insoluble salts. The resulting filtration was given in water and extracted with DCM twice. The organic layer was dried over $MgSO_4$, and the solvent was removed in vacuo. The product was isolated by column chromatography on silica gel (eluent dichloromethane (DCM)/petroleum ether, 1:2) Yield: 56%.
^{1}H-NMR ($CDCl_3$ 300 MHz): δ(ppm) = 1.70 (m, 4 H, CH_2)1.82 (m, 4 H, CH_2), 2.08 (m, 4 H, CH_2), 2.62 (m, 1 H, OCH), 6.89 (s, 1 H, ArH), 7.10 (d, ^2J=5.1 Hz, 1 H, ArH), 7.30-7.36 (m, 1 H, ArH), 7.43-7.46 (m, 4 H, ArH) 7.50-7.73 (m, 10 H, ArH). ^{13}C-NMR ($CDCl_3$): δ(ppm) = 18.15 (CF_3), 29.72 (CF_2), 30.36 (CF_2), 30.68 (CF_2), 30.96 (CH_2), 31.44 (CH_2), 44.93 (CH), 116.57 ($C_{Ar}H$), 120.74 ($C_{Ar}H$), 127.09 ($C_{Ar}H$), 127.65 ($C_{Ar,q}$), 128.13 ($C_{Ar}H$), 128.47 ($C_{Ar}H$), 130.03 ($C_{Ar,q}$), 131.22 ($C_{Ar}H$), 136.97 ($C_{Ar,q}$), 138.71 ($C_{Ar,q}$), 147.44 ($C_{Ar,q}$) , 173.75 (COO). LRMS (MARDI m/z): calc. for [$C_{50}H_{30}F_{34}O_2$]: 1308.17; measured: 1308.20.

2,3-Bis(methoxy)-6,11-diphenyltetracene **(GT1)** :

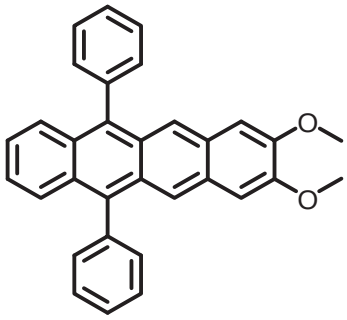

2,3-Bis(methoxy)tetra-6,11-quinone (1.13g, 3.55 mmol) was given in 10 mL THF under argon and cooled down in an ice bath. 6 mL of PhLi (1.8 M in dibutyl ether) were added dropwise and the reaction stirred in the melting ice bath over night. Afterwards, the solution was given in a saturated NH_4Cl-solution and extracted with diethyl ether twice. The organic layer was dried over $MgSO_4$, and the solvent was removed in vacuo. The residue was

dissolved in 20 mL of diethyl ether, protected from light, and heated to reflux. A 10 mL volume of HI (57% in water) was added dropwise under reflux and the mixture stirred at reflux for another 20 min. The reaction was allowed to cool, added to a 10% $Na_2S_2O_5$ solution, and extracted with diethyl ether. The organic layer was dried over $MgSO_4$, and the solvent was evaporated. The product was isolated by column chromatography on silica gel (eluent dichloromethane (DCM)/petroleum ether, 1:2) Yield: 37%. To obtain the product in a solid state, it can be crystallized from DCM/MeOH.

^{1}H NMR ($CDCl_3$, 300 MHz): δ (ppm) 3.92 (t, 3J = 6.5 Hz, 6 H, OCH3), 6.96 (s, 2 H, ArH), 7.21 (m, 2 H, ArH), 7.54-7.65 (m, 12 H, ArH), 8.05 (s, 2 H, ArH). ^{13}C NMR ($CDCl_3$, 300 MHz): δ (ppm)) 55.88 (OCH3), 104.56(CArH), 122.94 (CArH), 124.40 (CArH), 126.89 (CAr,q), 127.44(CArH), 128.46 (CArH), 128.53 (CAr,q), 128.96 (CArH), 131.62 (CAr,q),136.22 (CArH), 139.69 (CAr,q), , 140.30 (CAr,q).

HRMS (ESI, positive ions): m/z calcd for $[C_{32}H_{24}O_2]^+$ 440.1770,measd 440.1785.

2,3-Dimethoxy-5,6,11,12-tetraphenyltetracene **(R1)**:

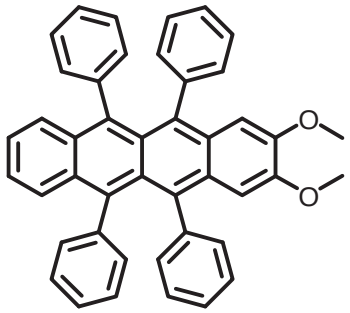

2,3-Dimethoxy-6,11-diphenyltetracene-5,12-dione (150 mg, 3.19×10^{-4} mol) was given in 10 mL THF under argon and cooled down in an ice bath. 0.9 mL of PhLi (1.8 M in dibutyl ether) were added dropwise and the reaction stirred in the melting ice bath until it reached r.t. The reaction continued stirring 30 mins at 65 ^{o}C. Afterwards, the reaction was allowed to cool down and given in a saturated NH_4Cl-solution and extracted with diethyl ether twice. The combined org. phases were washed with water, dried over $MgSO_4$ and the solvent was evaporated. The residue was dissolved in diethyl ether, protected from light and refluxed. 2 mL of HI (57% in water) were added slowly under reflux, which was continued for another 25 min. Afterwards, the reaction was allowed to cool down and given in a 10% $Na_2S_2O_5$-solution and extracted with diethyl ether. The org. phase was washed with water, dried over $MgSO_4$ and the solvent was removed in vacuo. The product was isolated by column chromatography on silica gel (eluent: DCM/ petroleum ether, 1:2) and crystallized from DCM/MeOH to give a red-orange powder in quantitative yield.

^{1}H-NMR (THF-d_8, 300 MHz): δ (ppm) = 3.48 (t, ^3J=6.3 Hz, 6 H, OCH_3), 6.51 (s, 2 H, ArH), 6.84-6.87 (m, 8 H, ArH), 7.01-7.09 (m, 14 H, ArH), 7.31 (m, 2 H, ArH).

^{13}C-NMR (THF-d_8, 200 MHz): δ(ppm) = 68.2 (OCH_3), 103.86 ($C_{Ar}H$), 125.25 ($C_{Ar}H$), 126.66 ($C_{Ar}H$), 126.69 ($C_{Ar}H$), 127.41 ($C_{Ar}H$), 128.22 ($C_{Ar}H$), 128.44 ($C_{Ar}H$), 129.41 ($C_{Ar,q}$), 129.59

($C_{Ar,q}$), 131.10 ($C_{Ar,q}$), 133.12 ($C_{Ar}H$), 133.38 ($C_{Ar}H$), 135.33 ($C_{Ar,q}$), 137.34 ($C_{Ar,q}$), 143.36 ($C_{Ar,q}$), 143.76 ($C_{Ar,q}$), 151.59 ($C_{Ar,q}$).
HRMS (ESI, positive ions): calc. for $[C_{44}H_{32}O_2]^+$: 592.2402; measured: 592.2406.

2,3-*bis*-decyloxy-9,10-*bis*-phenylethinyl-anthracene **(DDPEA)**:

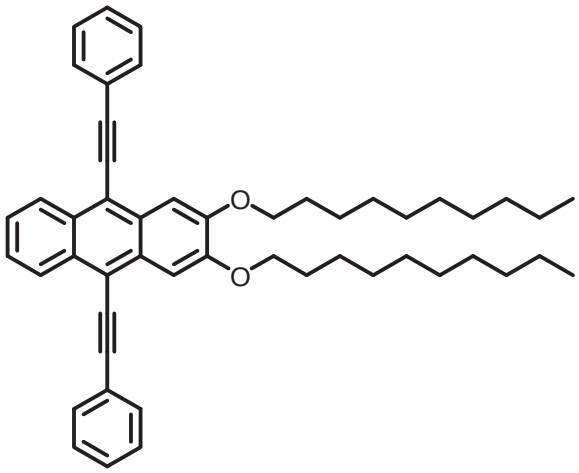

Phenylacetylene (0.21 mL, 1.92 mmol) was dissolved in 20 mL THF under argon and cooled down to -78°C. *n*-BuLi (1.6 M in hexanes, 1.25 mL, 2 mmol) was slowly added and the reaction stirred for 30 min at -78°C. 400 mg (0.77 mmol) 2,3-didecyloxy-anthraquinone were dissolved in 6 mL THF and slowly added to the solution. After another 30 min at -78°C, the reaction was allowed to reach rt and stirred for three days. Afterward, the reaction was added to 150 mL of water and extracted with diethyl ether. The organic layer was dried over $MgSO_4$, and the solvent was removed in vacuo. The residue was dissolved in 20 mL of diethyl ether, followed by $SnCl_2$ (520 mg, 2.3 mmol) and 20 mL HCl (2 M). The reaction was protected from light and heated to 60°C for 30 min, stirred at rt for 1.5 h and was given in water and extracted with DCM several times. The combined org. layers were washed with water, dried over MgSO4 and the solvent was evaporated. The product was isolated by column chromatography on silica gel (eluent: DCM/PET 1:4).
Yield: 42%.
^{1}H-NMR ($CDCl_3$): δ(ppm) = 0.88 (t, 3J=6.7 Hz, 6 H, CH_3), 1.20-1.46 (m, 24 H, CH_2), 1.55 (m, 4 H, CH_2), 1.97 (m, 4 H, CH_2), 4.25 (t, 3J=6.6 Hz, 4 H, OCH_2), 7.36-7.47 (m, 6 H, ArH), 7.55 (m, 2 H, ArH), 7.72 (m, 4 H, ArH), 7.84 (s, 2 H, ArH), 8.57 (m, 2 H, ArH). ^{13}C-NMR ($CDCl_3$): δ [ppm] = 14.11 (CH_3), 22.69, 26.17, 28.94, 29.37, 29.48, 29.60, 29.68, 31.92 (CH_2), 68.78 (OCH_2), 87.04 (Cq), 101.60 (Cq), 105.35 (CArH), 115.71 (CAr,q), 123.71 (CAr,q), 125.82 (CArH), 126.74 (CArH), 128.46 (CArH), 128.57 (CArH), 129.44 (CAr,q), 130.97 (CAr,q), 131.54 (CArH), 151.06 (CAr,q). HRMS (ESI, positive ions): calc. for $[C_{50}H_{58}O_2Na]^+$: 713.4329; measured: 713.4327.

2,3-*bis*-decyloxy-9,10-dicyano-anthracene **(DCNA)**:

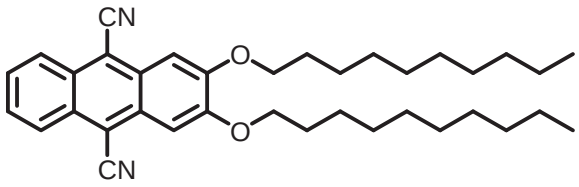

150 mg (0.23 mmol) 2,3-bis-decyloxy-9,10-dibromo-anthracene were suspended in 10 mL DMF under argon and 50 mg (0.56 mmol, 2.4 equiv.) CuCN were added. The reaction stirred at 170°C for three days. The reaction was allowed to cool and added to a mixture of 20 mL ethylene diamine and 60 mL water. It was extracted with Et_2O several times and the combined org. layers were washed with water, dried over $MgSO_4$ and the solvent was removed in vacuo. The residue was absorbed on silica gel and the product isolated by column chromatography (eluent: Started with DCM/PET, 1:4 and finished with DCM/PET, 1:2).
Yield: 76%.
^{1}H-NMR ($CDCl_3$): δ(ppm) = 0.86 (t, ^3J=6.5 Hz, 6 H, CH_3), 1.20-1.47 (m, 24 H, CH_2), 1.55 (m, 4 H, CH_2), 1.95 (m, 4 H, CH_2), 4.21 (t, ^3J=6.5 Hz, 4 H, OCH_2), 7.46 (s, 2 H, ArH), 7.69 (m, 2 H, ArH), 8.32 (m, 2 H, ArH). ^{13}C-NMR ($CDCl_3$): δ(ppm) = 14.10 (CH_3), 22.68, 26.01, 28.80, 29.35, 29.38, 29.57, 29.62, 31.91 (CH_2), 69.35 (OCH_2), 103.04 ($C_{Ar}H$), 107.72 ($C_{Ar,q}$), 116.51 (CN), 125.42 ($C_{Ar}H$), 128.30 ($C_{Ar}H$), 130.22 ($C_{Ar,q}$), 130.24 ($C_{Ar,q}$), 153.39 ($C_{Ar,q}$). HRMS (ESI, positive ions): calc. for $[C_{36}H_{48}O_2N_2]^+$: 540.78; measured: 540.12.

5.14 References

1. Bahlmann, K.; Hell, S. W. *J. Microscop.* **2000**, *200*, 59.
2. Glettner, B.; Liu, F.; Zeng, X.; Prehm, M.; Baumeister, U.; Ungar, G.; Tschierske, C. *Angew. Chem. Int. Ed.***2008**, *47*, 5862.

Compound list

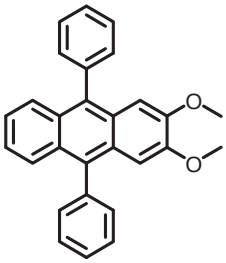

B1

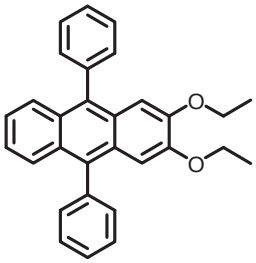

B2

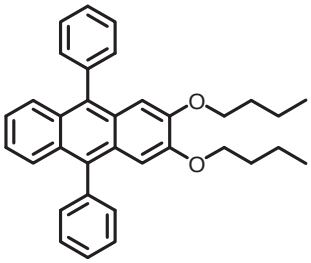

B4

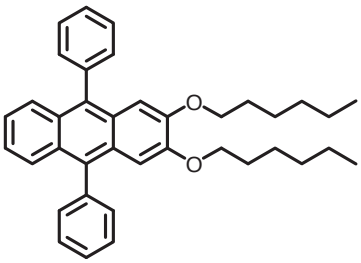

B6

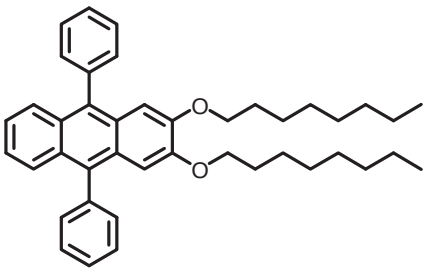

B8

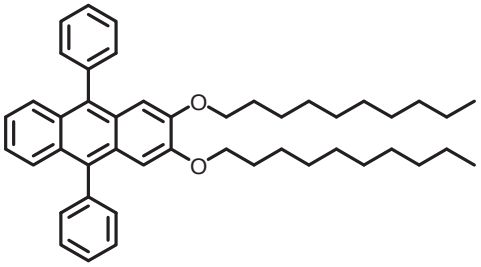

B10

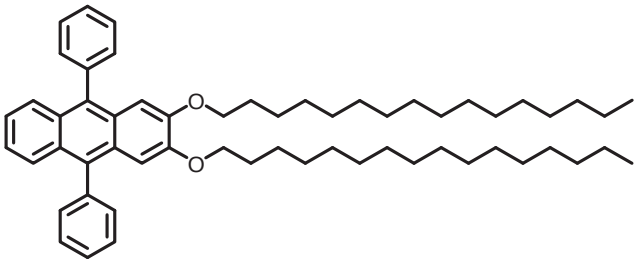

B16

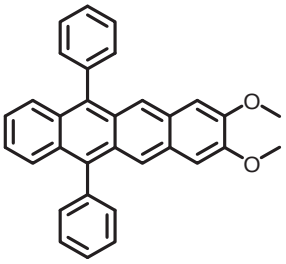

GT1

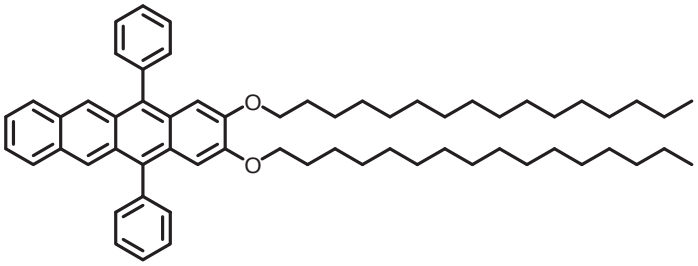

G16

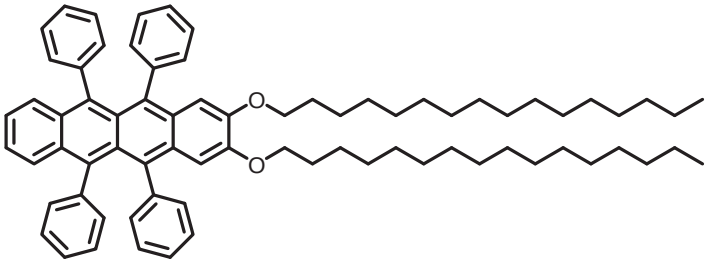

R16

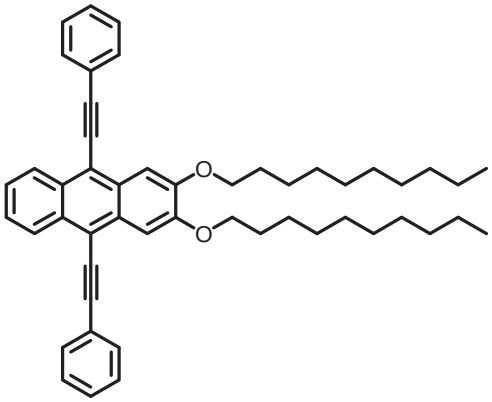

DDPEA

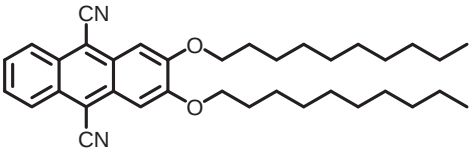

DCNA

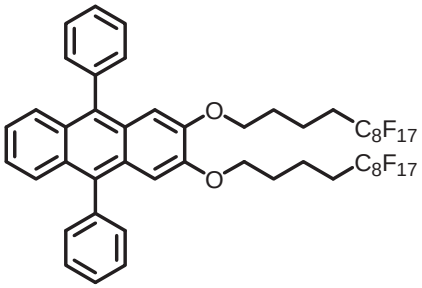

F17

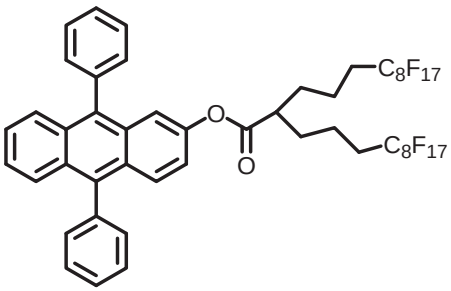

PT

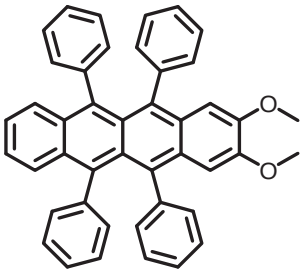

R1